Coastalock™ Performance on a Permeable Breakwater Slope

Model Tests on the Influence of a Permeable Core, Unit Modifications and Toe Support on the Hydraulic Performance of an Ecological Armour Unit

CIE5060-09: MSc Thesis

A.D. Ławniczak

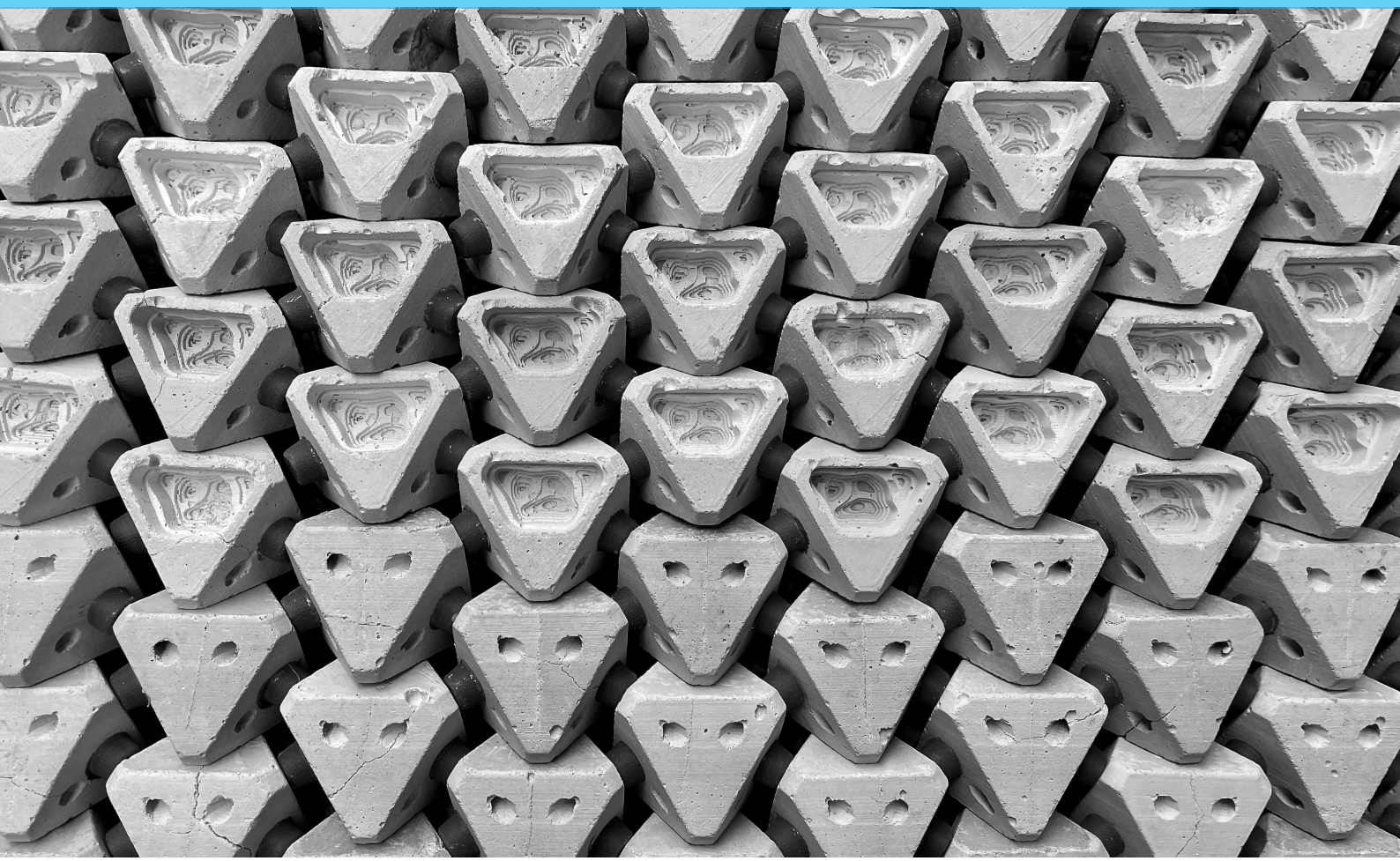

ECONCRETE

TU Delft

Coastalock™ Performance on a Permeable Breakwater Slope

Model Tests on the Influence of a Permeable Core, Unit Modifications and Toe Support on the Hydraulic Performance of an Ecological Armour Unit

by

A.D. Ławniczak

4482492

Faculty of Civil Engineering and Geosciences
Department of Hydraulic Engineering

April 3rd 2024

Thesis committee:

Dr. ir. B. Hofland,	TU Delft, Chair
Ir. J.P. Van den Bos,	TU Delft
Prof. dr. ir. M.R.A. Van Gent,	TU Delft
J. Gutiérrez Martínez, MSc.	ECOncrete Aqua SL

Cover image: Small-scale physical model setup of a Coastalock armour layer with long, 22.5% spacing, protrusions.

ECONCRETE

TU Delft

ECONCRETE

TU Delft

I would like to acknowledge the use of ChatGPT, an AI language model developed by OpenAI (2022), as a writing aid during the preparation of this thesis.

ChatGPT provided assistance with general language refinement, including:
suggestions on improving coherence, clarity enhancement for reader understanding,
correcting grammatical errors and punctuation usage,
and ensuring consistency in terminology and style.

Preface

The thesis presented here serves as the culmination of my Master of Science degree in Hydraulic Engineering from the Faculty of Civil Engineering at the Technical University of Delft. This research project was conceived, executed, and documented through a collaboration between TU Delft and ECOncrete.

I distinctly recall my first visit to the Hydraulic Engineering Laboratory at the age of 14, during a science class field trip to the TU Delft. The sight of the laboratory's physical model setups, intricate measurement instruments, and the impressive wave flumes left an lasting impression on me. Little did I know then that, 13 years later, I would have the privilege of conducting physical model tests in the same laboratory. During my time there, I enthusiastically chatted with anyone who crossed my path (regardless of whether they were willing listeners or not), be it teachers, students, visitors, or high-schoolers. When interacting with the latter, I found myself reminiscing about standing in the lab for the first time. Although, I rarely had the luxury of standing, as the project demanded meticulous placement a total of nearly 11 thousand Coastalock units on the slope, requiring me to work on my knees, alongside constant running from valve to valve to fill, level, or empty the wave flume. I fondly look back on the past year, during which I learned a lot about the subject matter of coastal engineering and physical scale modeling, as well as about myself.

This endeavour would not have been possible without the contributions of many individuals, making it truly a team effort.
Firstly, I extend my gratitude to my graduation committee for their unwavering support throughout this journey. Bas, as the Chair of the committee, I am grateful for your boundless positivity and insightful guidance during challenging times. Your enthusiasm for all aspects of hydraulic engineering, whether directly related to my project or not, was infectious and inspiring. Jorge, representing ECOncrete, I thank you for entrusting me with this project and providing invaluable insights into the inner workings behind the development of concrete armour units, as well as your guidance throughout this process. Jeroen, your oversight of the research's broader objectives and its relevance to ECOncrete's goals was instrumental. Marcel, your expertise and feedback significantly enhanced the quality and clarity of my final work.
I also extend my appreciation to the entire staff of the HE Laboratory. Chantal and Pieter, your critical insights were crucial in refining my physical model setup. You demonstrated that questions like 'What do you want to measure?' and 'How do you want to measure it?' are not always straightforward. Jennifer, your help with all programming or software-related challenges, and easing the daunting task of processing several hard drives worth of raw data, were absolutely essential for completing this project. Arie and Arno, your practical assistance and technical expertise were key in translating designs into tangible testing setups. I would never have known that I had to wash the stones before they were placed into the flume. Frank, your support in installing the measurement equipment was greatly appreciated. Furthermore, I am grateful to Noa and the Coastalock design team for their assistance in navigating the intricacies of the armour unit and protrusion design.
Lastly, I express my deepest gratitude to my parents and Vera for their unwavering support, both practical and emotional, throughout the duration of this project. Your dedication, even in mundane tasks such as cleaning 700 model units and attaching 1400 protrusions, not once but twice, in your spare time, made the work not only more efficient but also much more enjoyable.

Settle in, relax, and enjoy the read.

A.D. Ławniczak
the Hague, April 3rd 2024

Summary

Coastlines worldwide face increasing threats from erosion due to rising sea levels and more frequent extreme weather events. To mitigate these risks, coastal protection structures are crucial. Among these, concrete armour units are widely used for their durability and cost-effectiveness. However, traditional "armouring" methods often lead to habitat degradation and loss of biodiversity. In response, ECOncrete developed Coastalock, an innovative armour unit designed to integrate coastal protection with marine habitat creation. Initial tests on impermeable slopes under wave loading in deep water conditions revealed that tight placement of the units resulted in significant pore pressure gradients across the top layer, leading to failure (Molenkamp, 2022, Gutiérrez et al., 2023). Further quantification of the hydraulic performance of the armour unit is needed within its development cycle.

This thesis investigates the hydraulic performance of Coastalock armour layers, with and without modification, as part of permeable breakwater structures, with a focus on stability, overtopping, and reflection characteristics. The primary research objective is to:

> *Describe the hydraulic performance with respect to stability, overtopping and reflection of a Coastalock armour layer on a permeable breakwater slope supported by a toe.*

Drawing from an extensive literature review to establish theoretical frameworks and insights into Coastalock behavior, and similar units, this study includes physical model tests in the 2D wave flume at Delft University of Technology. The primary aim of the research is to address gaps in understanding Coastalock response to varying wave conditions and wave steepness. This investigation includes modifying units with protrusions to enforce armour spacing, a method utilized in preliminary research to address issues of limited permeability in the armour layer. Additionally, the study examines the impact of toe berms on diverse underlayers, assessing the armour layer's susceptibility to sliding.

To address the main research question, stability measurements were conducted based on video-based observations and Structure from Motion photogrammetry. The latter method enabled the creation of 3D models of the armour layer at various stages of exposure to waves, allowing for the tracking of armour layer deformation and monitoring of damage progression leading to eventual failure. Furthermore, measurements of overtopping discharge and reflection coefficient were performed to provide comprehensive insights into Coastalock performance.

The failure mechanism observed in a Coastalock armour layer on permeable core slopes attributed to built-up pressures exceeding self-weight and interlocking capabilities during wave run-down, resulting in a phenomenon known as 'breathing'. This involves upward movement perpendicular to the slope during wave run-down and downward movement during wave run-up. The movement of armour units during wave attack results in some units failing to return to their original positions, with those displaced furthest from the slope perpendicular being the last to resettle. Friction and partial interlocking contribute to the formation of a bulge in the armour layer, growing in size and magnitude, finally leading to extraction. Despite similarities to pressure-induced uplift in traditional block revetments, failure occurs before significant movement extends to surrounding structures. The observed gradual uplift may hint at an arching mechanism, as described by Van den Berg (2020).

The observed increase in 'breathing' and extraction thresholds with larger inter-unit void sizes, initially noted for an impermeable core (Molenkamp, 2022), was confirmed for the permeable core structure. The absence of a corresponding increase for s_{0p}=0.04 waves, compared to impermeable cores, may be attributed to reduced maximum run-down levels on permeable cores, affecting stability by minimizing variability in targeted areas. Nonetheless, the lack of comparative data for impermeable cores prevents definitive confirmation of this hypothesis. A noticeable decrease in the measured γ_f, was observed for both tested armour spacings compared to impermeable core results. A prediction equation is presented for reflection based on reanalyzed data from the impermeable core, incorporating considerations of armour spacing, wave steepness, and permeable core, for the 'San Diego' configuration.

The use of protrusions made the use of a new configuration mandatory due to the protrusion placement, called the 'Protrusion Optimized' configuration, with an orientation change from cavity upwards to downwards at SWL. In $s_{0p} = 0.04$ conditions, short protrusions reduced the stability number threshold for 'breathing' at 10% spacing, from N_s=3.6 to 3.2, maintaining extraction thresholds. Long protrusions at 22.5% spacing prevented filter layer migration seen at 20% spacing without protrusions and reached stability numbers up to 4.2 without 'breathing' or extraction. Long protrusions hinted at nearing the 'breathing' threshold at N_s=4.2, based on the comparison of maximum elevation changes of the armour layer. For s_{0p}=0.02, neither protrusion type showed 'breathing' or extraction, attributed to the 'reservoir effect'. γ_f results are presented in Table 1. Incorporating protrusions and transitioning to the 'Protrusion Optimized' configuration significantly increased reflection, attributed to increased surface area and reduced permeability due to void obstruction, diminishing internal dampening within the core.

Additionally, roughness coefficient based on a wider range for the breaker parameter, as presented in Table 1, was obtained, showcasing higher coefficients when compared to values for s_{0p}=0.04 ($\xi_{m-1,0} \approx 3$). This observation confirms the tendency for the roughness factor to exhibit a slight inclination for larger wave periods, resulting in higher levels of overtopping.

Spacing	Core	Configuration	$\gamma_{f,CL,wide}$	$\gamma_{f,CL,s_{0p}=0.04}$
S-10%	Impermeable	'San Diego'	0.76	0.75
S-10%	Permeable	'San Diego'	0.72	0.69
P-10%	Permeable	'PO-SWL'	0.71	0.65
S-20%	Permeable	'San Diego'	0.66	0.65
P-22.5%	Permeable	'PO-SWL'	0.67	0.65

Table 1: Comparison of roughness factors for the EuroTop equation (2018) derived from Coastalock model testing with simple spacing (S) or protrusions (P) in varying configurations on a slope with permeable core, for $3 < \xi_{m-1,0} < 5$ to s_{0p}=0.04 ($\xi_{m-1,0} \approx 3$).

Investigating orientation adjustments, shifting from cavity upwards to downwards at the midpoint between SWL and the bottom row resulted in increased 'breathing' and extraction thresholds to N_s=3.5 and 3.8, respectively. No extraction was observed when all units were oriented upwards for N_s=3.9. When considering the extraction location in relation to the rundown level, it corresponds to $R_{d,f}/H_s$ values of -1.3 for configurations with lowered orientation change or exclusively upwards-oriented units. This aligns closely with the critical loading location for traditional block revetments, just above maximum run-down, estimated at $R_{d2\%}/H_s$=-1.5 (CIRIA, 2007), nearly doubling the value compared to the shift at SWL. The presence and positioning of orientation changes adversely affected armour layer stability, likely due to buoyancy disparities from cavity placement. Contrary to expectations, upwards-facing units led to an increase in roughness coefficients, indicating smoother slopes, hypothesized as being caused due to water retention function of the cavities. An unexpected increase of 2% in reflection was observed for all units facing upwards. This increase is attributed to water retention within the upwards-facing cavities, impacting energy dissipation and resulting in higher reflection coefficients

The presence of toe berms, regardless of surface roughness, showed no significant impact on the damage progression or location of a Coastalock armour layer, regardless of protrusion length. No downslope movement of selection of Coastalock throughout the slope larger than $0.07D_{n,CL}$ was observed, well below the threshold of $0.20D_{n,CL}$ possibly indicative of near extraction.

Recommendations have been made for future armour unit development based on the promising results of the 22.5% protrusion. Considering a safety factor of 1.5 for overload conditions and the brittle nature of failure, a recommended design stability number of $N_s = 2.6$ is suggested for surging waves in deep water conditions. Additionally, the unit's demonstrated overtopping reduction capabilities, orientation flexibility, and an 11% reduction in unit count per slope based on measurements offer significant benefits. This reduction not only decreases concrete consumption but also shortens project duration by reducing the number of units required, lowering emissions and construction costs.

The findings presented here should be considered preliminary, serving as an initial examination into Coastalock application on breakwaters slopes, armour unit alterations in the form of protrusions, and the use of loose rock toe berms to support the armour layer.

Contents

Nomenclature

List of Symbols

Greek

Symbol	Definition	Unit
α_b	Slope angle of breakwater	[°]
α_f	Foreshore slope angle	[°]
α_r	Relative angle between the armour unit sections according to schematised S-profile (Van den Berg et al., 2020)	[°]
α_t	Toe slope angle	[°]
α_δ	Wave damping fitting coefficient	[-]
β	1. Angle of wave attack relative to normal on structure 2. Deviation of the armour sections' angle from the design slope (Van den Berg et al., 2020)	1. [°] 2. [°]
γ	JONSWAP peak enhancement factor	[-]
γ_b	Overtopping influence factor for a berm	[-]
γ_f	Overtopping influence factor for the permeability and roughness for elements on the slope	[-]
γ_v	Overtopping influence factor for a vertical wall on the slope	[-]
γ_β	Overtopping influence factor for oblique wave attack	[-]
Δ	Relative density, defined as $\Delta = \frac{\rho_{CL} - \rho_w}{\rho_w}$	[-]
δ	Dimensionless damping coefficient	[-]
ζ	Iribarren breaker parameter	[-]
ζ_p	Iribarren breaker parameter related peak wave period	[-]
ζ_{0p}	Iribarren breaker parameter for irregular waves	[-]
Λ	Leakage length	$[m]$
ρ	Mass density	$[kg/m^3]$
ρ_{CL}	CoastaLock mass density	$[kg/m^3]$
ρ_{sw}	Salt water mass density	$[kg/m^3]$
ρ_w	Fresh water mass density	$[kg/m^3]$
ϕ	Packing density	[-]
ϕ_F	Filter layer piezometric head	$[m]$
ϕ_T	1. Top layer piezometric head	$[m]$

Latin

Symbol	Definition	Unit
A	Cross sectional area	$[m^2]$
a	Intercept parameter of Coastalock reflection prediction equation	[-]
B	Crest width	$[m]$
b	1. Core width 2. Slope parameter of Coastalock reflection prediction equation	1. $[m]$ 2. [-]
B_t	Toe width	$[m]$

Symbol	Definition	Unit
c	Spacing parameter of Coastalock reflection prediction equation	[-]
C_a	Viscous coefficient of hydraulic gradient	[-]
C_b	Drag coefficient of hydraulic gradient	[-]
C_c	Inertia force coefficient of hydraulic gradient	[-]
C_D	Drag coefficient	[-]
C_I	Inertia coefficient	[-]
C_L	Lift coefficient	[-]
C_r	Reflection coefficient	[-]
D	1.Top layer thickness 2. Dimensionless incoming to internal wave length scaling factor	1. $[m]$ 2. [-]
d	Core permeability parameter of Coastalock reflection prediction equation	[-]
d_F	Filter layer thickness	$[m]$
D_n or d_n	Nominal armour unit diameter	$[m]$
d_T	Top layer thickness	$[m]$
f	Influence coefficient of rock size on notional permeability	[-]
F_C	Force due to interlocking	$[N]$
F_D	Drag force	$[N]$
F_F	Friction force	$[N]$
F_f	Flow force	$[N]$
F_G	Gravitational force	$[N]$
F_I	Inertial force	$[N]$
F_L	Lift force	$[N]$
F_p	Pressure force	$[N]$
$F_{R,B}$	Resistance to movement by friction between blocks	$[N]$
$F_{R,S}$	Resistance to sliding by friction with slope	$[N]$
F_S	Seepage force	$[N]$
F_w	Wave force	$[N]$
g	1. Acceleration of gravity 2. Influence coefficient of layer thickness on notional permeability	1. $[m/s^2]$ 2. [-]
H	Local wave height	$[m]$
H_{m_0}	Spectral significant wave height	$[m]$
h_m	Water depth in front of structure	$[m]$
h_l	Leeward berm or shoulder level	$[m]$
H_s	Significant wave height (equal to H_{m0}	$[m]$
h_t	Seaward toe level	$[m]$
i	Hydraulic gradient	[-]
k	Wave number	$[m^{-1}]$
KC	Keulegan-Carpenter number	[-]
K_d	Hudson stability factor	[-]
k_F	Filter layer permeability	$[m/s]$
k_T	Top layer permeability	$[m/s]$
L	1. Characteristic loading length 2. Wave length	$[m]$
L_1	Length of section 1 of schematized approach (Van den Berg et al., 2020)	$[m]$
L_1	Length of section 2 of schematized approach (Van den Berg et al., 2020)	$[m]$
L'	Wave length inside permeable structure	$[m]$
L_0	Deep water wave length	$[m]$
$L_{m-1.0}$	Wave length calculated of the first negative moment of the wave spectrum	$[m]$
L_p	Peak wave length	$[m]$

Symbol	Definition	Unit
m_0	Zero-th moment wave energy	$[m^2]$
n	Porosity	[-]
$N_{\#d}$	Number of armour units within strip of breakwater	[-]
N_{od}	Number of displaced units	[-]
N_s	Stability number	[-]
P	Notional permeability	[-]
q	Overtopping discharge per meter of structure	$[m^3/m/s]$
R_c	Crest freeboard	$[m]$
R_d	Run-down level	$[m]$
R_u	Run-up level	$[m]$
Re	Reynolds number	[-]
S	Armour spacing	[-]
S_l	Leeward shoulder width	$[m]$
S_s	Seaward shoulder width	$[m]$
s_0	Wave steepness with deep water wave length (= H/L)	[-]
T	Wave period	$[s]$
t_a	Armour layer thickness	$[m]$
T_p or T_{0_p}	Peak wave period	$[s]$
$T_{m-1.0}$	Wave period of the first negative moment of the wave spectrum	$[s]$
t_t	Toe thickness	$[m]$
t_u	Underlayer thickness	$[m]$
$\hat{u}_\delta$	Characteristic near bed velocity	$[m/s]$
V	Volume	$[m^3]$
v	Flow velocity	$[m/s]$
v_F	Filter layer flow velocity	$[m/s]$
v_T	Top layer flow velocity	$[m/s]$

1

Introduction

This chapter serves as an introduction to the research at hand and provides a roadmap for the remainder of the report. The aim of this research is to investigate the hydraulic performance of Coastalock, a single layer uniformly placed concrete armour unit designed to mimic inter- and sub-tidal habitats, to offer insights for coastal engineering applications. The chapter begins with an overview of the relevant background information on breakwaters, concrete armour units, and introduces Coastalock by ECOncrete, along with the relevance of physical modelling. The subsequent section provides an analysis of the research problem, followed by an outline of the scope and the limitations of the study. The next section is dedicated to state the research objective and accompanying research questions, as well as the method of approach. Finally, the chapter concludes with an overview of the subsequent chapters of that explore particular aspects of the research.

1.1. Background information

1.1.1. Relevance

The prediction of an ever-accelerating influx of people to coastal zones over the coming decades has heightened concerns over the potential dangers of coastal erosion caused by natural hazards (Neumann et al., 2015). Hard stabilization methods, such as breakwaters, sea walls, groynes and revetments, have traditionally been employed to mitigate coastal erosion. Concrete armour is widely used due to its high level of durability, robustness, ease of production and cost effectiveness (Cooke et al., 2020; Pilkey and Cooper, 2012). According to Chapman (2011), it is inevitable that coastline "armouring" will continue to rise because of the growing human population, rapid urbanization, and heightened desire for and value of coastal property, in contrast to projected changes in sea level and storm surges induced by climate change. The alteration of the shorelines, as a result of "armouring" is of great effect on shallow-water coastal systems, resulting in a degradation or destruction of habitats and the loss of ecologically trivial species that thrive in such habitats (Gittman et al., 2015). Key contributors to the degradation of habitats are the low surface complexity and non-natural composition of coastal marine infrastructure, failing to provide favourable conditions for the development of diverse marine habitats (Firth et al., 2015). This results in a less diverse ecosystem dominated by non-indigenous species (Glasby et al., 2007), and marine growth on breakwaters significantly differing from that found in adjacent habitats (Lam et al., 2009). It is ECOncrete's goal to design an ecological armour unit that will enhance breakwaters and shoreline protection systems by encouraging development of healthy marine ecosystems, while maintaining all structural and functional qualities.

1.1.2. Breakwaters

Breakwaters are a crucial component of coastal defence systems and are commonly found in coastal areas. They serve various functions, such as protecting man-made structures from incoming wave attack, guiding currents, providing safe anchorage and mooring to ships in ports and harbours, or protecting beaches from erosion. Different types of breakwaters exist, with varying structural features, including mound types, monolithic types, and composite types.

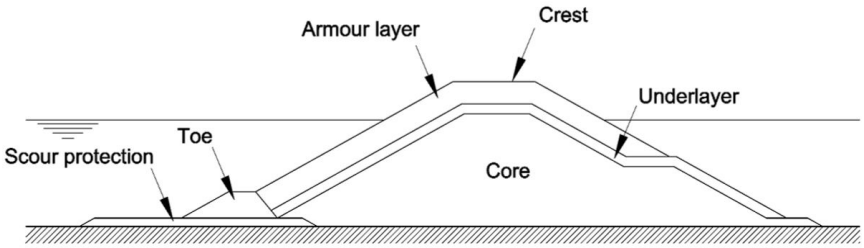

Figure 1.1: Typical mound breakwater cross-section (CIRIA, 2007).

This thesis focuses solely on mound-type breakwaters, which dissipate the incoming wave energy through wave breaking and reflection. Typically, a mound-type breakwater consists of a protective armour cover layer, one or more under- or filter layers, and a wide-graded material core. The toe structure provides support to the armour layer and is located where the breakwater contacts the seabed or seaside scour protection. The toe structure typically consists of a granular filter and foundation layer positioned above it, followed by a rubble toe berm.

Mound-type breakwaters can feature various revetment types, including a permeable layer composed of randomly placed loose rock or concrete elements, a semi-permeable layer made up of pattern placed blocks, or an impervious layer consisting of asphalt or concrete. Even under identical loading conditions, the design and dimensions of these revetment types differ significantly due to the underlying mechanisms of load transfer, from external to internal and from internal to structure feedback. These differences can be explained by the principle of leakage length. More on this topic can be found in Section 2.2.

1.1.3. Concrete armour units

Concrete armour units are an alternative when the required armour stone size is unavailable or not cost-effective. A multitude of concrete armour units have been designed and tested as the main armour layer for breakwaters, gaining stability through mechanisms such as their own weight, interlocking, and/or friction. The shape of an armour unit can be simple, such as cubes, or complex. Placement can be in single or double layer configurations, in a random or uniform fashion. Single layer armour units have seen a surge in popularity due to their high degree of interlocking, hydraulic performance, reduced concrete consumption, and increased placement speed compared to traditional methods (Bakker et al., 2019; Reedijk et al., 2018).

1.1.4. Coastalock

The Coastalock armour unit by ECOncrete, is designed to blend coastal protection with marine habitat creation. The octahedral design of the armour unit is designed to mimic inter-tidal and inundated habitats, with micro and macro morphological features in the concrete unit that provide niches for various species. The key features of Coastalock is the cavity that is integrated into the design. Depending on the orientation of the unit, the cavity can serve different functions: facing upward, it acts like a tide pool; sideways orientations can create caves, and facing downwards can form an overhang, providing shelter for marine life.

Figure 1.2: Coastalock armour unit concept (ECOncrete Tech Ltd., 2019).

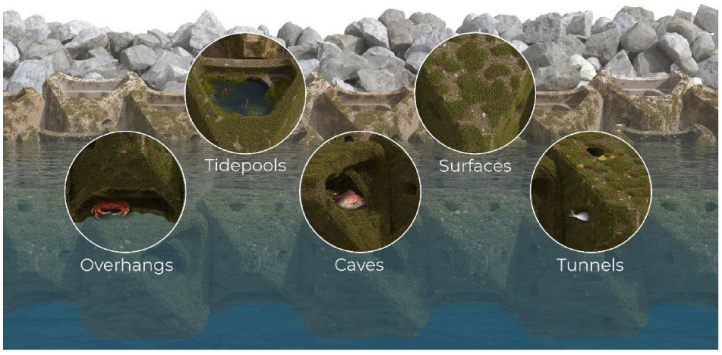

Figure 1.3: Coastalock installation orientation options to create multiple habitats (ECOncrete Tech Ltd., 2023).

The interlocking capabilities of the regularly placed armour unit are independent of the orientation of the surrounding blocks, creating the possibility for versatile and flexible arrangements. The armour unit has been specifically developed to be deployed on very steep structure slopes, up to 3V:4H (ECOncrete Tech Ltd., 2019).

Research has been conducted to assess the ecological and structural performance of Coastalock in large-scale settings. A pilot study is being conducted at Harbour Island in the Port of San Diego, USA, where traditional riprap protection against low waves has been replaced by 37 Coastalock armour units in each of the two designated areas. The configuration of cavities facing up above mean low water, and cavity facing sideways below mean low water has been dubbed the 'San Diego' configuration. A representation of the configuration can be seen in Figure 1.4.

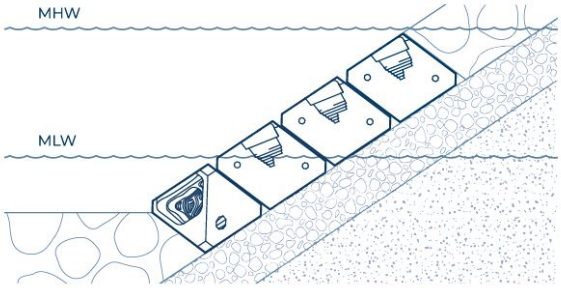

Figure 1.4: Coastalock 'San Diego' configuration (ECOncrete Tech Ltd., 2019).

The monitoring program includes multiple Coastalock armour units distributed at upper, middle, and lower tidal heights on the two sites, as well as control patches on the original riprap control site. All three underwent monitoring events at 8, 14, 20, and 26 months post-deployment to assess pools during low tide and caves during high tide. When compared to the decades-old control, Coastalock was reported by ECOncrete (2023) to enhance marine biodiversity, fostering higher diversity across all tidal heights. This improvement is attributed to the newly introduced water-retaining species-specific habitats in the form of the cavity, the micro irregularities, as well as the unique texture and unique ECOncrete admixture of Coastalock (ECOncrete Tech Ltd., 2023).

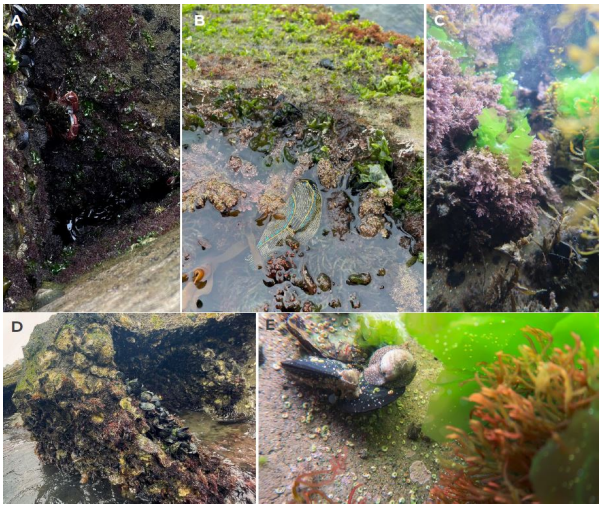

Figure 1.5: Biological development on the Coastalock units 26 months post deployment (ECOncrete Tech Ltd., 2023).

Additionally, at the beginning of 2023, a pilot study, monitored by the Technical University of Denmark, was initiated in the Bouzas region of the Port of Vigo, Spain, with results currently underway. In this study, 100 Coastalock units have been deployed with the intention of providing coastal stabilization, habitat creation, and ecological enrichment.

1.1.5. Physical model testing

Physical modelling is a well-established approach in hydraulic research, based on the principle of similitude between a model and the real world. Quantities measured in a physical model can be used to estimate real-world parameters such as wave loads and armour stability, while taking into account scale effects that result from differences between the model and the real world. Physical model tests are particularly useful in the domain of concrete armour units, where numerical simulation would require significant computational resources and assumptions about underlying processes and boundary conditions, if feasible at all. In contrast, physical models directly incorporate physical phenomena and can provide insight into complex or poorly understood processes. Despite their limitations, physical models persist as one of the preferred tools for gaining knowledge in the field of hydraulic engineering (Frostick et al., 2011; S. A. Hughes, 1993).

1.2. Problem analysis

Within the development cycle of Coastalock, further quantification of the hydraulic performance of the armour unit is called for. Extensive physical model tests are necessary to achieve a safe, accurate and economical design when concrete units are used as primary armour.

First tests were conducted as a part of a MSc thesis in the Hydraulic Engineering Laboratory of the Delft University of Technology on a 2V:3H impermeable slope in deep water conditions (Molenkamp, 2022, Gutiérrez et al., 2023). These highlighted that with tight placement of the armour units significant pore pressure gradients across the top layer, resulted in failure. To address the issue of limited permeability in the armour layer, spacings were introduced between the armour units by removing columns of units and spreading the remaining units in the cross-slope direction. Several armour unit spacing ranging between 5% to 25% were tested to effectively emulated a more permeable armour layer. Test results have shown that the stability of the units increases with increasing inter-unit void size on an impermeable slope in deep water conditions. No failure by extraction occurred with spacing configurations above 10% (Molenkamp, 2022). The thesis also considered the effects of variations in the underlayer thickness, and different block orientation patterns on stability. Additionally, for an impermeable slope, the study determined the roughness factor for overtopping for spacings of 10% and above. It also derived an equation for the reflection coefficient, dependent on the wave steepness and armour layer spacing.

Given these observations, an optimization of the design of the units was proposed to mitigate the impact

of pressure and augment the top layer's permeability. The suggested optimization incorporates external concrete protrusions on the blocks, ensuring a predetermined separation between them, and reducing the influence of 3D effects, such as those caused by oblique waves. This alteration is anticipated to increase stability while simultaneously reducing the number of blocks needed per unit area of slope. This reduction offers several potential advantages, including decreased material consumption, shorter construction project durations, and reduced construction costs. However, the optimization brings forward new considerations. The reduced contact area may compromise the benefits of interlocking and friction-based stability inherent in the original design. Moreover, the channels formed between the protruded blocks might become susceptible to clogging due to the bio-enhancing characteristics of the material, which promotes organic growth.

While the obtained results shed light on Coastalock application for impermeable protections, the armour unit has yet to be assessed as part of a permeable breakwater or other permeable shoreline revetment structures. The armour unit may react in unforeseen ways, or even exhibit different or even more dominant failure modes in conditions differentiating from the initial tests. The effects of a crown, slope, toe, permeable core and foreshore are still unknown among other things. Gaining knowledge on these aspects is an important next step toward specification of design rules and further real life implementation of Coastalock.

1.3. Scope

Given the vast potential for exploring the behaviour of Coastalock, constraints have to be applied to the scope of the research due to time limitations. The thesis's main emphasis lies on the hydraulic performance of Coastalock armour layer characterized by its stability, overtopping, and reflection. The investigation is focused on the slope of a breakwater with permeable core, from toe up to, the top row of the armour layer, but excluding the transition to the crest and the crest itself. An additional aspect of this research is the examination of a toe berm on diverse subsurface's, probing the armour layer's susceptibility to sliding. It has to be noted that toe scour, an important and complex failure mechanism of an armour layer of a breakwater, that can lead to toe failure, generally followed by failure throughout the entire structure, is not considered in this thesis.

It was decided that this research will exclusively utilize a 2V:3H slope, experimenting with varying armour spacings, the introduction of two types of protrusions, along with configuration pattern changes including these protrusions, while being subjected to wave attack of increasing height and varying steepness at a constant water level. Tests investigating the effect of a toe are limited to the armour units with protrusions, as these are deemed most crucial for the further development of the armour unit.

1.4. Research objective and sub-questions

The aim of this MSc thesis is the further investigation of the application limits of a Coastalock armour layer. This thesis intends to gain insight into its behaviour of the armour unit, as part of a breakwater structure, and obtaining the hydraulic parameters that will serve to specify a hydraulic design. The main research objective is to:

> *Describe the hydraulic performance with respect to stability, overtopping and reflection of a Coastalock armour layer on a permeable breakwater slope supported by a toe.*

The following sub-questions support the main research objective

1. *Which failure mechanism causes Coastalock as a part of a permeable core breakwater structure to fail and in what way?*
2. *What effect does the presence of a permeable core, compared to an impermeable core, have on the stability, overtopping, and reflection characteristics of a Coastalock armour layer, considering different armour layer spacings and varying wave steepness?*
3. *How do variations in the form of protrusions influence the stability, overtopping, and reflection characteristics of a Coastalock armour layer on a breakwater slope with a permeable core, considering varying wave steepness?*

4. *How do variations in armour unit orientation influence the stability, overtopping, and reflection characteristics of a Coastalock armour layer with protrusions on a breakwater slope with a permeable core?*
5. *How does the introduction of a toe berm influence the progression of damage in a Coastalock armour layer with protrusions on a permeable slope?*

1.5. Method of approach

For this research, firstly a literature study was performed to provide the relevant theory as a means of an answer to the research questions, together with gaining comprehension on physical model testing, and the behaviour of Coastalock during these tests. Second, a physical model testing program is set up and executed in 2D wave flume of the Hydraulic Engineering Laboratory of the Delft University of Technology. The testing program consists of multiple test series, explained in detail in Chapter 3.5.2. After completion the testing program, the results are analysed and reported on.

1.6. Thesis outline

The thesis is structured as follows to answer the research question in an orderly fashion:

1. Introduction: Serves as an introduction to the subject matter and states the problems and objectives at hand.
2. Literature Review: Performs a literature study to obtain the necessary knowledge on the relevant topics and analyze the previous study on Coastalock.
3. Physical Model Test Set-up: Provides a comprehensive description of the employed physical model test set-up, including measuring techniques, equipment, and an overview of the testing program.
4. Data processing: Describes the methodology for acquiring and processing data to create 3D models of the test series utilizing the structure-from-motion principle.
5. Results and Analysis: Presents the results and analyzes them.
6. Discussion: The output is discussed.
7. Conclusion: The main conclusions are given.
8. Recommendations: The thesis ends, giving recommendations on further investigation of the subject.

This structure provides a clear and systematic overview of the thesis and helps the reader navigate the different chapters in a logical order.

2

Literature study

This chapter starts with an overview of breakwater design, including its components and relevant failure mechanisms. The second section explains the principles of wave-structure interaction and leakage length theory. The three revetment archetypes are briefly explored, followed by the theory of placed block revetments and the armour layer failure mechanisms that are relevant to observed Coastalock behavior. The concept of the stability number is also introduced. The third and fourth sections examine reflection and overtopping. The final section investigates the influence of a permeable core on the flow inside and outside a breakwater. This includes the influence of core permeability on stability formulae and the observed effect of permeable cores on interlocking armour units are discussed. As background information, Appendix A provides additional information on hydraulic aspects like wave characteristics and waves breaking on a slope. Subsequently, Appendix B provides information concerning the stability of concrete armour units as a balance of loads and stabilizing forces. Appendix C, is dedicated to toe design and failure modes of the toe, and contains an overview of toe stability approaches and parameters relevant for design. Last, Appendix D provides a comprehensive guide on the phenomenon of scaling and physical modelling of breakwaters.

2.1. Breakwater design

2.1.1. Components of a mound breakwater

This section provides an overview of the design of single-layer high-crested breakwaters consisting of interlocking concrete armour units. The breakwater crest height, R_c, is determined based on the functional requirements, which include overtopping discharge and wave transmission considerations. The crest width, B, should generally be sufficient to accommodate at least three concrete armour units to withstand severe overtopping (CIRIA, 2007). However, this requirement may vary depending on the specific block type.

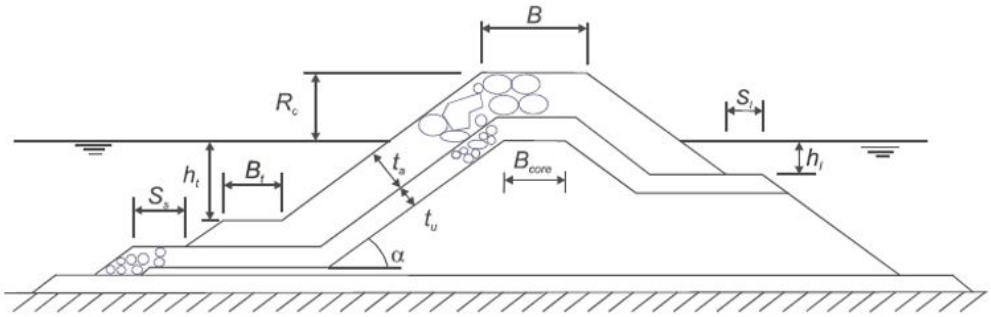

Figure 2.1: Rubble mound breakwater definition sketch (CIRIA, 2007).

Several variations of crest designs for a single-layer interlocking concrete armour unit breakwater are presented in Figure 2.2. The slope angle, α, is selected to be as steep as possible to minimize material consumption while maintaining hydraulic and geotechnical stability. Slope angles for concrete armour units layers generally range from 1V:1.33H to 2V:3H (CIRIA, 2007). Interlocking effects are less effective and stability is compromised with milder slope angles. The armour layer thickness, t_a, is a function of the armour type and size, which in turn is is determined based on hydraulic loads from waves and currents during design conditions. Meanwhile the under layer thickness, t_u, is chosen to ensure protection against erosion and pressure build up caused by waves and currents. Its primary function is to prevent the underlying layer, be it a filter layer or core, from being washed away, all while maintaining its own resistance to erosion. The core, not depicted in the figure, typically consists of quarry run - a finer fraction of the quarry yield curve.

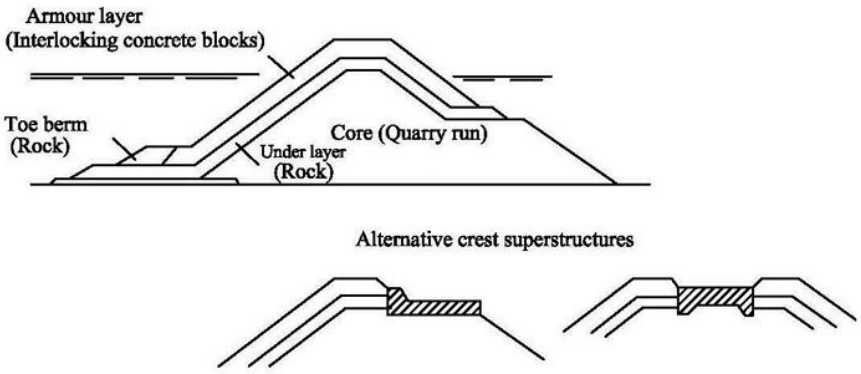

Figure 2.2: Single layer rubble-mound breakwater with interlocking concrete armour units (PIANC-MarCom WG 196, 2016).

The seaward toe level, h_t, is generally constructed at least $1.5H_s$ beneath low water level, and the leeward toe is indicated with h_l. The toe berm width, B_t, must be wide enough to accommodate at least three stones on top. A wider toe, serving as a falling apron when its stones are displaced, may be used in cases where severe scour is expected (CIRIA, 2007). The seaward and leeward shoulder widths, S_s and S_l, respectively, must be at least 2 m in standard cases, or up to a minimum of $6m$ or H_s when scour problems are anticipated (CIRIA, 2007).

2.1.2. Breakwater failure mechanisms

The safety assessment of a breakwater or any other coastal structure requires a comprehensive understanding of its structural response under various loading conditions, which is typically achieved through an identification and analysis of potential failure mechanisms. Neglecting any critical failure mechanism can significantly affect the safety of the structure. Therefore, it is essential to identify and evaluate all potential failure modes or mechanisms. Burcharth (1992) categorized various failure mechanisms of rubble mound breakwaters, as shown in Figure 2.3. This study focuses on the failure mechanisms associated with both the armour layer and the toe berm, detailed in Sections 2.2.4 and C.2, respectively. Additionally, other relevant failure mechanisms, though not the primary focus, will be briefly discussed to provide a comprehensive overview.

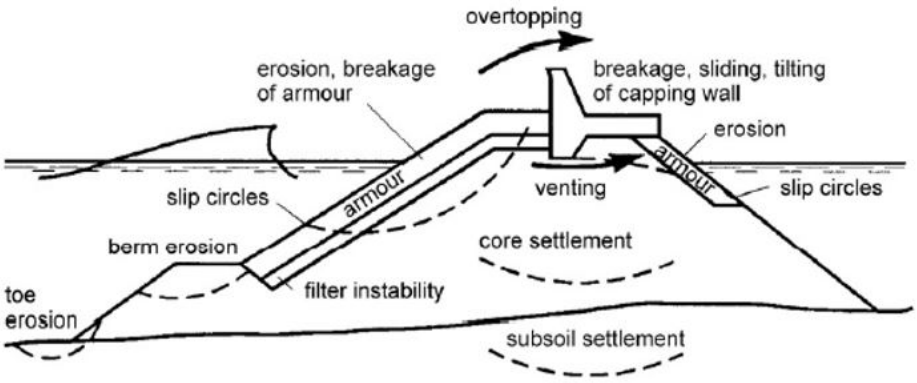

Figure 2.3: Failure mechanisms for rubble mound breakwaters (H. Burcharth, 1992).

Geotechnical failure mechanisms
Geotechnical factors can give rise to several types of failure modes in breakwaters. One of the most significant of these is the formation of slip circles, which according to De Rouck and Van Damme (1996) can result from the combined effects of hydrodynamic forces generated by wave attack on the seaward slope and the underlying soil's instability. Slip circles can manifest, as a circular pattern of soil sliding, that can affect a portion or the entire slope. Various factors like geometry, wave forcing, geotechnical conditions, and pore water pressures all influence their development.

Another geotechnical failure mode involves the settling of the subsoil or core, which can occur when a heavy structure is built on soft, compressible soil, or when the core is compressed under the weight of the structure above. This settling can lead to a lowering of the crest freeboard height, which, in turn, can increase the likelihood of overtopping and possibly trigger other failure modes such as inner slope erosion. Settlement of the rockfill core primarily occurs during construction, although additional settlement is possible due to the movement of the core material into a more stable position or breakage. The design of the structure's height must account for expected immediate settlement, primary consolidation, and creep. One approach to mitigate the effects of weak soil underneath the breakwater is to replace it with more stable soil, which can be achieved through dredging.

Filter instabilities
Under wave loading, pressure gradients can develop in the permeable core of a breakwater. If the filter layer fails to meet certain criteria, fine material can be washed out through the coarser armour layer, leading to erosion and potential collapse of the armour layer. This can lead to instability of the entire structure and result in failure.

Crown damage
The failure of a breakwater due to crown damage can occur when horizontal wave forces during wave run-up and uplift pressure forces underneath exceed the friction forces beneath the capping element, causing the superstructure to slide backwards. This may result in sliding, tilting, and eventual toppling of the superstructure. Tilting in the forward direction may also occur, which is typically associated with armour or geotechnical failure. In the absence of a superstructure, top armour units act as crest protection elements. The loading on these units is unique, as the wave run-up induces horizontal forces on top of the armour units, parallel to the crest, while their strength is reduced since they are not held down by the weight of above-placed units. Thus, failure of the crest components needs to be accounted for independently.

Venting
Venting is another potential failure mechanism of breakwater structures, where water and air pressures induced by waves can cause erosion under the superstructure and at the lee side of the breakwater. When water penetrates the filter layer and permeable core, it can displace infill material and create vents that increase the potential for further erosion. The formation of vents can be exacerbated by high

wave pressures, particularly during storm events. As a result, the superstructure may be undermined, leading to structural failure, or the inner slope may fail, causing the breakwater to collapse.

Inner slope erosion
Inner slope erosion is a common failure mechanism that can occur in rubble mound breakwaters due to heavy wave overtopping, also known as overwashing. The erosion process typically starts with the displacement of the crest and rear armour layer due to the impact of wave overtopping, which causes the inner slope to become exposed to the wave action. The wave action then washes down the inner slope material, leading to the formation of a gully or trough on the lee side of the breakwater. The gully can rapidly deepen and widen, eventually leading to a failure of the entire structure if left unchecked.

2.2. Armour layer design

2.2.1. Wave-structure interaction

The wave-structure interaction, as explained in the systematic approach proposed by Pilarczyk (1998), can be divided into three main components. These so called transfer functions link the behaviour of the water, soil and structure, to explain phenomena crucial to understanding the strength, deformation and ultimately failure of the structure during loading. The three transfer function are:

I. The transfer function between the overall hydraulic conditions and the hydraulic condition along the external surface of the protection; i.e. from hydraulic conditions to external load in the form of force or pressure.

II. The transfer function between hydraulic conditions along the external surface to those along the internal surface, as an internal load in the form of force or pressure.

III. The transfer function combining both into the structural response of the protection i.e. the strength.

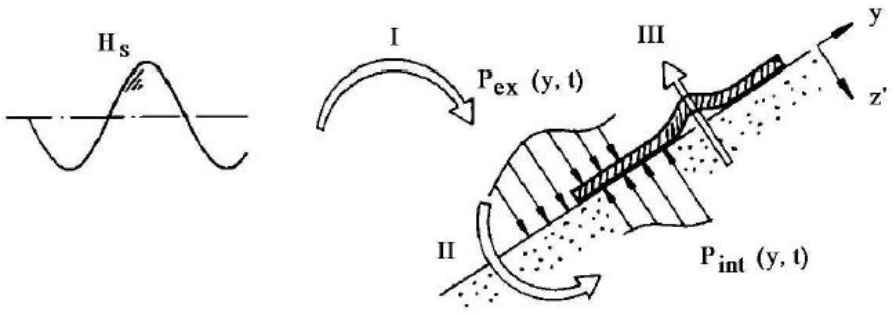

Figure 2.4: Wave-structure interaction according to transfer functions (Pilarczyk, 1998).

As mentioned in the introduction the dimension and design of a revetment, even under identical loading conditions (identical transfer from hydraulic to external loading) differs considerably, depending on the type of stable protection. The response of the protections varies due to differences in the second and third transfer function and can partially be explained by considering the phenomenon of leakage length.

2.2.2. Leakage length

The leakage length is a measure for the exchange of external wave loads and internal loads. The empirical factor as described by an analytical model, based on placed stone revetment on granular filter theory, takes into account physical parameters relevant to the stability, as described in detail by De Waal (1998) and Pilarczyk (2003). For an impermeable core and relatively thin underlayer (in which uniform flow is assumed), it is defined as the protection length in which the flow resistance, through both the

top and bottom layer are equal. This can be expressed by:

$$\Lambda = \sqrt{\frac{k_F d_F d_T}{k_T}} \tag{2.1}$$

where d_F and d_T are the filter and top layer thickness, and the permeability of the filter and top layer is expressed by k_F and k_T, respectively. The exchange of external and internal loads, and with it head difference build up, is governed by the ratio between the leakage length and the characteristic length of the external load, L. With larger leakage lengths the pressure head difference over the layer will increase. The opposite holds for smaller leakage lengths.

For concrete armour units on breakwaters, the general relationships continues to be relevant, providing a means to evaluate the influence of the porosity of the armour layer. However in reality the role of core permeability and its impact on energy dissipation should be considered as well.

Revetment types
As mentioned in Section 1.1.3, stable protection against waves can be divided into three archetypes based on the principle of leakage length.

The first archetype is loose and permeable rocks or armour units, where $\Lambda << L$. In this case, there is minimal head difference between the outside and inside due to the low resistance to exchange. The pressure gradients in the load are primarily determined by the characteristic loading length. Uprush and downrush, which result in drag forces on single units, are governing factors, as porous flow is of minor importance compared to external forces. Strength of loose material revetments is generally provided by self-weight and friction between the elements (and if designed for, interlocking as well).

The second archetype is impermeable asphalt or concrete protections, where $\Lambda >> L$. In this case, there is little exchange between the outside and inside, as the impermeable structure stops the piezometric level in the filter from following the outside level. This leads to high pressure gradients underneath the protective layer, which can try to lift it up and is the governing factor for stability. Prolonged wave impact should also be considered for this type of protection.

The third archetype is placed block revetments, which are considered a complex case with a leakage length of $\Lambda \approx L$. A thorough description of this type of protection will follow in Section 2.2.3.

2.2.3. Placed block revetment theory

Placed block revetments are usually made of only one layer of concrete elements, of which the elements are placed in a pattern. Design for strength by friction or interlocking against forces permits a reduction in size and weight. In the latter, the stability of the blocks is increased by the neighboring blocks in the direction perpendicular to the water line. The cover or armour layer is the main protecting element of the structure against external and internal loading. Withstanding external loads is achieved primarily by the weight of the blocks. The cover layer is placed on one or more appropriate layers, called the filter layer(s), with a subsoil beneath. The permeability ratio of the armour layer and filter layer(s) determines the internal loading. The subsoil, or core in this case, may have an effect on the stability of the cover layer as well, depending on the phreatic level inside the structure.

Placed block loading mechanisms
For a semi-permeable placed block revetment, the characteristic loading length is approximately equal to the leakage length, which means that $\Lambda \approx L$. There are many possible loading mechanisms that may play a role in the overall stability of the armour layer under wave attack. Figure 2.5 provides an overview of these possible mechanisms. The quasi-stationary pressure due to wave set-up and the pressure due to the wave front have been identified as the dominant forces (Schiereck and Verhagen, 2019).

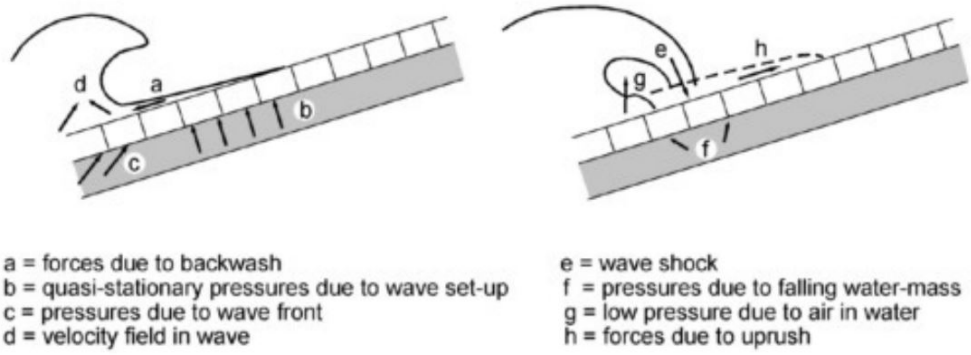

Figure 2.5: Loading mechanisms present in placed block revetments (Schiereck and Verhagen, 2019).

External loads are described at the moment of critical loading in the approach, as proposed by Pilarczyk (1995). This approach simplifies the description of the time- and location-dependent wave pressures on the revetment. The critical loading by active forces occurs at maximum run-down, when the pressure on the block in front of the wave is low. Meanwhile, internal loads occur, which can be divided into high pressure under the placed blocks relative to the pressure on the blocks, causing uplift, and a hydraulic gradient under the cover layer. The critical loading situation is shown in Figure 2.6A.

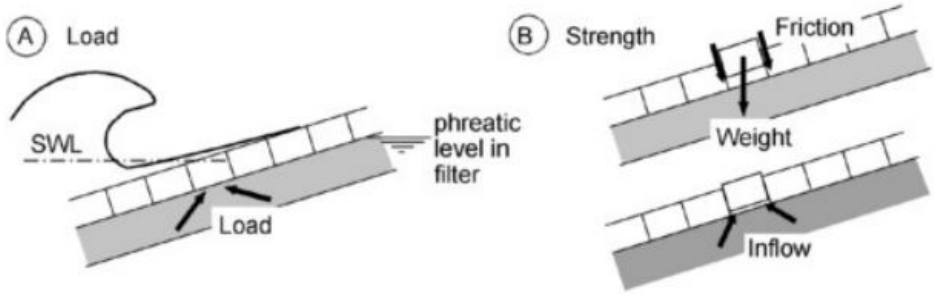

Figure 2.6: Load and strength of placed blocks on a slope (Schiereck and Verhagen, 2019).

The leakage length is an important parameter for the determination of the magnitude of the uplift force. A simplified model, to demonstrate the importance of leakage length, is used in the PIANC Report 114 by Dorst *et al.* (2012), in which the porous flow through the filter layer is assumed parallel to the slope, while the flow through the cover layer is assumed to be perpendicular to it, as can be seen in Figure 2.7a.

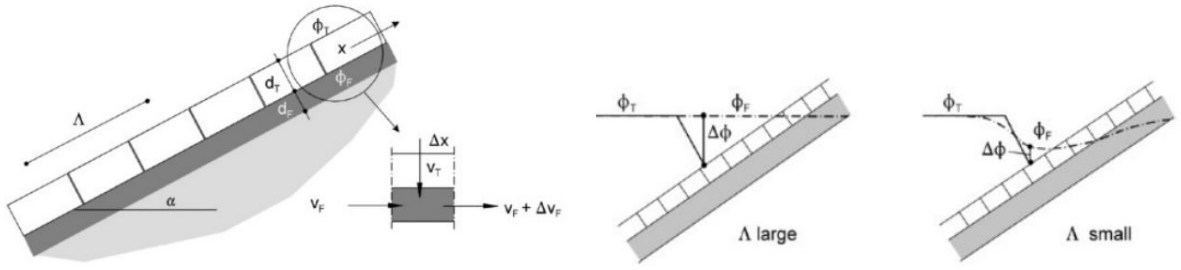

(a) Simplified flow through block revetment.

(b) Head difference over block revetment for large and small Λ.

Figure 2.7: Flow through placed block revetment and resulting piezometric head (Schiereck and Verhagen, 2019).

The head difference over the top layer depends directly on the leakage length, as depicted in Figure

2.7b. From this it can be concluded that small leakage lengths are favourable for the stability of placed block revetments. To achieve this a permeable top layer would ideally be situated on a relatively thin underlayer with low permeability. The minimum thickness of the underlayer should be guaranteed taking into account other mechanisms. A shorter leakage length can also be guaranteed by implementing sufficient open spaces in between the blocks. However, sufficient contact between the blocks needs to be maintained for friction and interlocking to have effect. The spacing between the blocks can also be limited by the size of the filter material, as washing away of the underlayer is highly undesirable.

2.2.4. Failure mechanism of uniformly placed single layer armour units

The behavior of uniformly placed single layer armour units, contrary to what the name might suggest, displays many similarities to placed-block revetments. Due to the relatively close proximity of the neighbouring blocks, needed to achieve interlocking capabilities or friction based resistance, pressure buildup underneath the armour layer is often problematic. Low armour layer porosity and small distance between the armour units is to blame for the over pressures created from inside the breakwater.

The preliminary Coastalock performance tests (Molenkamp, 2022) showed behavior and failure mechanism reminiscent to that of placed block revetments for lower armour spacings. During physical model testing of another regularly placed single layer armour unit, XBlocPlus, similar traits were also noted (Van den Berg et al., 2020, Rada Mora, 2017, Vos, 2017). On the other hand, randomly placed single layer armour units like Accropode, CORE-LOC or irregularly placed single layer cubes, omit this problem, as the irregular placement usually guarantees enough porosity of the armour layer (Bakker et al., 2003).

A breakwater cover layer made up of orderly placed single layer armour units can fail in several ways. Armour layer failure is generally split between erosion and breakage of the armour. Armour layer breakage is not considered in small-scale model testing, as the behavior and characteristics of the concrete are not illustrative of the real world. However, movements of the armour layer that may lead to damage or breakage of the armour units or otherwise lead to failure should be monitored closely. The following failure mechanisms of the armour layer can be considered:

Uplift

When pressures from underneath the armour units exceed the stabilizing self-weight, friction, and interlocking capabilities, uplifting of the blocks can occur in two possible ways. The first, a piston-type failure, manifests itself when a single block is displaced from the cover layer. The latter, a beam-type failure, occurs when the pressure underneath the armour layer lifts not only a single block but the surrounding blocks with it. Due to the tight placement of the armour units, normal forces are passed on to the surrounding blocks, eventually ending up at the bordering structure. Subsequently, an entire block row is lifted from the slope. Both cases leave the underlayers and core exposed.

Arching mechanism

The arching mechanism of breakwater elements was described for the first time in model tests investigating the influence of the underlayer configuration on the interlocking capacity and stability of XblocPlus by Van den Berg et al. (2020). The observations revealed that, during tests conducted on an S-shaped slope in the cross-shore direction, sudden failure resulted in the lower part of the slope moving upwards perpendicular to the slope, while the upper part moved downward perpendicular to the slope. This phenomenon was also observed in test series where no failure occurred. The movement was attributed to a combined effect of the weight of the upper armour and the hydraulic pressure of the remaining water under the top layer. A simplified model based on S-profiles was proposed, treating elements above and below the convex shape as rigid bodies, accounting for wave-induced forces. The model considers the influence of the relative angle between the armour unit sections, α_R, and the deviation of the armour sections' angle from the design slope, β.

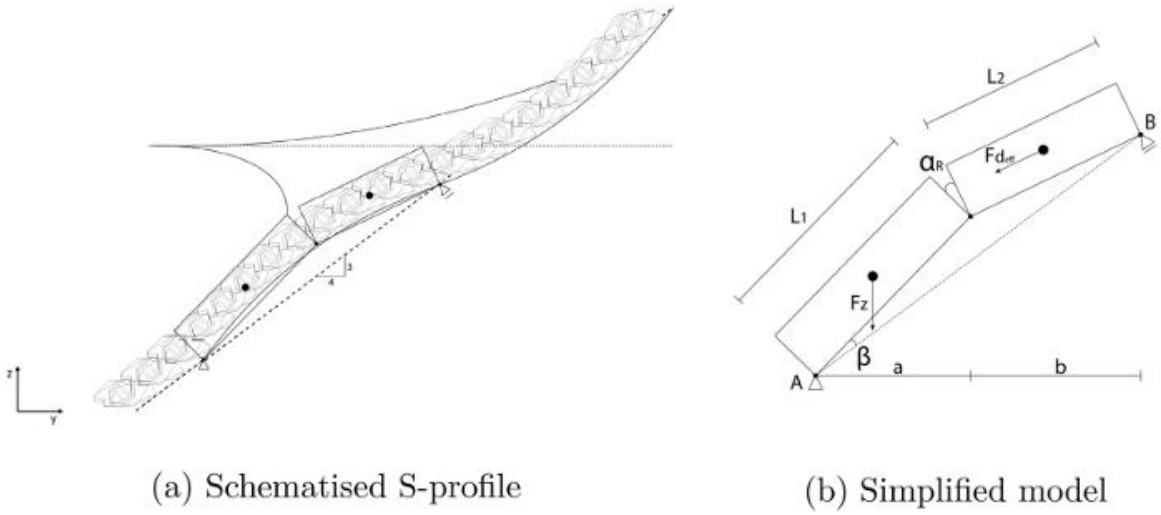

Figure 2.8: Schematisation of S-profile into simplified model (Van den Berg et al., 2020).

The interplay of α_R and β determines the stability, and if the resisting moment is outweighed by the acting moment, the rigid bodies lift, causing failure.

The resulting trend line of the armour layer is given by equation:

$$N_s = \frac{H_s}{\Delta D_n} = 0.1(\alpha_R + \beta) + 5.7 \tag{2.2}$$

The angles α_R and β being dependent of each other, as described by the following relation:

$$\alpha_R \approx \beta(1 + \frac{L_1}{L_2}) \tag{2.3}$$

While the model aligns with test measurements, deviations suggest a potential oversight of underlayer movements. Further details can be found in the original paper (Van den Berg et al., 2020).

Breathing or 'flapping'
In the preliminary research on Coastalock, Molenkamp (2022) identified 'breathing' or flapping as a potential failure mechanism. The up-and-down movement of parts of the armour layer perpendicular to the slope, recurring with each incoming critical wave, is not unique to Coastalock but is common in other placed block revetments (Klein Breteler, Mourik, and Bosters, 2014). 'Breathing' occurs due to a significant pressure difference between the underlayer and the exterior of the armour layer, most pronounced during the wave run-down, leading to an imbalance of forces and subsequent movement. This unwanted movement can result in abrasion, deterioration, or breakage of the blocks due to forces between each other, followed by extraction from the armour layer. During the downward movement, impact between the armour layer and underlayer is inevitable, causing damage to or breakage of the armour layer or erosion of the underlayer. The 'breathing' of the armour layer could potentially cause a migration of underlayer material, creating a concave S-shape. Such change weakens the interlocking capacity of the armour layer and, once the underlayer is compromised, necessitates extensive reconstruction, as individual armour unit replacement is not feasible due to their interlocking nature.

Settlement
Significant settlement and changes in packing density can occur before the extraction of armour units. Single-layer interlocking armour units exhibit limited flexibility in adapting to settlements due to their complex arrangement. This can result in changes in the packing density, leading to a loss of interlocking

when the local density becomes too sparse, compromising the stability of the armour layer (Van Gent and Luis, 2013). Both the magnitude and gradient of settling are crucial, as they can significantly impact interlocking capabilities. Settlements of armour units are not necessarily evenly distributed across the structure's width, even in 2D tests. In an application on a trunk section, it was observed that unit extractions could occur when the settlement reached values exceeding $0.2D_n$ (Hofland and van Gent, 2016). On the other hand, when the packing density is higher than intended, pressure buildup could exert additional destabilizing forces on the armour layer. This is due to the decrease in permeability and the increase in leakage length, ultimately leading to a decrease in stability (Pilarczyk et al., 1995).

Sliding
The stability of an armour layer on a slope depends on the slope angle, specific weight, pore pressure due to water level differences and wave attack, internal friction, and interlocking. Sliding often occurs along the interface between two different materials: the armour layer and the underlayer. A sudden displacement of a large portion or entirety of the tightly placed main armour can occur on steep slopes. The situation occurs when the horizontal support of the toe structure is insufficient and downrush-induced pull acts on the slope. Pore pressures from inside may result in uplift and loss of friction and interlocking. Slopes with an impermeable cover layer and relatively permeable filter are especially susceptible to sliding.

2.2.5. Stability number

The stability number is a dimensionless parameter used to assess the stability of a breakwater structure. It is defined as the ratio of the sum of stabilizing forces to the sum of destabilizing forces acting on the structure. An overview of these force can be found in Appendix B. For sloping coastal structures under wave attack, the relation between the governing wave condition, expressed by the significant wave height, $H_s(m)$, the characteristic armour size, $D_n(m)$, and the relative buoyant density of the armour material, Δ (-), is given by the stability number:

$$N_s = \frac{H_s}{\Delta D_n} \tag{2.4}$$

Placed block stability formula
The passive forces contributing to the strength of the placed block revetment are the friction or interlocking between the blocks, gravity working on the mass and the resistance to lifting of the block occurs due to suction of water into the created void while being displaced, driven by uplift resulting from hydrostatic pressure beneath an impermeable layer. A crude approach of the stability of the most unfavourable block of just in front of the wave front is given by Schiereck and Verhagen (2019), as presented in Figure 2.9.

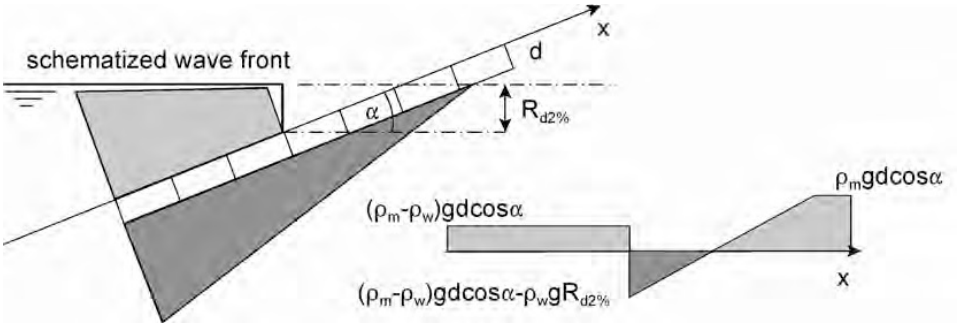

Figure 2.9: Schematized stability of block revetment (Schiereck and Verhagen, 2019).

It is based on the run-down formula of EuroTop (2018) $R_d = -0.33H_s\xi$ and the assumption that the strength of the blocks is only provided by the weight:

$$N_s = \frac{H_s}{\Delta D} = 3\frac{cos\alpha}{\xi} \tag{2.5}$$

The constant value of 3 was assumed to be safe. However, in reality, the load will be influenced by factors such as leakage length, friction, and interlocking strength.

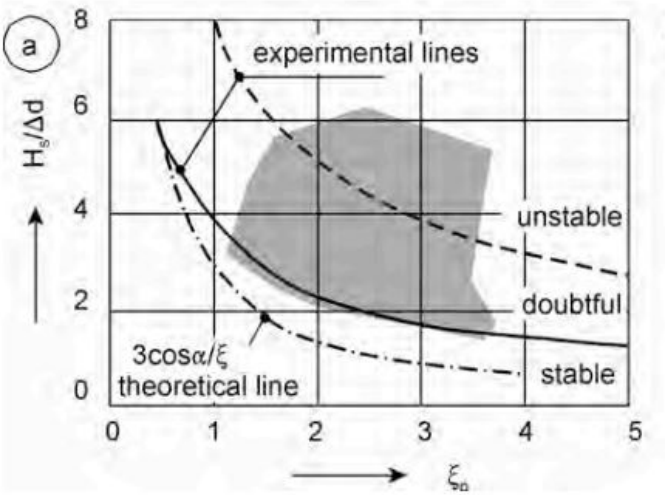

Figure 2.10: Test results for placed blocks revetments on a filter layer (Schiereck and Verhagen, 2019).

Coastalock's stability number
The design of Coastalock aims to achieve an anticipated stability number for design of approximately $N_s = 2.5$, assuming a safety factor of about 1.5 for sudden failure in general physical model test. In preliminary testing, start of armour movement potentially leading to failure was identified by the visual observation of 'breathing' of the armour layer. This involved substantial and repeated movements of the armour layer perpendicular to the slope before. Complete failure was defined as extraction. Notably, the difference in wave height causing both phenomena was of minor magnitude. Molenkamp (2022) observed stability numbers around 2.0 for spacings of 0%, 5%, and 7.5% due to wave loading ($s_{0p} = 0.035$) on a deep water impermeable slope slope. Breathing and extraction events were last observed for a spacing of 10% corresponding to a stability number of approximately $N_s = 4.0$. For spacings of 15% and above, no failure occurred when subjected to waves, as the maximum significant wave height of the wave generator was reached, indicating that $N_s > 4$.

Common design methods for the prediction of stability as proposed by Dorst et al. (2012) are not suitable for use due to the steeper breakwater slope. The method for semi-permeable cover layers as proposed by Pilarczyk (2003), when examined by Molenkamp (2022), was not able to predict the stability of Coastalock, or even applied for armour spacing of larger than 10% due to function limits. It has to be kept in mind that no well-established design rules for interlocking blocks exists. Most interlocking structures have been in the past been designed on basis of practical knowledge.

2.2.6. Damage number

The damage to an armour layer of placed concrete units can be quantified by the damage number, denoted as N_{od}, which represents the count of partially or fully displaced armour units $N_{\#d}$ within a strip of breakwater slope B (m), with a width equal to the nominal diameter D_n (m):

$$N_{od} = \frac{N_{\#d}}{B/D_n} \tag{2.6}$$

Concrete armour unit manufacturers typically provide specific guidelines for defining partially displaced units and determining damage numbers, which indicate the initiation of damage, intermediate damage, or failure. Additionally, considerations for rocking or other undesired movements may be incorporated when calculating the damage number and establishing its threshold.

The Rock Manual (2007) suggests that interlocking single-layer armour units are designed for no-damage conditions, where $N_{od} = 0$, with the start of damage occurring when $N_{od} > 0$. Single layer elements

demonstrate a much more brittle failure in comparison with double layer armour elements. In addition, the repair of single layer interlocking armour units is hard, as the layer has to be removed in its entirety. High safety coefficients are applied for design purposes with single layer armour units accordingly. Under design conditions the armour should show no damage and only minor movement for overload conditions.

2.3. Overtopping

High water levels combined with high waves can result in overtopping of the breakwater crest. During overtopping, there is no constant flow, but a process that varies in time, space, and volume. The highest waves push large volumes of water over the crest in short periods of time, while lower waves may not result in any overtopping at all. The EuroTop manual (2018) defines overtopping as the average discharge per linear meter of width per unit of time q [l/m/s]. The severity of the overtopping is described by the combination of the average overtopping and the wave height that contributed to it. Allowable overtopping discharge rates depend primarily on the function of the breakwater, concerning protection of property or people, but also on structural requirements, as severe overtopping may lead to disastrous failures of the inner slope, resulting in complete collapse.

Overtopping discharge formulation

The general overtopping discharge on a slope according to the EuroTop manual (2018) is based on a mean value approach and can be used for predictions and comparison with measurements. The symbol definitions can be found in the list at the start of the thesis. The equation is as follows:

$$\frac{q}{\sqrt{gH_{m0}^3}} = \frac{0.023}{\sqrt{tan\alpha}} \cdot \gamma_b \cdot \xi_{m-1,0} \cdot \exp[-(2.7\frac{R_c}{\xi_{m-1,0} \cdot H_{m0} \cdot \gamma_b \cdot \gamma_f \cdot \gamma_\beta \cdot \gamma_v})^{1.3}] \tag{2.7}$$

The equation has a maximum value of:

$$\frac{q}{\sqrt{gH_{m0}^3}} = 0.09 \cdot \exp[-(1.5\frac{R_c}{H_{m0} \cdot \gamma_f \cdot \gamma_\beta \cdot \gamma^*})^{1.3}] \tag{2.8}$$

For the case without a berm, oblique wave attack, wave wall, or promenade: $\gamma_b = \gamma_\beta = \gamma_v = \gamma^* = 1$. Steep breakwater slopes, ranging from 1:2 to a maximum of 4:3, in general, result in overtopping following the maximum presented in Equation 2.8. This equation provides the average of the measured data, making predictions and comparison with measurements possible.

The factor that describes the influence of the roughness elements on a slope on the overtopping discharge, γ_f, is of main interest. It is widely used as a comparison measure with regards to overtopping performance for different types of rock layers or armour units. The roughness parameter takes into account the porosity, permeability, and placement pattern of the armour units, as well as individual roughness when testing concrete armour units.

Type of armour layer	γ_f
Rocks (1 layers)	0.45
Rocks (2 layers)	0.40
Cubes (1 flat layer)	0.49
Cubes (2 random layers)	0.47
Xbloc, CORE-LOC, ACCROPODE	0.44
XblocPlus (Delta Marine Consultants, 2023)	0.45
Cubipod (1 layer)	0.49
Cubipod (2 layer)	0.47

Table 2.1: Roughness factor for permeable rubble mound structures with slope of 2:3 (Van der Meer et al., 2018)

However, other influencing factors not present in the overtopping formulation can also affect the roughness factor. The complexity of water motion at the structure makes it challenging to predict the

individual and combined influence of these factors on overtopping. Roughness factors, as given in the EuroTop manual (2018), based on test configurations of 2:3 permeable rubble mound structures for breaker parameters in the range of $\xi_{m-1,0} = 2.8 - 4.5$ can be found in the Table 2.1. For breaker parameters $\xi_{m-1,0} > 5.0$ an increase of the influence factor is advised, with a maximum of 0.60:

$$\gamma_{mod} = \gamma_f + (\xi_{m-1,0} - 5) \cdot (1 - \gamma_f)/5.0 \tag{2.9}$$

Molenkamp (2022) tested the influence of armour spacings on overtopping in his work on the hydraulic performance of Coastalock. Only model tests of the 'San Diego' configuration, on a $2d_{n50}$, under $s = 0.035$ waves on an impermeable deep-water slope have been used in the derivation of the roughness parameter for the different spacings. For values below 10%, the overtopping discharges in the model were too small to draw conclusions on the overtopping reducing abilities of the armour unit. For armour unit spacing of 10, 15, 20, and 25%, significantly larger discharges could be measured, and relations could be derived. The roughness factor seemed to have an exponential relation to the significant wave height, reducing the overtopping with increased spacing between the units. Equation 2.8 was found to underestimate the results based on the roughness factors for low armour spacing and low wave heights. However, as the spacing and wave height increased, the underestimation decreased until it became conservative for the highest spacings and wave heights.

Spacing	$\gamma_{f,CL}$
0.10	0.73
0.15	0.70
0.20	0.67
0.25	0.61

Table 2.2: Roughness factors of Coastalock for EuroTop equation based on model tests (Molenkamp, 2022).

2.4. Reflection

After a wave encounters a structure or boundary, a part of the incoming wave may be reflected back. The effect of reflecting waves is significant on the open coast and near and in harbors. The interaction of incoming and reflected waves can lead to dangerous sea states near the entrance of a harbor, and undesirable reflection can hamper vessels, whether maneuvering or moored. Besides, reflection may contribute to sediment scour as littoral near bed currents may be increased, leading to structure destabilization. Rubble mound structures absorb most of the wave action, thus reflecting less wave energy than comparable impermeable or smooth slopes. The average reflection coefficient is described as the ratio between the squares of the reflected and incoming wave energy. When random waves are considered, the reflection factor may be defined using the significant incident and reflected wave height representing the wave energy:

$$C_r = \frac{H_{s,r}}{H_{s,i}} \tag{2.10}$$

Wave reflection prediction

Wave reflection of high-crested rubble mound breakwaters is governed by wave energy by breaking and wave penetration into the structure. Most literature approaches consider the ratio of slope angle and wave steepness as the primary parameter governing wave reflection for rubble mound breakwaters. The effect of porosity, which relates to wave penetration, is frequently neglected, and the focus lies solely on the wave action on the breakwater slope. Empirical approaches that use the breaker index assume that wave energy dissipation on the breakwater slope is primarily determined by wave breaking, and any remaining wave energy that is not dissipated will be reflected. In their study on wave reflection of steep rubble mound breakwaters, Muttray *et al.* (2006) summarized several empirical wave reflection formulas. They came to the conclusion that the predicted reflection coefficients deviate significantly from measured coefficients. According to the experimental results performed on steep-sloped breakwaters, the impact of wave breaking and permeability has a nearly equal effect on the reflection coefficient. Equations that rely on the surf similarity parameter for prediction overestimate the effect of wave breaking and are

therefore not suitable for rubble mound breakwaters with steep front slopes since they don't account for the impact of permeability.

In their work, one of the equations deemed suitable for the prediction of the reflection coefficient is that proposed by Van der Meer (1992), as it incorporates not only the breaker index but also the permeability of the structure. This equation considers the combination of the armour layer, underlayer, and core as a whole by using the notional permeability. The equation, with a standard deviation of 0.12, has the following form:

$$C_r = 0.07 \cdot (P^{0.08} + \xi), \text{ using: } \xi = \frac{tan^{0.62}\alpha}{(H/L_0)^{0.46}} \tag{2.11}$$

Besides, an empirical wave reflection formula was developed by Muttray *et al.* (2006), applicable for 1:1.5 sloped rubble mound breakwaters with a core porosity of about 40%, based on the relative water depth:

$$C_r = \frac{1}{1.3 + 3h\frac{2\pi}{L_0}} \tag{2.12}$$

The standard deviation of the proposed formula was 0.02 for irregular waves.

In the preliminary study of the reflection of a Coastalock armour layer, Molenkamp (2022) proposed a formulation that considered wave steepness and spacing as the governing factors, while excluding underlayer thickness due to its negligible effects in predicting the coefficient of reflection. The reflection coefficients used to derive the formulation were averages of all measured reflection coefficients for tests with $1.5 \leq N_s \leq 2$, as these significant wave heights were present in all test series, allowing for comparisons under comparable conditions. The contribution of wave steepness was determined by adapting the formula proposed by Muttray *et al.* (2006), while the contribution of armour spacing was quantified by a straight linear fit. This resulted in the following equation, based on the weighted Least Squares Error method:

$$C_{r,\text{Coastalock}} = 0.2 + 2.34 \cdot C_{r,\text{M}} - 0.25 \cdot S \tag{2.13}$$

Here, S represents the armour unit spacing in decimal form, and $C_{r,\text{M}}$ is the reflection coefficient according to Equation 2.12. Molenkamp (2022) suggested approaching the equation with caution, considering it as indicative rather than definitive predictions of the behavior of Coastalock unit due to unexplained anomalies observed in validation tests.

2.5. Core

Volume-filling core material, obtained from quarries, is characterized by geotechnical properties like typical shear strength, placed porosity and permeability. These properties are closely related and influenced by the width of the stone grading and amount of fines present. Depending on rock quality and production method, core permeability can be substantially affected by the presence of fines, decreasing the core permeability. Constructing the core out of dredged sediment or the application of sand and geotextile container cores can result in an impermeable core. For optimal design of a breakwater, understanding is needed of the performance of different types of core materials under specific conditions.

Influence of permeability on flow on and in a breakwater

The permeability of a slope has a significant impact on the flow on and inside the breakwater. In structures with an impermeable or less permeable slope, water movement causes the highest possible velocities only in the outermost part of the structure. However, with a permeable core, flow will also take place inside the structure. The outside water motion is connected, via the cyclic in and outflow through the armour layer and filter layer, to the flow inside the pores of the core.

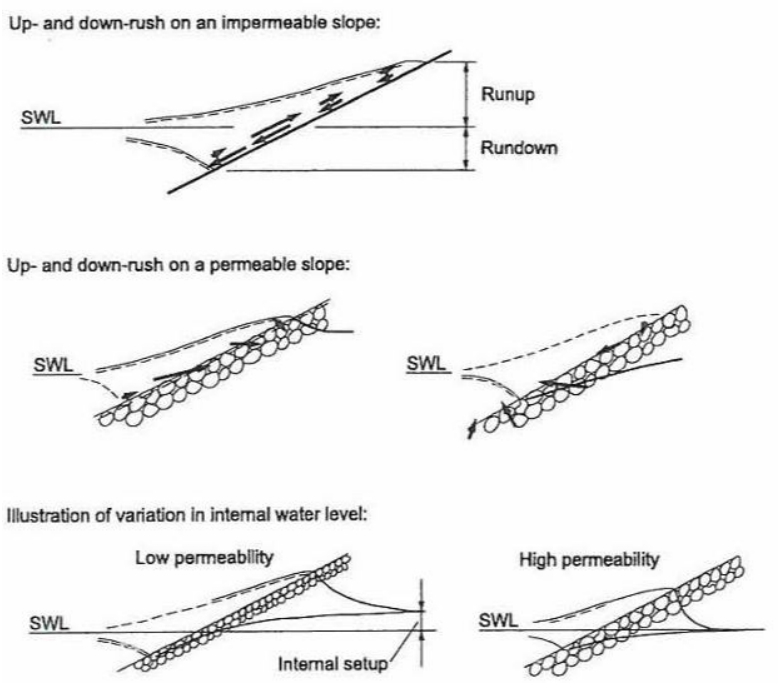

Figure 2.11: Up- and down rush on slopes (H. F. Burcharth, 1993).

According to Hald (1998), an increase in permeability reduces flow velocities in the outer layers, compared to an impermeable core. During the uprush, the period of inflow is larger than the period of outflow during downrush, which results in a rise of the internal water level inside the breakwater. This leads to a complex flow field inside the structure, for which no simple prediction models exist. Consequently, a comprehensive understanding of these velocities requires a combination of physical and numerical modeling. The most critical flow field interaction occurs when the downrush of the previous wave meets the uprush of the succeeding wave, just below the still water level.

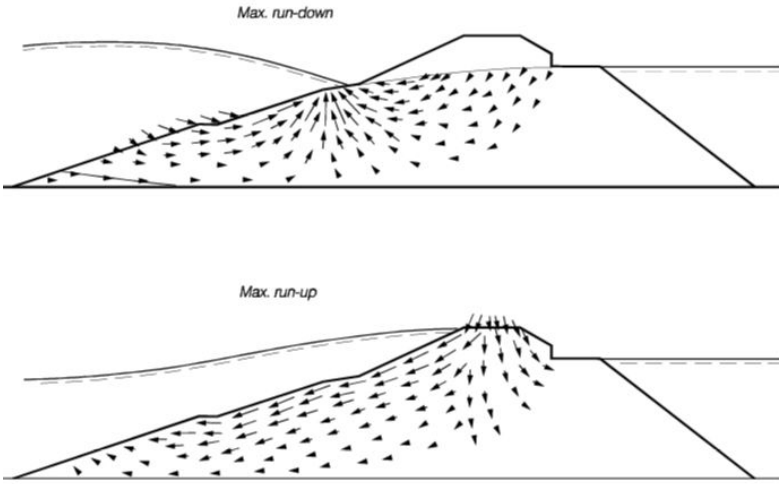

Figure 2.12: Depiction of internal velocity typical for maximum run-up and run-down on a slope (Barends and Hölscher, 1988).

Accurate predictions of the performance of permeable coastal structures depend on unraveling these complex interactions and understanding how pore pressures, pore velocities and wave attenuation within the permeable structure influence hydraulic stability, wave overtopping, and reflection

2.5.1. Influence of core porosity on stability formulae

During wave attack on a breakwater, the wave penetrates the structure into the rubble mound and dissipates its energy by turbulent flow. When the porosity of the core is low or the core is impermeable, higher degrees of reflection occur, increasing the loads on the armour. Core permeability can have a large influence on the required armour size; lower core permeability can lead to significantly larger required diameters of the armour layer (Reedijk et al., 2008). Over the years researchers have tried to approximate this aspect of wave structure interaction. Designs are based on empirical relations, physical model tests and real life experience. A few design approaches are considered below.

Van der Meer

The effect of permeability on the stability of rock slopes is accounted for in the method, as proposed by Van der Meer (1988), by introducing the term of notional permeability P. The term lacks a physical definition. It solely is based on curve fitting of the result three test setups; assuming an intermediate fourth state. A structure consisting of only armour stones, hence being fully homogeneous ($P = 0.6$), a rock armour placed directly on a permeable core ($P = 0.5$ with $d_{armour}/d_{filter} \approx 3$), an armour-filter layer combination on a permeable core which has been assumed and not tested ($P = 0.4$ with $d_{filter}/d_{core} \approx 4$), and a 'impermeable' core ($P = 0.1$).

$$\text{For plunging waves: } \frac{H_s}{\Delta D_{n50}} \propto P^{0.18} \tag{2.14}$$

$$\text{For surging waves: } \frac{H_s}{\Delta D_{n50}} \propto P^{-0.13} \xi_m^P \tag{2.15}$$

According to the proposed method, plunging waves can result in a difference up to 38% in required diameter. The difference is even more extreme for surging waves, depending on the period of the waves that influences the breaker parameter.

Van Gent

The ratio between the nominal armour layer diameter and the nominal core diameter is used in the stability formulation by Van Gent et al. (2003) to described the influence of core permeability on the stability of rocks on a slope with shallow foreshores.

$$\frac{H_s}{\Delta D_{n50}} \propto (1 + \frac{D_{n50-core}}{D_{n50}})^{2/3} \tag{2.16}$$

In the case a fully permeable core, comprised of armour material, is compared to an structure with an impermeable core, the required armour size difference amounts to 59%.

Hudson

Based on data gathered by Van der Meer (1988) and Van Gent et al. (2003), the Rock Manual (2007) gives a guideline on the stability factor present in the equation as proposed by Hudson.

$$\frac{H_s}{\Delta D_{n50}} \propto K_d^{1/3} \tag{2.17}$$

Values of 1 have been proposed for structures with impermeable cores, while permeable cores with a value of 4; a approximately 59 % difference in diameter. Under specific circumstances this, approach may lead to an overestimation of the required armour diameter. The Rock Manual highly suggests predicting the stone diameter by means of alternative stability formulations and to verify the predictions based on case specific physical model tests.

2.5.2. Effect of core permeability on armour stability of interlocking units

No general guidelines are present for interlocking concrete armour units, be it random or orderly placed, on the topic of the effect of core permeability on armour layer stability. Physical model testing is required for obtaining empirical parameters for correction. Over the years several tests have been performed concerning this topic.

Accropodes
In the study on the influence of core permeability on hydraulic stability, Burcharth (1998) found a significant relation. Test were performed with irregular waves, with a corresponding surf-similarity parameters of 3.75 and 5.0, on two types of core material: fine and coarse. The notional permeability of both cores could be approximated by a value of 0.2 and 0.4 respectively. The armour stability for both surf-similarities increased substantially when comparing the less permeable to more permeable core. For a no damage scenario when subjected to short waves a 46% increase of diameter would be required. For long waves the differences increased to an order of 100%. What was noticeable during the tests, was the difference in failure; the coarse core structures failed very suddenly, while the failure of the fine core structures developed much slower. Burcharth concludes that the Accropode armour layer is much more sensitive to variations in core permeability when compared to conventional rock armour.

Xbloc and XblocPlus
Delta Marine Consultants (DMC) (2023) provides correction factors for specific breakwater design, with the goal of giving a first estimate of the required block size used. These factors are based only on project specific model tests. For detailed design and optimization, physical model testing is highly advised. While the guidelines provided by DMC focus solely on the design of Xbloc and XblocPlus structures, DMC believes that the phenomena described above can also be applied to other concrete interlocking armour units.

	Xbloc	XblocPlus
Impermeable core ($P = 0.1$)	2	1.5
Low permeability core ($P = 0.2$)	1.5	1.25

Table 2.3: Correction factor on unit weight of Xbloc and XblocPlus due to core permeability (Delta Marine Consultants, 2023).

In her MSc thesis on the investigating of failure mechanisms of an Xbloc armour layer for structures with three different permeabilities, Verdegaal (2013) identified key failure mechanisms, including settling of the armour layer, rocking of units, lifting of armour units, and collapsing waves. These mechanisms varied due to differences in water motion in the tested structures. Decreasing permeability resulted in increased run-down levels and hydraulic gradients in the Xbloc armour layer, impacting stability. Settling of the armour layer, induced by downward forces and friction loss, reduced rocking, suggesting not all settling is inherently negative. In open cores damage progression was influenced by low interlocking forces, especially in the form of rocking. Meanwhile, settling and lifting played a significant role in the 'normal' core structure. Verdegaal found no increase of stability for a core with a higher porosity than a 'normal' core, contrary to what Van der Meer (1988) proposed for rock armour structures. The decrease of stability number coinciding with a lower core permeability was on the other hand confirmed; the effect was even stronger than assumed by DMC. This finding was however not adopted in the DMC guidelines.

2.5.3. Influence of core porosity on overtopping

According to the EuroTop manual (2018) the maximum run-up can even decrease by $1/3^{rd}$ when comparing an impermeable breakwater core ($R_{u2\%}/H_s = 3$) to a permeable breakwater core ($R_{u2\%}/H_s = 2$). For impermeable slopes, the surging waves slowly oscillate up and down the slope, causing all the water to stay in the armour layer, resulting in high run-up. The surging wave behaves like a wave on a steep and smooth slope, and roughness has less influence. In contrast, breakwaters with permeable cores can effectively dissipate more wave energy than those with impermeable cores due to the infiltration and seepage of water through the core, creating hydrodynamic pore pressures that aid in wave energy dissipation. The presence of a permeable core alters the run-up process by allowing waves to penetrate into the armour layer and sink into the under layers and core, resulting in a reduction of wave run-up on the seaward slope of the breakwater. The relation between run-up and overtopping is that lower run-up levels generally result in lower overtopping rates. This is because as the waves reach lower elevations on the seaward slope of the breakwater, they are less likely to exceed the crest height and spill over the top of the structure.

2.5.4. Influence of core porosity on reflection

Breakwaters with permeable cores cause less wave reflection due to the permeability of the core, allowing for wave energy to dissipate through the breakwater. This results in lower wave reflection coefficients compared to breakwaters with impermeable cores. The porosity of the core allows for the passage of water, reducing the amount of wave energy reflected back to the sea.

3

Physical model test set-up

The present chapter outlines the experimental set-ups used in the model tests. The first section outlines the specifications of the flume, followed by a discussion of the hydraulic parameters. The third section presents a cross-section of the set-ups employed, as well as the accompanying structural parameters. Measuring techniques and equipment are discussed next. This includes the measurements of wave characteristics, stability measurements through video-based observation and the application of the structure from motion principle, and the measurements of the average overtopping discharge. Finally, armour layer configurations are discussed and the test series are introduced, explained, and an overview is provided. Additionally, Appendix E contains detailed cross-sections of the test setups used, and Appendix G contains an overview of the procedures carried out during the testing phase.

3.1. Wave flume

The wave flume utilized in this study is located in the Hydraulic Engineering Laboratory of the TU Delft and has a length of $39.00m$, width of $0.79m$, and a height of $1.00m$. The generation of waves is achieved through an electrically driven piston-type generator with a horizontal stroke length of $2.00m$, capable of producing both regular and irregular waves. The practical limit of achievable significant wave height is approximately $0.18m$. The flume is equipped with an Active Reflection Compensation system which measures reflected waves propagating towards the wave boards and compensates for these waves.

3.2. Hydraulic parameters

3.2.1. Wave spectrum

To enable easy comparison with other concrete armour units, the JONSWAP wave spectrum is chosen. It represents common coastal sea states in physical model testing, with shape parameters γ of 3.3, σ_a of 0.07 and σ_b of 0.09.

3.2.2. Wave height

After constructing the model, it was subject to lower energy waves to facilitate the settling of the armour units into a more stable configuration. This was achieved by exposing the model to small waves, in the range of 50-60% of intended test conditions, simulating the early stages of a storm (following Frostick et al., 2011). The spectral significant wave height of the shake-down waves is chosen to be $0.07m$. This guided by the targeted stability number for design of approximately N_s = 2.5, assuming a safety factor of about 1.5 for sudden failure, and previous findings for spacings of 10% and above. For subsequent runs, the wave height is increased by $0.015m$ in each run until failure, the designated time for the test series expired, or the limit set at $0.175m$ is achieved.

3.2.3. Storm duration
The shake-down waves were limited to 500 waves. Subsequent test runs are extended to a duration of 1000 waves. The total duration of each test series can be approximated using the equation: $D = T_P \cdot N$, where D is the duration, T_P is the peak period, and N is the number of waves. This duration excludes the time needed by the wave generator to reach operating conditions in which it generates the waves with the desired characteristics. It is presumed that operational conditions are achieved after a duration of $10 \cdot T_p$ following the arrival of the first wave.

3.2.4. Wave steepness
To investigate the impact of wave steepness on Coastalock armour damage on a permeable slope, two different wave steepness values were considered: s_{0p} of 0.02 and 0.04. The first one was expected to cause higher levels of armour damage, while the latter is representative of a typical wave steepness found in coastal environments and commonly used in physical modeling experiments. Both wave steepness values lead to surging waves after breaking. While maintaining a constant wave steepness for each step in significant wave height, the peak period is adjusted accordingly.

3.2.5. Water depth
The structure was tested with a constant Still Water Level (SWL) of 0.60 m measured from the bottom of the flume, ensuring comparability with the results obtained by Molenkamp (2022).

3.3. Structural parameters
3.3.1. Cross-sections
During testing, two set-ups were distinguished. The first involved replicating the relevant geometry to correspond with the preliminary research of Molenkamp (2022), aiming to examine the impact of the permeable core on the stability, overtopping, and reflection of a Coastalock armour layer. In this setup, the bottom row of Coastalock units is upheld by a stationary beam, extending in alignment with the slope of the armour layer towards the base of the flume, thus emulating conditions akin to deep water. Therefore, this set-up will be referred to as the 'Deep Water' set-up. This lower section of the slope was designed to be interchangeable.

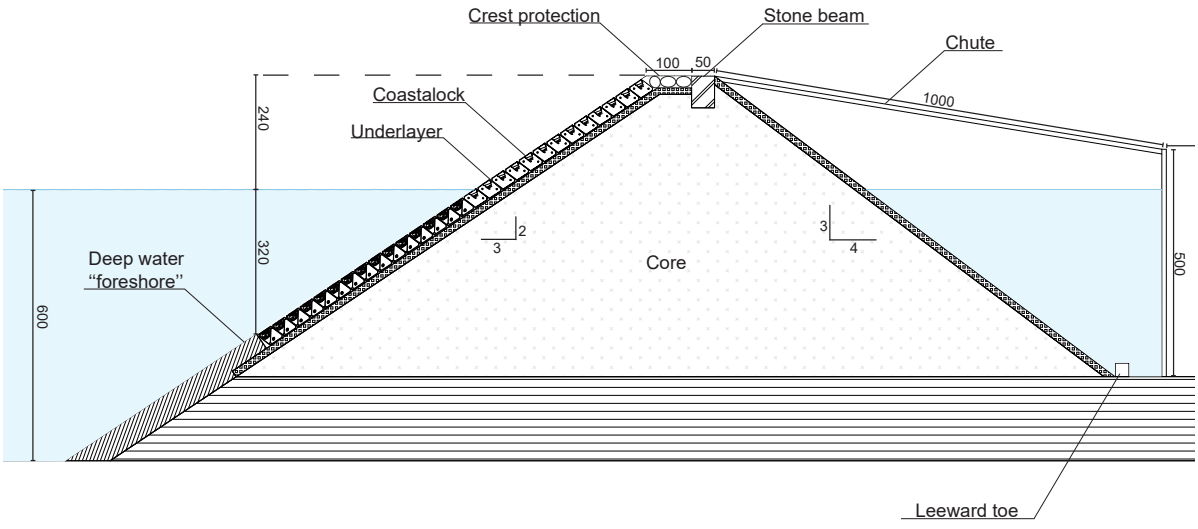

Figure 3.1: Cross-section structure: 'Deep Water' set-up; measurements are given in mm.

Subsequently, without the removal of the core and with only a partial reconstruction of the lower portion of the underlayer, the deep water "foreshore" can be substituted with a plateau. On this plateau, a loose rock toe berm could be placed to emulate a toe situated in deep-water conditions, elevated above the seabed. The placement could be executed on an interchangeable bottom profile featuring varying roughness. This was carried out to assess the susceptibility of the Coastalock armour layer to sliding,

effectively mimicking its placement on an underlayer or directly on a rocky surface. Henceforth, these set-ups will be referred to as the 'Toe Berm on Rough' and 'Toe berm on Smooth' set-ups.

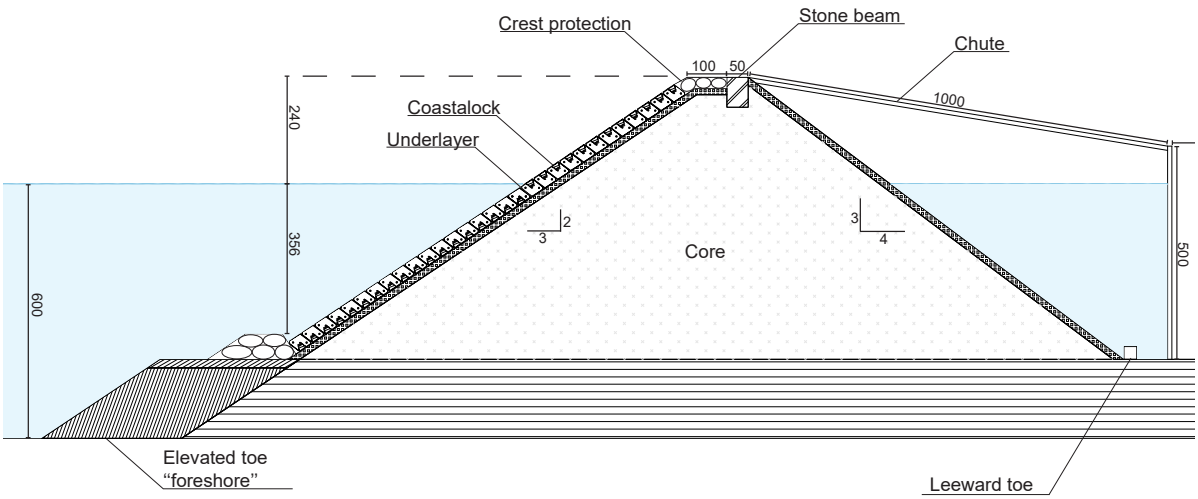

Figure 3.2: Cross-section structure: 'Toe berm on Smooth' set-up; measurements are given in mm.

Please refer to Appendix E for a comprehensive depiction, including cross-sections of the entire flume for both designs, as well as cross-sections and detailed views specifically focusing on the structures.

3.3.2. Armour layer

Coastalock model units

The Coastalock model units feature an intended nominal diameter of $0.03m$, which is a factor of about 37.4 smaller than the corresponding prototype units. This particular block size was selected by Molenkamp (2022) to strike a balance between being small enough to ensure damage even with the largest waves practically achievable in the wave flume, yet large enough to mitigate laminar flow scale effects at lower wave heights. The prototype units were designed with a density of approximately 2400 kg/m^3, yielding an ideal relative density of 1.33 (2019) compared to seawater, with an assumed density of 1030 kg/m^3. Measurements of the model units, post-production, conducted by Molenkamp, are available in Table 3.2. For an in-depth description of the model unit creation process and characteristics, please refer to Molenkamp's work (2022). The resulting overall model scale factor for stability, taking the relative density difference into account, equals 38.5.

Armour unit spacing

Horizontal spacings, as introduced by Molenkamp (2022), in between the armour units were used as a measure to test the responsiveness of Coastalock armour units to generated uplift pressures. This was achieved by removing a given percentage of Coastalock columns, thereby reducing the block count across the slope width. Spacings, S, of 0%, 10%, and 20% are slated for testing in the current program. The initial design, with 0% spacing features fully interlocking blocks, adhering to the original Coastalock design. Higher spacings were considered due to their increased stability and reduced concrete consumption. The 10% spacing is of particular interest, as it represents the largest spacing for which failure was observed on an impermeable slope. No failure was observed for higher spacings. The inclusion of a 20% spacing is intended to provide a comprehensive overview of the behavior of the armour units.

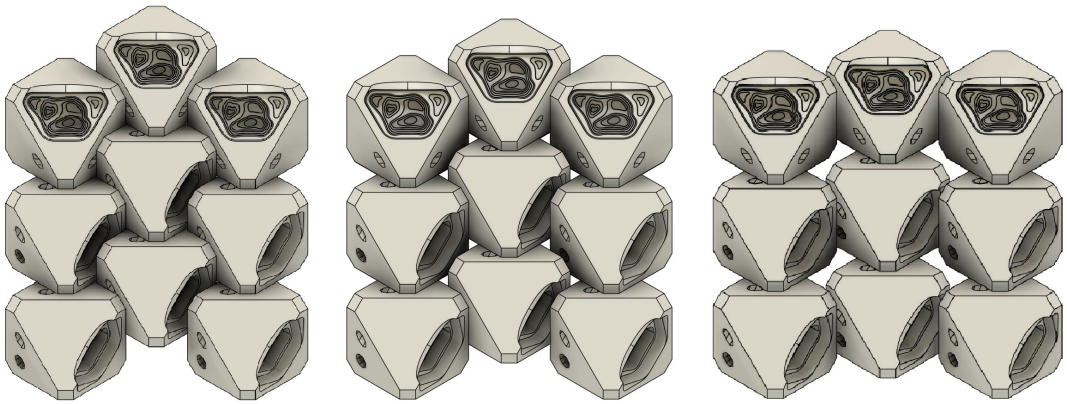

Figure 3.3: Depiction of a Coastalock armour layer with 0%, 10% and 20% spacing, showcasing the increase in inter-unit void size.

Armour unit protrusions

In collaboration with the design team of ECOncrete, two sets of protrusions were designed for addition to the original armour unit, aiming to ensure a predetermined separation between units. The protrusions took the shape of truncated cones, of which a visual representation is provided in Figure 3.4. The set of short protrusion results in a separation equal to that of the 10% spacing. Meanwhile, the set of long protrusions results in a separation equal to that of 22.5% spacing. This choice aligns with the previously mentioned spacing of interest and available flume width. The armour layers containing armour units with short or long protrusions are henceforth referred to as those containing 10% protrusion or 22.5% protrusion, respectively.

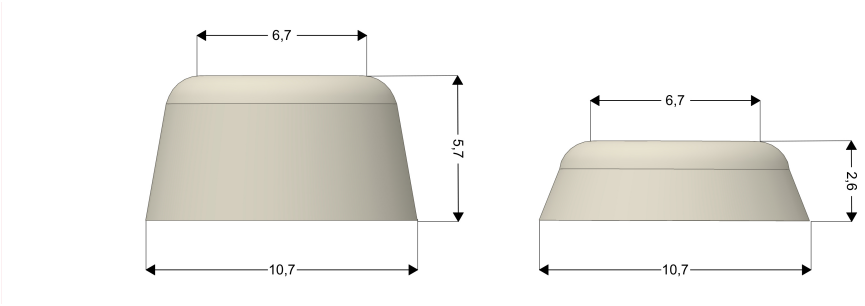

Figure 3.4: Protrusions models: on the left 22.5%, on the right 10%. Measurements are given in mm.

For the creating the two types of protrusions, Steel-filled Metal Composite PLA was selected as the filament due to its density of approximately $2300 kg/m^3$. The characteristics of the protrusions were measured using the submerged suspension technique, as outlined by Hughes (2005), and are as described in Table 3.1.

Protrusion type	$h_p[mm]$	$S[\%]$	$W_p[g]$	$V_p[mm^3]$
Short	2.6	10	0.40 ($\sigma = 0.006$)	181 ($\sigma = 2$)
Long	5.7	22.5	0.90 ($\sigma = 0.006$)	402 ($\sigma = 4$)

Table 3.1: Characteristics of protrusions.

A sealant suitable for adhering objects in wet conditions, was employed to affix the protrusions onto the armour units. The weight of the sealant and resulting changes in volume were omitted from the calculations due to the small amounts applied to each protrusion. A jig was designed and 3D printed to fit over the model units. The cut-out slot in the jig allowed for precise and consistent adherence of the protrusion at the intended location.

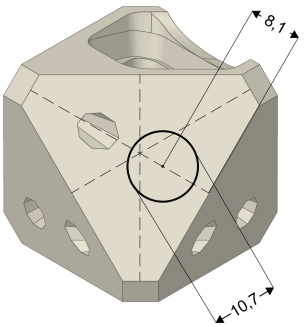

Figure 3.5: Protrusions placement on prototype Coastalock unit. Measurements are given in mm.

The characteristics of the prototype armour units, post-adherence, are detailed in Table 3.2. The addition of the protrusions slightly alters the moment of inertia, as they are lighter than acrylic resin of which the model units are comprised (density of $2275 kg/m^3$), while the lead ball used as compensation of the lower density is still situated in the center. However the change is deemed to be negligible based on the small changes compared with the original model units.

Armour unit type	$d_{n,CL}[m]$	$d_{n,CL}[\%]$	$\rho_{CL}[kg/m^3]$	$\rho_{CL}[\%]$	$\Delta[-]$	$\Delta[\%]$
Unaltered CL	0.0298	-	2299.44	-	1.30	-
10% protrusion CL	0.0300	+0.67	2298.26	-0.39	1.30	<0.1
22.5% protrusion CL	0.0301	+1.01	2297.77	-0.56	1.30	<0.1

Table 3.2: Characteristics of prototype Coastalock armour units including protrusions.

A representation of the Coastalock armour units without alterations and with 10% and 22.5% protrusions can be found in Figure 3.6.

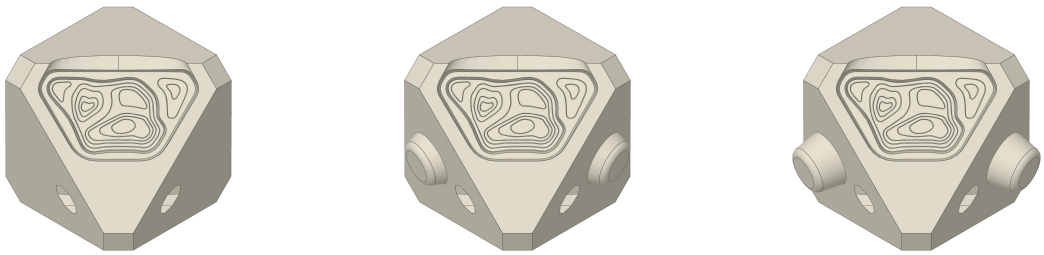

Figure 3.6: From left to right: Coastalock armour unit without protrusions, with 10% protrusions and with 22.5% protrusions.

Side elements

The preliminary research employed 3D-printed side elements inserted between the first and last Coastalock armour units of a slope row and the flume wall. This arrangement aimed to prevent shortening the leakage length by avoiding gaps in the armour layer sides. However, due to their low density compared to the model blocks, resulting in high buoyancy and reduced interlocking capabilities caused by the presence of the glass side wall, upward forces became problematic. These conditions were considered unrealistic. To address this issue, two chains were placed along the flume wall in the cross-shore direction. However, this solution could introduce a wall effect, wherein the relative movement of the side units is less than that of the middle units due to the presence of the chains.

The current research applied the same method for the test series without protrusions. For test series involving protrusions, no side elements were developed or used. Instead, only chains were applied to address possible movement of the armour units adjacent to the flume walls.

3.3.3. Under layer

In his preliminary research Molenkamp (2022) employed an underlayer with a d_{n50} of 8.34mm, featuring a relatively steep grading of d_{85}/d_{15} of 1.22, resulting in a relatively high ratio of $d_{n50,armour}/d_{50,underlayer}$ of 3.6, deviating from the recommended guideline. Strict geometrical limits apply to the transition between a breakwater armour layer and the first filter, especially under cyclic wave loading perpendicular to the slope. Schiereck and Verhagen (2019) recommend a weight ratio between the armour layer and the underlayer of less than 10 to 15, corresponding to a decrease in nominal diameter by a factor of less than 2.2 to 2.5. It is worth noting that diameter ratios of 3 have been successfully applied in practice. In the standard test cases, the underlayer thickness equaled $2d_{n50}$.

Despite deviations from the recommended guidelines, an underlayer with characteristics similar to those used by Molenkamp (2022) in his preliminary research was utilized for the sake of comparability. Based on calibration using the submerged suspension technique principle on 100 sample stones, an underlayer was selected with a d_{n50} of 7.28mm and d_{85}/d_{15} of 1.29. This reduction in nominal diameter resulted in an increased ratio of $d_{n50,armour}/d_{50,underlayer}$ to 4.01 and a further deviation of the guidelines. A standard underlayer of $2d_{n50}$, was implemented, yielding an underlayer thickness of 15mm.

3.3.4. Core

The decision was made to scale the core diameter using Froude scaling, considering the velocities within the core. In the absence of an existing prototype, a core prototype size was chosen to be half of the underlayer size. This results in a required d_{n50} of 3.72 mm. Subsequently, a core grading was established, characterized by a d_{50} of 4.62 and d_{85}/d_{15} of 1.68, based on a sieve analysis of the material. This results in a d_{n50} of 3.89mm.

3.3.5. Crest

The crest of the structure was located 0.24m above the initial SWL of 0.60m, allowing for comparability with the preliminary tests. The armour units extended to just below the crest. The total crest width, B, measured 140mm. The spaces between the top row of Coastalock units and the front seaward edge of the crest itself, spanning a width of 90mm, were protected by loose stones, the same stones used for the toe berm, with d_{n50} of 29.27mm. The leeward side of the crest was reinforced with a stone beam spanning the width of the structure, serving to stabilize the crest. A detail of the crest can be found in Figure 3.10.

3.3.6. Inner slope

Given that the inner slope of the structure is beyond the scope of this research, it was steepened to a 3V:4H slope to minimize material usage. The slope was protected by the underlayer rocks applied with the standard thickness of $2d_{n50}$. No protection by larger stones was applied as no wave overtopping was expected to damage the inner slope.

3.3.7. Toe berm

To prioritize the examination of the armour layer's response and its effects on stability, overtopping, and reflection, some measurements were conducted in the 'Deep Water' set-up. In this setup, the first row of armour units was supported by a fixed beam. In the latter part of the test series utilizing the 'Toe Berm' setup, the design of the toe berm itself followed the method proposed by Van der Meer (1998). This method was chosen due to its applicability range and suitability for designing toe berms situated in deep water conditions, elevated above the seabed. It was decided that the nominal diameter of the toe berm stones should not be larger than the armour units, as this would be unrealistic. Moreover, to maintain stability, a narrow rock grading was necessary.

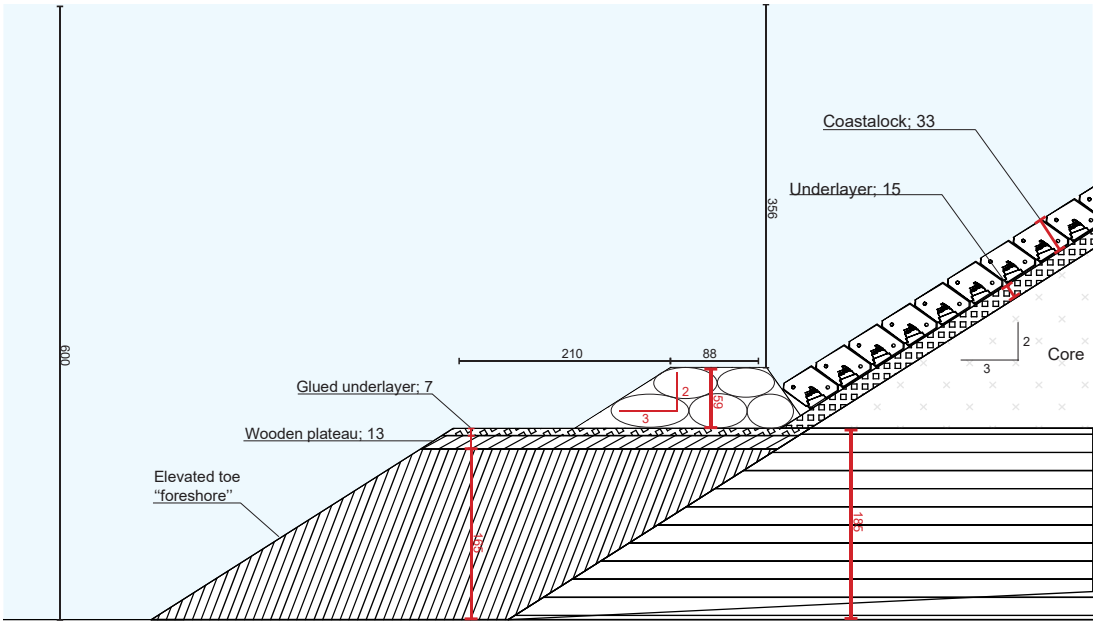

Figure 3.7: Cross-section detail: Elevated toe with rough surface; measurements are given in mm.

After initial sieving and strict selection, the following toe rock characteristics are obtained based on calibration using the submerged suspension technique principle on 100 sample rocks: a d_{n50} of 29.27mm, a d_{85}/d_{15} of 1.19 and a ρ_{toe} of 2591.13kg/m^3.

In order to assess the susceptibility of the armour layer to sliding, it was important to maintain stability of the toe berm, even under the influence of higher waves nearing the limit of the wave generator. This required lowering of the toe location and extending the armour layer by two rows of Coastalock units to satisfy the size criterion of the toe berm rocks and ensure the necessary stability of the toe berm. According to the Van der Meer formulation, no damage should have been observed for a H_s below 0.15m, as the value remained below the start of damage criterion of 0.5. Instability at the toe was anticipated for higher significant wave heights, as damage was expected to initiate for wave heights just above this threshold. However, failure was projected to occur at values of approximately H_s of 0.20m, a limit that was not expected to be reached due to limitations of the wave generator and flume.

A traditional "three-stones-wide, two-stones-high" toe berm was employed. Additional space for a wider toe berm, was reserved on the plateau in case the traditional toe berm could not support the armour layer.

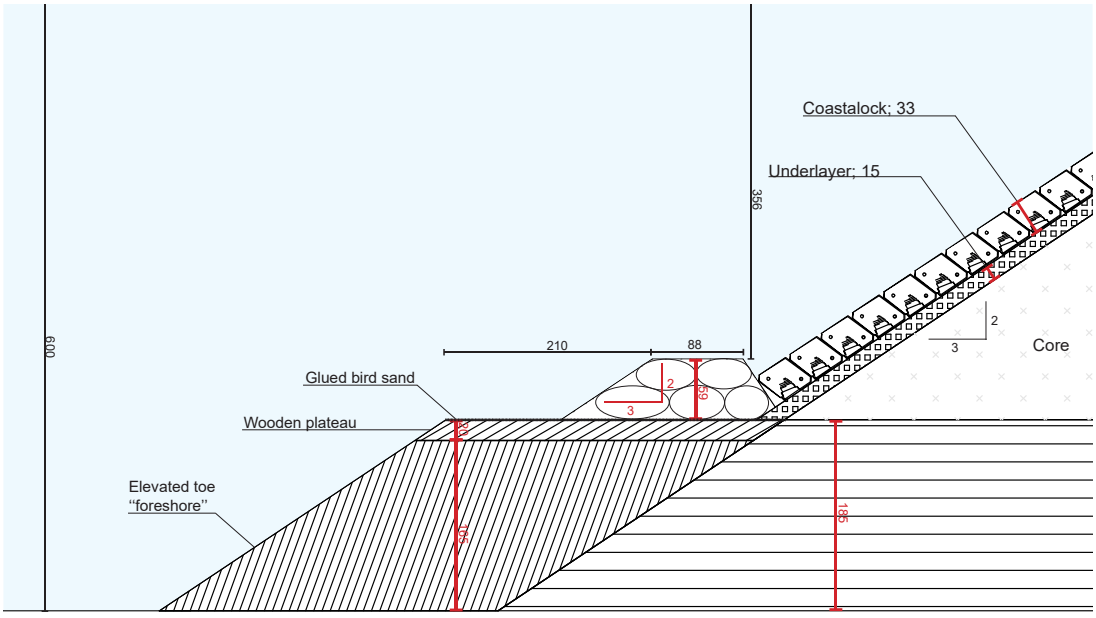

Figure 3.8: Cross-section detail: Elevated toe with smooth surface; measurements are given in mm.

The interchangeable wooden plateau on which the toe berm was built was available with two distinct top finishes. The first one was coated with a glued single layer thickness of the underlayer, simulating traditional placement, as seen in Figure 3.7. The second one was coated with a layer of glued bird sand, representing direct placement on a rocky seabed, as seen in Figure 3.8. The two different underlayer materials on which the toe berm rests are intended to alter the resistance to sliding and the interlocking capabilities of the toe berm rocks.

3.3.8. Foreshore

In this study, the foreshore slope in front of the toe had been chosen to match the breakwater slope of 2:3. However, it should be noted that the foreshore cannot be considered a traditional foreshore; rather, it is an integral part of the structure due to its steepness. In fact, it resembles a breakwater structure in deep water, where the toe is elevated above the sea bed. This design choice has been made to ensure that breaking of the highest waves primarily produced surging breakers, as opposed to plunging breakers (resulting from breaking on shallower foreshores). Plunging breakers could lead to more violent wave breaking on the structure and toe berm.

3.4. Measurement techniques and equipment

3.4.1. Wave characteristics

In the wave flume, two sets of three wave gauges are arranged in a line parallel to the wave propagation to measure wave characteristics. The wave gauges, manufactured by Deltares, were employed to measure generated incoming and reflected waves.

The first set of gauges, designed to measure waves generated by the wave generator, was positioned 5 meters away from the generator. This distance satisfies the criterion ensuring sufficient space for the wave probe array to assess incident and reflected waves near the wave paddle (Frostick et al., 2011).

For the second set of wave gauges, it is recommended to position the multi-gauge array at a distance greater than 0.4 times the peak wavelength from the structure. This positioning aims to reduce the effects from evanescent modes, ensuring more accurate measurements of incident waves near the structure and reflected waves by the structure (Frostick et al., 2011). The longest expected wavelength results from waves with a H_s of $0.16m$ and s_{0p} of 0.02, amounting to $8m$. Therefore, to fulfill this recommendation, the first wave gauge of the second set should be located at least $3.2m$ away from the structure.

The separation distance between the wave gauges was determined using the 3a method proposed by Mansard and Funke (1980) and optimized by Wenneker and Hofland (2014). The distance between the three gauges is determined by the following criteria: $\epsilon L_{max} < x_{12} < EL_{min}$ and $x_{23}/x_{12} = 0.50$, where $\epsilon = 0.04$ and $E = 0.95$. The shortest expected wave length is $1.25m$, which results from shakedown waves with a height of $0.05m$ and a steepness of 0.04. Thus, the spacing between the wave gauges is determined to be $0.32 < x_{12} < 1.18$. Eventually, the wave gauges were spaced at $x_{12} = 0.60m$ and $x_{23} = 0.30m$.

Figure E.1 provides a comprehensive overview of the cross-section of the wave flume, including the placement and distances to the structure of the wave gauges.

The wave decomposition is performed using `decomp`, a method originally developed by Bakkenes (2002) and Klaasman (2005) for MATLAB. In 2023, Jennifer Rodrigues Monteiro updated it for Python. This script is specifically tailored for wave signal decomposition in the wave flume of Delft University of Technology, performing a comprehensive spectral analysis of the wave signal.

3.4.2. Stability: Visual observations

The experimental setup utilized two GoPro Hero 10 cameras to document and analyze the response of the Coastalock armour units to wave loading. These cameras offer a resolution of 23 MP for capturing high-quality photos and the capability to shoot videos at a resolution of 4k120fps.

The first camera is positioned perpendicular to the slope on a secure rig to prevent any unintended movement. It captures perpendicular photos of the slope, ensuring consistent angles for accurate comparison and analysis. This angle consistency is crucial for monitoring and documenting the effects of the shake-down tests, including any settling of the structure and movements of the armour layer. The second GoPro camera is secured to capture side-view video footage during each test run, recording at a higher frame rate for a detailed examination of armour movement. Like the first camera, its role is to monitor and document the effects of the shake-down tests, including any settling of the structure and movements of the armour layer. Any further settlement, movement, or damage of the materials during the tests should also be documented and reported.

The method described above, has been employed in all test series without protrusions and in test series involving long waves, which required extensive amounts of time due to the longer wave period. However, in addition to employing the side-view camera, test series involving protrusions, as the primary focus of the stability research, utilized a distinct measuring techniques and equipment, as elaborated in the subsequent section.

3.4.3. Stability: Structure from motion

SfM photogrammetry theory

Structure from Motion (SfM) photogrammetry, utilizes overlapping two-dimensional images captured from various angles using standard compact cameras, along with geo-referencing data, to produce three-dimensional spatial information for modelling object surfaces.

The movement of objects within a set of captured images, as the camera changes perspective, provides depth information for estimating three-dimensional coordinates. Through multiple viewpoints, computer algorithms establish lines of sight to key points on objects from different camera angles. Intersections of these lines yield estimated 3D coordinates, forming a point cloud. Expanding the number of sight lines enhances the reliability of the 3D coordinates for each corresponding point. Consequently, it is customary to employ a multitude of images, ideally with significant overlap and diverse perspectives, to reconstruct accurate three-dimensional structures.

SfM photogrammetry generates a point cloud in a relative image-space coordinate system. To quantify them, alignment to a real-world object-space coordinate system is necessary. This alignment relies on a 3D similarity transform using ground control points (GCPs) precise locations tracked between object and photos. GCPs provide exact real-world coordinates and ensure model accuracy, especially when high global accuracy is required. Effective GCPs must be stationary, with well-defined locations in the chosen coordinate system, and identifiable in at least a subset of the photos used.

Goal of SfM methodology
By comparing the 3D models of the reference profile, created after the exposure of the structure to settling waves, with subsequent 3D models completed after specific test runs or after extraction occurred, the movement of the armour layer could be tracked, and damage progression leading to eventual failure of the Coastalock armour layer could be monitored.

For this research, the Agisoft Metashape photogrammetric processing software was chosen. A description of the SfM processing by Metashape, along with the general workflow and settings used to generate the 3D models, can be found in Appendix F. The comparison between models is performed in combination with 3D point cloud processing software CloudCompare and using Python, as specified further in Section 4.1.

SfM test set-up
The images employed for the Structure from Motion (SfM) method were acquired using a 12MP digital camera with a 26 mm focal length (35 mm equivalent), in accordance with the guidelines provided by the Agisoft Metashape manual (2023). These recommendations are aimed at ensuring the generation of high-quality orthographic outputs. They were saved directly in TIFF format with dimensions of 4032x3024 pixels to minimize compression and noise compared to other image formats. The choice to utilize handheld photography necessitated finding a balance among ISO, aperture, and exposure to ensure image quality and accuracy. High ISO values were avoided to maintain detail, typically ranging from 60 to 125. To maintain sharp focus on all markers, a wide depth of field was achieved with an aperture setting of F/1.6. Moreover, to minimize motion blur, shutter speeds were set well above 1/60, varying based on lighting conditions.

As mentioned before, to ensure accurate results with the SfM methodology, the use GCPs is essential. Initially, 20 unique circular 12-bit GCPs were generated using Metashape and strategically placed around the structure. These GCPs were arranged in pairs and printed on sheets consisting of two $0.3mm$ thick aluminum cover layers and a polyethylene core. This material was selected for its lightweight, rigidity, and strength, making it suitable for applications near moving water and adherable to flume or structure components. Maintaining flatness, preventing deformation of the GCPs and avoiding any changes to the coded targets was vital.

Figure 3.9: SfM test set-up showcasing the GCP pair placement on the flume walls and on the 'Deep Water' foreshore.

The GCPs were intentionally distributed across three different planes of orientation to optimize accuracy. Specifically, four GCPs were affixed to both foreshores (parallel to the slope): the deep water foreshore

(targets 17-20) and the foreshore in the toe berm configuration (targets 21-24). Additionally, four GCPs (targets 01/02/09/10) were placed on top of the flume walls (horizontal plane), while twelve GCPs (targets 03-08/11-16) were mounted on the flume walls (vertical plane). Borders were taped around the GCP plates on the flume walls, ensuring the GCPs remained unobstructed, to prevent the plates from loosening due to wave action. Additionally, the taped borders served as a background, providing contrast against the see-through glass. The distances between these GCPs were meticulously measured using 360-degree laser levels and laser measures with millimeter accuracy in a local coordinate system. The intentional pairing of GCPs during printing facilitated the addition of a scale bar—a representation of a known distance within the scene. The scale bar serves as a tool to incorporate additional reference data into the Metashape project. The distance between the GCPs was defined with sub-millimeter accuracy based on the original files used for printing.

For tests involving the fixed toe beam, a minimum of 60 pictures were captured. For tests involving the extended toe berm with two additional rows of Coastalock, this was increased to a minimum of 95 pictures, which included images of the toe berm. These photographs were taken from various angles, including perpendicular shots to the slope with an approximate 60% overlap based on the number of armour units, images from the four corners of the model set-up to capture GCPs and shots perpendicular to the flume bottom. Each photo was optimized to effectively utilize the frame size, ensuring maximum coverage of the armour layer. Adequate lighting was essential for optimal results, while efforts were made to minimize reflections and glares. Although wet model units presented sub optimal circumstances, all GCPs were dried before photography, and the flume was adequately drained to reduce reflections from standing water at the bottom.

Pictures were taken after the passing of the settle-down waves with a H_s of $0.07m$ and at increments of increasing significant wave heights of $0.03m$ instead of at $0.015m$, or after failure occurred. This decision was made due to the time-consuming process of draining and refilling the flume before and after each set of photos.

3.4.4. Overtopping

The breakwater crest was connected to the overtopping basin situated as close as possible behind the structure via a chute extending across the entire width of the flume. Keeping the chute as short and wide as possible is a major factor determining for accuracy (Frostick et al., 2011). The overtopping basin had an internal surface area of $753mm$ by $753mm$ and a maximum depth of $500mm$. A wave gauge was installed inside the overtopping basin to measure water level variations and consequent average discharge due to overtopping in relation to an initial water level present in the overtopping basin. There should be a few millimetres difference, which sets the limit of zero overtopping. After each test run, once the water level was steady, and the overtopping volume had been measured, water could be pumped out using a submersible pump. Pumping in the middle of the test run was to be avoided, but if overtopping was deemed too extreme, a submersible pump was used to pump the water into an enclosed basin next to the flume. After the test run, the water could be pumped back into the overtopping basin for volume measurements, and little to no water was lost during this procedure.

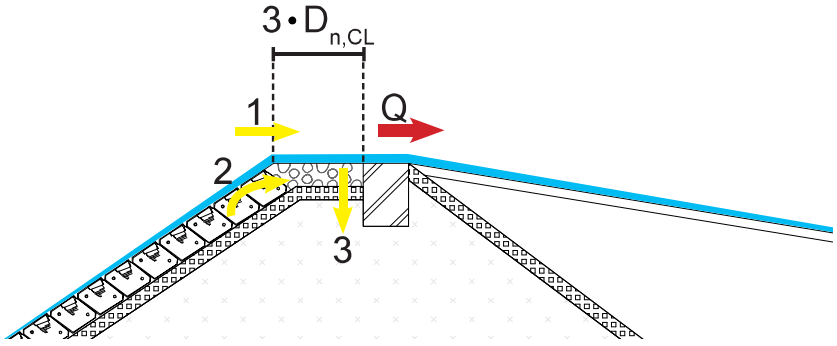

Figure 3.10: Cross-section detail of the crest indicating measured overtopping.

Since the overtopping chute did not rest on the structure itself, but was supported on rails adhered to

the flume walls, it would not lower with the structure during possible settlements. This could create a gap between the top of the crest and the overtopping chute, allowing water to enter. To prevent this, a watertight foil was applied to protect the inner slope from overtopping water. The stone beam at the leeward side of the crest served as a means to wrap a watertight foil under and over it, adhering it to the overtopping chute. This measure aimed to avoid measurement inaccuracies due to overtopping discharge loss and potential damage to the inner slope.

This study relied on measuring wave overtopping at a distance of $3D_{n,CL}$ from the seaward edge of the crest across the entire width of the structure. As illustrated in Figure 3.10, the majority of the overtopping discharge flows over the armour layer (1). Additionally, part of the overtopping discharge may travel through the armour layer (2) due to its permeability. The measured discharge is also influenced by the crest structure, composed of loose rocks and the stone beam. Consequently, water infiltration occurs through this section of the crest (3).

3.5. Test program

3.5.1. Tested armour layer configurations

The Coastalock units, initially without protrusions, were arranged in the 'San Diego' configuration. In this configuration, at Still Water Level (SWL), there was an orientation change: the armour units above SWL were positioned facing upwards, while those below SWL were oriented sideways, as depicted in Figure 3.11. This arrangement was chosen to facilitate direct comparability with preliminary results obtained on an impermeable slope. In his work, Molenkamp (2022) explored two additional configurations: one with all blocks facing upwards and the other with all blocks facing sideways. This was undertaken to discern the distinct effects associated with the two different orientations present in the 'San Diego' configuration. The study revealed an increase in stability when all cavities faced upward, particularly regarding the threshold for extraction. Conversely, when all units were turned sideways, a decrease in both the thresholds for 'breathing' and extraction was observed compared to the 'San Diego' configuration, which featured an orientation change at SWL. However, due to the limited number of data points available, no definitive conclusions could be drawn.

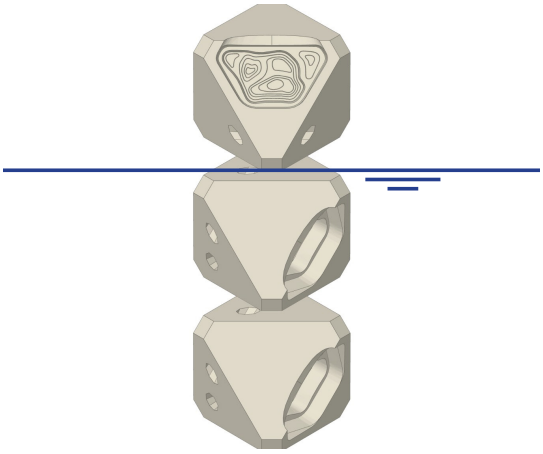

Figure 3.11: Schematization of Coastalock armour layer in the 'San Diego' configuration.

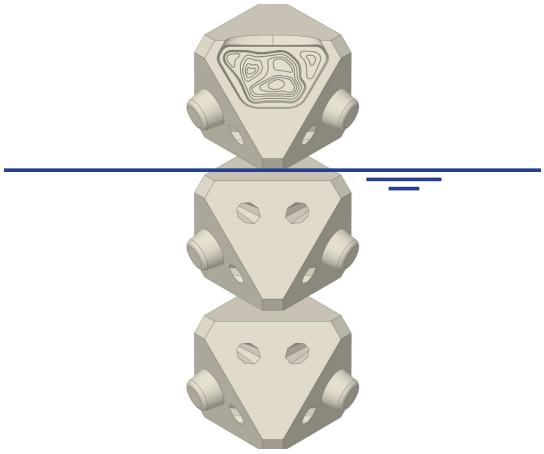

Figure 3.12: Schematization of Coastalock armour layer with protrusions in 'PO-SWL' configuration.

With the protrusions attached, an alternative configuration was required to ensure proper contact between the armour units. Sideways placement was hindered by the protrusion's location, restricting blocks to be oriented with the cavity either upwards or downwards. This protrusion-optimized configuration, where armour units change orientation from cavity upwards to cavity downwards, will henceforth be addressed as the 'PO' configuration.

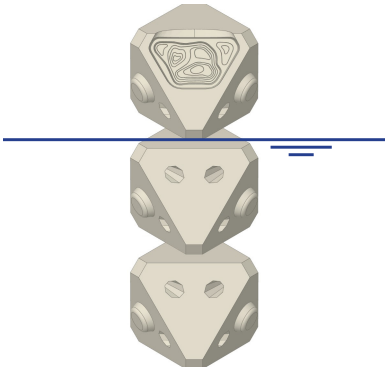

Figure 3.13: Schematization of Coastalock armour layer with 10% protrusions in the 'PO-SWL' configuration.

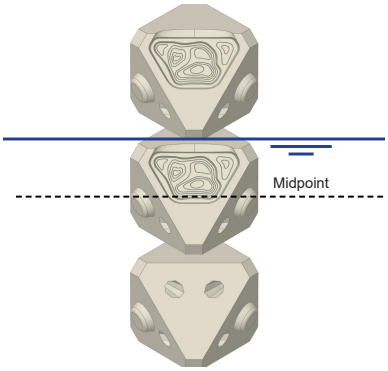

Figure 3.14: Schematization of Coastalock armour layer with 10% protrusions in the 'PO-Midpoint' configuration.

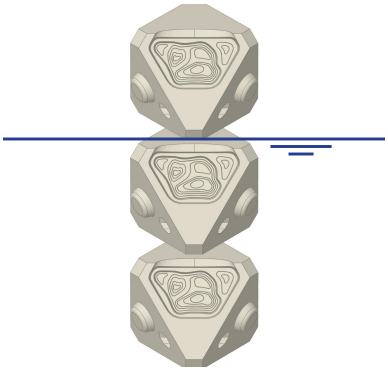

Figure 3.15: Schematization of Coastalock armour layer with 10% protrusions in the 'Upwards' configuration.

Tests were conducted using the 'PO' configuration, featuring an orientation change at SWL ('PO-SWL', Figure 3.13), as well as a variation with the orientation change lowered to the midpoint between SWL and the bottom of the armour layer ('PO-Midpoint', Figure 3.14). Additionally, a configuration where all units faced upwards ('Upwards', Figure 3.15) was tested. These tests aimed to investigate the effect of downward-facing orientation on stability.

3.5.2. Test series

Initially, test series without protrusions and with simple spacings were conducted. The aim was to assess the impact of a permeable core on the stability, overtopping, and reflection of a Coastalock armour layer compared to an impermeable core. The testing started with the 'Deep Water' set-up, conducting the s_{0p}=0.04 test series for the 0% spacing configuration (series 01), followed by the s_{0p}=0.02 test series (series 02). This procedure was repeated for 10% (series 03 and 04) and 20% (series 05 and 06) spacing.

Next, long protrusions were attached to the Coastalock units to investigate their influence on the stability, overtopping, and reflection characteristics on a slope with permeable core. This resulted in an armour spacing of 22.5%. Test series were conducted with s_{0p}=0.04 (series 07) and s_{0p}=0.02 (series 08). The elevated toe set-up was put into place to conduct test series with an unsecured toe, investigating the influence of a toe berm on the damage progression of a Coastalock armour layer with protrusions on a slope with a permeable core. Test series with s_{0p}=0.04 were conducted on both rough and smooth surfaces (series 09 and 10) to assess susceptibility to sliding.

Subsequently, short protrusions were attached, resulting in a 10% armour spacing. The test series continued with the elevated toe set-up, where s_{0p}=0.04 waves were conducted on a smooth surface (series 11) to minimize construction time, followed by the test series with a rough surface (series 12). The construction was altered to the 'Deep Water' set-up afterwards. Test series were conducted with s_{0p}=0.02 (series 13) and s_{0p}=0.04 (series 14). Afterwards, the PO configuration was tested where the orientation changes from cavity upwards to cavity downwards at the midpoint of the bottom row and the SWL (series 15), followed by the configuration with all cavities orientated upwards (series 16). However, due to the poor placement of the chains and subsequent movement of model units at the flume boundaries, it was decided to perform a rerun of this test series (series 17).

An overview of all sixteen unique test series and single rerun, and their specifications will be presented in Table 3.3 on the next page. Each test series commenced with a test run of 500 shake-down waves with a H_s of 0.07m, followed by 1000 waves of progressively increasing significant wave height by 0.015m. Testing continued until failure, reaching a maximum wave height of 0.175m, occurrence of toe berm failure, or the designated test time elapsed.

#	Test name	Arrangement	Steepness s_{0p}[–]	Spacing S[–]	Configuration	Toe Set-up	Stability Measurements
01	DWS00s4	Deep water, simple spacing 0%	0.04	0%	San Diego	Secured	Video-based
02	DWS00s2	Deep water, simple spacing 0%, long waves	0.02	0%	San Diego	Secured	Video-based
03	DWS10s4	Deep water, simple spacing 10%	0.04	10%	San Diego	Secured	Video-based
04	DWS10s2	Deep water, simple spacing 10%, long waves	0.02	10%	San Diego	Secured	Video-based
05	DWS20s4	Deep water, simple spacing 20%	0.04	20%	San Diego	Secured	Video-based
06	DWS20s2	Deep water, simple spacing 20%, long waves	0.02	20%	San Diego	Secured	Video-based
07	DWP22.5s4	Deep water, long protrusions	0.04	P-22.5%	PO-SWL	Secured	SfM
08	DWP22.5s2	Deep water, long protrusions, long waves	0.02	P-22.5%	PO-SWL	Secured	Video-based
09	TRP22.5s4	Toe on underlayer, long protrusion	0.04	P-22.5%	PO-SWL	Rough	SfM
10	TSP22.5s4	Toe on smooth surface, long protrusions	0.04	P-22.5%	PO-SWL	Smooth	SfM
11	TSP10s4	Toe on smooth surface, short protrusions	0.04	P-10%	PO-SWL	Smooth	SfM
12	TRP10s4	Toe on underlayer, short protrusions	0.04	P-10%	PO-SWL	Rough	SfM
13	DWP10s2	Deep water, short protrusions, long waves	0.02	P-10%	PO-SWL	Secured	Video-based
14	DWP10s4	Deep water, short protrusions	0.04	P-10%	PO-SWL	Secured	SfM
15	DWP10s4M	Deep water short protrusions, midpoint orientation change	0.04	P-10%	PO-Midpoint	Secured	SfM
16	DWP10s4U	Deep water, short protrusions, upwards cavity	0.04	P-10%	Upwards	Secured	SfM
17	DWP10s4U2	Deep water, short protrusions, upwards cavity, rerun	0.04	P-10%	Upwards	Secured	SfM

Table 3.3: Test program for Coastalock physical model testing.

4

Data processing: Structure from motion

This chapter offers an overview of the procedures involved in preparing the dense point clouds for processing, introduces the methods used for the assessment of armour layer elevation changes and settlements. The methods used for accuracy assessment of the generated dense point clouds, as well as those for evaluating elevation changes and settlements, are also detailed.

4.1. Procedure

During testing, it became evident that, despite best efforts, the four GCPs on both foreshores (targets 17/20/21/24) could not be consistently captured. Even after additional geo-referencing measurements after switching foreshores, consistency remained elusive, particularly after one GCP was damaged in later tests. Consequently, these GCPs were omitted from further application. Similarly, upon inspection of the pictures, it was determined that the four GCPs on top of the flume walls (targets 1/2/9/10) could not be consistently captured either. Therefore, they were also excluded from the final SfM procedure, leaving only the 12 GCPs (targets 03-08/11-16) affixed to the flume sides for use in subsequent analysis.

By following the outlined workflow detailed in Appendix F, 3D models were generated in Metashape and then exported in .LAS format to CloudCompare. In CloudCompare, several steps were undertaken. Initially, the boundaries were cut in xyz-directions. It was decided to exclude the three columns of armour units adjacent to the walls due to lacking overlapping images, and the final row was obscured by the side-chains. Additionally, the secured toe beam or loose rock berm at the bottom of the slope, as well as the crest at the top, were removed. Remaining noise was cleared. The slope was then reoriented to a horizontal profile, and finally, the dense point cloud was translated to position its corner at the origin of the xyz-coordinate system.

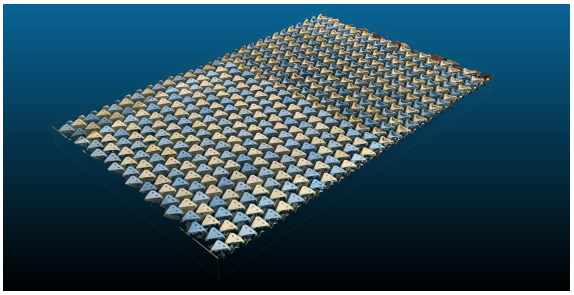

Figure 4.1: Dense Point Cloud reoriented to flat plane.

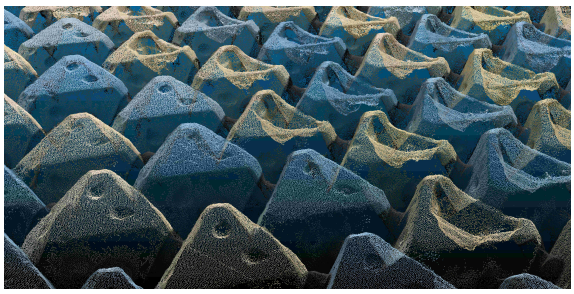

Figure 4.2: Detail of points within Dense Point Cloud.

The resulting product was exported in .pcd (Point Cloud Data) format for further processing, which involved assessing the elevation changes of the armour layers due to wave attack and evaluating settlements, as described in Sections 4.1.1 and 4.1.2, respectively.

4.1.1. Armour layer elevation change assessment

To assess the movement of the armour layer perpendicular to the slope, visualization and processing were performed in Python using the Open3D library (Zhou et al., 2018). This process entailed creating a staggered grid in the xy-plane, where each grid point was centered on a Coastalock armour unit. Each grid point was surrounded by a rectangular grid cell designed to match the dimensions of the armour unit, without overlapping with adjacent grid cells, as seen in Figure 4.3. Subsequently, the grid cells were expanded by $0.5D_{n,Cl}$ in all four directions. This decision was driven by the need to accommodate potential movement of the armour units in any direction, which could affect elevation calculations. Thus, enlarging the area of interest helped ensure comprehensive coverage in the analysis. After multiple iterations, the decision to use $0.5D_{n,Cl}$ was based on its ability to capture any unwanted movement of units while avoiding inclusion of blocks from the opposing side of gaps created by single extracted units.

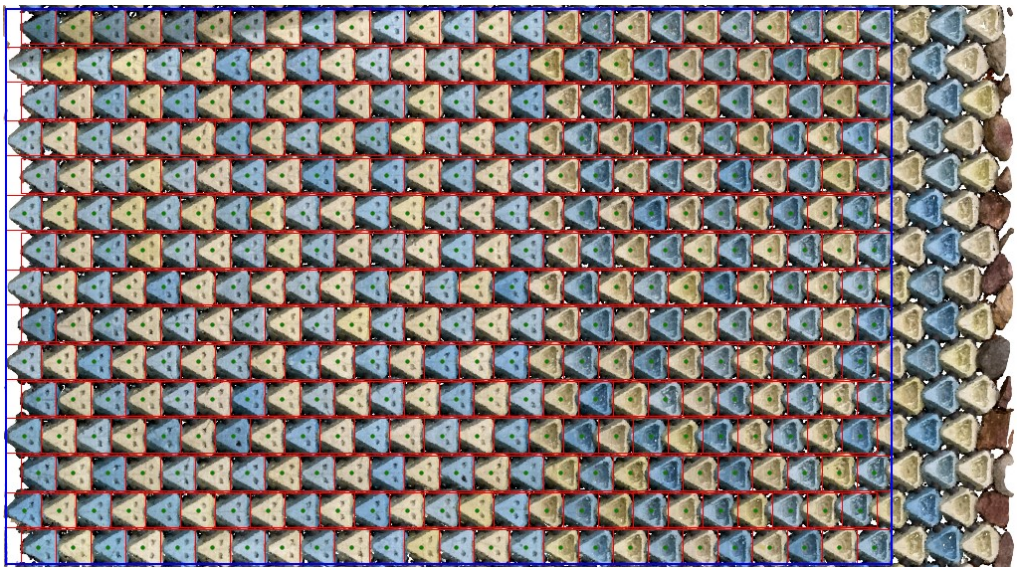

Figure 4.3: Initial gridding of Coastalock armour layer by non-overlapping rectangular grid cells in red, gird points in green, outside mask in blue.

In this step of process, it was chosen to omit the last three rows of each depth map as they lacked overlap in the source pictures used for the 3D model creation. Additionally, the first two rows were excluded from gridding in the loose toe berm set-ups because they were fully or partially obstructed by toe berm rocks or by extracted armour units left on the slope during the photography process. In all the cases described above, a masking procedure was implemented to exclude these areas from the elevation calculations

For the remaining armour units, the elevation, representing the z-coordinate perpendicular to the slope, was computed by determining the 95^{th} percentile of the z-coordinate and assigning it to the corresponding grid cell, thereby creating a depth map.

The comparison of these depth maps facilitated the generation of four output types, to assess the behavior of the armour layer:

- Elevation maps were utilized to compare the changes in the z-coordinate of grid cells after a specified test run with the reference profile established after settling waves. This elevation change was expressed as a fraction of the Coastalock nominal diameter. By enabling the tracking of individual grid cells, representing the individual armour units, this output provided insights into the elevation changes before and after breathing and extraction.

- The number of elevated units above a threshold, expressed as a fraction of the Coastalock nominal diameter, within a strip of breakwater slope with a width equal to the nominal diameter, was measured, as:

$$N_{od,elev} = \frac{\#\ units > threshold \cdot D_{n,CL}}{B/D_{n,CL}} \tag{4.1}$$

  This approach was based on the damage number approach detailed in Section 2.2.6, and would provide insight into $N_{od,elev}$ that would be indicative upcoming failure for a given threshold. As no information on movement or elevation threshold exists for Coastalock, it was chosen to define the threshold in terms of $0.10D_{n,CL}$, $0.25D_{n,CL}$, and $0.50D_{n,CL}$, for a wide overview and taking into account non-overlapping bound when taking into account measurement accuracy.
- The absolute maximum unit elevation, expressed as a fraction of the Coastalock nominal diameter, $|z_{max}|/D_{n,CL}$, was determined. In cases where extraction already occurred, the highest point after extraction was selected, after masking of the grid cell where extraction took place.
- The width-averaged slope elevation compared to the reference profile for the relevant test series was analyzed.

4.1.2. Armour layer settlement assessment

The settlements of the armour layer, crucial for assessing the influence of a loose toe berm and the potential sliding of the Coastalock units, were evaluated by tracking the movement of selected units in the y-direction (downslope). This was achieved using a polyline function in CloudCompare, allowing the tracing of a desired shape by point picking. The polyline, when closed, formed a 2D shape in the xy-plane perpendicular to the slope. For each selected Coastalock unit, a triangular shape was manually defined, and the centroid— the point of intersection of all the medians of the triangle— was calculated. By comparing the y-coordinates of these centroid points, the settlements of the units could be determined.

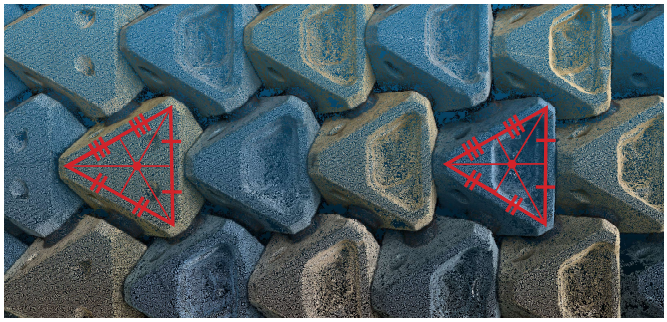

Figure 4.4: Representation of the triangular shape draw by means of the Polyline function for the determination of the centroid of the triangle of interest used for the settlement analysis.

Settlements were analyzed for all Coastalock units in the first row (corresponding to the third row of the entire armour layer), to investigate any signs of settlement or indications of sliding adjacent to the toe berm. Additionally, a grid-based selection of units was applied to provide an overall view of the movement of the armour layer, as observed in Figure 4.5 and 4.6, for the test set-ups with short and long protrusions respectively.

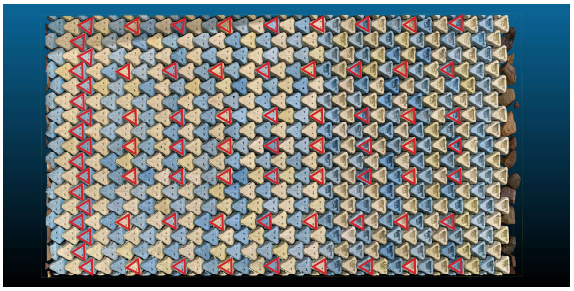

Figure 4.5: Representation of grid-based selection of Coastalock armour units with 10% protrusions used for the downslope settlement analysis in along slope direction.

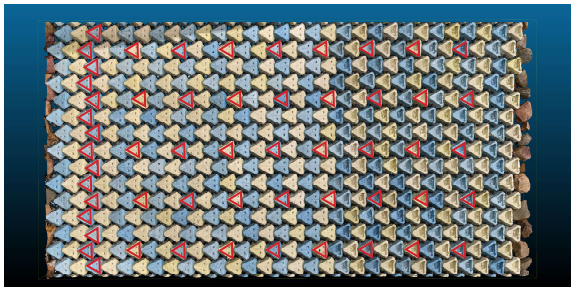

Figure 4.6: Representation of grid-based selection of Coastalock armour units with 22.5% protrusions used for the downslope settlement analysis in along slope direction.

4.2. Accuracy

The accuracy of the SfM methodology for analyzing the stability of a Coastalock armour layer can be divided into two main components. First, the dense point clouds generated using Agisoft Metashape and processed in CloudCompare form the basis of all measurements and observations. The second component is the accuracy of the methods used for calculating the elevation changes of the armour layer and its settlements, which rely on the dense cloud models.

4.2.1. Dense point cloud accuracy

For assessing the accuracy of the photogrammetry method using Agisoft Metashape, six sets of 55 pictures each were captured over the course of a single day of the breakwater slope with the armour layer in place and 22.5% protrusions attached. It was assumed that this configuration would result in the lowest overall accuracy due to the larger gaps between the individual armour units caused by the protrusions. This assumption was based on tests performed by Van den Berg (2020) on XblocPlus using a similar photogrammetry approach to capture armour layer movement. In her study, it was observed that accuracy was lowest in the transition gaps between the armour units, affecting the global accuracy of the dataset.

The set of pictures was scaled down to 55 intentionally to account for the possibility of some photos not meeting the criteria set by Metashape, as described in Appendix F. To simulate the wet conditions typically encountered after wave attack and flume drainage, the armour layer was sprayed with a hose. Additionally, the GCPs were wetted and dried to mimic testing conditions.

The resulting dense point clouds underwent pairwise comparisons. A cloud-to-cloud distance computation was conducted to measure the distance between two clouds. However, nearest neighbors may not always represent the true closest points on the surface, affecting accuracy. To address this, a 'Local Modeling Strategy' was employed, which calculates a local model around the nearest point to better approximate the surface and provide more accurate distance estimates. Specifically, a quadratic function with six parameters was utilized for its ability to represent smooth or curvy surfaces effectively, ensuring high precision in distance calculations. Therefore, the quadratic model, recommended by CloudCompare (2022), was utilized for its versatility and superior performance. This led to a total of 30 possible combinations suitable for comparison. The resulting threshold mean deviation of $0.52mm$ indicates the maximum deviation from the reference profile, representing the threshold bias. Meanwhile, the threshold standard deviation of $0.53mm$ reflects the threshold variability of measurements around the bias, providing insight into the precision of the measurements. These thresholds define the accuracy limits, under the assumption of undamaged slopes.

4.2.2. Elevation mapping accuracy

The same six sets were utilized to compare various statistical measures for determining the elevation (z-coordinate) of each grid cell and evaluating different grid cell sizes for the 375 present blocks. Out of these, 15 unique combinations without repetition were examined.

The statistical measures included the average, median, upper quantile, 95^{th} percentile, and 99^{th} percentile. Based on the maximum absolute differences, Welch's t-test of the bias and student t-distribution of

the standard deviation, the 95th percentile emerged as the most reliable method for estimating the z-coordinate. Welch's 90% confidence interval of the bias yielded a value of 0.27±0.036mm, while the Student's t-distribution for a 90% confidence interval resulted in 0.29±0.036mm for the standard deviation. The threshold observed bias was 0.73mm, and the threshold observed standard deviation was 0.45mm. Excluding the grid cells at the boundaries, the maximum absolute difference was 1.97mm. However, when including these boundary points, the maximum absolute difference increased to 2.64mm. Based on these observations a margin of error threshold is determined for a 90% confidence interval equal to approximately ±1.5mm.

Different grid cell sizes were tested, including sizes encompassing only the armour unit and expansions by distances of $0.25D_{n,CL}$, $0.50D_{n,CL}$, and $1.0D_{n,CL}$. The alteration of grid cell size had little to no significant influence on the accuracy of the statistical method applied above.

Furthermore, the differences between block orientations were measured. Specifically, the precision of capturing cavity downward Coastalock armour units was found to be slightly higher than that of cavity upward units. These comparisons were made by selecting only a part of the slope.

4.2.3. Settlement accuracy

The application of the polyline function directly on the dense point clouds, noted for their high accuracy as discussed in Section 4.2.1, allowed for the tracing of 2D triangles manually using a high zoom function. However, it should be added that due to the reliance on human observation and manual selection errors, achieving sub-millimeter accuracy cannot be guaranteed.

5

Results and analysis

The chapter begins with a summary of the measured wave conditions, followed by a reanalysis of previous research results. It outlines the observation from the stability analysis, encompassing both the outcomes from video-based analysis and SfM-analysis. The initial focus is placed on describing the observed failure mechanisms of a Coastalock armour layer on a permeable core. Subsequently, the effect of the permeable core on stability is quantified, followed by further exploration of protrusions, long waves, orientation changes, and the integration of a toe berm. Following this, the presentation of measured outcomes ensues, examining the impact of a permeable core, protrusions, wave steepness, configurations, and a comparative analysis with methodologies proposed in existing literature concerning both overtopping and reflection. Additionally, a prediction formulation for the reflection coefficient of a Coastalock armour layer on both an impermeable and permeable core is proposed. Appendix H addresses the resolution of issues such as clipping of the wave signal and missing wave data, along with a detailed measurement of wave characteristics. Furthermore, Appendix I encapsulates a comprehensive overview of the stability results obtained through the SfM method.

5.1. Wave measurements

5.1.1. Clipping of the wave signal

During the final testing phase, some wave profiles were found to be clipped. To assess the impact on wave decomposition, missing data was interpolated using spline interpolation. Despite this, no significant changes were observed in the relevant wave parameters derived from the tests, prompting the decision to proceed with the analysis using the clipped data. Further details are provided in Appendix H.

5.1.2. Current testing program results

The target values for the wave generator and the measured wave climate are seldom identical. Therefore, a comparison is conducted between the target significant wave heights and those measured in proximity of the structure. A comprehensive summary of this comparison for 4% steepness waves is provided in Table 5.1, while the comparison for 2% steepness waves can be found in Table 5.2. The values in both tables represent the range of significant wave heights and wave steepnesses observed for a given target wave height across test series. Please refer to Appendix H for all measurements of wave characteristics.

	Target		Near structure	
#	H_s	s_{0p}	H_{m0}	s_{0p}
1	0.070	0.040	0.065-0.067	0.036-0.038
2	0.085	0.040	0.079-0.080	0.038-0.039
3	0.100	0.040	0.094-0.095	0.037-0.038
4	0.115	0.040	0.107-0.108	0.038
5	0.130	0.040	0.123-0.124	0.037-0.038
6	0.145	0.040	0.137-0.143	0.038-0.041
7	0.160	0.040	0.147-0.152	0.36-0.039
8	0.175	0.040	0.165	0.036

Table 5.1: Summary of target and measured wave characteristics for 4% wave steepness.

Both wave steepnesses exhibit a decrease in significant wave height when comparing measurements in front of the structure to the target values. This reduction can be attributed to energy losses in the form of friction and steepness-limited breaking, particularly for higher target wave heights in combination with low wave steepenesses.

When comparing the target wave steepness to the measured values, it holds up well for the lower end of test runs. However, the difference becomes more noticeable for higher wave steepness. This discrepancy is primarily attributed to energy loss during wave breaking. As wave height increases and period decreases, the energy dissipation from breaking also increases, resulting in a larger disparity between target and measured conditions.

	Target		Near structure	
#	H_s	s_{0p}	H_{m0}	s_{0p}
1	0.070	0.020	0.067-0.068	0.019
2	0.085	0.020	0.079-0.083	0.018-0.020
3	0.100	0.020	0.097-0.099	0.020
4	0.115	0.020	0.114-0.116	0.019-0.020
5	0.130	0.020	0.120-0.128	0.018-0.021
6	0.145	0.020	0.129-0.141	0.017-0.020
7	0.160	0.020	0.141-0.150	0.018-0.019
8	0.175	0.020	0.152-0.153	0.017

Table 5.2: Summary of target and measured wave characteristics for 2% wave steepness.

Upon inspection, it was observed that all settlement test runs surpassed the 500-wave mark, while all other test series, where failure did not occur, counted well over 1100 waves, exceeding the intended 1000 waves. An exception to this was the last test run in the series with short protrusions and cavities facing upwards (series 17). Data was missing due to an operational error. The method used to handle this case, which involves using a polynomial model to predict the significant wave height reached in that test run, is explained in detail in Appendix H.

5.1.3. Reanalysis of previous testing program results

In the research conducted by Molenkamp (2022), it was found that approximately 10% of the MF3a method results for processing the wave data exhibited physically impossible values, with an additional 15% showing improbable values. Consequently, all the MF3a results were excluded from the analysis, the Goda and Suzuki (GS) method was utilized for the results and analysis in this thesis. The GS method, which utilizes 2 out of the 3 wave gauges per set, is widely recognized for resolving 2D spectra into incident and reflected components using a one-phase-angle approach. On the other hand, the MF3a method, which employs a three-point technique more common for 2D models, offers advantages such as a wider useful frequency range due to its two-phase-angle approach and is less sensitive to noise and deviations from linear theory (Frostick et al., 2011).

The comparison between the two methods of wave decomposition was necessary to ensure the integrity

of the analysis. Upon reviewing the wave files from Molenkamp's study (2022), it was identified that errors stemmed from undefined start and stop times for wave decomposition, as well as peaks in the variance spectrum of incoming and reflected energy, particularly for low significant wave heights. To resolve this issue, appropriate start and stop times were selected. Additionally, a maximum frequency boundary was imposed (instead of the automatic selection thereof by `decomp`) on the problematic wave files to eliminate the peaks in the variance spectrum. Since these peaks exclusively appeared in the very high frequency-low energy right tail-portion of the spectrum, their influence on the decomposition results was expected to be minimal.

The reanalysis was conducted using the MF3a method, for the near structure-group of wave gauges, for specific test series necessary to compare the results between hydraulic performance factors such as stability, overtopping, and reflection on both impermeable and permeable core slopes. These test series included the 0% spacing (series 05/06/16), 10% spacing (series 11/12), 15% spacing (series 13), 20% spacing (series 14) and 25% spacing (series 15) configurations of the 'San Diego' model under 4% wave steepness. Additionally, the reanalysis covered the 0% spacing configurations under 2% (series 09) , 3% (series 22), 5% (series 24) and 6% (series 07/08) wave steepness, and 10% spacing (series 23) configurations under 2% wave steepness. Finally, the 10% spacing series with all armour units positioned with their cavities facing upwards (series 21) was also included in the reanalysis. A summary of the results can be found in Table 5.3.

$H_s[m]$	$H_{m0}[\%]$	$C_r[\%]$	$T_p[\%]$
0.050-0.090	-4.3 to 47.0	-1.9 to 16.4	-6.9 to 13.8
0.100-0.130	-6.5 to 15.1	-0.9 to 4.5	-6.5 to 6.4
0.145-0.160	-7.2 to 3.8	-0.7 to 0.7	-11.3 to -5.8
0.170-0.190	-2.6 to -0.3	1.2 to 4.8	5.3 to 10.9

Table 5.3: Summary of relative comparison between wave characteristics reanalysis using the MF3a method and Molenkamp's (2022) results using the GD methods per target H_s.

All wave runs of the test series were examined for the number of waves. All settlement test runs surpassed the 500-wave mark. Most other test series, where failure did not occur, had well over 1200 waves, with some reaching values up to 1500 waves. However, the last test runs of the 10% spacing (series 12, run 1) and 20% spacing (series 14, run 9) with target wave heights of H_s=0.190m were cut short, not surpassing 1000 waves. The wave signal ceased after several minutes. As before, a polynomial model was utilized to predict the missing wave heights, as explained in Appendix H.

The results of the comparison of the reanalyzed data have implications for the rest of the study. The stability numbers used for comparison are reassessed, and overtopping calculations are also influenced by changes in significant wave height and duration, necessitating their recalculation to inspect any significant change in obtained roughness coefficients. Lastly, Equation 2.13, used for predicting the reflection coefficient, is omitted because it was derived from values that significantly differ from the reevaluated ones.

5.2. Stability

5.2.1. Failure mechanisms

When built-up pressures beneath the Coastalock units surpass the stabilizing self-weight, and interlocking capabilities, during wave run-down, an imbalance of forces occurs, resulting in upward movement perpendicular to the slope. Conversely, during wave run-up, the blocks move downward perpendicular to the slope, pushed by the incoming wavefront. This phenomenon, described as 'breathing' by Molenkamp (2022), was first observed during testing on an impermeable core for Coastalock, and was also observed during the presented research.

(a) After settling waves.

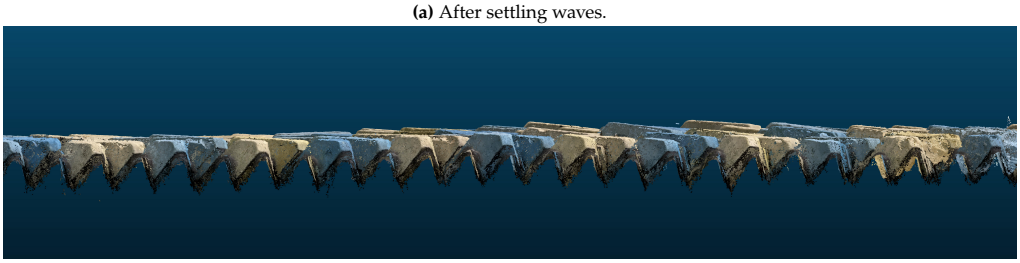

(b) After test run where 'breathing' was first observed, showcasing gradual lifting of several units from the slope.

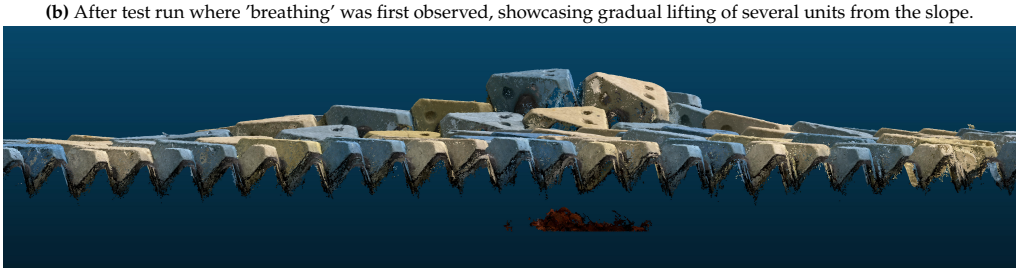

(c) After extraction occurred from the formed bulge, as a result of repeated 'breathing' motion.

Figure 5.1: Side view of three states of a Coastalock armour layer under wave attack on a permeable core slope.

Notably, on slopes with a permeable core, after the armour units exhibit initial signs of 'breathing', they do not consistently return to their original positions after wave run-up. As waves wash over the slope, armour units are progressively pulled on and off, with those displaced furthest in perpendicular direction to the slope being the last to return to their original positions. Due to friction and retaining partial interlocking, certain units start to protrude from the armour layer, as seen in Figure 5.1b. When another 'breathing' cycle occurs, the tight placement of the armour units causes normal forces to be passed on to the surrounding blocks, causing them to protrude as well, collectively forming a bulge as the phenomenon of 'breathing' intensifies, as seen in Figure 5.1c.

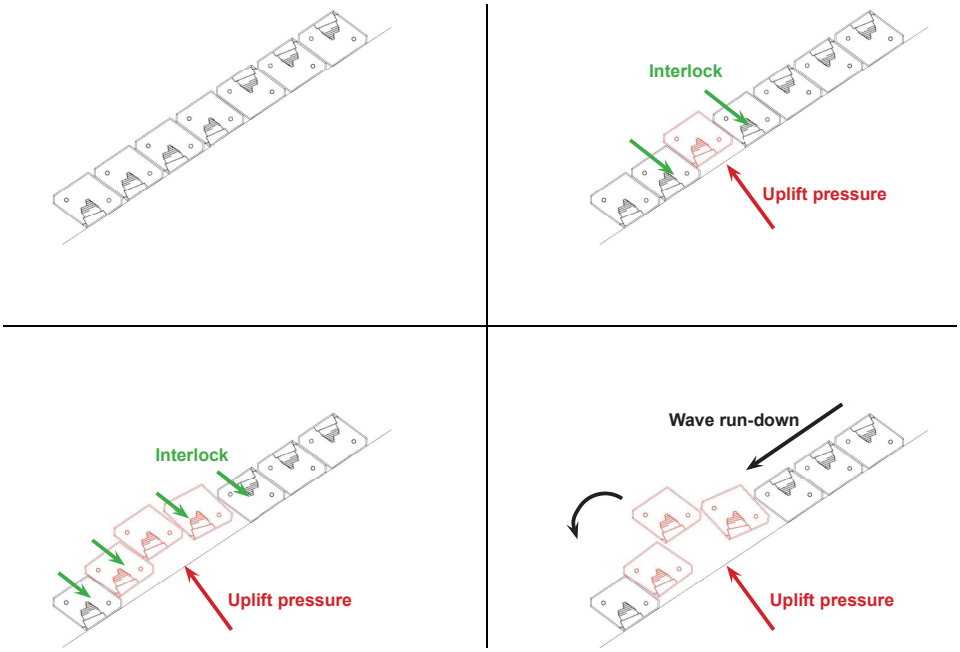

Figure 5.2: Schematizing of observed failure mechanism of a Coastalock armour layer on an permeable core breakwater slope.

The unevenness caused by differences in settlements of the armour units during 'breathing' can result in further uplift pressures exerted by high flow velocities during wave front rushing up the slope. Flow which is blocked by the armour unit, besides drag forces, exerts a pressures at the up slope part of the armour unit are transmitted to the filter layer, contributing to the uplift, and combined with the dominant influence of the curved streamlines over the block, result in a significant decrease in pressure exerted on the block itself. This process has been described for traditional placed block revetments (Klein Breteler, Mourik, and Provoost, 2014) acting as a destabilizing mechanism caused by the wave front in the run-up zone.

Extraction of one or more armour units occurred due to pressure differentials during wave run-down. In some instances, subsequent wave run-ups not only move these extracted units but also extract additional units up slope, exacerbating instability within the armour layer.

This failure mechanism bears resemblance to pressure-induced uplift observed in placed block revetments during beam-type failures. However, in this case, the mobilization of block movement does not extend to the surrounding superstructure; failure occurs before such movement can occur. On the other hand, the gradual uplift of a section of the armour layer could signal the initiation of an arching mechanism, as described by Van den Berg (2020). However, findings presented in the upcoming sections contradict this, as neither the depth maps nor the width-averaged slope profiles show movement of the up slope part of the armour layer in a downward direction perpendicular to the slope. During the observed test series, this remained mostly flat. Nevertheless, it is plausible to attribute the bulging of the lower part of the armour layer to a combined effect of the weight of the upper armour and the hydraulic pressure of the remaining water beneath the top layer.

The video-based approach provided insights into the three primary states of the Coastalock armour layer: stationary conditions, pressure-induced breathing, and failure, represented by the extraction of one or more Coastalock armour units. Subsequent sections present stability metrics corresponding to instances where the armour layer exhibited static behavior, breathing, or experienced extraction. This methodology facilitated comparisons with the findings of Molenkamp (2022). If a stability number is plotted as extraction without the phenomenon of 'breathing' observed in the previous test run, it indicates that 'breathing' was present for the first time at that stability number, and extraction occurred in the same test run.

5.2.2. Effect of the permeable core on stability

In test cases with 0% spacing, and consequently, the lowest armour layer permeability, breathing was observed across nearly the entire width of the structure. This behavior was similar to what was reported by Molenkamp (2022) for an impermeable core. It began with the largest wave in the test series, becoming more frequent and extending to a larger section of the armour layer. The maximum deviation perpendicular to the slope occurred near the middle section in width, just above the maximum rundown. As motion continued, a single element was extracted from the armour layer. The 'breathing' phenomenon of the armour layer was observed at a stability number of 1.68 for the permeable core, indicating a lower threshold compared to the impermeable core, where the threshold for 'breathing' was measured at 2.06. Failure occurred at a stability number of 2.44, which is higher than observed in all three tests performed with the permeable core, where failure was observed from a stability number of 2.11 onwards. However, due to the larger increments of significant wave height increase, it cannot be stated whether the threshold for extraction actually increased.

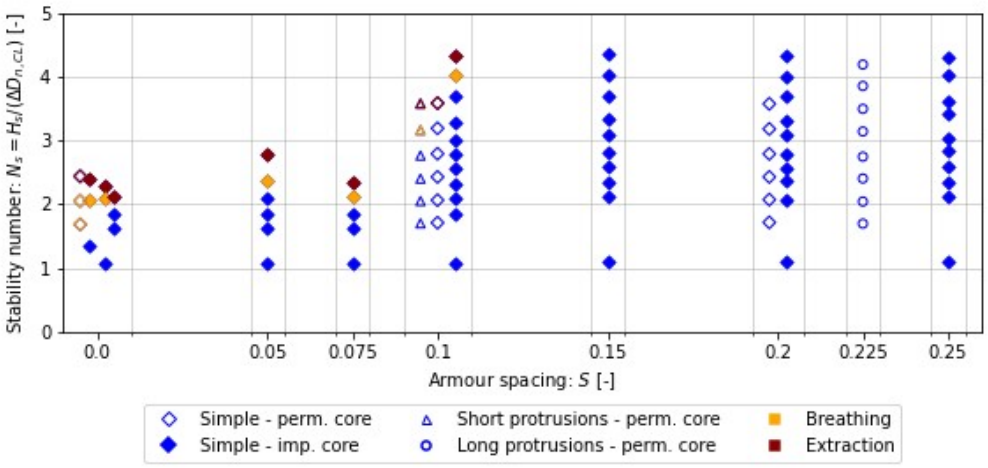

Figure 5.3: Test series overview on the influence of armour spacing on Coastalock stability under $s_{0p} = 0.04$, on an impermeable and permeable core. Test series executed with 'San Diego' configuration for simple spacing and 'PO-SWL' configuration for armour units with protrusions. Markers grouped within grid borders represent specific armour spacing along the x-axis.

Pressure-induced motion was observed in the middle segment of the slope with 10% spacing. A small section of several neighboring units was gradually displaced perpendicular to the slope by the larger waves until one armour unit was extracted from the bulging part of the armour layer following the observation of the breathing phenomenon, albeit on a more localized scale involving several units. At a stability number of 3.59, both 'breathing' and 'extraction' were observed. Comparatively, with an impermeable core at the 10% spacing, 'breathing' occurred at a stability number of 4.02, while 'extraction' occurred at 4.34. These results indicate that the performance of the permeable core was inferior in both the occurrence of 'breathing' and 'extraction' phenomena.

No breathing was observed for the 20% spacing. However, armour units near the maximum rundown in the middle of the slope gradually started to move over the course of the test runs. Sideways rotation of elements began in a central column, creating a larger gap on one side. This process continued, resulting in a collapse to the sides, further enlarging the gaps. Eventually, this led to the migration of the filter layer over the structure. The test series was stopped to prevent additional damage to the filter layer and to preserve the integrity of the core structure. Similar side ways rotation and translation was observed when examining the results on an impermeable core but to a lesser degree. This event was not classified as a failure of the armour layer since the individual elements of the armour layer remained stationary. The observed movement resulted from the erosion of the filter material caused by waves penetrating through the spacings in between the armour units. It is noteworthy that the filter layer was not designed to accommodate such large spacings but remained constant across all test series.

The observed increase in stability of the armour layer with the introduction of armour spacing, resulting

in larger inter-unit void sizes, was confirmed for the permeable core structure. This finding aligns with the leakage length theory, which suggests that as the permeability of the top layer increases, the leakage length becomes shorter, thereby enhancing stability.

It was anticipated that increasing core permeability would result in reduced wave loads on the armour layer, increasing stability and reducing required armour size, due to wave dampening within the permeable core, in contrast to an impermeable core. However, this expectation was not met for the test series with 0% and 10% spacing. One possible explanation is that wave penetration into the permeable core structure did not dissipate its energy sufficiently through turbulent flow. This would however not explain the reduction in stability. A possible explanation would be, that the increase in permeability may have led to decreased maximum run-down levels, affecting the location targeted by the highest pressures, negatively effecting stability, as the targeted area varies less, when comparing to an impermeable slope were the run-down is larger. No data comparing the run-down levels has been obtained for the impermeable core to verify this notion.

The sideways rotation and translation of the Coastalock observed in the test series with 20% spacing, eventually leading to the erosion of filter material, may be attributed to a combination of factors related to the permeable core structure. The flow within a structure with a permeable core, now also taking place inside the structure, combined with the loose material composition of the core, could contribute to this phenomenon. The cyclic in-and-outflow through the Coastalock layer and filter layer, connected to the flow inside the pores of the core, may cause the armour layer and filter layer on a permeable core, to react differently compared to a rigid impermeable core, lowering the threshold for rotation and translation.

5.2.3. Effect of the protrusions on stability

Short protrusion - 10% spacing

As depicted in Figure 5.3, the results illustrate a decrease in the threshold for initiating 'breathing', with the stability threshold reducing from 3.59 to 3.16. Additionally, a comparable failure threshold is observed when comparing the 10% spacing configuration with and without short protrusions. The decrease in the 'breathing' threshold can be attributed to the reduction in the inter-unit void size caused by the blockage from short protrusions. Consequently, this leads to a less permeable top layer, resulting in an increase in the leakage length and, leading to larger pore pressure gradients across the top layer, which contributes to a decrease in stability.

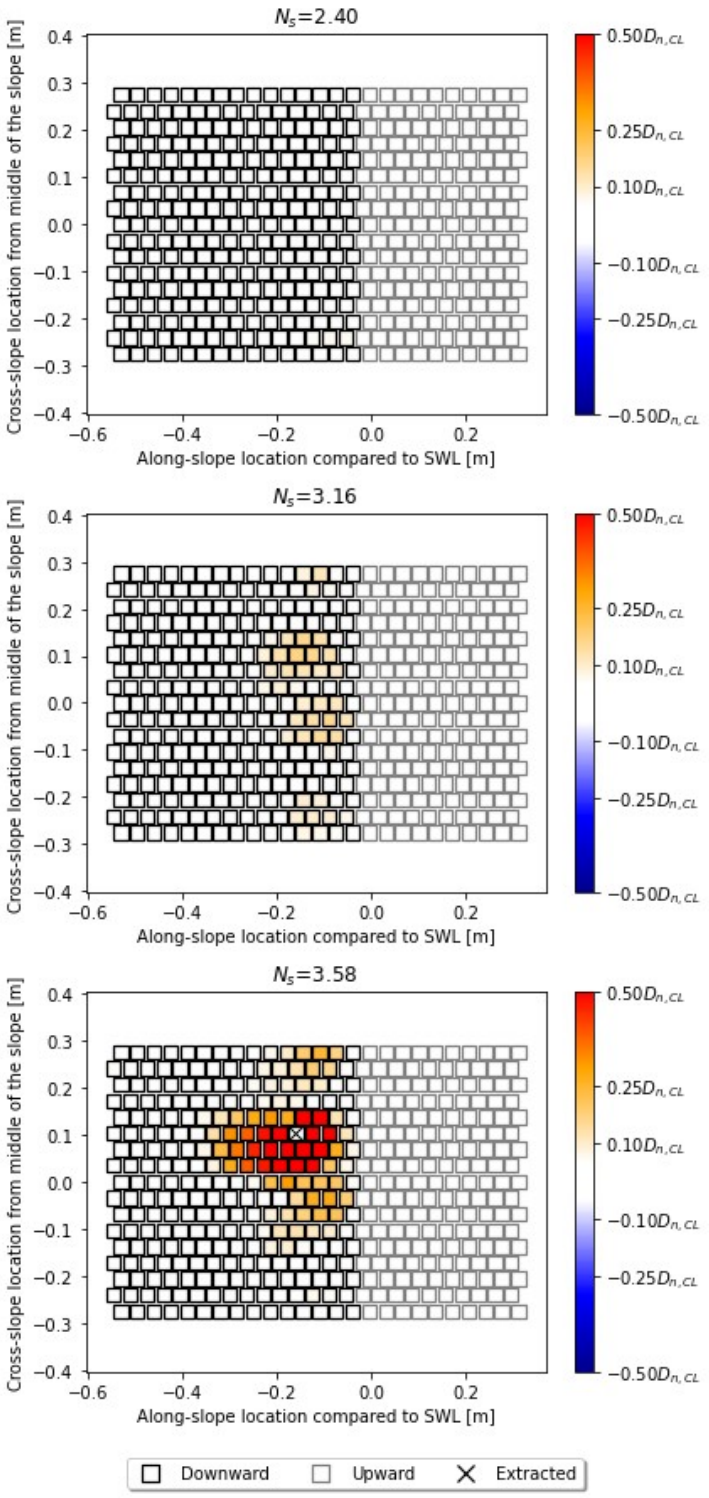

Figure 5.4: Elevation change after the test run, compared to the reference profile after settling waves, expressed as a fraction of the Coastalock nominal diameter, under s_{0p} = 0.04, for short protrusions with 10% spacing in the 'PO-SWL' configuration in the 'Deep Water' set-up.

The 10% spacing configuration with short protrusions exhibited a similar response to wave loading, to that observed in the absence of protrusions. Figure 5.4, showcases the elevation changes after the test run compared to the reference profile, clearly shows the formation of the bulge that consists of several neighboring units in the middle of the slope just below the waterline, below the orientation change

from cavity upwards to cavity downwards. The size of the bulge and the magnitude of the upwards elevation increase with each test run.

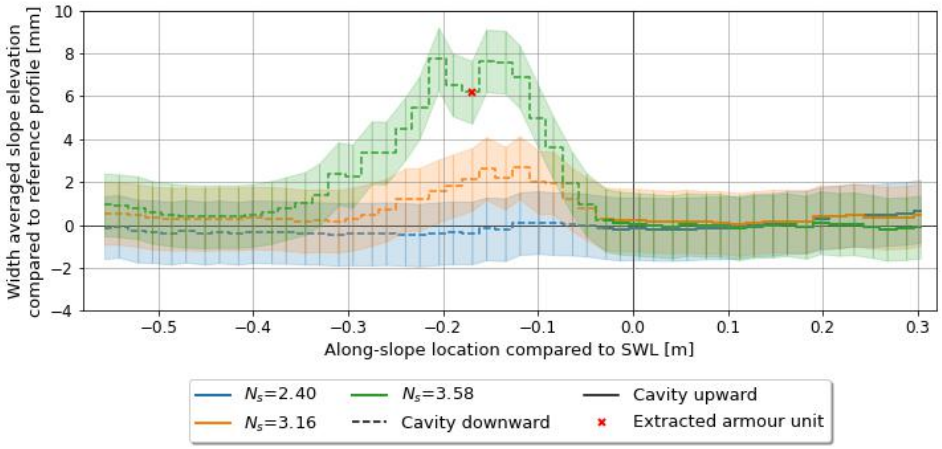

Figure 5.5: Width averaged slope elevation compared to reference profile, under s_{0p} = 0.04, for short protrusions with 10% spacing in the 'PO-SWL' configuration in the 'Deep Water' set-up.

The first signs of the significant upward elevation change are visible at N_s=3.16 in the same test run in which breathing was observed. It is important to note the absence of an up slope downward elevation change perpendicular to the slope, as observed in Figure 5.5. The breathing of the armour layer on a permeable slope did not lead to the formation of a concave S-shaped profile indicative of the migration of underlayer material from the up slope area, towards the area where the uplift of armour units occurred. However, it is worth noting that this observation does not exclude the possibility of filter material migration occurring, from up slope to downslope direction, directly underneath the bulge.

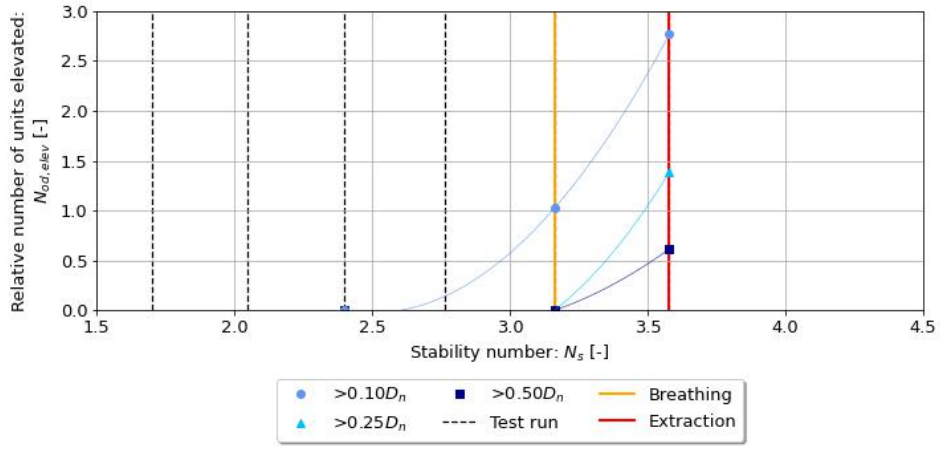

Figure 5.6: Number of elevated units above threshold expressed as a fraction of the Coastalock nominal diameter within a strip of breakwater slope, with a width equal to the nominal diameter, under s_{0p} = 0.04, for short protrusions with 10% spacing in the 'PO-SWL' configuration in the 'Deep Water' set-up.

Figure 5.6 illustrates that at N_s = 3.16, breathing was observed, and the threshold for movement did not exceed $0.25D_{n,CL}$, as depicted in Figure 5.7, where it was actually $0.17D_{n,CL}$. Only in the subsequent test run, at N_s = 3.58, when breathing intensified, did the thresholds of $0.25D_{n,CL}$ and $0.50D_{n,CL}$ get surpassed. This resulted in a maximum elevation change of $0.93D_{n,CL}$ for the most protruding armour unit after extraction occurred, of armour units remaining in the armour layer.

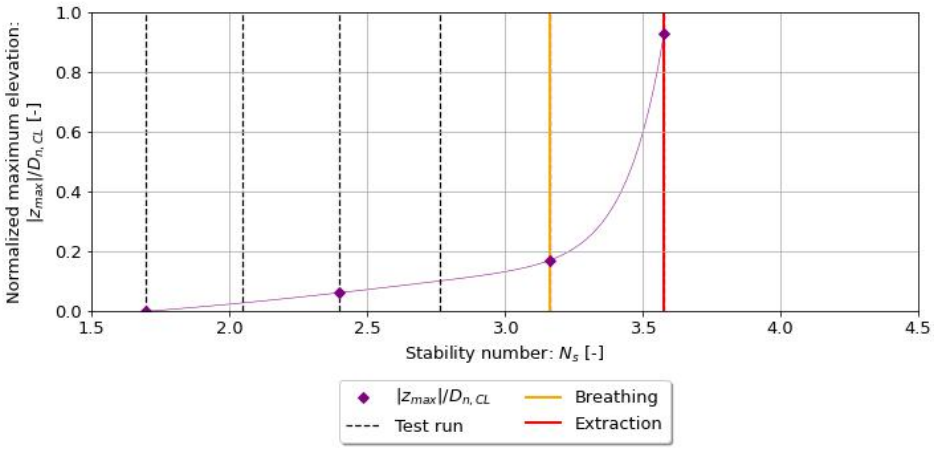

Figure 5.7: Maximum unit elevation expressed as a fraction of the Coastalock nominal diameter, under $s_{0p} = 0.04$, for short protrusions with 10% spacing in the 'PO-SWL' configuration in the 'Deep Water' set-up.

The observed damage progression in both $N_{od,elev}$ and $|z_{max}|/D_{n,CL}$ for the test series with short protrusions with 10% spacing is typical for single-layer interlocking armour units, where the movement of the armour layer increases slightly with increasing wave height, followed by sudden failure.

Long protrusion - 22.5% spacing

When comparing the test series with 20% spacing and 22.5% protrusions, a notable difference was observed: there was an absence of filter material migration out of the voids between the Coastalock units. This migration occurred at N_s=3.57 for the test without protrusions. The protrusions occupied enough space to prevent this migration from happening. Neither breathing nor extraction was observed in this case, as shown in Figure 5.3. The wave generator was operating near its maximum capacity when test series was halted, at N_s=4.19.

The overall width-averaged profile of the armour layer exhibited a gradual, but limited, upward movement perpendicular to the slope following initial settlements when compare to the reference profile, most present in the part above SWL.

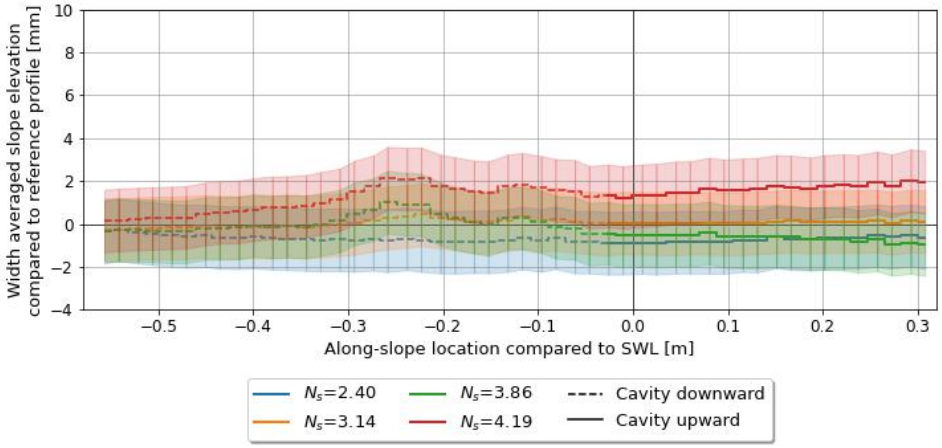

Figure 5.8: Width averaged slope elevation compared to reference profile, under $s_{0p} = 0.04$, for long protrusions with 22.5% spacing in the 'PO-SWL' configuration in the 'Deep Water' set-up.

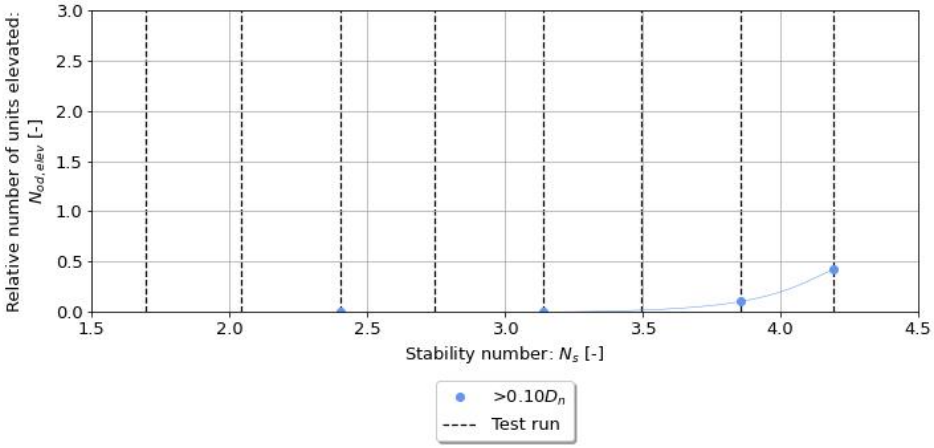

Figure 5.9: Number of elevated units above threshold expressed as a fraction of the Coastalock nominal diameter within a strip of breakwater slope, with a width equal to the nominal diameter, under $s_{0p} = 0.04$, for long protrusions with 22.5% spacing in the 'PO-SWL' configuration in the 'Deep Water' set-up.

No significant movement of the grid cells was observed until a stability number of $N_s = 3.86$, when the threshold of $0.10D_{n,CL}$ was surpassed for the first time, as shown in Figure 5.9. The maximum recorded elevation change observed at N_s of 4.19 was $0.15|z_{max}/D_{n,CL}|$, as seen in Figure 5.10. Comparing these results to those of the 10% spacing with short protrusions, especially in Figure 5.7, where 'breathing' was observed coinciding with $|z_{max}/D_{n,CL}|$ value of 0.17, suggests that the armour layer with 22.5% spacing and long protrusions could be approaching its stability limit in terms of 'breathing' and potential extraction. What is notable is that the elevation change perpendicular to the slope occurred without the visual observation of 'breathing'. This shows the capability of the SfM technique for the identification of pressure induced movement of small scale armour units after wave attack.

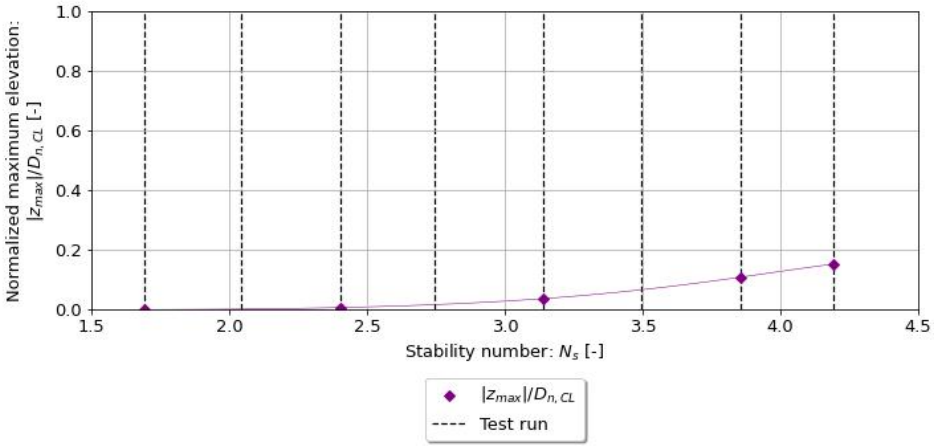

Figure 5.10: Maximum unit elevation expressed as a fraction of the Coastalock nominal diameter, under $s_{0p} = 0.04$, for long protrusions with 22.5% spacing in the 'PO-SWL' configuration in the 'Deep Water' set-up.

5.2.4. Long wave stability

For 0% spacings, when comparing the influence of a permeable core to that of an impermeable core on the stability of Coastalock, breathing of the armour layer was observed at the first tested stability number of 1.71, indicating that the threshold is slightly lower compared to 1.75 for an impermeable core. Failure occurred at a stability number of 2.03 on a permeable core, which is higher than on an impermeable core that failed at 1.87. However, once again, this is not indicative of a lower or higher threshold for 'breathing' and extraction due to the larger increments in significant wave height per test

run.

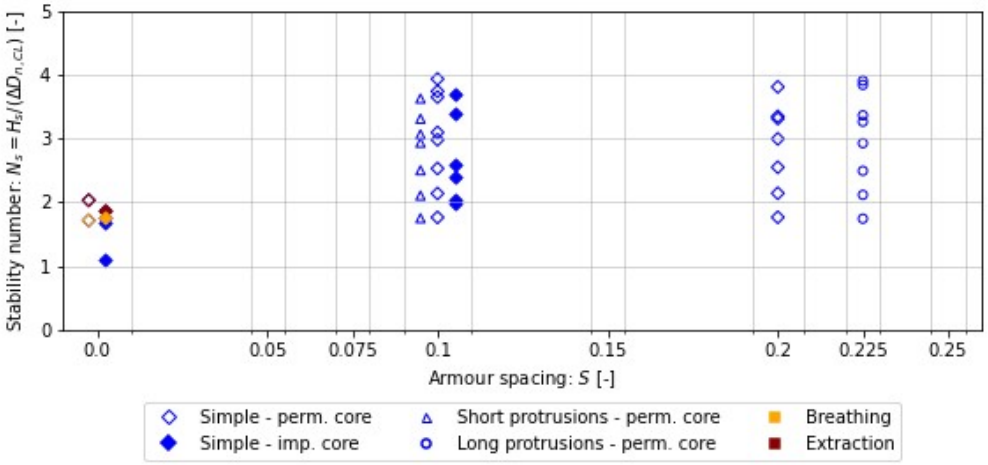

Figure 5.11: Test series overview on the influence of armour spacing on Coastalock stability under s_{0p} = 0.02, on an impermeable and permeable core. Test series executed with 'San Diego' configuration for simple spacing and 'PO-SWL' configuration for armour units with protrusions. Markers grouped within grid borders represent specific armour spacing along the x-axis.

In the remaining test series with spacings of 10%, 20%, and both short and long protrusions, no instances of breathing or pressure induced failure were observed during testing. In the test series with a simple spacing of 20%, erosion of filter material began between the armour units once again. Subsequently, the test series was halted to prevent further damage to the filter layer and to maintain the integrity of the structure's core. These remaining test series were concluded due to the wave generator nearing its operational limit and observed clipping of the highest waves.

When comparing the stability numbers for the 10% simple spacing on a permeable core and impermeable core structure, higher stability numbers were achieved without 'breathing' or extraction occurring.

An unexpected observation was the increase in stability number for s_{0p} = 0.02 waves for both the 10% spacing with and without protrusions, compared to s_{0p} = 0.04 waves, on a permeable core structure (see Fig. 5.3 and Fig. 5.11). For 10% spacing, 'breathing' and extraction were first observed at N_s = 3.59, while for long waves, neither was present at N_s = 3.93. For 10% protrusions, 'breathing' occurred at N_s = 3.16 and extraction at N_s = 3.58; for long waves, neither occurred at N_s = 3.63. However, since no 'breathing' or failure was observed in either test series, it is unclear to what extent stability improved for long waves. As long waves were considered critical, this result raised questions. A possible explanation for the stability increase could be attributed to a phenomenon termed the 'reservoir effect'. This effect suggests that the less frequent longer waves have more time to penetrate into the structure, reducing flow in the armour layer and resulting in increased stability compared to shorter waves, which have less time to penetrate into the structure, as observed in Acropode unit tests (H. F. Burcharth et al., 1998). However, this explanation does not account for why there was no increase in the threshold for 'breathing' or extraction in the case of 0% simple spacing.

5.2.5. Effect of orientation change on stability

When comparing the findings of the 'PO-SWL' configuration with those of the 'PO-Midpoint' and 'Upwards' configurations, several differences emerge.

As observed in Molenkamp's study (Auke, 2022), the orientation of the armour layer significantly influences its stability. Analysis of the 'breathing' and extraction thresholds, depicted in Figure 5.12, reveals notable variations between different configurations. Specifically, the 'PO-Midpoint' configuration exhibited higher thresholds, with 'breathing' occurring at N_s = 3.52 and extraction at N_s = 3.76, compared to the 'PO-SWL' configuration, where these events were observed at N_s = 3.16 and N_s = 3.58, respectively. Interestingly, the 'Upwards' configuration demonstrated 'breathing' at N_s = 3.52, identical to the 'PO-Midpoint' configuration, while extraction did not occur at N_s=3.88.

It is important to note that in the initial test series featuring the 'Upwards' configuration, movement of the armour layer towards the right side of the flume was observed due to poor chain placement. Despite the weakening of the armour layer, a higher threshold for breathing motion and extraction was reached compared to the test series in the 'PO-SWL' configuration, although this is not depicted in Figure 5.12. The rerun, illustrated in Figure 5.12, was carried out with correct side chain placement. Only the results of the rerun have been considered further in the stability analysis using the SfM methodology.

Figure 5.12: Influence of the location of the orientation change on Coastalock stability with 10% protrusions, in the 'PO' configuration with an orientation change at 'SWL' or 'Midpoint', in the 'Upwards' configuration, compared to 10% spacing in the 'San Diego' configuration, under $s_{0p} = 0.04$.

When comparing elevation changes, it is of utmost interest to observe the differences in damage location. Figure 5.13 illustrates the final test run of each test series.

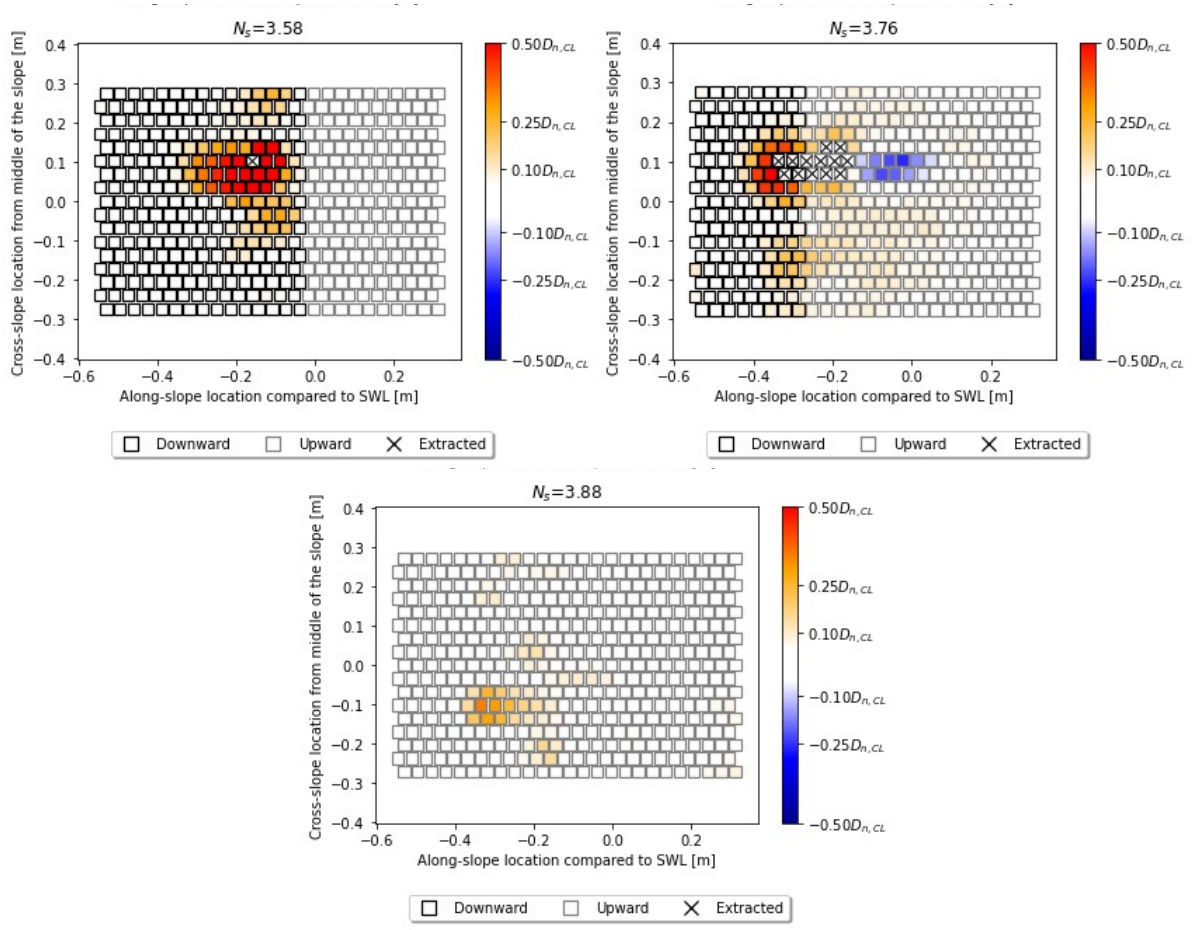

Figure 5.13: From top left, top right, to bottom: Elevation change after the test run, compared to the reference profile after settling waves, expressed as a fraction of the Coastalock nominal diameter, under s_{0p} = 0.04, with 10% protrusions in the 'PO-SWL', 'PO-Midpoint' and 'Upwards' configuration in the 'Deep Water' set-up.

Comparing the 'PO-SWL' configuration to the 'PO-Midpoint' configuration reveals notable differences. In the 'PO-Midpoint' configuration, the bulge formed by the elevated units shifts downslope and concentrates around the point of orientation change. Additionally, the first extracted armour unit in the 'PO-Midpoint' configuration occurred from the 12th row, 0.35m down slope compared to SWL, whereas in the 'PO-SWL' configuration, it happened from the 7th row, 0.17m downslope compared to SWL. Besides, the 'PO-Midpoint' configuration resulted in a particularly brittle failure. While previous cases saw up to two units extracted from the armour layer, in this instance, ten units were extracted at once by a single wave. Furthermore, when the wave maker was stopped just before the waves settled, three more units were extracted. Moreover, significant settlements occurred for the first time just up slope of the extracted armour units in the 'PO-Midpoint' configuration, indicating the formation of an S-profile for a narrow section of the slope.

For the 'Upwards' configuration, a similar trend was observed, with units starting to be elevated from the armour layer at a lower position below the waterline compared to the 'PO-SWL' configuration and in line with the 'PO-Midpoint' configuration, as the maximum elevation change was also found in the 7th row.

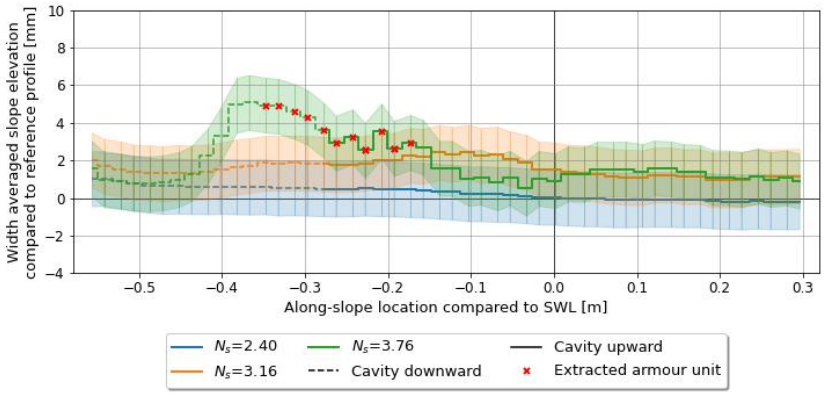

Figure 5.14: Width averaged slope elevation compared to reference profile, under $s_{0p} = 0.04$, with 10% protrusions in the 'PO-Mid' configuration in the 'Deep Water' set-up.

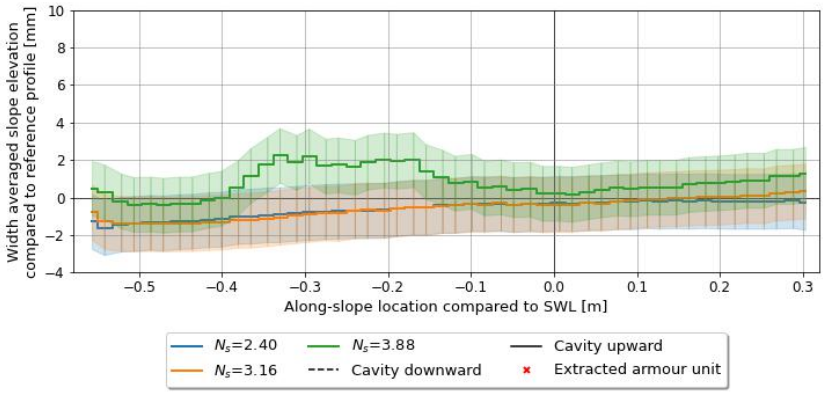

Figure 5.15: Width averaged slope elevation compared to reference profile, under $s_{0p} = 0.04$, with 10% protrusions in the 'Upwards' configuration in the 'Deep Water' set-up.

When expressing the extraction location in terms of the rundown level (vertical distance to SWL), this translates to $R_{d,f}/H_s$ values of -1.3 and -0.7 for the 'PO-Midpoint' and 'PO-SWL' configurations, respectively. Similarly, the value for the 'Upwards' configuration, representing the maximum elevated unit without extraction, equaled -1.3 as well. This showcases the distinct downwards shift in the damage location and aligning the results of the 'PO-Midpoint' and 'Upwards' configuration with the critical loading location for placed block revetments, observed just above maximum run-down, where the pressure due to wave set-up and the pressure due to the wave front are the dominant forces. This critical loading location approximated by $R_{d2\%}/H_s = -1.5$ according to the Rock Manual (2007). Just above that location, the elevation changes were the largest, and extraction occurred, as can be examined on Figures 5.14 and 5.15.

The impact of the orientation change is also evident in the maximum elevation changes observed in each test series. For a detailed examination of each test series, including the stability numbers recorded at intermediate points, refer to Appendix I. Figure 5.16 offers a comparison between the three tested configurations, excluding the indication of individual test runs for clarity. Notably, the presence and positioning of the location of orientation change on the slope of downward-facing Coastalock armour units are shown to have a negative effect on the maximum elevation of the armour layer after wave attack.

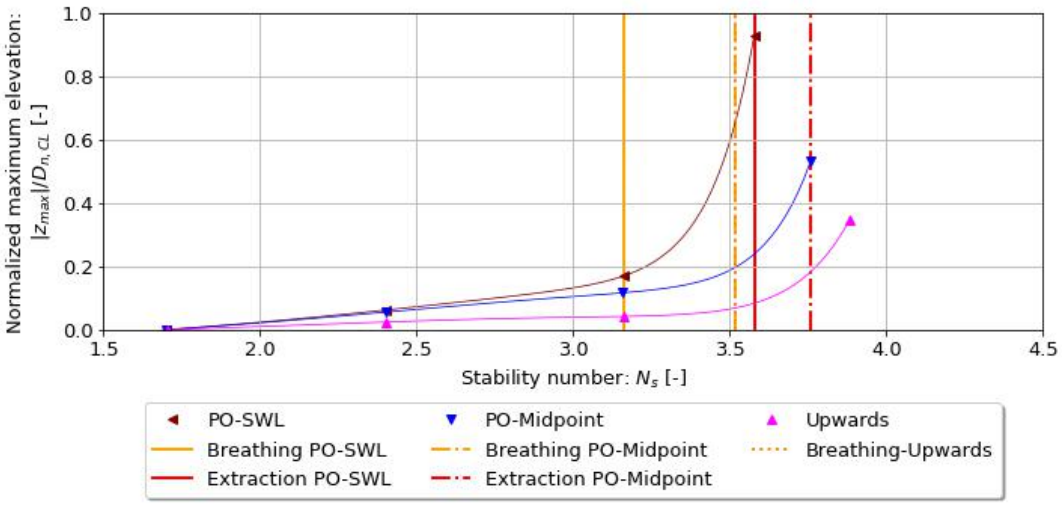

Figure 5.16: Maximum unit elevation expressed as a fraction of the Coastalock nominal diameter, under $s_{0p} = 0.04$, with 10% protrusions for 'PO-SWL', 'PO-Midpoint' and 'Upwards' configuration in the 'Deep Water' set-up.

In addition to the alteration in geometry affecting the flow dynamics around the armour unit during wave action, another significant factor influencing the stability decline may be the disparity in buoyancy between the two orientations of the Coastalock armour unit, caused by the cavity's placement. This discrepancy results in a potential 12% variation in submerged volume when the unit's orientation is modified. As volume is a component of the stability equation, represented by the relative density to water, this alteration in submerged volume could bring an approximate 10% reduction in stability, in the most unfavourable situation. However, this factor alone may not fully explain the observed stability changes. Notably, no tests have been conducted with a configuration where all cavities face downward, precluding a direct comparison.

5.2.6. Effect of toe berm on stability

Short protrusion - 10% spacing

Throughout both test series involving 10% protrusions, no movement of toe berm rocks was detected for either subsurface, nor was sliding observed as a failure mechanism. As depicted in Figure 5.17, the threshold for 'breathing' remained consistent across all three test series. However, failure occurred at a lower stability number due to extraction for the 'Toe Berm on Rough' setup.

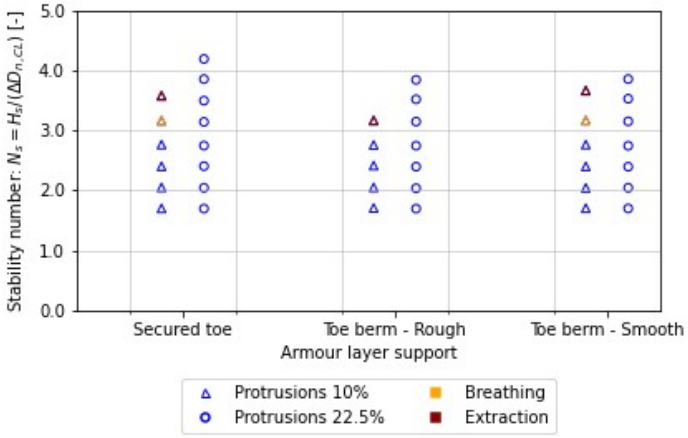

Figure 5.17: Influence of the 'Toe berm on Rough' and 'Toe berm on Smooth' set-ups on stability compared to the 'Deep Water' set-up, with 10% and 22.5% protrusions respectively, under $s_{0p} = 0.04$.

In both test set-ups with a loose toe berm, a central part of the armour layer just below the orientation change gradually increased in elevation due to initiated up- and down-motion caused by the excess pressures. Ultimately, elements within the bulge lost interlock, leading to their extraction from the slope. The elevation change pattern observed in each series where extraction occurred shows similar pattern in elevation increase and extraction locations, as can be seen in Figure 5.19.

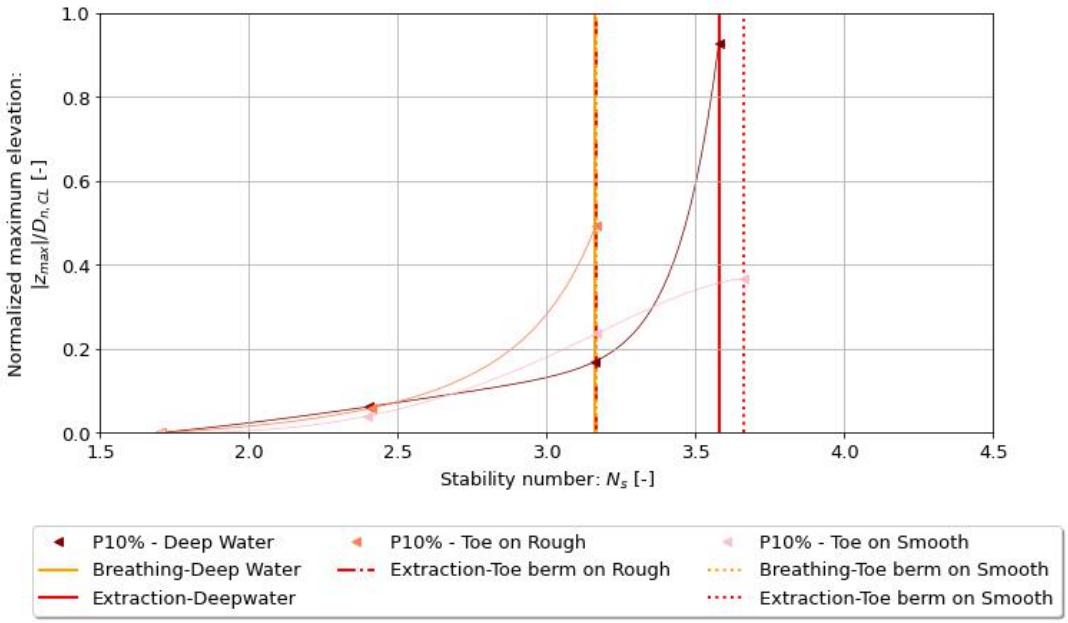

Figure 5.18: Maximum unit elevation expressed as a fraction of the Coastalock nominal diameter, under $s_{0p} = 0.04$, with 10% protrusions in the 'Deep Water', 'Toe on Rough' and 'Toe on Smooth' set-up.

When comparing the maximum elevation changes among the three setups, as illustrated in Figure 5.18, an initial increase is evident for N_s around 2.4. Subsequently, breathing occurred in all three test series for N_s around 3.2, resulting in varying maximum displacements. Notably, the displacement of the 'Deep Water' and 'Toe on Smooth' setups remained below the $0.25D_{n,CL}$.

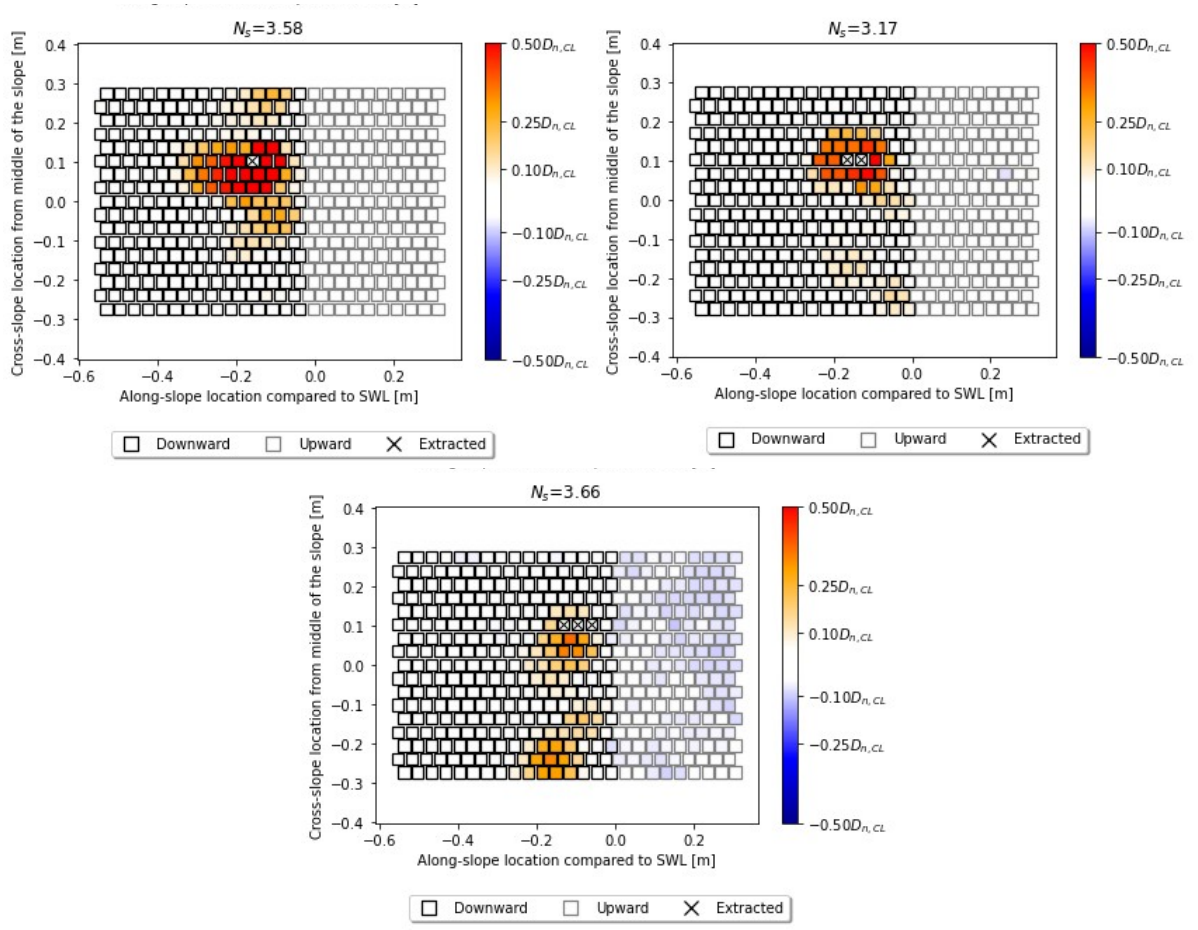

Figure 5.19: From top left, top right, to bottom: Elevation change after the test run, compared to the reference profile after settling waves, expressed as a fraction of the Coastalock nominal diameter, under s_{0p} = 0.04, with 10% protrusions in the 'PO-SWL' configuration in the 'Deep Water', 'Toe on Rough' and 'Toe on Smooth' set-up.

When comparing the y-coordinates of the centroid points of the first row (equivalent to the third row of the entire armour layer) and the grid-based selection of units to assess settlement or sliding adjacent to the toe berm and to provide an overall view of the movement of the armour layer, it was observed that the maximum downslope settlement did not exceed $0.07D_{n,CL}$ for tests with 10% protrusions, as indicated in Tables 5.4 and 5.5. Slightly larger up slope movements were also observed, but both did not surpass the threshold value of 0.20 of relative displacement, which suggests potential settlement-induced failure.

N_s[−]	Max. $y/D_{n,CL}$[−]	Min. $y/D_{n,CL}$[−]
2.41	0.06	-0.04
3.17	0.06	-0.10

Table 5.4: Maximum settlement comparison to reference profile of Coastalock units with 10% protrusions in 'Toe on Rough' set-up under s_{0p} = 0.04.

$N_s[-]$	Max. $y/D_{n,CL}[-]$	Min. $y/D_{n,CL}[-]$
2.40	0.003	-0.08
3.17	0.06	-0.12
3.66	0.07	-0.10

Table 5.5: Maximum settlement comparison to reference profile of Coastalock units with 10% protrusions in 'Toe on Smooth' set-up under $s_{0p} = 0.04$.

The introduction of a loose rock toe berm, be it on a smooth or rough surface, has not been observed to influence the damage progression or the dominant failure mechanism of the Coastalock armour layer with short protrusions in the 'PO-SWL' configuration under deep water conditions.

Long protrusion - 22.5% spacing

In the test series involving long protrusions with 22.5% spacing, the toe berm remained stable for stability numbers below 3.52. Beyond this threshold, rocking of multiple toe berm stones ensued, followed by minor displacement that did not alter the overall shape of the toe berm. At stability numbers of 3.84 and above, significant displacement of the toe rocks occurred, resulting in a considerable migration, and rocks falling down the slope of the elevated foreshore. Notably, no significant movement of the armour layer was observed during these events, nor did sliding occur. Subsequently, both test series were halted.

When comparing the maximum elevation changes of the three set-ups for long protrusions at 22.5% spacing, as depicted in Figure 5.20, nearly identical results were obtained for the 'Deep Water' and 'Toe on Smooth' set-ups. Despite the 'Toe on Rough' set-up exhibiting a significantly larger maximum elevation compared to the other two for the first two measurements after the reference profile was taken, the upwards movement of the armour layer seemingly halted and was at the same level as the other two for N_s of approximately 3.8.

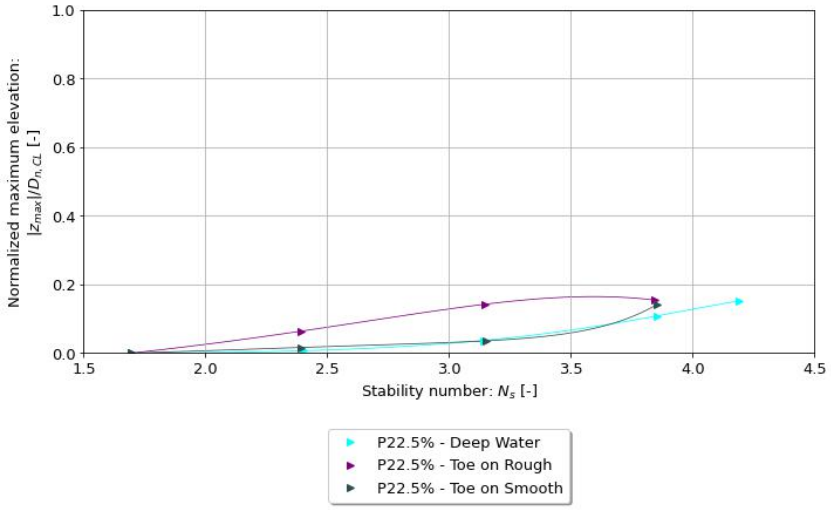

Figure 5.20: Maximum unit elevation expressed as a fraction of the Coastalock nominal diameter, under $s_{0p} = 0.04$, with 22.5% protrusions in the 'Deep Water', 'Toe on Rough' and 'Toe on Smooth' set-up.

When examining the y-coordinates of the centroids to detect signs of settlement or indications of sliding adjacent to the toe berm and to gain a comprehensive understanding of the movement of the armour layer, it was found that the maximum downslope settlement did not surpass $0.07D_{n,CL}$, and slightly greater up slope movements were measured, in tests involving long protrusions with 22.5% armour spacing, as detailed in Tables 5.6 and 5.7. Once again, these values did not surpass the threshold value of 0.20 of relative displacement suggestive of potential settlement-induced failure.

$N_s[-]$	Max. $y/D_{n,CL}[-]$	Min. $y/D_{n,CL}[-]$
2.39	0.01	-0.06
3.15	0.03	-0.06
3.84	0.02	-0.08

Table 5.6: Maximum settlement comparison to reference profile of Coastalock units with 22.5% protrusions in 'Toe on Rough' set-up under $s_{0p} = 0.04$.

$N_s[-]$	Max. $y/D_{n,CL}[-]$	Min. $y/D_{n,CL}[-]$
2.39	0.003	-0.08
3.15	0.06	-0.12
3.86	0.07	-0.10

Table 5.7: Maximum settlement comparison to reference profile of Coastalock units with long protrusions at 22.5% spacing in 'Toe on Smooth' set-up under $s_{0p} = 0.04$.

Similar to previous findings, the introduction of a loose rock toe berm, be it on a smooth or rough surface, has not been noted to affect the damage progression or the dominant failure mechanism of the Coastalock armour layer with long protrusions in the 'PO-SWL' configuration under deep water conditions.

5.3. Overtopping

5.3.1. Measured wave overtopping

The overtopping volume was measured for each test series, and the mean overtopping rate was subsequently calculated by dividing the measured overtopping volume by the duration of the test. The resulting overtopping discharge is expressed in the form of a dimensionless overtopping rate $q/\sqrt{gH_{m0}^3}$, where H_{m0} is the significant wave height measured near the structure. This dimensionless rate is plotted against the dimensionless freeboard, defined as R_c/H_{m0}, or deep water wave steepness $s0p$. This transformation allows for comparisons between varying structural or hydraulic parameters characteristics. For the analysis, only measurements were used for which the wave duration extended beyond 1000 waves, as this is considered the minimum amount of waves for obtaining meaningful results on the overtopping characteristics of a Coastalock armour layer. The measurements have been plotted, taking into account the measurement error of the wave gauge in the overtopping basin, which affects the overtopping discharge per meter of structure q. This is illustrated by the inclusion of lower and upper error bounds in the plots of the dimensionless overtopping rate. It is noteworthy that the measurement error rarely exceeds the size of the plotted measurement markers, primarily due to the y-axis being depicted on a logarithmic scale.

The test setup for measuring overtopping using the wave gauge did not include measurements for overtopping volumes at 0% spacing. Minor splashes of water ended up on the overtopping chute but were too little to end up in the overtopping basin to be measured. This was the case for both test series with $s_{0p} = 0.02$ and $s_{0p} = 0.04$ waves; the layer failed before that could occur. No comparison could be made between the effect of the permeable core compared to the impermeable core. These measurements were consistent with findings from the preliminary study (Molenkamp, 2022), where the average overtopping discharge was found to be minimal, if present at all. Stability was found to be limiting over the exceeding of potential overtopping limits.

For armour spacings of 10% and above, the situation differs. With data points available, overtopping volumes increase, and overtopping emerges as a potential limiting mechanism in design. The following results focus on spacings of 10% and above, inclusive of configurations with and without protrusions.

Influence of core permeability

When comparing the relative overtopping on a permeable core to that on an impermeable core for varying spacings in the 'San Diego' configuration, as illustrated in Figure 5.21, it can be observed

that an increase in armour layer spacing generally results in lower measured relative overtopping rates. However, the 15% armour spacing on the impermeable core appears to be an exception to this trend.

This phenomenon can be explained by findings from large-scale physical model tests (Van Steeg et al., 2016) conducted on column-type placed block revetments (Hillblock, RONA, Taille, and Verkalit GOR), characterized by openings between the blocks forming channels for water passage. An investigation was carried out to examine the influence of these channels on the roughness coefficient for mean-wave overtopping discharge, utilizing the TAW method (Van der Meer, 2002). Existing literature did not provide insights into the roughness coefficient for mean-wave overtopping discharge specifically for block revetments with channel-shaped configurations. The study revealed that the channel-shaped characteristics of the blocks led to a reduction in wave run-up height, with the extent of reduction likely increasing with the volume of these channels. Consequently, it was observed that under the given conditions, and in line with the developed theoretical model, revetments featuring channel-shaped blocks significantly mitigate wave overtopping discharge. The underlying principle of the developed theory suggests that a portion of the volume of each wave run-up tongue is diverted into the channels of the blocks, preventing overtopping. As a result, the total volume of wave overtopping during each event is diminished by the collective volume of the hollow sections along the entire slope above SWL.

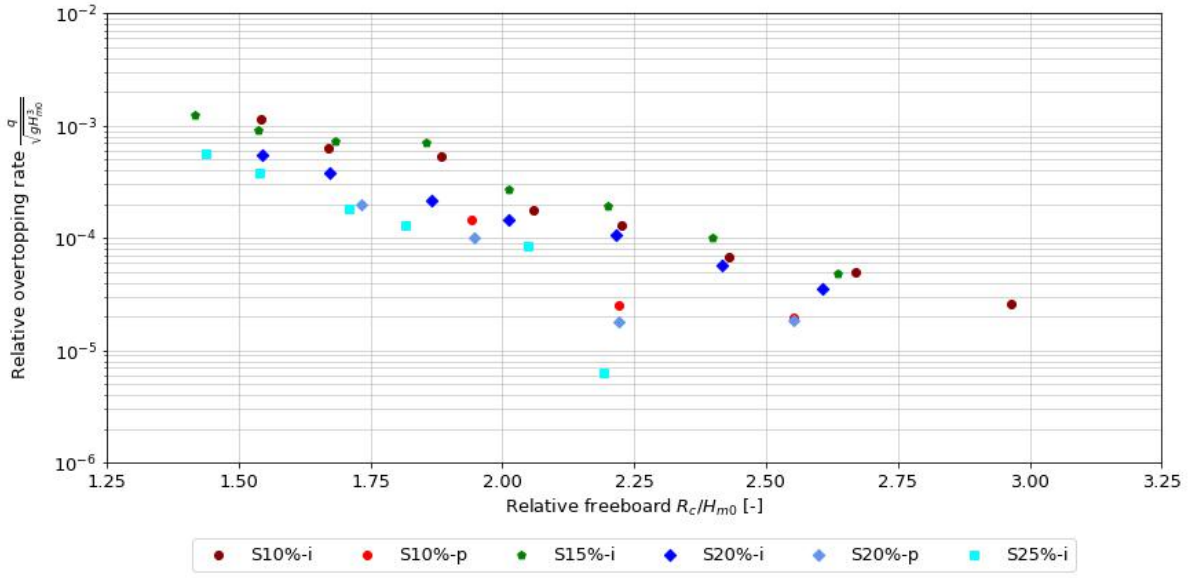

Figure 5.21: Measured relative overtopping discharge of a Coastalock armour layer, for varying simple spacings (S), in the 'San Diego' configuration, on an impermeable (i) and permeable (p) core structure, under $s_{0p} = 0.04$.

Comparing spacings tested on both permeable and impermeable cores, a decrease in relative overtopping can be clearly observed for the case with a permeable core. This can be attributed to the increased permeability of the core, allowing water infiltration through the structure, which decreases run-up and results in lower wave overtopping discharge. However, this reduction could be partially attributed to the method used to measure the overtopping volume. As described in Section 3.4.4 and illustrated in Figure 3.10, the measurement of wave overtopping occurs at a distance of $3D_{n,CL}$ from the seaward edge of the crest. This introduces a section of the crest where the water flow over the structure may be influenced by the crest itself. Consequently, water infiltration occurs through this section.

Influence of protrusions

When examining the measurements with 10% protrusions in the 'PO-SWL' configuration on a permeable core, Figure 5.22 illustrates a decrease in measured overtopping discharge compared to measurements without protrusions in the 'San Diego' configuration. The measured relative overtopping could be affected in several ways by the introduction of protrusions. Firstly, the addition of these protrusions, acting as obstructing elements, makes the roughness profile of the armour layer more jagged, which

affects water interaction during up-rush, leading to a decrease in relative wave overtopping. On the other hand, the obstruction of the voids between the armour units by the protrusions would result in less diversion of the overtopping into voids, leading to more overtopping, in accordance with the theory proposed by Van Steeg et al. (2016) for channel-shaped placed block revetments. Lastly, the introduction of the orientation change and with it a different roughness profile for a section of the slope or the slope as a whole may contribute to variations in relative overtopping as well. Further research on these three types of wave-structure interactions should be conducted to quantify the influence of the protrusions on overtopping characteristics. Currently, it remains uncertain why comparing the results of 10% armour spacing set in the 'San Diego' configuration to the 10% protrusions set in the 'PO-SWL' configuration result in a decrease in relative overtopping.

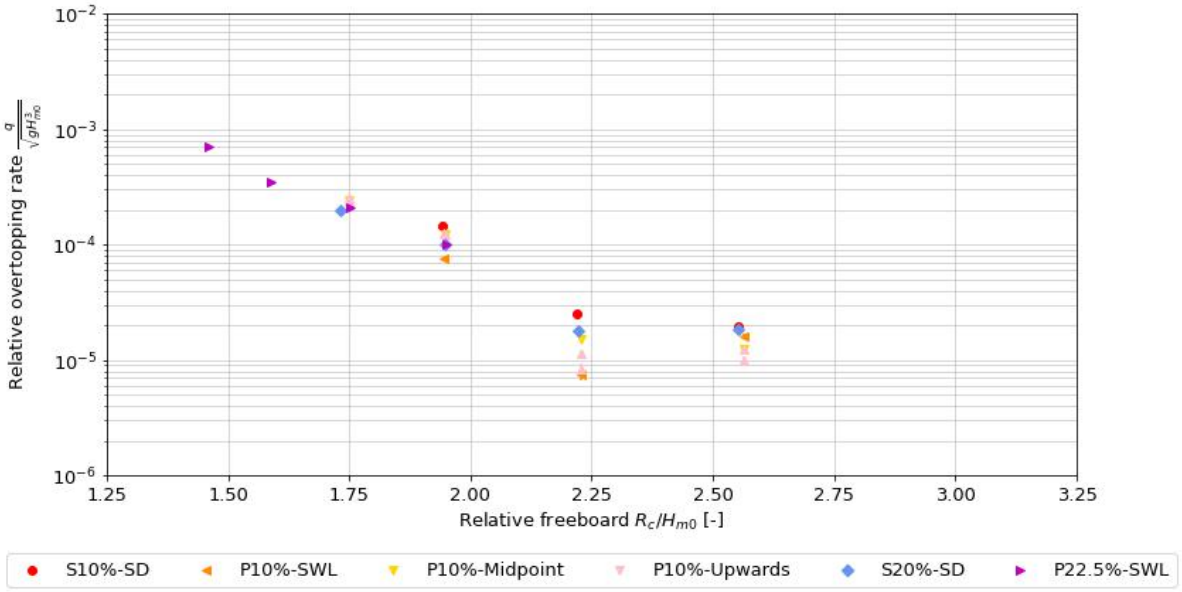

Figure 5.22: Measured relative overtopping discharge of a Coastalock armour layer, for varying simple spacings (S) in the 'San Diego' (SD) configurations, and protrusions (P) in varying configurations, on a permeable core structure, under to $s_{0p} = 0.04$.

Regarding the comparison of the 20% spacing and the 22.5% protrusion, making a comparison is difficult as the measurements have little overlap with regards to relative freeboard. At first glance, it seems that the increase in distance between the units is balanced by the obstruction caused by the 22.5% protrusion and the change in roughness introduced by the downward-facing cavity armour blocks.

Influence of wave steepness

In Figure 5.23, the relative overtopping has been plotted in terms of deep-water wave steepness for the comparison of $s_{0p} = 0.04$ and $s_{0p} = 0.02$. To enable a comparison, given that overtopping is influenced by wave height H_{m0}, it was necessary to select measurements with comparable a relative freeboard. Due to a discrepancy between measured relative overtopping rates for significant wave heights and a lack of measurements due to stability with certain test series, only one range of measurements was usable for comparison. This set of measurements is selected for R_c/H_{m0} between 1.86 and 2.00.

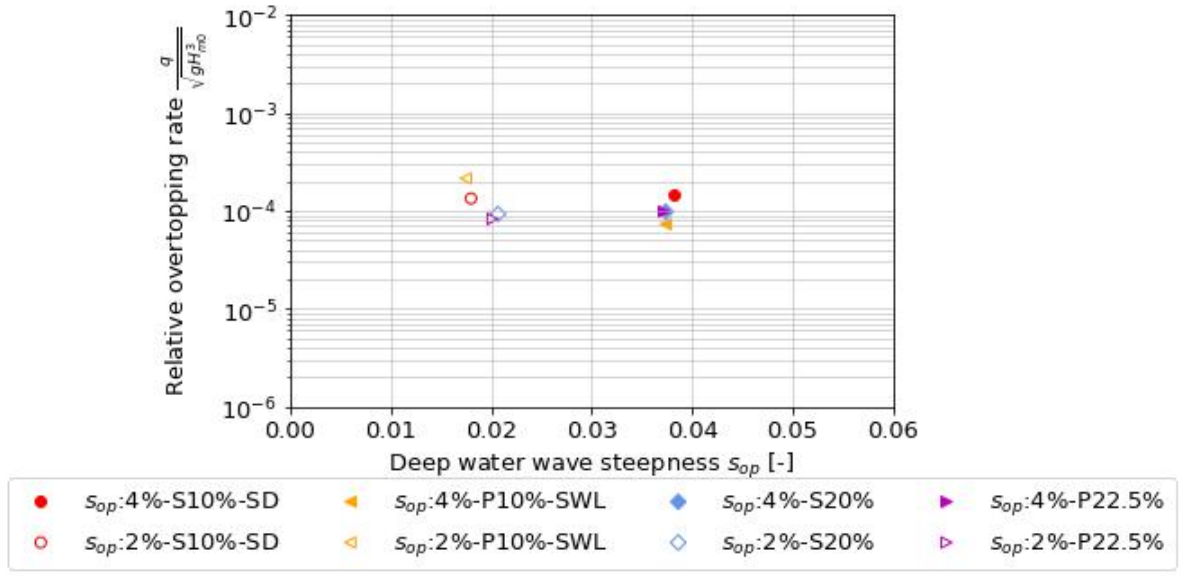

Figure 5.23: Comparison of relative overtopping discharge of a Coastalock armour layer, for a R_c/H_{m0} range of 1.86-2.00, under $s_{0p} = 0.02$ and $s_{0p} = 0.04$, for varying simple (S) in the 'San Diego' configuration, and protrusions (P) in the 'PO-SWL' configuration, on a permeable core structure.

No clear trend appears to emerge regarding the influence of wave steepness on the overtopping performance of a Coastalock armour layer, based solely on the examination of the two tested wave steepness values.

Influence of configuration

When the results of test series, each featuring 10% protrusions on a permeable slope, are presented together in Figure 5.22, it enables the comparison of the effect of orientation change. However, the effect of lowering the orientation change from cavity upwards to cavity downward to the midpoint between SWL and the bottom row of Coastalock in the 'PO-Midpoint' configuration or changing the orientation to all blocks facing upwards in the 'Upwards' configuration does not clearly increase or decrease the measured overtopping. One might expect that increasing the number of upward cavities would lead to a rougher slope profile, thereby decreasing overtopping discharge.

5.3.2. Comparison with EuroTop formula

The EuroTop (2018) equation, as expressed in Eq. 2.8, serves as the industry standard for comparing overtopping performance across various types of rock layers or armour units, particularly on steep breakwater slopes. Of primary interest within this equation is the factor γ_f, which characterizes the influence of roughness elements on slope overtopping discharge. Roughness factors are derived for each armour spacing, or armour layer configuration, by employing the Least Squares Error method to the data for each spacing or configuration individually. This method aims to minimize the sum of the squares of the differences between the observed and predicted values of overtopping discharge, thus determining the best-fit value for γ_f that optimally describes the observed data.

After reanalysis of Molenkamp's (2022) results, utilizing the adjusted H_{m0} and duration data, the last test runs of the 10% spacing (series 12, run 1) and 20% spacing (series 14, run 9) were excluded. This decision was made due to their abrupt ending, resulting in an unknown H_{m0} and potentially skewed duration in both cases, which could have affected the final outcomes. The results have been reevaluated and are presented in Table 5.8. The reevaluated approach resulted in roughness factors that were higher relative to the previous analysis, with an increase ranging from 0.3% to 2.0%.

Influence of core permeability

The results obtained from measurements on a permeable core are presented alongside those from an impermeable core in Table 5.8. A notable decrease in the measured roughness factor is observed for both

tested armour spacings. Specifically, when comparing the results for a 10% spacing, a relative decrease of 8.0% is noted. This decrease diminishes to 3.0% for a 20% spacing. This behavior can be explained by the fact that impermeable slopes experience high run-up as waves oscillate within the armour layer. In contrast, permeable core breakwaters dissipate more wave energy through water infiltration, resulting in reduced run-up. Lower run-up levels generally lead to lower overtopping rates because waves are less likely to exceed the crest height and spill over the top of the structure. It is important to note that due to the employed measuring technique and large increments in significant wave height, only 3 to 4 data points of overtopping per test series are present, resulting in uncertainty regarding the prediction of the roughness factor.

Spacing %	Impermeable core $\gamma_{f,CL,i}$	Permeable core $\gamma_{f,CL,p}$	Difference
10	0.75	0.69	-0.06
15	0.72	-	-
20	0.67	0.65	-0.02
25	0.62	-	-

Table 5.8: Roughness factors for EuroTop equation (2018) derived from Coastalock model testing, in 'San Diego' configuration, under $s_{0p} = 0.04$, on slopes with an impermeable (Molenkamp, 2022) and permeable core.

The fitting of the formula results in a rather poor fit for the lower armour spacings on an impermeable core, particularly noticeable for low relative freeboard, as shown in Figure 5.24. This fit is characterized by a significant underestimation of the relative discharge for that region. Furthermore, the fitting of a formula reveals a clear trend for both permeable and impermeable slopes: higher spacings result in a steeper fit, meaning a higher roughness, leading to lower roughness factor.

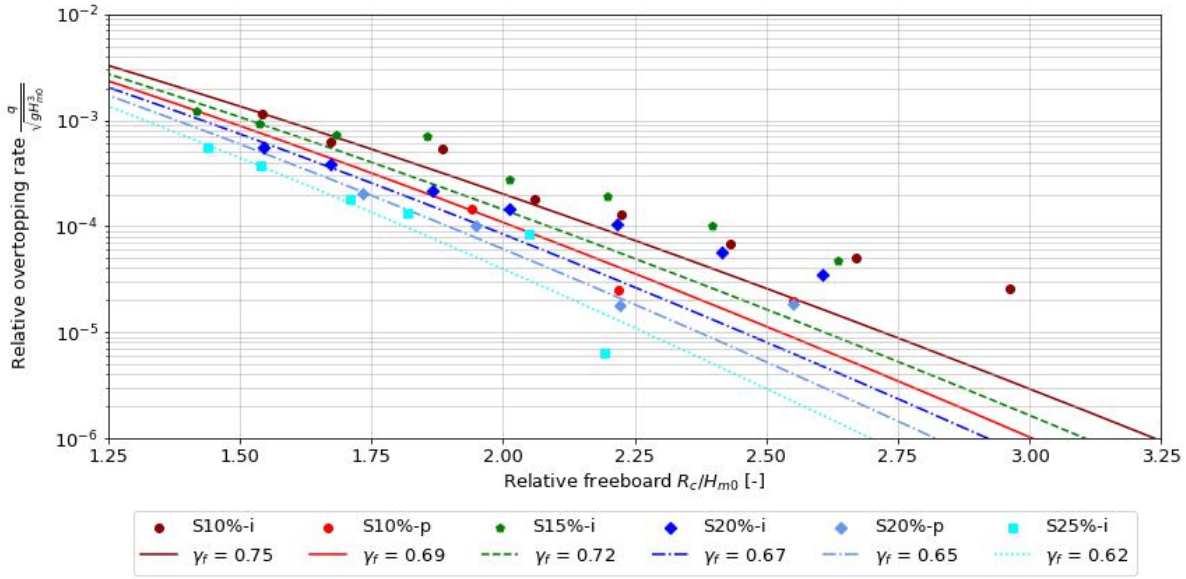

Figure 5.24: EuroTop equation (2018) fitted for varying simple spacings (S) of a Coastalock armour layer, in 'San Diego' configuration, on an impermeable (i) and permeable (p) core structure, under $s_{0p} = 0.04$.

Influence of protrusions

When applied to the measurements related to protrusions, a distinct decrease in the roughness factor is evident when comparing the results for a 10% simple spacing in the 'San Diego' configuration to the 10% protrusions in the 'PO-SWL' configuration, amounting to 5.8%, as illustrated in Table 2.7.

In contrast, when comparing the 20% spacing in the 'San Diego' configuration to the 22.5% spacing in the 'PO-SWL' configuration, no significant change in the roughness coefficient was observed.

Spacing	Configuration	$\gamma_{f,CL}$
S-10%	'San Diego'	0.69
P-10%	'PO-SWL'	0.65
P-10%	'PO-Midpoint'	0.67
P-10%	'Upwards'	0.67
S-20%	'San Diego'	0.65
P-22.5%	'PO-SWL'	0.65

Table 5.9: Roughness factors for the EuroTop equation (2018) derived from Coastalock model testing with simple spacing (S) or protrusions (P) in varying configurations on a slope with permeable core, under $s_{0p} = 0.04$.

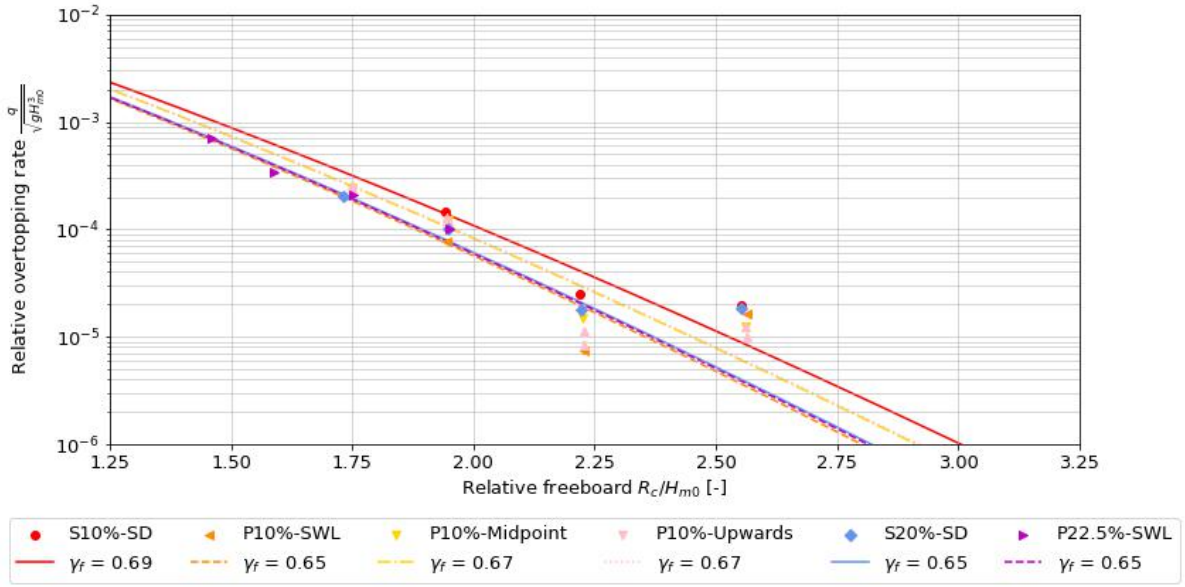

Figure 5.25: EuroTop equation (2018) derived from Coastalock model testing with simple or protrusion spacing in varying configurations on a slope with permeable core for $s_{0p} = 0.04$.

Influence of configurations

When comparing the results of the 10% protrusions in the 'PO-SWL' configuration to the other two tested configurations, an unexpected finding emerges regarding the roughness coefficient. Contrary to expectations, there is an increase in the roughness coefficient with the introduction of a lowering orientation change to the midpoint between SWL and the bottom row of Coastalock in the 'PO-Midpoint' configuration, as well as with the orientation change to all blocks facing upwards in the 'Upwards' configuration. An increase in the overtopping trend and a decrease in the roughness coefficient would have been anticipated; however, the opposite is observed for both the 'PO-Midpoint' and 'Upwards' configurations, where the roughness coefficient is relatively 3.1% higher compared to the 'PO-SWL' configuration, indicating a smoothing of the slope. A possible explanation for the observed phenomenon is provided in Section 6.3.5.

Derivation of roughness parameter for broad range spectrum

To obtain a more reliable measure for the roughness coefficient, the datasets for test series were combined into a set with a larger range of wave steepnesses ($s_{0p} = 0.02$ and 0.04), in accordance with guidelines from the EuroTop manual (2018). The manual specifies that influence factors on roughness are derived for breaker parameters in the range $\xi_{m-1,0} = 2.8$ to 4.5. Within this range, the roughness factor remains fairly constant, with a slight tendency for larger wave periods to result in slightly larger overtopping. For measurements with a breaker parameter $\xi_{m-1,0} > 5$, it is advised to introduce a modification factor when calculating the roughness factor. To ensure adequacy, the breaker parameter was evaluated for values $\xi_{m-1,0} < 5$ exclusively when calculating the roughness parameter. This adjustment was applied for the 10% spacing on both impermeable and permeable cores without protrusions, as well as for the

10% protrusions and the 22.5% protrusions on a permeable core. The wide-range roughness factors for $3 < \xi_{m-1,0} < 5$ are presented in Table 5.10.

Spacing	Core	Configuration	$\gamma_{f,CL,wide}$	$\gamma_{f,CL,s_{0p}=0.04}$	Difference
S-10%	Impermeable	'San Diego'	0.76	0.75	+0.01
S-10%	Permeable	'San Diego'	0.72	0.69	+0.03
P-10%	Permeable	'PO-SWL'	0.71	0.65	+0.06
S-20%	Permeable	'San Diego'	0.66	0.65	+0.01
P-22.5%	Permeable	'PO-SWL'	0.67	0.65	+0.02

Table 5.10: Comparison of roughness factors for the EuroTop equation (2018) derived from Coastalock model testing with simple spacing (S) or protrusions (P) in varying configurations on a slope with permeable core, for $3 < \xi_{m-1,0} < 5$ to s_{0p}=0.04 ($\xi_{m-1,0} \approx 3$).

When comparing the roughness coefficient of the wide-range results with the $s_{0p} = 0.04$ ($\xi_{m-1,0} \approx 3$) outcomes, an increase in the roughness coefficient is evident across all cases. A higher roughness factor suggests an increase in relative overtopping. This observation confirms the tendency for the roughness factor to exhibit a slight inclination for larger wave periods, resulting in slightly higher levels of overtopping.

The fit for the extended set of measurements is depicted in Figure 5.26, along with the 90% confidence band, denoted by the ±5% lines, and lines representing a rough slope and rubble mound breakwater. The confidence interval is determined based on the fitted roughness factor and the reliability of Equation 2.8, as specified by $\sigma(0.09) = 0.0135$ and $\sigma(1.5) = 0.15$ in the EuroTop manual (2018). The accuracy of the fit varies considerably across the test series, with the 10% simple spacing exhibiting the poorest performance and the 22.5% protrusions yielding the strongest fit.

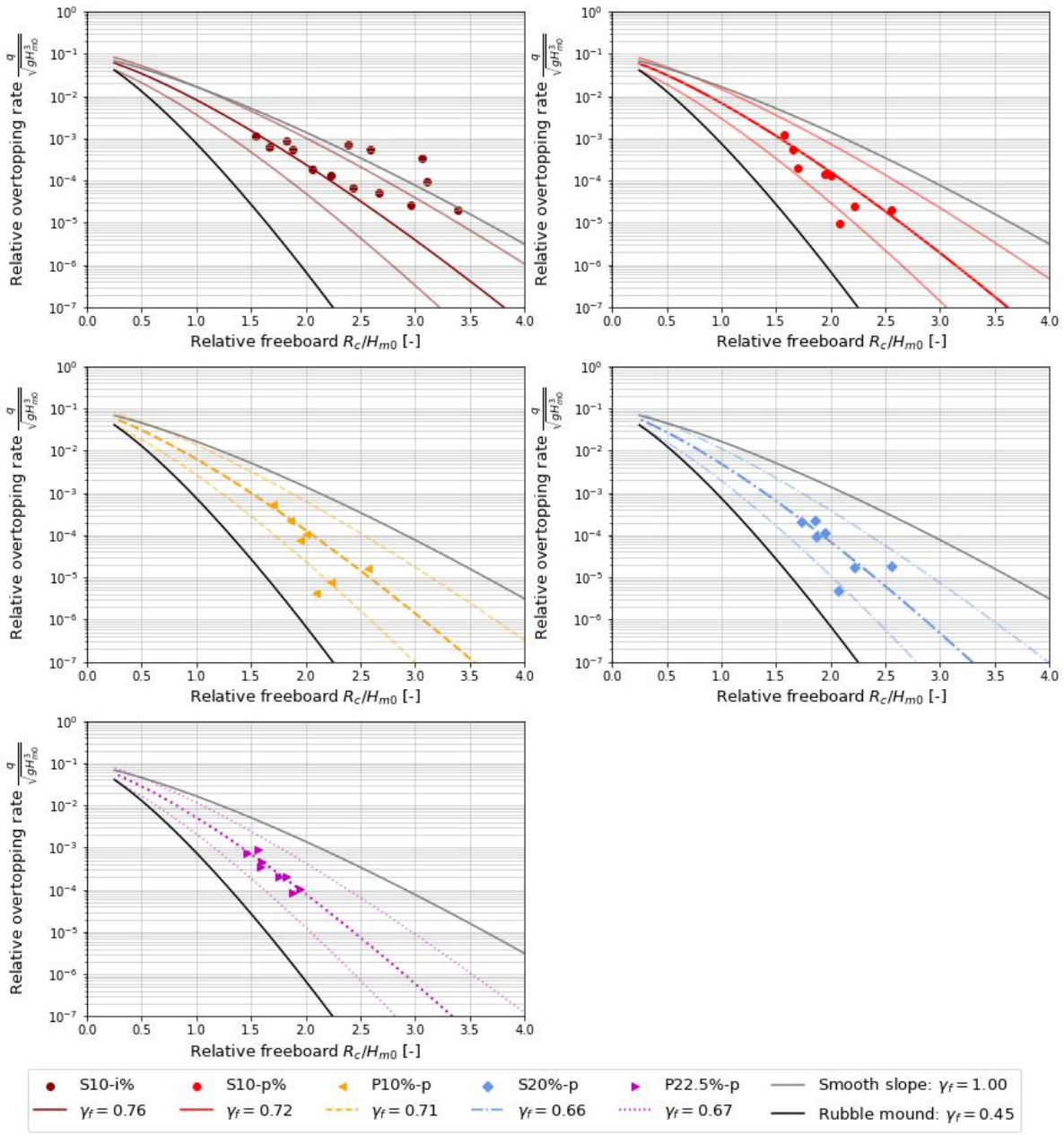

Figure 5.26: EuroTop equation (2018) fitted from Coastalock model testing with simple spacing (S) or protrusions (P) in varying configurations on a slope with permeable core, for $3 < \xi_{m-1,0} < 5$.

5.4. Reflection

5.4.1. Measured reflection coefficient

The results of the reflection coefficient analysis are based on the averaged measured reflection coefficient for values of H_s between $0.065m$ and $0.085m$, corresponding to N_s ranging from 1.67 to 2.18. These stability numbers were present across all test series conducted on both permeable and impermeable cores. By averaging the wave conditions within this range, it allows for the identification of influential parameters, such as armour spacing, core permeability, protrusions, configuration changes, and wave steepness.

Influence of armour spacing

Primarily, a consistent trend emerges from the measured reflection coefficients for varying Coastalock armour layer spacings on both permeable and impermeable slopes. An increase in armour spacing

correlates with a decrease in the reflection coefficient, as depicted in Figure 5.27. This trend is attributable to the increased inter-void space within the armour layer, resulting in a more permeable armour layer, that makes absorption of a larger portion of incident wave energy possible by the underlying layers.

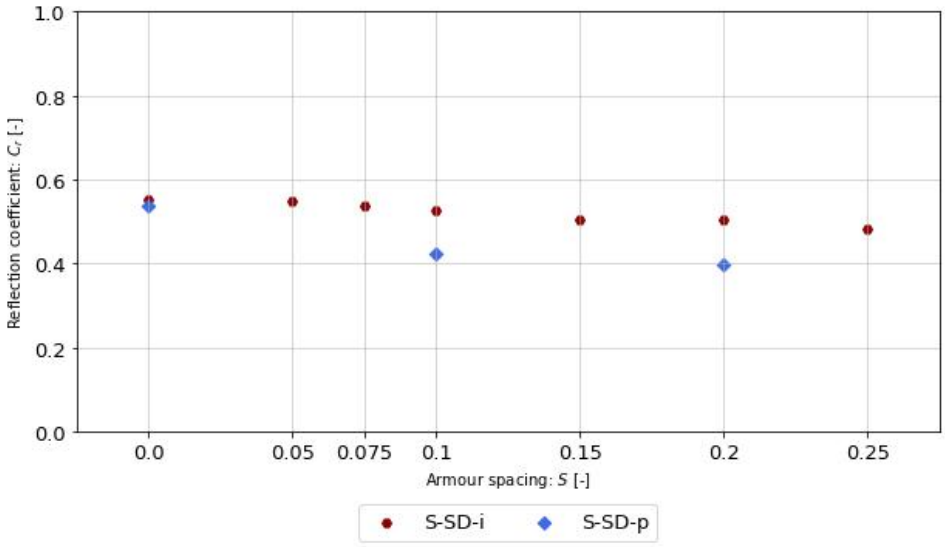

Figure 5.27: Influence of armour spacing on the reflection coefficient of a Coastalock armour layer with simple spacing (S), in the 'San Diego' configuration, under s_{0p}=0.04.

Influence of core permeability

When comparing the results in Figure 5.27 of 0% armour spacing to those of 10% and 20% spacing, it is evident that the permeable core ($C_r \approx 0.4$) consistently exhibits lower reflection coefficients compared to the impermeable core ($C_r \approx 0.5$). However, the permeable core demonstrates a notably greater dampening of incoming wave energy in comparison to the impermeable core for the 10% and 20% spacing test series. As with these test series a larger part of the underlayer is exposed for which waves are able to penetrate into the structure and be damped by internal reflection within the core to a stronger degree.

Influence of protrusions

The combined effect of introducing protrusions and changing the orientation from 'San Diego' to 'PO-SWL' resulted in a significant increase in reflection, as observed in Figure 5.28. This can be attributed to the presence of additional material available for reflection, facilitated by the protrusions. Additionally, the obstruction of inter-unit voids led to a reduction in the permeability of the armour layer, consequently decreasing internal dampening within core of the structure.

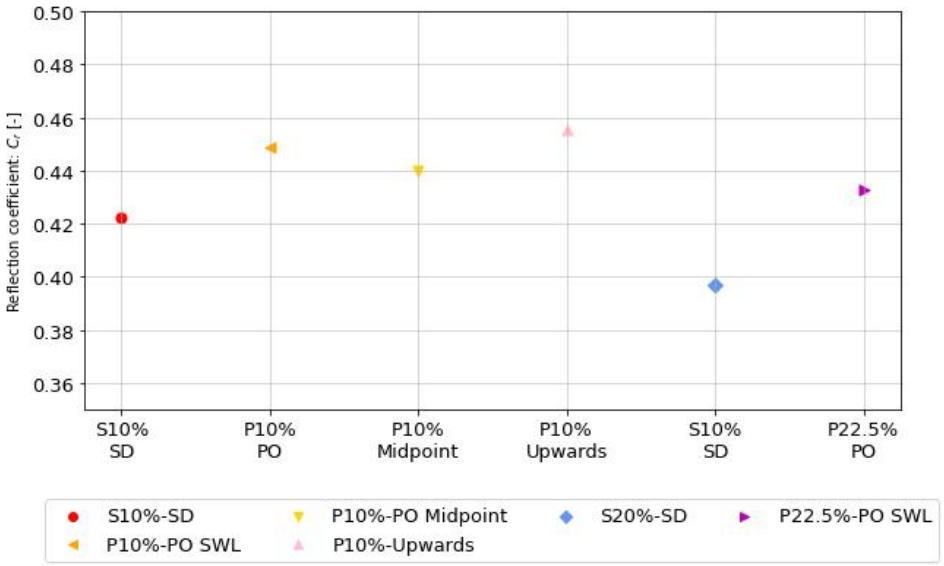

Figure 5.28: Influence on the reflection coefficient of a Coastalock armour layer, of protrusions (P) and armour layer configurations on reflection coefficient, compared to simple spacing (S), on a permeable core, under s_{0p}=0.04.

Influence of wave steepness

The third factor examined was wave steepness, which, according to Muttray et al. (2006), is considered the most significant determinant of the reflection coefficient. In test series conducted on both permeable and impermeable cores, a notable reduction in the reflection coefficient was observed with an increase in wave steepness. Interestingly, this reduction appeared to be more pronounced in the case of impermeable cores. Despite a clear trend observed when comparing the slopes of the fitted lines for a permeable slope, which had a mean of -7.4 (with a 90% student-t confidence Interval of:-7.7, -7.0) the limited scope of the current measurement program, which included only two wave steepness values, excludes definitive conclusions regarding the broader impact of varying deep water wave steepness at this stage.

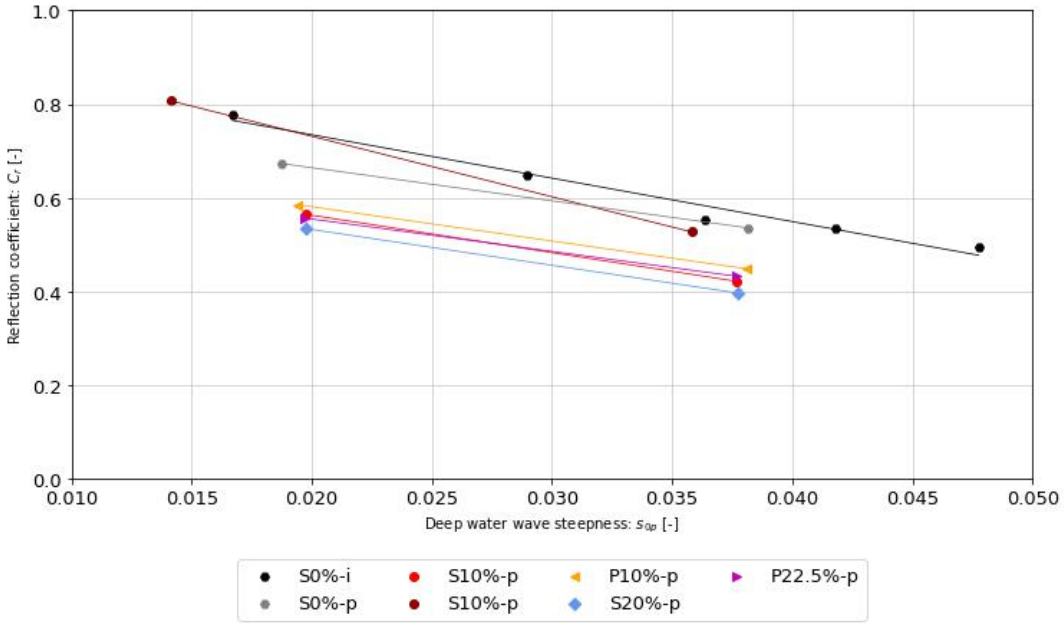

Figure 5.29: Influence of wave steepness on the reflection coefficient of a Coastalock armour with varying simple spacing (S) in the 'San Diego' configuration and protrusion (P) in the 'PO-SWL' configuration, on an impermeable (i) and permeable core (p).

5.4.2. Influence of configuration

As for the final influencing factor, which involves comparing the effect of upward and downward cavity orientations on reflection, it was anticipated that reducing the number of downward-oriented cavity units from the 'PO-SWL' configuration to the 'PO-Midpoint' configuration would result in a decrease in the reflection coefficient. This anticipation was based on the assumption that fewer units facing incoming waves with a smooth surface would result in more micro-irregularities introduced by the cavity, consequently reducing reflection. The observed reduction was, accounted for a -0.01 (relative decrease of 2%) difference in the reflection coefficient, as observed in Figure 5.28. Unexpectedly, when all cavities were turned upwards, contrary to expectations, they resulted in a higher reflection coefficient, exhibiting a +0.01 increase compared to the 'PO-SWL' configuration (relative increase of 2%). This occurrence parallels a similar finding noted in a study by Molenkamp (2022) on the effect of armour layer configurations on the reflection coefficient, where the upward configuration resulted in higher reflection coefficient than the sideways cavity configuration. However, another possible explanation for why higher reflection coefficients might occur with the presence of more upwards-facing units is provided in Section 6.3.5.

5.4.3. Comparison to empirical formulas

The two appropriate methods for assessing the impact of the reflection coefficient on a permeable breakwater structure, as detailed in Section 2.4, were compared with the measured outcomes. The first being the Van der Meer's (1992), presented in Equation 2.11, which evaluates the influence of armour layer spacing with and without the permeable core and wave steepness. The second being the formulation proposed by Muttray et al. (2006), represented by Equation 2.12, which assesses the impact of wave steepness only.

The procedure as proposed by Van der Meer (1992) where the notional parameter would be used as a proxy for the variation in armour spacing and core permeability. However, it's crucial to recognize that this notional permeability parameter differs from the actual spacing of armour units. The results depicted in Figure 5.30 indicate an underestimation of the reflection coefficient for P values of 0.1 for the impermeable core structure and 0.4 for the permeable core structure.

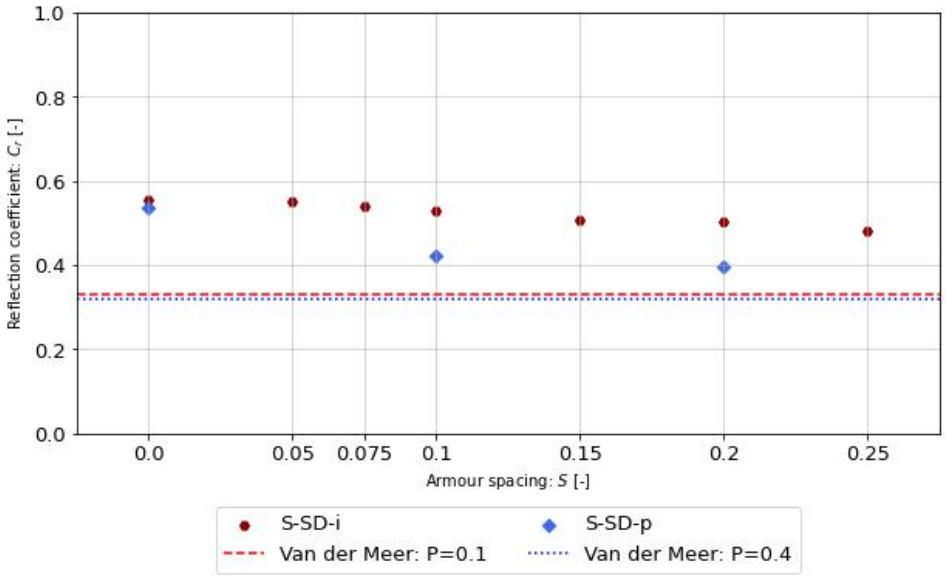

Figure 5.30: Influence of armour spacing (S) on the reflection coefficient of a Coastalock armour layer in the 'San Diego' configuration, on an impermeable core (i) and permeable core (p), under s_{0p}=0.04.

When comparing the predictions made by both Van der Meer (1992) and Muttray et al. (2006), it's observed that both models, one using a modified breaker parameter and the other employing wave length, exhibit similar overall shape to the measured data. However, Figure 5.31 reveals a significant underestimation between the predictions and the measurements. The latter approach, intended for

rubble mound breakwaters with a permeable core, results in a smaller underestimation for results on a permeable core compared to those on an impermeable core, as expected.

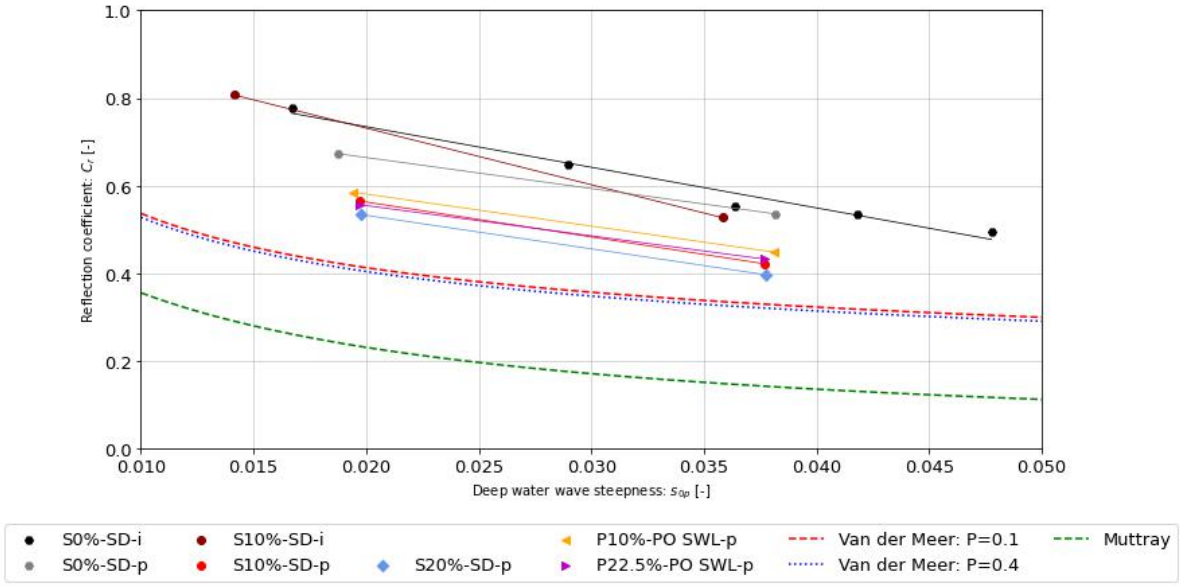

Figure 5.31: Influence of wave steepness on the reflection coefficient of a Coastalock armour layer, with varying simple spacing (S) in the 'San Diego' configuration and protrusion (P) in the 'PO-SWL' configuration, on an impermeable core (i) and permeable core (p), under s_{0p}=0.04.

5.4.4. Formulation of Coastalock reflection equation

An equation is proposed for predicting the reflection coefficient, drawing from Molenkamp's (2022) methodology. It leverages reanalyzed data from the impermeable core and incorporates the influence factor of the permeable core. Notably, the formulation is based solely on measurements for the 'San Diego' configuration, given its extensive testing. The equation takes into account the impact of armour spacing by incorporating a linear fit parameter. This approach is preferred over adopting Van der Meer's (1992) methodology due to its better suitability in shape, and the physical and theoretical discrepancies. Additionally, it considers wave steepness by adopting the approach used by Muttray et al. (2006), which is considered the most appropriate for a breakwater structure. Furthermore, it integrates a parameter to account for the effect of the permeable core on the reflection coefficient. The equation takes the following form:

$$C_{r,CL} = a + b \cdot C_{r,Muttray} + c \cdot S + d \tag{5.1}$$

The effect of armour spacing, based on data under $s_{0p} = 0.04$, and wave steepness, based on data for 0% spacing, were both derived from tests conducted on an impermeable core. Parameters a, b, and c were estimated using a weighted Least Squares Error method, with the inverse of the standard deviation as weights. Subsequently, a Least Squares Error method was employed for measurements of 0%, 10%, and 20% spacing under $s_{0p} = 0.04$ to incorporate the effect of a permeable core, as parameter d. The equation was solved, yielding the following parameters and the eventual predictive equation:

$$C_{r,CL} = 0.25 + 2.01 \cdot C_{r,Muttray} - 0.31 \cdot S + d, \text{ with: } \begin{cases} d = 0.00 & \text{for impermeable core} \\ d = 0.05 & \text{for permeable core} \end{cases} \tag{5.2}$$

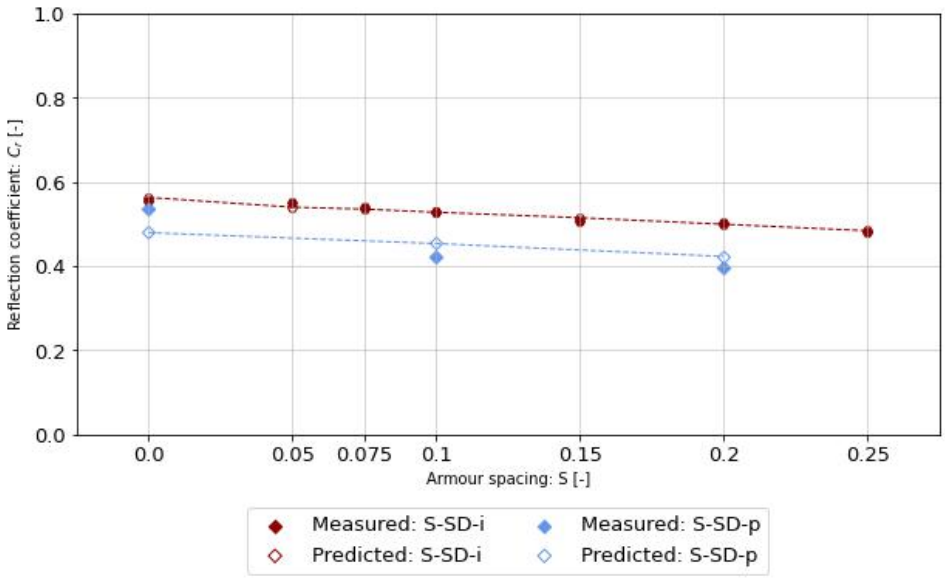

Figure 5.32: Fitting of Eq. 5.2 for the influence of spacing (S) of a Coastalock armour layer in the 'SD' configuration, under s_{0p}=0.04, on an impermeable (i) and permeable (p) core.

The optimal parameters, a, b and c, obtained for the impermeable core, as seen in Figures 5.32 and 5.33, result in a mean error of 1.0% and with a standard deviation of 0.8%. However, when considering the permeable core case, these metrics increase to a mean error of 3.8% with a standard deviation of 1.4%. This increase in error can be attributed to the limited availability of data on the effect of armour spacing on a permeable core and the fact that the results for a permeable core are less appropriate to a straight linear fit.

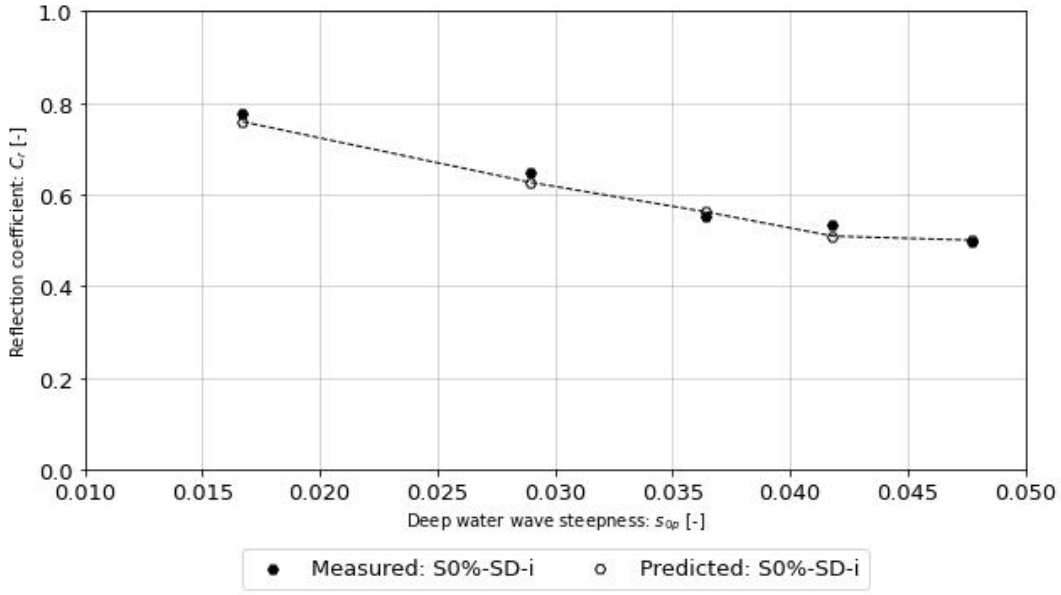

Figure 5.33: Fitting of Eq. 5.2 for the influence of s_{0p} of a Coastalock armour layer with 0% spacing in the 'SD' configuration, on an impermeable core.

For the validation of the proposed equation, the reflection coefficient of several test series not included in the formulation of the equation was plotted against the predicted reflection coefficient. This functioned as the first evaluation of the equation's accuracy beyond the datasets on which it was originally formulated. Figure 5.34 demonstrates that Equation 5.2 is capable of providing a good first estimate

of the reflection coefficient. The equation yields reasonable predictions for measurements involving protrusions and orientation changes for $s_{0p} = 0.035 - 0.40$. However, it tends to overestimate the results on an impermeable core, while underestimating the results for long waves in tests series with protrusions on a permeable core.

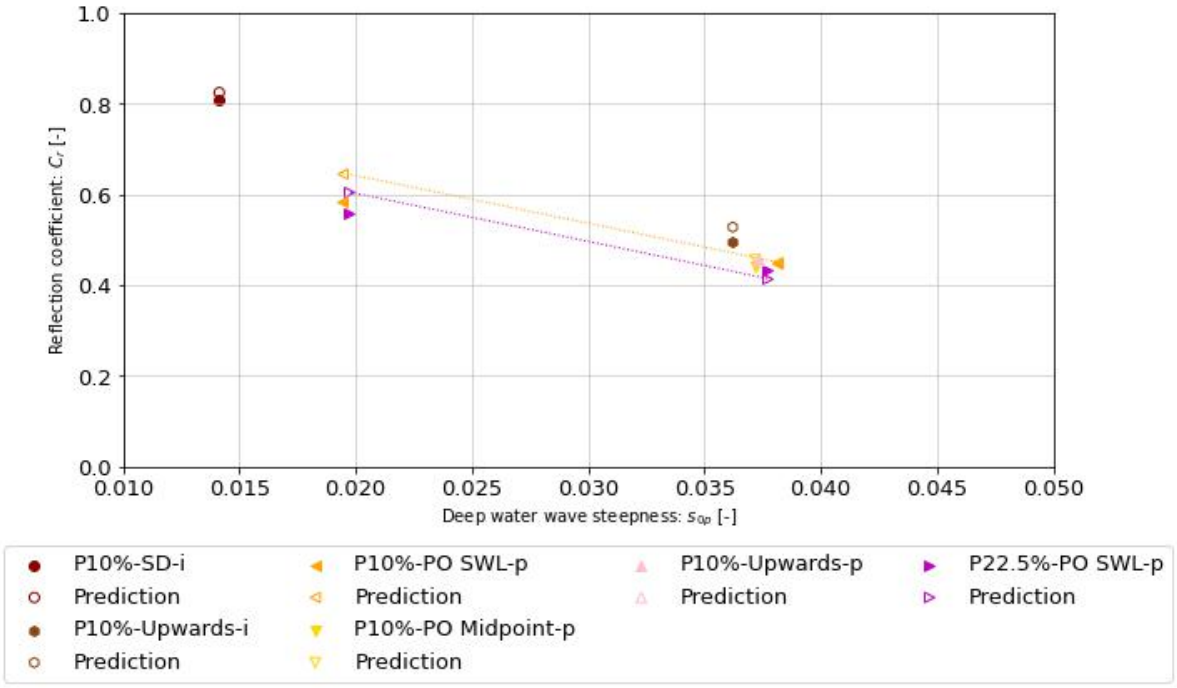

Figure 5.34: Validation of Equation 5.2 for test series 21 and 23 on an impermeable core (i), and test series 07, 08, and 13-17 on a permeable core (p).

The discrepancies between the measurements and predicted values can be attributed to several factors, including the limited abundance of tested spacings for a permeable core, the absence of consideration for the effect of wave steepness for larger spacings in both impermeable and permeable cores, the lack of consideration for protrusions, and the restriction to the 'San Diego' configuration without accounting for variations in armour layer configurations.

6

Discussion

The chapter commences with an examination of the applicability of the research findings, offering insights into the decisions made and potential enhancements concerning the physical model test setup, test program, and methodologies. Given the impact of these decisions on the outcome of the results, their significance is underscored. The section concludes with a reflection on the validity of the results.

6.1. Physical model test set-up and test program

As this study represents the second investigation into Coastalock, following the work of Molenkamp (2022) as the sole publicly available reference, certain limitations were imposed on the physical model setup and testing program to ensure the generation of meaningful and comparable results within the scope of this thesis. In that light, it is important to state that the findings presented in this work are not entirely conclusive. However, this thesis represents a first leap in the application of Coastalock on breakwaters or other permeable slope revetments and the introduction of support of the armour layer by a loose rock toe berm. Additionally, it provides an initial examination of the effects of armour unit alterations in the form of protrusions, with variations in their size, as well as the introduction of new armour layer configurations out of necessity for correct placement of the armour units with protrusions.

6.1.1. Hydraulic parameters

Large increments of significant wave height were intentionally chosen, as the behavior of Coastalock as part of a breakwater structures, with or without toe and protrusions, was still unexplored. This approach was necessary to ensure that the entire testing program could be completed within a day. However, this choice resulted in some loss of detail regarding the behavior, and fewer comparison materials were available for analysis, be it stability, overtopping or reflection.

The same can be said for the wave steepness, as only the two most critical values were tested. This limited range of testing may restrict the depth of understanding of the behavior of Coastalock as part of a breakwater structure under varying wave steepness conditions.

6.1.2. Structural parameters

Regarding the physical model setup itself, maintaining consistency and facilitating comparison necessitated retaining certain aspects while adjusting others to the best extent feasible, bringing with it deviations from guidelines. The 'Deep Water' configuration employed an identical SWL, crest height, and overall armour layer dimensions. To accommodate the introduction of the toe berm, a further lowering of the bottom row was necessary to address stability concerns with the toe berm rocks, constrained by the Coastalock units' nominal diameter, by choice to represent a somewhat realistic representation. Both configurations exhibited an elongated slope relative to the employed armour unit size, resulting in a disproportionately thin armour layer compared to water depth. For perspective, similar armour units like Xbloc and Xbloc Plus typically incorporate a maximum of 20 or 25 rows,

respectively for that reasoning (Delta Marine Consultants, 2023). In this study, both the 'Deep Water' and 'Toe Berm' setups surpassed this limit, featuring 28 and 30 rows, respectively, which presently lacks Coastalock-specific guidelines.

For the sake of comparability, an underlayer similar to that used in Molenkamp's preliminary research (2022) was employed, despite initial deviations from guidelines. However, in this study, the underlayer further diverged from recommendations, resulting in a ratio of $d_{n50,armour}/d_{50,underlayer}$ of 4.01, an 11% increase from the original ratio of 3.6. This deviation may have had an impact on the stability of the armour layer on top. According to the leakage length theory, the reduction in filter nominal diameter and consequently the thickness of the filter layer would result in a shorter length by 3.3%, thereby potentially increasing stability. However no increase in stability was observed during testing. This decrease in nominal diameter could also account for the observed migration of underlayer material during testing with 20% spacing.

In the absence of an existing prototype, a core prototype size was chosen to be half of the underlayer size. The sieve analysis of the material revealed a steepness of the grading equal to 1.68, which is considered wide. However, in retrospect, this grading could be deemed too wide for small-scale physical test modeling. A steeper grading would have been more suitable, as a more uniform rock diameter would reduce the probability of scale effects due to permeability issues arising from the presence of smaller or larger stones in the grading.

6.1.3. Addressing real-life complexity

The current testing program does not include several real-life aspects that could significantly influence the stability, overtopping, and reflection of a Coastalock armour layer, as part of a breakwater structure. The most critical of these aspects will be briefly discussed.

Water depth and foreshore

Breakwaters or other revetments are seldom found in deep water configurations reminiscent of those tested. In many practical scenarios, coastal structures are situated in relatively shallow water. In shallow water conditions, the wave load changes as the distribution of wave heights deviates from the Rayleigh distribution. The shape of the spectrum changes, and the waves become more peaked and skewed, eventually leading to depth-limited wave breaking.

Verhagen et al. (2007) compared results of steep and gentle foreshore slopes with identical deep water incident wave heights. It was found that steeper slopes resulted in larger damage compared to gentle slopes, both in cases of identical incoming waves at deep water and at the toe of the structure. The most significant increase in damage occurred during the transition from spilling to plunging breakers. A steep foreshore is therefore critical for armour layer stability, as it can influence breaker type and the breaking point. Plunging breakers, forming a heavier load for a protection than the spilling type by its jet-like behaviour (Schiereck and Verhagen, 2019), are more likely to occur on a steep foreshore, shifting the breaking point closer to the structure.

Small-scale model tests are highly recommended for coastal structures placed on steep sea bottoms experiencing depth-limited breaking wave conditions, including those incorporating Coastalock.

Oblique waves

The influence of oblique waves on the stability of armour layers, depending armour layer type, and the type of wave loading (long-crested or short-crested waves), is significant, as it can reduces the required armour size compared to the required armour size for perpendicular wave attack (van Gent, 2014). This reduction is attributed to the fact that oblique waves exert smaller wave pressures, especially when waves are breaking. An optimization of required armour size can reduce construction costs.

It is essential to confirm the stability of any breakwater structure exposed to oblique wave attack through physical model tests (CIRIA, 2007). As for a Coastalock, no tests have yet assessed stability under oblique waves. The concrete protrusions, which are still in a rudimentary design phase in this study, are intended to ensure a predetermined separation between units and to mitigate the influence of 3D effects, such as those caused by oblique waves. However, it is necessary to not only their effect of overall stability of the armour layer, but also to asses their strength, as oblique wave attack introduces lateral forces and stresses not present in perpendicular wave attack.

Short crested waves
Multi-directional (3D), or short-crested waves, are characterized by a complex pattern of multiple wave crests occurring simultaneously in different directions. In contrast to long-crested waves (2D), which typically exhibit a single dominant direction, short-crested waves feature wave crests oriented in various directions, leading to a more irregular and chaotic wave field. In reality, wind sea waves generated by local wind are irregular and short-crested.

Three dimensional physical model testing is required when representing three-dimensional structures or if the wave action at the structure is short-crested (Frostick et al., 2011). This is especially important in roundheads, which are often the most exposed sections of breakwaters. Studies comparing the stability effects of short-crested and long-crested waves on cube and Cubipod armour on roundheads found a reduction in stability under 3D wave conditions compared to 2D waves (H. Burcharth et al., 2011).

So far, no tests have been conducted to assess the performance of Coastalock under short-crested wave conditions. Additionally, the application of Coastalock on curved sections, such as roundheads, has not been assessed. Two key considerations in such scenarios are the placement of the columns of units with respect to the protrusions' contact and the transition between different Coastalock sizes. It is important to optimize these aspects, as designing a structure with uniform armour unit sizes on the roundhead and trunk may not be cost-effective or structurally efficient.

Bio-growth
Coastalock aims to integrate coastal protection with the establishment of marine habitats. As organisms colonize the newly formed habitat, they promote organic growth across the armour unit, potentially altering the shape, surface roughness, and the size of the channels between protrusions of Coastalock. The presented results indicate that the latter change significantly influences the stability, overtopping, and reflection characteristics of the armour layer. Factors such as the type of organism, its location on the slope, and seasonal variations in population size may also contribute to the complexity of this phenomenon. Therefore, this assessment will be crucial for ensuring the long-term effectiveness and optimized design.

6.2. Data processing: Structure from Motion

First of all, it must be emphasized that the SfM methodology, with its accuracy just above 1 mm, has proven highly suitable for monitoring movements and detecting changes in elevation perpendicular to the slope before failure occurred. This is particularly useful for brittle failure-prone armour layers like Coastalock.

However, it's important to acknowledge that the methodology employed for data acquisition and processing to obtain a Dense Point Cloud may introduce errors that could impact the final results.

1. In this study, extensive data batches were utilized to create depth maps, aiming to maintain consistency across all models by filtering out subpar images. However, variations in image quality, quantity, and overlap may impact the accuracy of the resulting 3D models.
2. The accuracy of the process is also influenced by the placement and detection of GCPs. While GCPs were positioned on the replaceable foreshores, intended to remain stationary during testing and return to the exact positions after replacement, errors occurred due to marker movement even after additional measurements. It is crucial to emphasize that GCPs must remain in their original locations for precise results. Precision in GCP detection is crucial for accurate results, and while manual measurement and establishment of a coordinate system were conducted using laser tools, human-induced errors are still possible.
3. It was discovered at a later stage that GCPs were not being detected by automatic detection software, and manual selection of a subset of pictures did not improve results.
4. The filtering process employed to optimize the Sparse Point Cloud before constructing the Dense Point Cloud, the primary output of Agisoft, adhered to standard practices for high-quality image processing in photogrammetry. However, it's noteworthy that this process was not specifically customized for small-scale photogrammetry applications.

5. The evaluation of individual Coastalock units regarding elevation changes perpendicular to the slope was constrained by the grid-based approach utilized. Tracking a proxy grid cell rather than the actual position of the units themselves led to approximations of armour layer elevation changes rather than precise unit movements. Additionally, the expansion of grid cells to accommodate potential unit movement in any direction further exacerbated this discrepancy, affecting elevation calculations. The masking procedure applied to the boundaries of the area of interest resulted in elevation changes of grid cells being based on a smaller selection of points at the sides of the Dense Point Cloud, impacting comparability with the rest of the slope
6. Relying on manual methods to determine along-slope movement, of only a selection of the slope, despite the utilization of digital tools, may introduce human error and uncertainty.

6.3. Results and analysis

6.3.1. 'Breathing'

The expectation of pressure-induced failure aligns with preliminary findings and previous studies on single-layer interlocking concrete armour units. However, the distinct up- and down-breathing motion observed on a permeable core, particularly for larger armour spacings, was unexpected. This raises questions about the choice of armour layer scaling and whether it reflects a scale effect of permeability scaling in the current testing program. Resulting to different core scaling procedures or testing Coastalock in a larger scale model setting is advised to discern this concern.

6.3.2. Quantification of armour layer permeability

In this thesis, the permeability of the armour layer is expressed in terms of armour spacing between Coastalocks, which has limited practical use. To gain deeper insights into the influence of inter-unit void size and potentially establish a connection to leakage length theory or quantify its role in pressure-induced failure, it is essential to reassess this approach. Evaluating armour layer permeability based on the 2D area for which water can infiltrate or utilizing the 3D volume created by the introduction of spacings and protrusions would provide parameters for creating a better understanding of the armour unit's behavior.

6.3.3. Overtopping

The overtopping measurements, conducted using a wave gauge within the overtopping basin, yielded only 3 to 5 measurements per test series, introducing uncertainty regarding the results and the fitted EuroTop (2018) equation. Originally, small overtopping was planned to be measured by weight at the outset of the testing program. However, due to technical constraints, this method was omitted, and only measurements using the wave gauge were performed. This limitation combined with the design of the overtopping basin, which was intended to handle larger overtopping volumes expected for spacings of 10% and above for progressively increasing wave heights. Consequently, small amounts of water that entered the overtopping basin were too insignificant to register for lower wave heights by the wave gauge, resulting in fewer measurements for low relative crest height values.

The maximum value approach of the EuroTop (2018), represented by Equation 2.8, stands as the industry standard for assessing overtopping performance across diverse rock layers or armour units on steep breakwater slopes. Despite its widespread adoption and common use for comparison purposes, this approach has inherent limitations in predicting overtopping, as it relies solely on crest height and roughness factor as parameters, with overtopping discharge per meter of structure and significant wave height serving as variables. Although expressions for surging waves on dikes (Van der Meer, 2002) or rubble mound breakwaters (Van der Meer et al., 2018) predict no influence of wave steepness or slope angle, recent studies have demonstrated the contrary, advancing overtopping prediction methods.

One of these methods is the approach proposed by van Gent et al. (2022), which is based on physical model tests and later refined using numerical modeling (Irías Mata and van Gent, 2023). The physical model tests, conducted over a wide range of relevant parameters, were used to develop and validate a set of expressions. Subsequently, numerical model computations were performed for various geometries of rock-armoured rubble mound breakwaters. The studies revealed important insights. Firstly, wave overtopping discharges at such structures depend on wave steepness, as confirmed by both physical

and numerical models, even for non-breaking waves. Furthermore, while the derived expressions from physical tests were obtained based on a common slope of 1:2 for rubble mound structures, numerical modeling incorporating slopes ranging from 1:1.5 to 1:4 revealed a notable dependence on slope angle: the gentler the slope, the lower the overtopping discharges, regardless of the wave steepness (Irías Mata and van Gent, 2023). The observed disparities between structures with differing slopes underscore the importance of considering such factors in overtopping predictions. To further enhance understanding, it was recommended to verify the effects of slope angle variations through physical model tests and to investigate additional factors such as the use of concrete armour units in place of rock in armour layers.

6.3.4. Coastalock reflection equation

Caution should be exercised when interpreting the predictive equation for the coefficient of reflection. As depicted in Figure 5.31, Equation 5.2 exhibits a discontinuity between wave steepness values, particularly in the range of s_{0p} 0.04-0.05, which contradicts the expected smooth trend. This deviation may stem from the utilization of the measured wavelength rather than the theoretical deep-water wavelength to fit the predictive equation. Additionally, discrepancies could be attributed to the averaging technique used for obtaining the measurements.

The limited abundance of tested spacings for a permeable core, the absence of consideration for the effect of wave steepness for larger spacings in both impermeable and permeable cores, the lack of consideration for protrusions, and the restriction to the 'San Diego' configuration without accounting for variations in armour layer configurations used for fitting the formulation contribute to this uncertainty. Therefore, it is advisable to approach Equation 5.2 with caution and consider it an indication rather than a definitive prediction of the Coastalock armour layer reflection characteristics.

6.3.5. Effect upwards facing cavities on overtopping and reflection

Unexpectedly, the introduction of orientation changes in the 'PO-Midpoint' and 'Upwards' configurations led to a 3.1% relative increase in the roughness coefficient compared to the 'PO-SWL' configuration. This result contrasts with the anticipated decrease in roughness coefficient with the introduction of more upwards-facing cavities, suggesting a smoothing of the slope despite expectations of increased overtopping. Similarly, turning all cavities upwards resulted in a higher reflection coefficient compared to the 'PO-SWL' configuration, contrary to expectations. This finding aligns with a similar observation made by Molenkamp (Molenkamp, 2022).

One hypothesis is as follows: upwards facing units may increase the roughness of the slope during wave run-down. When a wave front reaches the structure and washes up and down the slope, it leaves water pooled in the cavities of Coastalocks, which are meant for water retention. This remaining water alters the roughness of the slope for subsequent run-up events, resulting in a smoother slope that facilitates wave run-up and increases overtopping, ultimately leading to a lower roughness coefficient. The lack of difference between the 'PO-Midpoint' and 'Upwards' configurations is primarily attributed to the orientation of all cavities facing upwards in the wave run-up zone, suggesting that the lower part of the slope does not significantly influence the roughness factor. Additionally, the water-retaining quality of upwards-facing cavities can also alter the reflection coefficient. With a layer of water on the slope rather than a relatively dry slope, when the cavity is placed downward or to the side, there may be less energy dissipation, resulting in more reflection.

This hypothesis could be tested by conducting additional test series with variations in the orientation of the armour units on the slope. By systematically altering the placement of the units—whether upwards, downwards, or sideways—across different sections along the slope, their respective effects on the overtopping and reflection characteristics of Coastalock could be examined.

6.4. Validation

The reliability of the results presents a challenge to quantify independently, primarily because test series within the current program have not been replicated, except for the 'Upwards' configuration due to concerns regarding the positioning of securing chain elements. Furthermore, apart from Molenkamp's (2022) study, which focused on tests conducted on an impermeable core, there is no literature available to the topic of Coastalock behaviour.

7

Conclusion

This section of the thesis provides a summary of the research, reiterating its relevance, aim, research objectives, and sub-questions formulated to reach a definitive conclusion. The sub-questions are addressed systematically to draw a final conclusion on the topic of the hydraulic performance of a Coastalock armour layer as a part of a permeable breakwater structure.

7.1. Summary of the research at hand

The projected increase in coastal populations raises concerns about erosion due to natural hazards, driving the demand for hard stabilization methods like breakwaters and sea walls. Concrete armour, known for its durability and cost-effectiveness, is extensively utilized in coastal protection. However, this "armouring" of coastlines can lead to habitat degradation and loss of biodiversity. Coastal marine infrastructure often lacks surface complexity needed for diverse habitats, resulting in ecosystems dominated by non-native species. ECOncrete aims to address this challenge by developing Coastalock, an ecological armour unit designed to blend coastal protection with marine habitat creation. However, further quantification of the hydraulic performance of the armour unit is needed within its development cycle. Initial tests on impermeable slopes in deep water conditions revealed that tight placement of the units resulted in significant pore pressure gradients across the top layer, leading to failure. While these findings shed light on Coastalock application for impermeable protections, its performance as part of permeable breakwaters structures remains unexplored. Thus, the aim of this MSc thesis was to investigate the application limits of Coastalock, focusing on its behavior as part of a breakwater structure and obtaining hydraulic parameters to inform design specifications. The primary research objective is to:

> *Describe the hydraulic performance with respect to stability, overtopping and reflection of a Coastalock armour layer on a permeable breakwater slope supported by a toe.*

The following sub-questions support the main research objective

1. *Which failure mechanism causes Coastalock as a part of a permeable core breakwater structure to fail and in what way?*
2. *What effect does the presence of a permeable core, compared to an impermeable core, have on the stability, overtopping, and reflection characteristics of a Coastalock armour layer, considering different armour layer spacings and varying wave steepness?*
3. *How do variations in the form of protrusions influence the stability, overtopping, and reflection characteristics of a Coastalock armour layer on a breakwater slope with a permeable core, considering varying wave steepness?*
4. *How do variations in armour unit orientation influence the stability, overtopping, and reflection characteristics of a Coastalock armour layer with protrusions on a breakwater slope with a permeable core?*
5. *How does the introduction of a toe berm influence the progression of damage in a Coastalock armour layer with protrusions on a permeable slope?*

This research starts with a literature review to establish theory and understand physical model testing and Coastalock behavior. Subsequently, a physical model testing program was conducted in the 2D wave flume at Delft University of Technology. After testing, the results are analyzed and reported on.

7.2. Coastalock failure mechanism on a permeable core breakwater structure

The failure mechanisms observed in Coastalock armour layers on permeable core slopes are primarily attributed to built-up pressures exceeding self-weight and interlocking capabilities during wave run-down, resulting in a phenomenon known as 'breathing'. This involves upward movement perpendicular to the slope during wave run-down and downward movement during wave run-up. However, the units do not consistently return to their original positions during this movement, leading to a progressive displacement of units and the formation of bulges on the slope. The uneven settlements of armour units during breathing can further exacerbate instability, resulting in the extraction of units during subsequent wave run-downs.

This failure mechanism bears resemblance to pressure-induced uplift observed in traditional block revetments, although failure occurs before significant movement extends to the surrounding superstructure. While the observed gradual uplift may suggest the initiation of an arching mechanism, the lack of movement in the up slope part of the armour layer contradicts this hypothesis (Van den Berg et al., 2020). Nonetheless, the bulging of the lower armour layer could be attributed to a combined effect of the upper armour's weight and the hydraulic pressure of the remaining water beneath the top layer.

7.3. Effect of a permeable core on stability, overtopping and reflection

Stability

For s_{0p} = 0.04, the permeable core decreased the stability number threshold for 'breathing' at 0% spacing from 2.06 to 1.68 compared to an impermeable core, while the threshold for extraction increased from 2.11 to 2.44. However, due to the larger increments of significant wave height increase, it cannot be definitively stated whether the threshold for extraction actually increased. The introduction of the permeable core for 10% spacing adversely affected the thresholds for both 'breathing' and extraction, initially at N_s=4.02 and 4.34 respectively, reducing to 3.59 for both. Testing for 20% spacing was halted due to migration of the filter layer. It is noteworthy that the filter layer was not designed to accommodate such large spacings but remained constant across all test series. In conclusion, the observed increase in the threshold for 'breathing' and extraction of Coastalock with the introduction of armour spacing, leading to larger inter-unit void sizes, was confirmed for the permeable core structure. However, the absence of a corresponding increase when compared to the impermeable core is tentatively attributed to the reduction of maximum run-down levels on permeable cores, affecting stability by reducing variability in targeted area. Nevertheless, the lack of comparative data for impermeable cores precludes definitive confirmation of this hypothesis.

For s_{0p} = 0.02, the permeable core reduced the stability number threshold for 'breathing' at 0% spacing from 1.75 to 1.71 compared to an impermeable core, while the threshold for extraction increased from N_s=1.87 to 2.03. However, due to the larger increments of significant wave height increase, it cannot be definitively stated whether the threshold for extraction actually increased. No instances of 'breathing' or pressure-induced failure were observed during testing for the remaining test series with spacings. For the 10% spacing, stability improved with N_s reaching 3.63, compared to s_{0p} = 0.04. Additionally, a higher filter migration threshold was present for 20% spacing. The stability increase for long waves is attributed to the 'reservoir effect' of the permeable core for longer waves (H. F. Burcharth et al., 1998).

Overtopping

No comparison could be made between the effect of the permeable core compared to the impermeable core for the 0% spacing, as no overtopping was measured.

Regarding the relative overtopping on a permeable core for s_{0p}=0.04 with 10% and 20% spacing in the 'San Diego' configuration, an increase in armour layer spacing leads to lower measured relative overtopping rates. This reduction is attributed to a portion of the volume of each wave run-up tongue being diverted into the inter-unit voids of the blocks, thereby preventing overtopping, as proposed by Van Steeg et al. (2016).

Furthermore, a notable decrease in the measured roughness factor, is observed for both tested armour spacings compared to impermeable core results. For a 10% spacing, a relative decrease of 8% is noted, diminishing to 3% for a 20% spacing. This reduction could be due to increased permeability allowing water infiltration into the slope and reducing run-up, or it may be influenced by measurement methodology, where water flow over the crest introduces infiltration possibilities.

Additionally, when determining the roughness factor based on a wider range for the breaker parameter, increasing reliability, incorporating both s_{0p}=0.02 and 0.04 ($3 < \xi_{m-1,0} < 5$), and comparing it to result for s_{0p}=0.04 ($\xi \approx 3$), the relative roughness factor increase equates to 4% and 2% for 10% and 20% armour spacing respectively. A higher roughness factor suggests an increase in relative overtopping. This observation confirms the tendency for the roughness factor to exhibit a slight inclination for larger wave periods, resulting in higher levels of overtopping.

Derived roughness factors for Coastalock on an impermeable and permeable slopes are presented in Table 7.1.

Reflection

The permeable core consistently exhibits lower reflection coefficients compared to the impermeable core, demonstrating greater dampening of incoming wave energy, particularly noticeable with increasing armour spacing. As larger spacings expose more of the underlayer to wave penetration, the dampening effect becomes more pronounced. Deep-water wave steepness plays an even larger role, with an increase resulting in significantly lower reflection coefficients.

$$C_{r,CL} = 0.25 + 2.01 \cdot C_{r,Muttray} - 0.31 \cdot S + d, \text{ with: } \begin{cases} d = 0.00 & \text{for impermeable core} \\ d = 0.05 & \text{for permeable core} \end{cases} \tag{7.1}$$

Drawing from Molenkamp's (2022) methodology, Equation 7.1 is presented as a model for reflection coefficients. This equation is based on reanalyzed data from the impermeable core, incorporating considerations of armour spacing (S) and wave steepness for the 'San Diego' configuration. In contrast to Van der Meer's (1992) methodology, this approach is favored for its better alignment with observed data and theoretical insights. Furthermore, it incorporates wave steepness using the approach outlined by Muttray et al. (2006), deemed most suitable for breakwater structures. Notably, the equation is includes a parameter to accommodate the influence of the permeable core on the reflection coefficient.

7.4. Effect of a protrusions on stability, overtopping and reflection

Stability

In the context of $s_{0p} = 0.04$, the inclusion of short protrusions leads to a decrease in the stability number threshold for 'breathing' under identical armour spacing conditions of 10%, from N_s=3.59 to 3.16, while maintaining a comparable extraction threshold. This reduction is attributed to the reduced inter-unit void size resulting from the blockage caused by short protrusions, leading to larger pore pressure gradients across the top layer. The maximum elevation change of armour units remained well below $0.10D_{n,CL}$, reaching 0.17 only after the occurrence of 'breathing' at $N_s = 3.16$. The observed damage progression aligns with the typical behavior of single-layer interlocking armour units, characterized by slight movement with increasing wave height followed by sudden failure. In contrast, no instances of 'breathing' or extraction were observed for long protrusions with 22.5% spacing. These protrusions effectively prevented filter layer migration observed at 20% spacing without protrusions. Although no significant elevation change was noted until a stability number of 3.86, the maximum recorded value, equating to $0.15D_{n,CL}$, at N_s=4.19, suggests that the armour layer was nearing its stability limit for 'breathing' and potential extraction compared to the elevation change after 'breathing' for short

protrusions. This highlights the capability of the SfM technique for identifying pressure-induced movement of small-scale armour units after wave attack.

For s_{0p}=0.02, no instances of 'breathing' or extraction were observed for both protrusion types. At 10% spacing, N_s = 3.93 was reached. However, since no 'breathing' or failure was observed in either test series, it remains unclear to what extent stability improved for long waves. Nonetheless, it can be concluded that Coastalocks with protrusions also benefit from the 'reservoir effect' (H. F. Burcharth et al., 1998).

Overtopping

The inclusion of protrusions in the 'Protrusion Optimized' configuration, accompanied by an orientation change at SWL, resulted in a 5.8% rise in the roughness factor compared to the 10% spacing in the 'San Diego' configuration. This enhancement is primarily ascribed to modifications in the roughness profile induced by the protrusions, along with the obstructed voids, consequently leading to increased overtopping in line with the theoretical framework outlined by Van Steeg et al. (2016). Furthermore, the transition from cavity sideways to downward orientation could contributed to this increase. In comparing the 22.5% protrusion configuration to the 20% spacing, the marginal enlargement in inter-unit void size was counterbalanced by the introduction of protrusions and the orientation shift. The roughness coefficients based on s_{0p}=0.04 and the wide-range roughness factors are also presented in Table 7.1.

Spacing	Core	Configuration	$\gamma_{f,CL,wide}$	$\gamma_{f,CL,s_{0p}=0.04}$
S-10%	Impermeable	'San Diego'	0.76	0.75
S-10%	Permeable	'San Diego'	0.72	0.69
P-10%	Permeable	'PO-SWL'	0.71	0.65
S-20%	Permeable	'San Diego'	0.66	0.65
P-22.5%	Permeable	'PO-SWL'	0.67	0.65

Table 7.1: Comparison of roughness factors for the EuroTop equation (2018) derived from Coastalock model testing with simple spacing (S) or protrusions (P) in varying configurations on a slope with permeable core, for $3 < \xi_{m-1,0} < 5$ to s_{0p}=0.04 ($\xi_{m-1,0} \approx 3$).

It has to be stated that the accuracy of the fit varies strongly across the test series. Investigating alternative methodologies could enhance the precision of forecasting overtopping discharge for a Coastalock armour layer.

Reflection

The combined implementation of protrusions along with the configuration change from 'San Diego' to 'PO-SWL' notably amplifies reflection. This increase is attributed to both the increased surface area available for reflection facilitated by the protrusions and the obstruction of inter-unit voids, leading to a reduction in the permeability of the armour layer and diminishing internal dampening within the core of the structure. Nonetheless, it's essential to note that wave steepness remained the predominant governing factor.

7.5. Effect of armour unit orientation on the stability, overtopping and reflection

Stability

Lowering the orientation change from cavity upwards to downwards from SWL to the midpoint between SWL and the bottom row increased the 'breathing' threshold from N_s =3.16 to 3.52 and the extraction threshold from N_s =3.58 to 3.76. The increase was even more pronounced with all units turned upwards, where the 'breathing' threshold remained at N_s=3.52 but no extraction occurred. Additionally, a downward shift in the damage location along the slope was observed. When expressing the extraction location in terms of the rundown level, this corresponds to $R_{d,f}/H_s$ values of -1.3 for both the 'PO-Midpoint' and the 'Upwards' configuration, aligning with the critical loading location for placed block revetments, as approximated by $R_{d2\%}/H_s$=-1.5 (CIRIA, 2007). The $R_{d,f}/H_s$ remained at -0.7 for the 'PO-SWL' configuration. It can be concluded that the presence and positioning of the

orientation change negatively affect the stability of the armour layer during wave attack. The potential cause for this effect is attributed to the buoyancy disparity resulting from cavity placement between different orientations. Overall, the study highlights the importance of orientation changes in Coastalock stability.

Overtopping
The observed increase in the roughness coefficient for both the 'PO-Midpoint' and 'Upwards' configurations contradicts expectations of increased overtopping and decreased roughness. Relatively 3.1% higher compared roughness coefficients have been found, compared to the 'PO-SWL' configuration, indicating a smoothing of the slope. This discrepancy suggests that upwards-facing units may trap water during wave run-down, altering slope roughness and potentially leading to smoother slopes and higher roughness coefficients. The similarity between the 'PO-Midpoint' and 'Upwards' configurations roughness factors, indicate that the lower part of the slope has less impact on overtopping characteristics.

Reflection
The comparison between configurations initially showed a 2% relative decrease in the reflection coefficient when transitioning from the 'PO-SWL' to the 'PO-Midpoint', as anticipated. This expectation stemmed from the assumption that fewer units facing incoming waves with a smooth surface would introduce more micro-irregularities, thereby reducing reflection. However, the unexpected increase of 2% observed in the 'Upwards' configuration mirrored findings from Molenkamp's study on impermeable core armour layer configurations. This increase was attributed to the phenomenon of water retention in upwards-facing cavities, impacting energy dissipation and reflection coefficients when cavities are oriented downward or to the side.

7.6. Effect of the introduction of a toe berm of damage progression

The presence of toe berms, regardless of surface roughness, showed no significant impact on the damage progression, location, or primary failure mechanisms of Coastalock armour layers, regardless of protrusion length and spacing. This implies that toe berms may not substantially enhance stability for Coastalock structures in deep water conditions. The absence of toe berm-related failures such as sliding suggests that current design configurations, particularly the 'PO-SWL' orientation, demonstrate robust stability even with loose rock toe berms. Additionally, no downslope movement of the 3rd row of Coastalock or a grid-based selection of armour units throughout the slope larger than $0.07D_{n,CL}$, well below the threshold of $0.20D_{n,CL}$ possibly indicative of near extraction (Hofland and van Gent, 2016). Nevertheless, broader research under various conditions, especially in relatively shallower waters typical for coastal structures, is needed to validate these findings conclusively.

8

Recommendations

The final chapter of this thesis aims to provide valuable recommendations for both current and future testing programs related to Coastalock characteristics, as well as to propose avenues for further Coastalock development.

8.1. Recommendations for current testing program

In light of the discussions presented in Section 6, several recommendations can be made regarding the physical model testing program conducted in this study.

Testing increments

The deliberate selection of large increments of significant wave height and wave steepness was made due to the unexplored nature of Coastalock behavior within breakwater structures, especially in the presence of toe and protrusions. While this approach facilitated the completion of the testing program within a constrained time frame, it resulted in a loss of detail and limited comparison materials for analysis, thereby restricting the depth of understanding of Coastalock behavior. It is recommended to repeat the current testing program, while decreasing the increments of both significant wave height and wave steepness in future testing, thereby increasing the size of test series to enhance the understanding of Coastalock behavior within breakwater structures, be it in terms of stability, overtopping or reflection.

Core permeability

In the absence of an existing prototype, a core prototype size was chosen to be half of the underlayer size. with a wide grading. A steeper grading would have been more suitable, as a more uniform rock diameter would reduce the probability of scale effects due to permeability issues arising from the presence of smaller or larger stones in the grading. Besides, tests were only conducted on a single permeable core. It is recommended to explore the effect of different core sizes to understand the impact of core permeability variability on Coastalock hydraulic performance and the potential for scale effects.

Accuracy of SfM methodology

Improvements in the SfM methodology can be achieved through several key factors, particularly in terms of input quality and process optimization:

1. Enhancing image quality is essential for improving the accuracy of the SfM process. This can be accomplished by using cameras with higher pixel counts, reducing ISO settings, employing tripods for stable shots, and optimizing lighting conditions to capture clearer images, while maintaining constant overlap.
2. While lasers were utilized for the geo-location of GCPs, employing a total station could further enhance accuracy and yield superior results.

3. The challenges encountered in GCP detection underscore the importance of thorough on-site verification processes. Conducting on-site checks for GCP detection can help identify and address issues promptly.
4. It is recommended to conduct further research on the dedicated application of photogrammetry for small-scale physical model testing to optimize its efficacy.
5. Automation through advanced algorithms like MatchTemplate from OpenCV holds significant potential for enhancing the SfM methodology. These algorithms could facilitate comprehensive 3D tracking of all armour units within Dense Point Clouds, leading to more robust analysis and a deeper understanding of armour unit behavior. Moreover, introducing a new set of model units in various high-contrast colors could optimize detection during processing.

Overtopping
To enhance the reliability of overtopping predictions, it is advisable to refine the measuring method to discern smaller quantities of overtopping volume. This could be achieved through techniques such as weighing. furthermore, exploring alternative methodologies has the potential to improve the accuracy of predicting overtopping discharge for a Coastalock armour layer, thus optimizing its design.

8.2. Recommendations for future testing programs

Besides several key aspects already presented in Section 6.1.3, concerning the effect of a foreshore in relatively shallow water, oblique and short crested waves and bio-growth, suitable for further Coastalock testing, several other recommendations are made here.

Effect of armour layer orientation
Based on the observations presented in this thesis, it is clear that the orientation of the armour layer, along with the placement of any orientation changes, can significantly influence its stability, overtopping, and reflection characteristics. Therefore, it is recommended to conduct a testing program that systematically quantifies the effects of each orientation individually and in combination with others, in along shore direction. Furthermore, exploring orientation changes in the cross-shore direction could enhance habitat creation flexibility by introducing more variation.

Filter layer
Inadequate attention to filter criteria may lead to the erosion of the filter layer, jeopardizing the stability of the structure. Despite the presence of protrusions, filter material extraction through gaps in the armour layer can occur if poorly designed. Therefore, it is advisable to optimize spacing size, protrusion size, and shape while adhering to traditional filter criteria. Achieving the optimal balance among these factors is essential to ensure the effectiveness and stability of Coastalock armour layers. Systematic exploration of various combinations can help identify configurations with optimal performance in terms of stability and resistance to pressure-induced failure. Conducting research on optimizing the underlayer beneath Coastalock armour units is thus highly recommended.

Crest
It is recommended to conduct tests to assess the performance of Coastalock armour units when used as crest elements, under both low- and high-crested waves. Notably, in the studies available at the time of writing, no crest made of Coastalock was constructed in the physical model tests. Crest elements may experience reduced stability due to the diminished weight from blocks being absent above them. A separate crest designs could be considered to address this potential stability issue.

Toe support
During testing, it was observed that arranging the first row and subsequent rows in a proper configuration to mitigate issues during the construction of higher rows was challenging and time-consuming. This difficulty arises from the unique shape of the armour units and their interlocking mechanism. While placement by hand in a dry flume is feasible, real-life applications often involve underwater placement under sub-optimal conditions. It is recommended to investigate and develop adequate placement techniques or consider the design of dedicated bottom row units for the Coastalock armour layer.

Pressure-induced failure mechanism
Further investigation into pressure-induced failure mechanisms in single-layer concrete armour units, like Coastalock, is warranted given the lack of comprehensive theoretical frameworks addressing this phenomenon. While leakage length has been commonly used, with varying degree of success, to explain pressure-induced behavior on both impermeable and permeable cores, it does not fully account for all variables at play due to simplifications or the influence of core permeability and the associated energy dissipation within the core. Future research endeavors should prioritize the development of refined models that incorporate the interactions among armour, filter layer, and core permeability, alongside factors such as pressure gradients and energy dissipation. To achieve this, conducting tests to measure underlying pressures within the armour layer, underlayer, and/or core is crucial for gaining a comprehensive understanding of the phenomenon and facilitating the development of accurate predictive formulations. This research can not only benefit the design and performance evaluation of Coastalock, once accurate, but also potentially inform the design and analysis of single-layer concrete regularly placed armour units or placed block revetments in general.

8.3. Recommendations for further Coastalock development

The findings of this thesis provide valuable insights and recommendations for the continued development of the Coastalock armour unit.

Incorporating rudimentary shaped protrusions into the design of the units, as suggested in the work of Molenkamp (2022), offered a promising avenue for optimization. Two types of protrusions were tested: short protrusions with 10% spacing and long protrusions with 22.5% spacing, representing possible next steps in Coastalock design.

Despite the reduction in contact area compromising interlocking and friction-based stability, the mitigation of pressure impact by enhancing permeability and ensuring separation between layers proved beneficial. Both protrusion types resulted in increased stability, mitigating 'breathing' and extraction phenomena, with the long protrusions showing superior performance. Further development should focus on designs with larger protrusion spacings, such as the 22.5% protrusion type, which exhibited enhanced stability without signs of 'breathing' or extraction up to stability numbers of N_s = 4.2. However, maximum armour layer movement observed during testing may indicate proximity to failure, warranting further investigation. No significant changes in armour layer elevation were observed for N_s=3.9. Typically, under design conditions, single-layer concrete armour units should exhibit no damage and only minor movement in overload conditions. Considering a safety factor of 1.5 for overload conditions and the brittle nature of failure, a recommended design stability number of N_s = 2.6 is suggested, for surging waves in deep water conditions. The long protrusion design also demonstrated superior overtopping reduction capabilities compared to short protrusions, while both types showed similar reflection coefficients.

In addition to the improved stability, there is a simultaneous reduction in the number of blocks required per unit area of slope. Comparing the scaled packing density, ϕ, and the number of armour units needed per unit area of slope, N, based on the area used for the SfM methodology across all test series, while considering only entire units, the armor unit with 10% protrusions exhibited values of N=0.59 and ϕ=0.47, whereas the design with 22.5% protrusions shows values of N=0.53 and ϕ=0.42. This indicates that the 22.5% protrusion results in a reduction of about 11% in the number of armour units required on the slope. This reduction not only significantly decreases concrete consumption but also shortens project duration by reducing the number of units needing to be placed, thereby reducing emissions and construction costs.

The high stability of designs with larger spacing protrusions facilitates the introduction of orientation changes for habitat creation purposes, without compromise of performance. However, it is recommended to reassess the design of the Coastalock armour unit to ensure that the introduction of protrusions does not compromise its ecological flexibility. Currently, the protrusions in one of the three configurations render it unsuitable for supporting marine life, thereby limiting its potential for habitat creation. Exploring adjustments to protrusion shape or placement to maintain habitat features while enhancing hydraulic performance is recommended. Further research into different design concepts accounting for the potential impact of channel orientation on hydraulic performance and permeability is also

advised.

Bibliography

Agisoft. (2023). *Agisoft metashape user manual: Professional edition, version 2.1* [Copyright © 2023 Agisoft LLC].

Bakkenes, H. (2002). *Observation and separation of bound and free low-frequency waves in the nearshore zone* [Master's thesis, Delft University of Technology].

Bakker, P., Berge, A., Hakenberg, R., Klabbers, M., Muttray, M., Reedijk, B., Vos-Rovers, I., Delta, A., & Consultants, M. (2003). Development of concrete breakwater armour units. *Proceedings, Annual Conference - Canadian Society for Civil Engineering*, *2003*.

Bakker, P., Jacobs, R., van de Koppel, M., Reedijk, B., & Muttray, M. (2019). Hydraulic stability and practical application of xblocplus breakwater armouring. In N. Goseberg & T. Schlurmann (Eds.), *Coastal structures 2019* (p. 98). Bundesanstalt für Wasserbau. https://doi.org/10.18451/978-3-939230-64-9_011

Barends, F., & Hölscher, P. (1988). 4. modelling interior process in a breakwater. *Design of Breakwater, Proc. of the Conf.: Breakwater '88*, pp. 49–80. https://doi.org/10.1680/dob.13513.0005

Batjes, J. (1974). *Computation of set-up, longshore currents, rum-up and overtopping due to wind-generated waves* [Doctoral dissertation, Delft University of Technology].

Van den Berg, I., Hofland, B., & Reedijk, B. (2020). Influence of irregularities in the rock underlayer on the stability of xblocplus. *Coastal Engineering*, *157*, 103637. https://doi.org/https://doi.org/10.1016/j.coastaleng.2020.103637

Betlem, P., & Rodes, N. (2024). *Geo-sfm: Teaching multiview stereo structure-from-motion photogrammetry*. The University Centre in Svalbard. https://unisvalbard.github.io/Geo-SfM/landing-page.html#

Brebner, A., & Donnelly, P. (1962). Laboratory study of rubble foundations for vertical breakwaters. *Coastal Engineering Proceedings*, *1*(8), 24. https://doi.org/10.9753/icce.v8.24

Broos, J.-W. (2019). *Stability of the first row of an xblocplus armour layer: A physical model study using digital displacement analysis* [Master's thesis, Delft University of Technology].

Burcharth, H. F. (1993). The design of breakwaters. In M. B. Abbott & W. A. Price (Eds.), *Chapter 28, coastal and harbour engineering reference book*. E & FN SPON, UK.

Burcharth, H. F., Christensen, M., Jensen, T., & Frigaard, P. (1998). Influence of core permeability on accropode armour layer stability. In N. W. H. Allsop (Ed.). Thomas Telford.

Burcharth, H. F., Liu, Z., & Troch, P. (1999). Scaling of core material in rubble mound breakwater model tests. In G. P. Mocke (Ed.). COPEDEC.

Burcharth, H., Andersen, T., & Medina, J. (2011). Stability of cubipod armoured roundheads in short-crested waves. a comparison between cubipod and cube armour stability. *Proceedings of the International Conference on Coastal Engineering; No 32 (2010): Proceedings of 32nd Conference on Coastal Engineering, Shanghai, China, 2010.; structures.39*, *1*. https://doi.org/10.9753/icce.v32.structures.39

Burcharth, H. F., & Liu, Z. (1992). Design of dolos armour units. *Coastal Engineering Proceedings*, *1*(23). https://doi.org/10.9753/icce.v23.%p

Burcharth, H. (1992). *Reliability evaluation of structures at sea* (tech. rep.) (Proc. Of the Short Course on Design and Reliability of Coastal Structures, Venice 1992). Italy, Tecnoprint Bologna.

Chapman, M., & Underwood, A. (2011). Evaluation of ecological engineering of "armoured" shorelines to improve their value as habitat. *Journal of Experimental Marine Biology and Ecology - J EXP MAR BIOL ECOL*, *400*, 302–313. https://doi.org/10.1016/j.jembe.2011.02.025

CIRIA. (2007). *The rock manual: The use of rock in hydraulic engineering*.

CloudCompare. (2022). *Cloudcompare (version 2.6.1) user manual*. GPL software. http://www.cloudcompare.org/

Cooke, S. J., Bergman, J. N., Nyboer, E. A., Reid, A. J., Gallagher, A. J., Hammerschlag, N., Van de Riet, K., & Vermaire, J. C. (2020). Overcoming the concrete conquest of aquatic ecosystems. *Biological Conservation*, *247*, 108589. https://doi.org/10.1016/j.biocon.2020.108589

Delta Marine Consultants. (2023). *Xbloc and xblocplus design guidelines 2023*. Retrieved March 24, 2023, from https://www.xbloc.com/design

Docters van Leeuwen, L. (1996). *Toe stability of rubble-mound breakwaters* [Master's thesis, Delft University of Technology].

Dorst, K., Provoost, Y., & Verhagen, H. (2012). Stability of pattern placed revetment elements. *COPEDEC 2012: Proceedings of the 8th International Conference on Coastal and Port Engineering in Developing Countries*. http://resolver.tudelft.nl/uuid:84541e27-6382-4cb2-ae35-c5365aa7be90

Ebbens, R. (2009). *Toe structures of rubble mound breakwater: Stability in depth limited conditions* [Master's thesis, Delft University of Technology].

ECOncrete Tech Ltd. (2019). Coastalock: Technical product information.

ECOncrete Tech Ltd. (2023). Tide pool armor in the port of san diego: Fourth monitoring report | 26 months post deployment | may 15-18, 2023 [Internal report].

Firth, L., White, F., Schofield, M., Hanley, M., Burrows, M., Thompson, R., Skov, M., Evans, A., Moore, P., & Hawkins, S. (2015). Facing the future: The importance of substratum features for ecological engineering of artificial habitats in the rocky intertidal. *Marine and Freshwater Research*, *67*. https://doi.org/10.1071/MF14163

Frostick, L., McLelland, S., & Mercer, T. (2011). *Users guide to physical modelling and experimentation: Experience of the hydralab network*. CRC Press. https://doi.org/10.1201/b11335

Van Gent, M., Smale, A., & Kuiper, C. (2003). Stability of rock slopes with shallow foreshores. *Coastal Structures 2003 - Proceedings of the Conference*. https://doi.org/10.1061/40733(147)9

Van Gent, M., & Luis, L. (2013). Application of cubes in a single layer. *Proc. 6th SCAR-International Short Course/Conference on Applied Coastal Research*.

van Gent, M. R. (2014). Oblique wave attack on rubble mound breakwaters. *Coastal Engineering*, *88*, 43–54. https://doi.org/https://doi.org/10.1016/j.coastaleng.2014.02.002

Van Gent, M., & van der Werf, I. (2014). Toe stability of rubble mound breakwaters. *Coastal Engineering Proceedings*, *1*(34), structures.22. https://doi.org/10.9753/icce.v34.structures.22

van Gent, M. R., Wolters, G., & Capel, A. (2022). Wave overtopping discharges at rubble mound breakwaters including effects of a crest wall and a berm. *Coastal Engineering*, *176*, 104151. https://doi.org/https://doi.org/10.1016/j.coastaleng.2022.104151

Gerding, E. (1993). *Toe structure stability of rubble mound breakwaters* [Master's thesis, Deflt University of Technology].

Gier, F., Schuttrumpf, H., Mönnich, J., van der Meer, J., Kudella, M., & Rubin, H. (2012). Stability of interlocked pattern placed block revetments. *Coastal Engineering Proceedings*, *1*(33), structures.46. https://doi.org/10.9753/icce.v33.structures.46

Gittman, R., Fodrie, F., Popowich, A., Keller, D., Bruno, J., Currin, C., Peterson, C., & Piehler, M. (2015). Engineering away our natural defenses: An analysis of shoreline hardening in the us. *Frontiers in Ecology and the Environment*, *2015*, 301–307. https://doi.org/10.1890/150065

Glasby, T., Connell, S., Holloway, M., & Hewitt, C. (2007). Nonindigenous biota on artificial structures: Could habitat creation facilitate biological invasions? *Marine Biology*, *151*, 887–895. https://doi.org/10.1007/s00227-006-0552-5

Gutiérrez, J., Bezner, M., Molenkamp, A., Bos, J. v., Hofland, B., Leblanc, P., Rella, A., Rosenberg, Y., & Sella, I. (2023). Physical evaluation of the hydrodynamic stability of an eco-engineered armouring unit, papers.35. https://doi.org/10.9753/icce.v37.papers.35

Hald, T. (1998). *Wave induced loading and stability of rubble mound breakwaters* [Doctoral dissertation, Hydraulics & Coastal Engineering Laboratory, Department of Civil Engineering, Aalborg University].

Hofland, B., & van Gent, M. (2016). Automatic settlement analysis of single-layer armour layers. *Proceedings of the 6th International Conference on the Application of Physical Modelling in Coastal and Port Engineering and Science*. http://resolver.tudelft.nl/uuid:96ab0638-b62c-483e-b237-2c9ef83c7b8f

Hughes, S. (2005). Archimedes revisited: A faster, better, cheaper method of accurately measuring the volume of small objects. *Physics Education*, *40*. https://doi.org/10.1088/0031-9120/40/5/008

Hughes, S. A. (1993). *Physical models and laboratory techniques in coastal engineering*. WORLD SCIENTIFIC. https://doi.org/10.1142/2154

Irías Mata, M., & van Gent, M. R. (2023). Numerical modelling of wave overtopping discharges at rubble mound breakwaters using openfoam®. *Coastal Engineering*, *181*, 104274. https://doi.org/https://doi.org/10.1016/j.coastaleng.2022.104274

Klaasman, H. (2005). *Wave signal decomposition using matlab, the use of decomp.m in the tu delft wave flume* (Technical Report). TU Delft.

Klein Breteler, M., Mourik, G., & Bosters, M. (2014). Stabiliteit van steenzettingen bij golfaanval: Samenvatting onderzoeksresultaten 2003-2013. *1208045-016-HYE-0007 for RWS-WVL*.

Klein Breteler, M., Mourik, G., & Provoost, Y. (2014). Stability of placed block revetments in the wave run-up zone. *Coastal Engineering Proceedings*, *1*, 24. https://doi.org/10.9753/icce.v34.structures.24

Lam, N., Huang, R., & Chan, B. (2009). Variations in intertidal assemblages and zonation patterns between vertical artificial seawalls and natural rocky shores: A case study from victoria harbour, hong kong. *Zoological Studies*, *48*.

Mansard, E. P., & Funke, E. (1980). The measurement of incident and reflected spectra using a least squares method. In *Coastal engineering 1980* (pp. 154–172).

Van der Meer, J. (1988). *Rock slopes and gravel beaches under wave attack* [Doctoral dissertation, Delft University of Technology]. Delft Hydraulics Laboratory. http://resolver.tudelft.nl/uuid:67e5692c-0905-4ddd-8487-37fdda9af6b4

van der Meer, J. (1992). Conceptual design of rubble mound breakwaters. *Proc. of the Short Course on Design and Reliability of Coastal Structures*, 447–510.

Van der Meer, J. (1998). Chapter 9: Geometrical design of coastal structures. *Dikes and Revetments: Design, Maintenance and Safety Assessment*. https://doi.org/https://doi.org/10.1201/9781315141329

Van der Meer, J. (2002, May 1). *Technical report wave run-up and wave overtopping at dikes* (tech. rep.). Rijkswaterstaat. Rijkswaterstaat, DWW.

Van der Meer, J., Allsop, W., Bruce, T., Rouck, J., Kortenhaus, A., Pullen, T., Schüttrumpf, H., Troch, P., & Zanuttigh, B. (2018, January). *Eurotop: Manual on wave overtopping of sea defences and related sturctures - an overtopping manual largely based on european research, but for worlwide application (2nd edition)*.

Molenkamp, A. (2022). *Hydraulic performance of coastalock armour units* [Master's thesis, Deflt University of Technology].

Muttray, M. (2013). A pragmatic approach to rock toe stability. *Coastal Engineering*, *82*, 56–63. https://doi.org/10.1016/j.coastaleng.2013.08.002

Muttray, M., Oumeraci, H., & ten Oever, E. (2006). Wave reflection and wave run-up at rubble mound breakwaters. *Proceedings of the Coastal Engineering Conference*. https://doi.org/10.1142/9789812709554_0362

Muttray, M., Reedijk, B., Rover, R., & Zwicht, B. (2014). Investigations on quarry stone toe berm stability. *Coastal Engineering Proceedings*, *1*, 77. https://doi.org/10.9753/icce.v34.structures.77

Neumann, B., Vafeidis, A. T., Zimmermann, J., & Nicholls, R. J. (2015). Future coastal population growth and exposure to sea-level rise and coastal flooding - a global assessment. *PLOS ONE*, *10*(3), 1–34. https://doi.org/10.1371/journal.pone.0118571

OpenAI. (2022). OpenAI GPT [Accessed: 2023/2024].

Over, J. R., Ritchie, A. C., Kranenburg, C. J., Brown, J. A., Buscombe, D., Noble, T., Sherwood, C. R., Warrick, J. A., & Wernette, P. A. (2021). *Processing coastal imagery with agisoft metashape professional edition, version 1.6—structure from motion workflow documentation* (Open-File Report No. 2021–1039). U.S. Geological Survey. https://doi.org/10.3133/ofr20211039

PIANC-MarCom WG 196. (2016). Criteria for the selection of breakwater types and their related optimum safety levels. *196*.

Pilarczyk, K. (Ed.). (1998). *Dikes and revetments: Design, maintenance and safety assessment* (1st). Routledge. https://doi.org/10.1201/9781315141329

Pilarczyk, K. (2003). *Design of revetments*. Rijkswaterstaat, DWW. http://resolver.tudelft.nl/uuid:c5028d6d-54f5-4a6f-b425-8a1a1e6b2f02

Pilarczyk, K., Klein Breteler, M., & Bezuijen, A. (1995). Wave forces and structure response of placed block revetments on inclined structures. http://resolver.tudelft.nl/uuid:a34d8fc4-82e9-4b46-a889-cf4dfa1982ee

Pilkey, O. H., & Cooper, J. A. G. (2012). "alternative" shoreline erosion control devices: A review. In J. A. G. Cooper & O. H. Pilkey (Eds.), *Pitfalls of shoreline stabilization: Selected case studies* (pp. 187–214). Springer Netherlands. https://doi.org/10.1007/978-94-007-4123-2_12

Podgorski, K., Rychlik, I., & Machado, U. (2000). Exact distributions for apparent waves in irregular seas. *Ocean Engineering*, *27*, 979–1016.

Rada Mora, B. (2017). *Hydraulic performance of xbloc+ armor unit* [Master's thesis, Deflt University of Technology].

Reedijk, B., Eggeling, T., Bakker, P., Jacobs, R., & Muttray, M. (2018). Hydraulic stability and overtopping performance of a new type of regular placed armor unit. *Coastal Engineering Proceedings*, *1*(36), papers.111. https://doi.org/10.9753/icce.v36.papers.111

Reedijk, B., Muttray, M., Berge, A., & de Rover, R. (2008). Effect of core permeability on armour layer stability. https://doi.org/10.1142/9789814277426_0278

de Rouck, J., & Van Damme, L. (1996). Overall slope stability analysis of rubble mound breakwaters. *Coastal Engineering Proceedings*, *1*(25). https://doi.org/10.9753/icce.v25.%p

Sargent, C. (2022). *Museums of the north west photogrammetry hub: Building virtual 3d futures - creating 3d models with agisoft metashape*. University of Liverpool. https://www.liverpool.ac.uk/media/livacuk / victoriagalleryandmuseum / garstangmuseum / Guide , for , Agisoft , Metashape, - ,Museums,of,the,North,West,Photogrammetry,Hub.pdf

Schiereck, G., & Verhagen, H. (2019). *Introduction to bed, bank and shore protection: 2nd edition*. Delft Academic Press. http://resolver.tudelft.nl/uuid:df203dde-6cca-4375-85d2-8b2dbce613cb

Van Steeg, P., Klein Breteler, M., & Provoost, Y. (2016). Large-scale physical model tests to determine influence factor of roughness for wave run-up of channel shaped placed block revetments.

Vanneste, D., & Troch, P. (2014). A revision of the scaling method for core material in rubble-mound breakwaters. In *From sea to shore–meeting the challenges of the sea* (pp. 112–121). https://doi.org/10.1680/fsts.59757.012

Veladi, H., & Khodadadi, N. (2020). An experimental study on assessing the behavior of quay walls under the action of irregular waves using artificial neural network.

Verdegaal, I. (2013). *The influence of core permeability on the stability of interlocking, single layer armour units* [Master's thesis, Delft University of Technology].

Verhagen, H. J., Reedijk, B., & Muttray, M. (2007). The effect of foreshore slope on breakwater stability. In *Coastal engineering 2006: (in 5 volumes)* (pp. 4828–4840). World Scientific.

Vos, A. (2017). *Exploration into the mechanisms that govern the stability of an xbloc+ v1 armour unit* [Master's thesis, Deflt University of Technology].

De Waal, J. (1998). *Alternative open slope revetments, summarizing report a2.96.04* (Rep. No. H1930). Deltares (WL).

Wenneker, I., & Hofland, B. (2014). Optimal wave gauge spacing for separation of incoming and reflected waves. *Proc., 5th Int. Conf. Coastlab 14, Application of Physical Modelling to Port an Coastal Protection*.

Wolters, G., Van Gent, M., Hofland, B., & Wellens, P. (2014). Wave damping and permeability scaling in rubble mound breakwaters. *Proceedings to Coastlab*, *14*.

Zhou, Q.-Y., Park, J., & Koltun, V. (2018). Open3D: A modern library for 3D data processing. *arXiv:1801.09847*.

A

Hydraulic Aspects

The following Appendix contain information on hydraulic aspects as wave characteristics, waves breaking on a slope and the flow on a breakwater.

A.1. Wave characteristics

A wave, in a time record of the surface elevation, is defined as the surface elevation profile in between two consecutive downward crossings of the mean of surface elevations; the so called zero-crossing. The wave height is defined as the height of the crest relative to the prior through. The time it takes between the two downward zero-crossing is called the wave period.

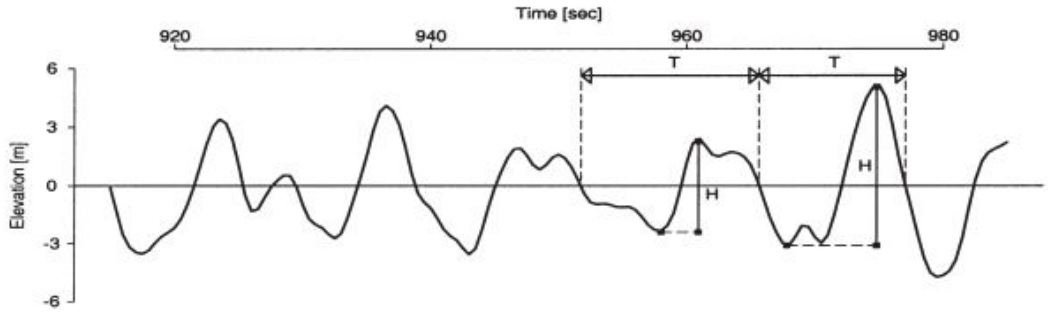

Figure A.1: Wave definition by zero-downcrossing method - heights H and periods T (Podgorski et al., 2000)

Irregular waves are generated by local turbulent wind. Such waves are characterized by their short crests and irregularity in height, shape and period. Linear wave theory has its limitation when describing the behaviour of such waves. An irregular wave field can be described by an energy-density spectrum; the energy distribution over the various wave frequencies. Only "fresh" sea state or wind-generated waves are considered in this report, as these prove to be the most crucial wave type with regards to breakwater stability. For typical wind-sea conditions a JONSWAP spectrum is used, a spectrum representing a still developing sea state.

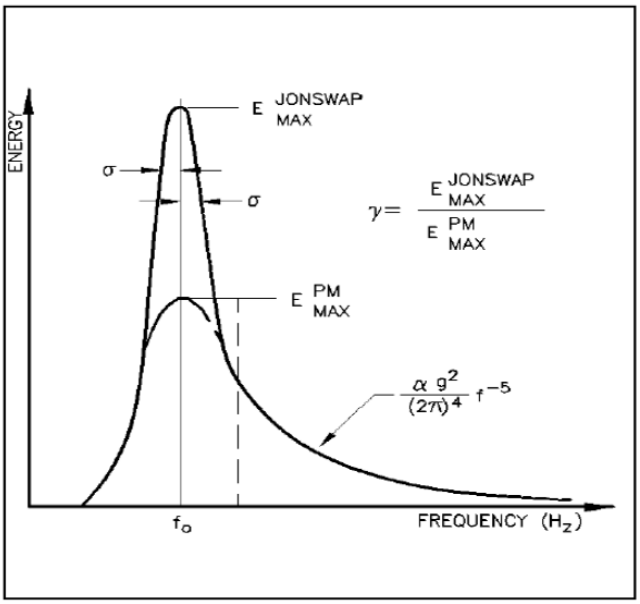

Figure A.2: Comparison of the JONSWAP and Pierson Moskowitz (Veladi and Khodadadi, 2020)

A fully developed sea state, which is not limited by fetch distance of the wind or the water depth, can be described by a Pierson-Moskowitz spectrum. The Pierson-Moskowitz spectrum equals the JONSWAP spectrum via multiplication with a peak enhancement factor, γ, generally taken equal to 3.3.

Wave height
The incoming wave field is commonly characterized by the significant wave height H_s, defined as the average height of the highest one-third of waves in a time series. While traditional methods relied on visual estimations, modern spectral analysis techniques provide a more accurate determination of the significant wave height, expressed as H_{m_0}, which is obtained by integrating the energy density spectrum.

Wave period
Widely used measures for the characteristic wave period are the so-called mean period, T_m, or peak period, T_p or T_{0_p}, for the wave periods corresponding to the mean or the peak of the spectrum.

Wave length
In general, the wavelength of an irregular wave is not well-defined as it varies with time and location along the wave profile. However, for irregular waves, the spectral peak period T_{0_p} is often used as an approximation of the dominant wavelength. Therefore, for irregular waves, the peak period is often used as a parameter to describe the wave conditions.

Wave steepness
The definition of wave steepness is given by the ratio of wave height over wavelength. The fictitious wave steepness is commonly used. Fictitious, as the ratio of the local wave height at the toe of the structure and deep-water wavelength, $L_0 = gT^2/2\pi$, are used. For fresh wind waves values between 0.04 up to 0.06 are representative of the wave steepness. For swell, much smaller values are found, as low as 0.01 (Van der Meer et al., 2018). It has to be noted that sea waves also can become low steepness waves when breaking occurs on a gentle foreshore.

Water depth in front of structure
The water level at the base of a breakwater is important because it determines what type of loading is exerted on what part of the structure.

A.2. Wave breaking on a slope

When waves reach a structure, they break. The Iribarren number, a surf similarity parameter introduced by Battjes (1974), is an important hydraulic factor for understanding the type of wave breaking and the subsequent wave run-up and run-down on the slope. For regular waves, the parameter can be written as:

$$\zeta = \frac{tan\alpha}{s_0} = \frac{tan\alpha}{\sqrt{H/L_0}} \tag{A.1}$$

where it represent the ratio between the slope steepness, α, and a fictitious wave steepness, s_0. The influence of the wave period on breaking is exerted by the presence of the wave length in deep water.

For irregular waves a similar formulation holds:

$$\zeta_{0p} = \frac{tan\alpha}{\sqrt{s_0}} = \frac{tan\alpha}{\sqrt{H_s/L_{0p}}} = \frac{tan\alpha}{\sqrt{\frac{2\pi}{g}\frac{H_s}{T_p^2}}} \tag{A.2}$$

As a result of instabilities of the wave profile, the wave can no longer exist. A wave breaks when it becomes too steep, the water becomes to shallow, or a combination of both. The different types of wave breaking, such as spilling, plunging, and surging, are classified based on the values of the Iribarren number. A transition zone exists between non-breaking and breaking waves, where the waves may break or not depending on various factors for values of ζ around 2.5 - 3 (Schiereck and Verhagen, 2019). The values for each breaker type found in Figure A.3 are typical but not definitive, and the transition between the types is gradual rather than abrupt."

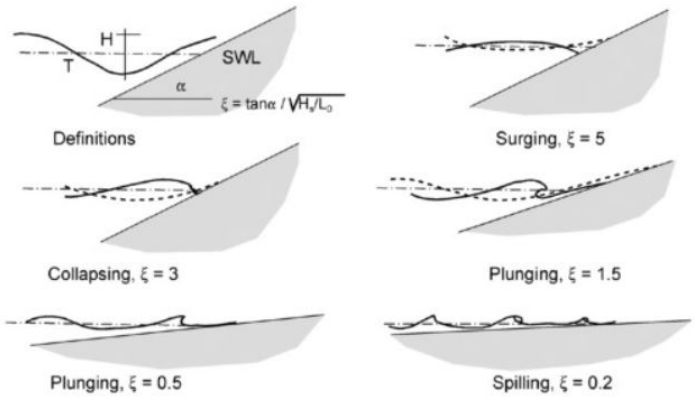

Figure A.3: Breaker types of waves on slopes (Schiereck and Verhagen, 2019)

A.3. Flow on a breakwater

After breaking the water moves up and down the slope resulting in wave run-up and run-down.

Wave run-up

Wave run-up is the phenomenon where the crest of an incoming wave moves up along the slope and oscillates over a vertical range higher than the original wave crest level. The maximum height reached by the wave during a single period is called the run-up height (R_u). When waves exceed the crest level of the structure, they may also overtop the breakwater.

Wave run-down

Similarly, wave run-down (denoted as R_d) is defined as the minimum water level on a slope during a wave period, relative to the still water elevation.

B

Stability, a balance of loads and forces

The equilibrium of forces acting on a rock under wave attack, is somewhat comparable to an armour unit placed on a slope, despite the fact that they differ in magnitude. The forces can be divided between those that stabilize or those that destabilize the armour unit. An individual armour unit stays immobile as long as the summation of forces in every direction and moments are equal to zero.

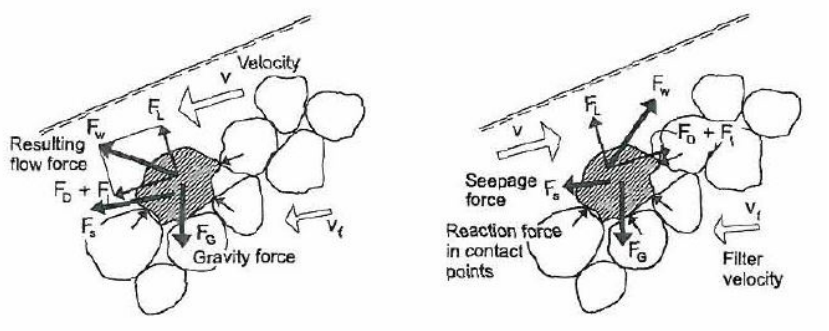

Figure B.1: Forces on a rock during up- and downrush (Hald, 1998)

B.1. Stabilizing forces

The stabilizing forces on a single layer interlocking armour unit in a rubble mound structure are:

- The gravity force, F_G, acting on the self weight of the block, is always present and is constant in direction. The contribution to the stability depends on the slope angle the armour unit is situated on and if the unit is partially or fully submerged. Water can cause buoyant forces in that case, resulting in less stabilization.
- The friction force can be divided in to two. First the wall friction between the single armour units, indicated by $F_{R,S}$. The wall friction forces are a major contributing factor to the stability of placed block revetments, but are expected to be of less significance to rubble mound structures (Schiereck and Verhagen, 2019). Second the friction force between the block and the sub layer, $F_{R,B}$, parallel to the slope, but in opposite direction to the wave force.
- The interlocking capabilities of the armour unit are represented by the interlocking force, F_C. The weight of the surrounding blocks, transferred through the contact points, contributes to the stabilizing forces keeping the armour unit from moving.

Simple force balance model are insufficient when trying to predict interlocking behaviour of complex shaped armour units. The contribution to the total stability of all three depends on the slope angle of the structure, as can bee seen in Figure B.2. It is recommended to investigate the increase in stability

due to interlocking by performing large scale physical tests. Results of small scale tests may be disputed due to model effects associated to processes in the subsoil (Gier et al., 2012).

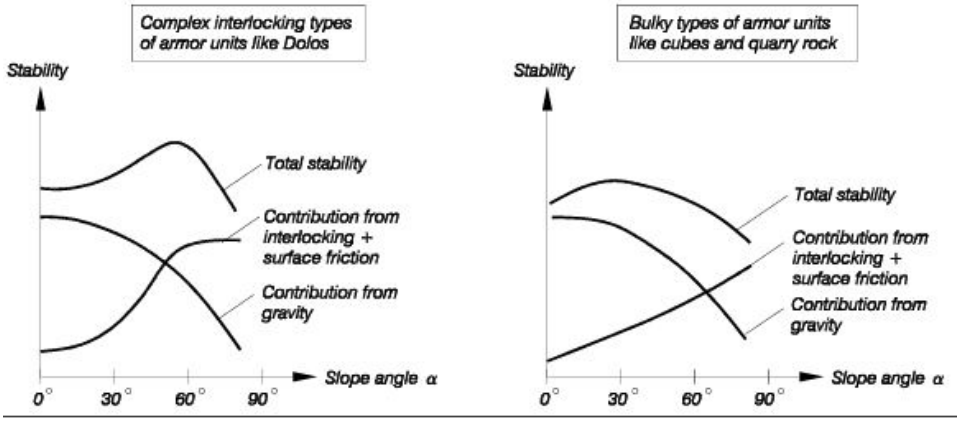

Figure B.2: Influence of slope angle on the stabilizing effects of the gravitational force, surface friction and interlocking (H. F. Burcharth and Liu, 1992)

B.2. Destabilizing forces

Water flowing up and down the slope during wave attack, exerts forces when moving over and around the armour unit, or mobilizes forces coming from within the structure. It can be divided into the following:

- The drag force, F_D, due to the flow of water around the rock depends on the flow direction. The flow works parallel to the slope in downward direction during downrush and parallel to the slope in upward during uprush. It is described by:

$$F_D \approx C_D \rho_w A v|v| \tag{B.1}$$

- The lift force, F_L, caused by the curvature of the flow around the armour unit:

$$F_L \approx C_L \rho_w A v|v| \tag{B.2}$$

- The inertia force, F_I, caused by the resistance to velocity changes of the moving water:

$$F_I \approx C_M \rho_w V \frac{dv}{dt} \tag{B.3}$$

Where the factors C_D, C_L, C_I, are the corresponding drag, lift and inertia coefficient. Their values depend on stone shape, Reynolds number, Re, and Keulegan-Carpenter number, KC. The cross sectional area at right angles to the mean velocity of the water and the armour unit volume are depicted as A and V.

- Hydrostatic pressure buildup, F_p:

$$F_p \approx \frac{V}{1-n} \frac{\delta p}{\delta x} \tag{B.4}$$

- The internal flow force, F_f:

$$F_f \approx \rho_w g \frac{V}{1-n} i \tag{B.5}$$

$$i = C_a v_f + C_b v_f |v_f| + C_c \frac{\delta v_f}{\delta t} \tag{B.6}$$

where:

$\frac{\delta p}{\delta x}$	:	Pressure gradient
n	:	Porosity of core material
V	:	Volume of armour unit
i	:	Hydraulic pressure gradient
v_f	:	velocity of water outflow
C_a, C_b, C_c	:	Viscous, drag and inertia force coefficients.

The hydrostatic pressure combined with the internal flow out of the structure exerts a seepage force on the armour unit, F_s, that contributes to the total normal force. The seepage force is governed by the permeability. High hydrostatic pressures build up when the permeability is low. The resulting internal flow force is small since only small water level fluctuations are allowed inside the structure. The reversed is true for cases with high permeability, as the internal water level tends to follow the up and down rush on the slope. The importance of the seepage force on the stability is unresolved. The seepage force may be responsible for the initiation of movement by lifting (Hald, 1998).

C

Toe structures for rubble mound breakwater

Appendix C provides details on toe design, pertinent failure modes, and various approaches to toe stability.

C.1. Toe design

When designing the toe of a breakwater, it's crucial to consider the combination of design wave heights and water levels and deduce the loading conditions that will govern the structure's performance. The Rock Manual (2007) provides a subdivision for the design of toe structures of rock rubble mound breakwaters based on the governing water depth and subsoil conditions. However, variations in design occur when structures are placed in very shallow or deep water or when the subsoil is sand versus rock. In relatively deep water conditions where the subsoil is sand, a smaller stone size is often used in the toe to support the main armor. In very deep water conditions, the toe is usually raised above the seabed, resulting in a high toe. In contrast, in shallow water, the required rock diameter of the toe increases with increased wave attack. Wave breaking on the structure may require the armor layer to be extended to the bottom, and in extreme cases, placing the armor layer in a dredged trench may be necessary for additional support.

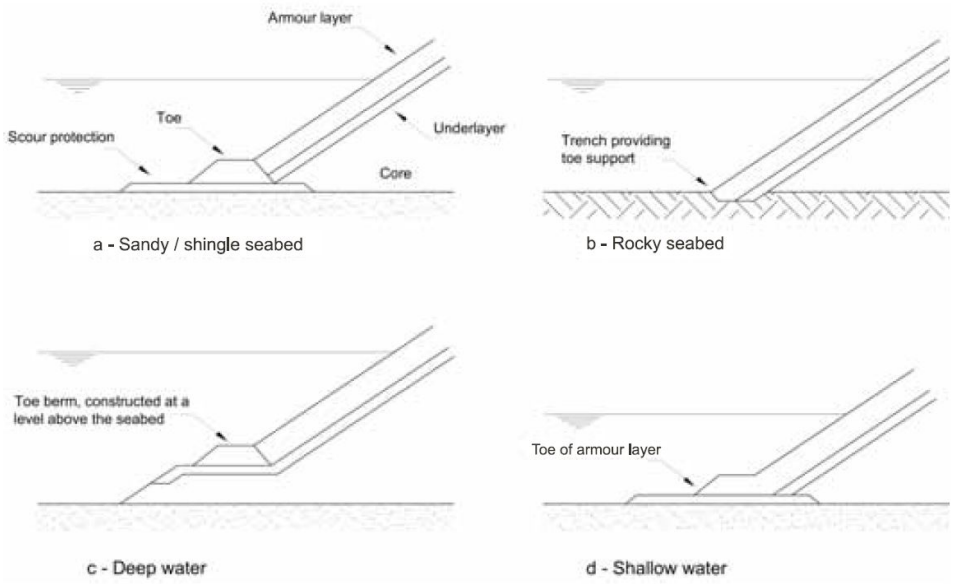

Figure C.1: Typical toe design for rock rubble mound breakwaters (CIRIA, 2007)

Furthermore, the placement of the toe berm on a foundation layer has been observed to enhance stability, primarily due to increase in friction and degree of interlocking of toe berm rocks with the foundation layer, as has been observed by Broos (2019), when testing the influence of a foundation layer on the stability of the first row of an XblocPlus armour layer. When designing the toe of a breakwater with a foreshore made of rocks, trench digging or driving piles into the rock may be required as the smooth texture provides little resistance against sliding of the toe structure.

For concrete armor units, the designs generally do not differ significantly, but it's important to note that the developer of the armor unit should provide specifications for each unit and design details. As CoastaLock has not been tested in a situation containing a toe structure, no specific guidelines are available yet.

C.2. Toe failure modes

Erosion of the toe berm leads to a compromise of its role in supporting the main armour, leading to subsequent failure and sliding of the armour layer.

C.3. Toe stability approaches

Over the years, there has been extensive research on the stability of breakwater toes, with many physical model tests investigating the key parameters that influence their hydraulic performance. This literature study on toe stability focuses specifically on research related to rubble mound breakwaters and their performance when subjected to irregular waves.

Van der Meer

The first formula, as proposed by Van der Meer (1998) is based on a reanalysis of the physical model tests performed by Gerding (1993), that have been validated by Docters van Leeuwen (1996). The work of Van der Meer has later been confirmed for depth limited conditions by Ebbens (2009), as it originally implied deep water conditions and breaking on the slope of the breakwater.

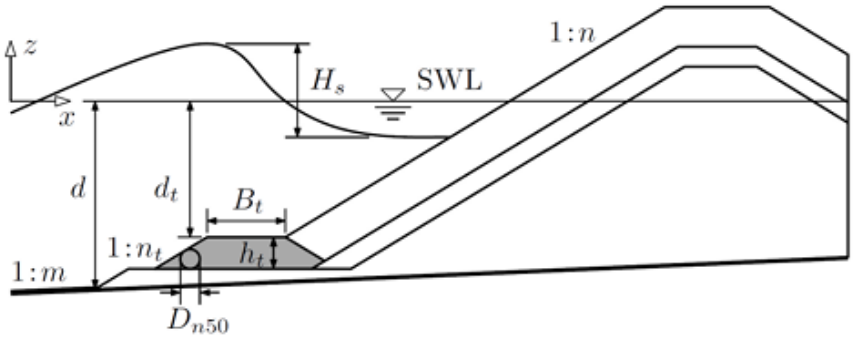

Figure C.2: Toe berm geometry definition (Muttray et al., 2014)

The original Van der Meer formula reads as follows:

$$\frac{H_s}{\Delta d_{n50}} = (6.2(\frac{d_t}{d})^{2.7} + 2)N_{od}^{0.15} \tag{C.1}$$

With d_t being defined as the depth of the toe berm and d as the the water depth in front of the structure. The approach is applicable in the ranges of $0.4 < \frac{h_t}{h_m} < 0.9$ and $3 < h_t/D_{n50} < 25$. It includes the stability number, indicating that the wave height and nominal armour unit diameter are linearly dependant in the case that the remaining parameters remain constant. The relative height of the toe berm, initially identified as a governing parameter for rock toe berm stability in front of vertical breakwaters by Brebner and Donnely (1962), is commonly denoted as the relative water depth, by the ratio d_t/d. Although submergence would lead to improved stability of a breakwater toe berm, it is not immediately clear why stability would decrease with increasing water depth. This would apply only in cases where the incoming waves are depth-limited. However, even then, the stability of the toe berm would be determined by the wave height rather than the water depth. Moreover, cases where no damage is accepted, would lead to a stability equal to zero.

Muttray
Muttray (2013) re-examined the experimental results by Gerding (1993) and Ebbens (2009) and developed an analytical framework to describe the primary processes that influence toe berm stability, in an Izbash type method, which was then empirically validated and adjusted as needed. The method has been compared to the Van der Meer (1998) formulation. This resulted in the following stability formula for foreshore slopes not steeper than 1:10, as these may lead to an overestimation of the stability:

$$\frac{H_s}{\Delta D_{n50}} = \frac{2.4N_{od}^{\frac{1}{3}}}{1.4 - 0.4\frac{d_t}{H_s}} \tag{C.2}$$

Besides, the formula is only applicable for: $d_t < 3H_s$. The formula shows a similar bias and larger scatter when compared to the Van der Meer equation; the conservative toe stability formula is founded in physics rather than plain curve fitting.

Van Gent and Van der Werf
The work of Van Gent and Van der Werf (2014) introduced a method for the prediction for the amount of damage to the toe, based on the characteristic near-bed velocity. The stability prediction is based on the deep water velocity estimate, independent of the depth at which the structure is situated; be it in deep or shallow water. More complex estimates of the characteristic velocity did not improve the results, hence they were omitted for sake of simplicity. The influence of the toe thickness, h_t, toe berm width, B_t, slope of the breakwater, slope roughness and berm armour type where also tested. The following

expression for the stability of the toe and characteristic near bed velocity are used:

$$\frac{H_s}{\Delta D_{n50}} = (0.032 \frac{h_t}{H_s} (\frac{B_t}{H_s}^{0.3}) \frac{\hat{u}_\delta}{\sqrt{gH_s}} N_{od})^{\frac{1}{3}} \tag{C.3}$$

with:

$$\hat{u}_\delta = \frac{\pi H_S}{T_{m-1,0}} \frac{1}{sinh(kd_t)} \tag{C.4}$$

and:

$$k = \frac{2\pi}{L_{m-1,0}} = \frac{2\pi}{\frac{g}{2\pi} T^2_{m-1,0}} \tag{C.5}$$

The use of the proposed formula is restricted to toe structures that comply to: $0.1d < h_t < 0.3d$, $1.2H_s < d < 4.5H_s$ and $n = 1.5 \vee 2$.

Muttray et al.
Muttray et al. (2014) verified all three above approaches concerning toe stability against model test results, to come up with guidelines for design. All three where capable to provide a more or less rough estimate of the required armour diameters and actual stability numbers. However, when used to predict damage to the toe structure, the results would be a mere indication at most, performing very poorly. It was concluded that the toe stability formulas suffered from a lack of accuracy and general validity. With the lack of accuracy referring to uncertainties between 30% and 60%. The lack of general validity, the main shortcoming of all three, referred to the inability to be used outside the experimental data set the formulae were based on, without significantly degrading the accuracy. This shortcoming is mainly due to interdependence between the two main parameters, the water depth above the toe and the wave height. The choice of wave model setup and test program is pointed to as possible culprit.

An empirical approach based on physically meaningful parameter combinations was performed to derive the following formula:

$$\frac{H_s}{\Delta D_{n50}} = (1.8 + \frac{d_t}{L_p} m) N_{od}^{\frac{1}{3}} = ((4n_t)^{\frac{1}{3}} + \frac{d_t}{L_p} m) N_{od}^{\frac{1}{3}} \tag{C.6}$$

for application with a minimum damage number of 0.25, foreshore slopes less than 1:50 ($m = 50$ if slope is more gentle), toe berms situated under water (no negative values of d_t. The right equations contains the toe berm slope, which provides increased stability when flattened out. No test have been performed with values besides $n_t = 1.5$. While many aspects of the proposed toe stability formula still require further verification, it is currently considered a working hypothesis and not yet a fully validated design formula.

Conclusion on relevant toe stability parameters
The preceding paragraphs have provided a brief overview of the hydraulic and structural parameters investigated in the aforementioned methods on toe stability. However, it is noteworthy that not all parameters considered in the associated research have been consistently integrated into the formulations, with some having their influence substituted by related parameters. For detailed information, reference to the specific works is recommended.

In conclusion, the study of predicting toe stability remains an ongoing subject of research due to its complexity. Both experimental formulations and attempts to address the problem from a physical understanding have yet to yield consistent success. Despite these challenges, certain key parameters have been identified as significant contributors to toe stability. Among the hydraulic parameters, wave height, wave length, and water depth of the toe stand out, while the size of the toe berm rocks emerges as the most crucial structural parameter.

D

Scaling and physical modelling of breakwaters

As noted in the Users Guide to Physical Modelling and Experimentation (Frostick et al., 2011), faithfully replicating important wave conditions and structural parameters in a model requires choosing the appropriate scale while ensuring sufficient measurement accuracy. This is achieved through three types of similarity: geometric, kinematic, and dynamic. Geometric similarity is achieved when the model's geometric lengths have a constant relation to the corresponding lengths in the prototype, while kinematic similarity requires that time-dependent processes in the model have a constant time relation to those in nature. Dynamic similarity ensures that forces in the prototype and model have a constant relation, with the assumption that geometrically similar models have kinematic similarity. The key to a correct representation of a geometrically similar model is dynamic similarity, which leads to commonly used scaling laws. The selection of scaling numbers depends on the importance of individual attacking forces. It is crucial to carefully consider scaling laws and parameters to ensure that the scale model accurately represents the full-scale structure and that the results of physical modeling are reliable, as neglecting scaling considerations can result in inaccurate or unreliable model outcomes

D.1. Scaling laws

In rubble mound breakwater modeling, forces such as gravity, friction, and surface tension are important. Achieving true dynamic similarity between the model and prototype requires identical Froude (Equation D.1), Reynolds (Equation D.2), and Weber (Equation D.3) numbers, which is often impossible due to difficulties in finding an appropriate model fluid. However, using the Froude model law and ensuring that the Reynolds and Weber numbers are in the same range as the prototype, sufficient similarity can be achieved. The impact of the Reynolds and Weber numbers is usually negligible if these conditions are met. However, when modeling flow through structures and drag forces on them, accurately modeling waves and currents is crucial, and Reynolds similarity becomes more important in these cases. Nonetheless, if the Reynolds number is large enough, and fully turbulent flow conditions exist in the armor and filter layer(s), Froude scaling alone may be sufficient.

$$Fr = \frac{u}{\sqrt{gL}} \tag{D.1}$$

$$Re = \frac{uL}{v_k} \text{ or } Re_D = \frac{\sqrt{gH_sD_n}}{v_k} \text{ (for flow conditions in the armour layer)} \tag{D.2}$$

$$We = \frac{\rho_w u^2 L}{\sigma} \tag{D.3}$$

Summarized, to achieve similitude in rubble mound breakwaters the following conditions have to be met:

- Geometrically scaled rubble mound structural dimensions without model distortions in length scale: a reasonable approximation of the shape and size distribution of the armour layer;
- Flow hydrodynamics modelled according to the Froude criterion: Froude number similarity in the armour layer
- Presence of turbulent flow conditions in the armour layer: $Re_D > 30000$).

Typical scaling relations, acquired form the Froude law, are expressed in term of length scale factor n_L:

Wave height (m)	$n_H = n_L$
Time (s)	$n_T = \sqrt{n_L}$
Velocity (m/s)	$n_u = \sqrt{n_L}$
Acceleration (m/s^2)	$n_a = 1$
Mass (kg)	$n_M = n_\rho n_L^3$
Pressure (kN/m^2)	$n_P = n_\rho n_L^3$
Force (kN)	$n_F = n_\rho n_L^3$

Scale effects occur when scaling laws do not accurately replicate physical conditions from the prototype at the model scale, often due to oversimplification or exclusion of governing forces.

Stability scaling
Stability scaling ensures that the stability number is the same in the model and in the prototype. To ensure that the model accurately represents the stability of the armor units in the prototype, it is necessary for the stability number in the model to be equivalent to the stability number in the prototype. The scaling relation based on armor diameter looks as follows:

$$n_D = n_L/n_\Delta = n_L \frac{\Delta_{model}}{\Delta_{prototype}} \tag{D.4}$$

Although absolute geometric similarity of armour unit dimensions is not always maintained, the effect on the results of model experiments are generally less than 5 to 10 %, if the armour geometry is correctly reproduced.

Permeability scaling
In the testing of physical scale models of permeable coastal structures, Froude scaling is crucial to maintain the proper ratio of inertia to gravity, ensuring accurate scaling of surface gravity waves. However, using a single length scale may result in the inaccurate reproduction of forces. Typically, in the geometric scaling of rubble-mound breakwaters, viscous scale effects are not a concern in the primary or secondary armour layers as the Reynolds number, based on the characteristic dimension of the armour unit, is usually high enough to ensure turbulent flow. However, in subsequent underlayers and core materials, the Reynolds number may fall below the critical value required to avoid scale effects. This can lead to conservative estimates of armour stability (larger damage and overtopping in the model) as the in- and outflow out of the breakwater is limited, increasing the flow around the armour caused by a lack of permeability of the downscaled material in comparison with the prototype (Vanneste and Troch, 2014).

According to the EuroTop manual (2018) the stone size in the core of small scale rubble mound breakwaters has to be scaled according to the velocities in the core rather than the stone dimensions, as achieved by the method proposed by Burcharth (1999). The method suggests that similarity between the flow fields in the prototype and model cores would be required to ensure an unbiased hydraulic response. The hydraulic gradient at the interface between rock layers in the prototype and model should be equal. The scaling is achieved by equating the Forchheimer resistance of the materials, which takes into account both the viscous and inertial resistance to flow. This ensures that the permeability of

the model core and underlayers is representative of the permeability of the prototype structure, even though the physical dimensions are scaled down.

In the work of Wolters et al. (2014), wave dampening within breakwater models at varying scales was investigated. The research proposed a straightforward scaling rule for physically modeling porous flow. This involved a proposed analytical solution of the shallow-water equations within a permeable structure, coupled with the application of a scale-dependent correction factor in describing the damping coefficient and hydraulic gradient, thereby enabling the scaling of the core diameter. The results indicated that a Froude scaled core diameter larger than $7mm$ and Reynolds numbers in the filter, denoted as Re_f, greater than 300 were necessary to ensure kinematic similarity. In such cases, no correction factor was required. The approach was deemed inapplicable for diameters below $2mm$. As it is essential to maintain a minimum structure/stone size. Viscous effects in the model can be mitigated by using diameters larger than 3–5 mm in model scale (Frostick et al., 2011).

The benefits and drawbacks of permeability scaling require careful evaluation, considering the study's objectives and the specific research requirements or client preferences.

Friction scaling
Besides possibly minor bottom friction scale effect (due to the relatively large breakwater model length scale), discrepancies can arise due to improper scaling of contact friction between adjacent armour units (S. A. Hughes, 1993). In small-scale physical models tests, frictional forces between armour units may not be in similitude with the prototype due to relative surface roughness differences. If there is appreciable friction between the model armour units, higher stability would be measured. By making the model units smooth, friction between the units can be reduced. This can be obtained by painting the units with enamel paint or casting the units in plastics. Relatively smoother armour units will result in slightly conservative stability results.

D.2. Model discrepancies and limitations

Model effects can impact the accuracy of modelling results. Model effects occur due to the laboratory set up; be it incorrect representations of the prototype structure, waves or contamination by boundary conditions of the flume.

Lower limit boundaries, based on considerations of the the Reynolds and Weber numbers, can be derived as:

- $h > 0.05m$
- $H_s > 0.05m$
- $T > 0.35s$
- $L >> 0.02m$
- $d_{rock} > 3 - 5mm$

Concrete armour units sizes are limited by the availability. In practice nominal armour diameters often start at $30mm$, as detection of rocking is increasingly hard for decreasing size.

E

Cross-sections

This appendix contains detailed cross-sections of the tests set-ups used.

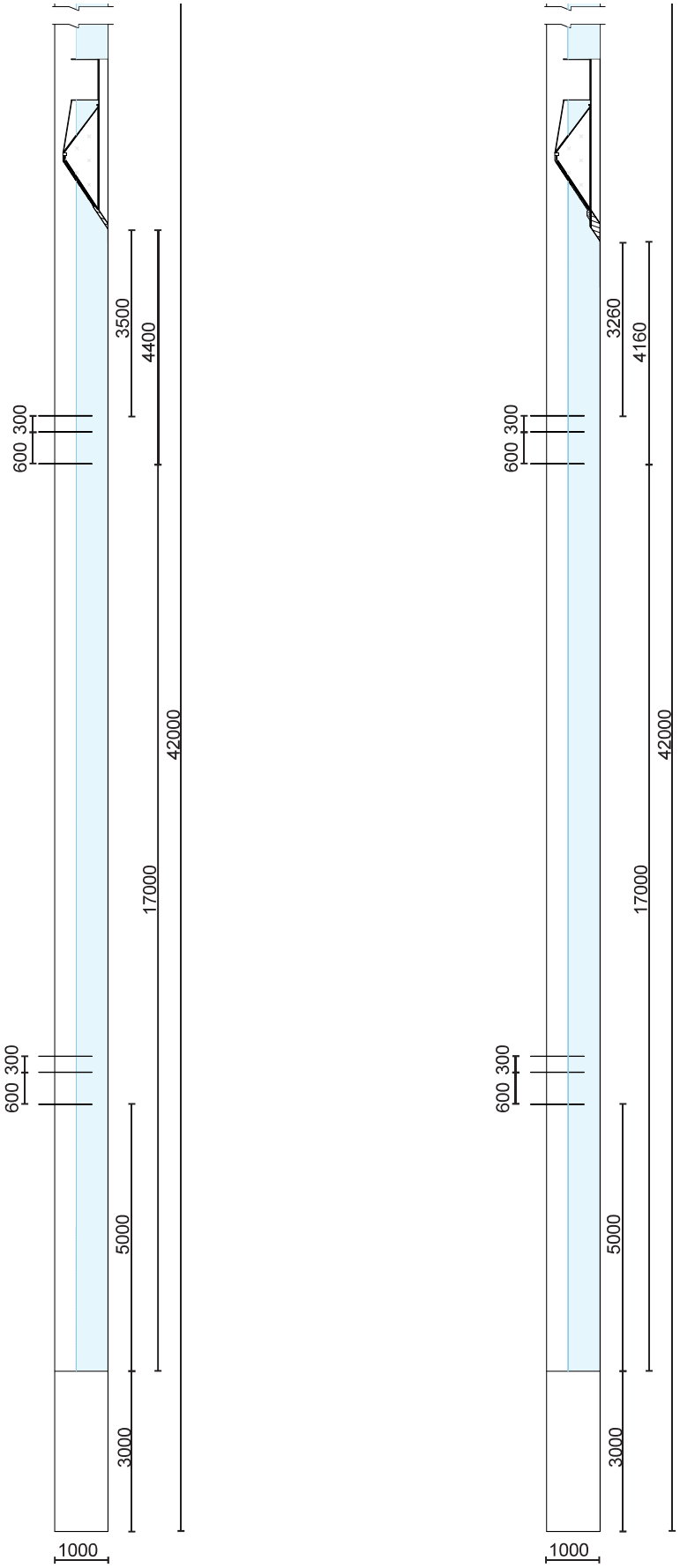

Figure E.1: Cross-section wave flume; measurements are given in mm

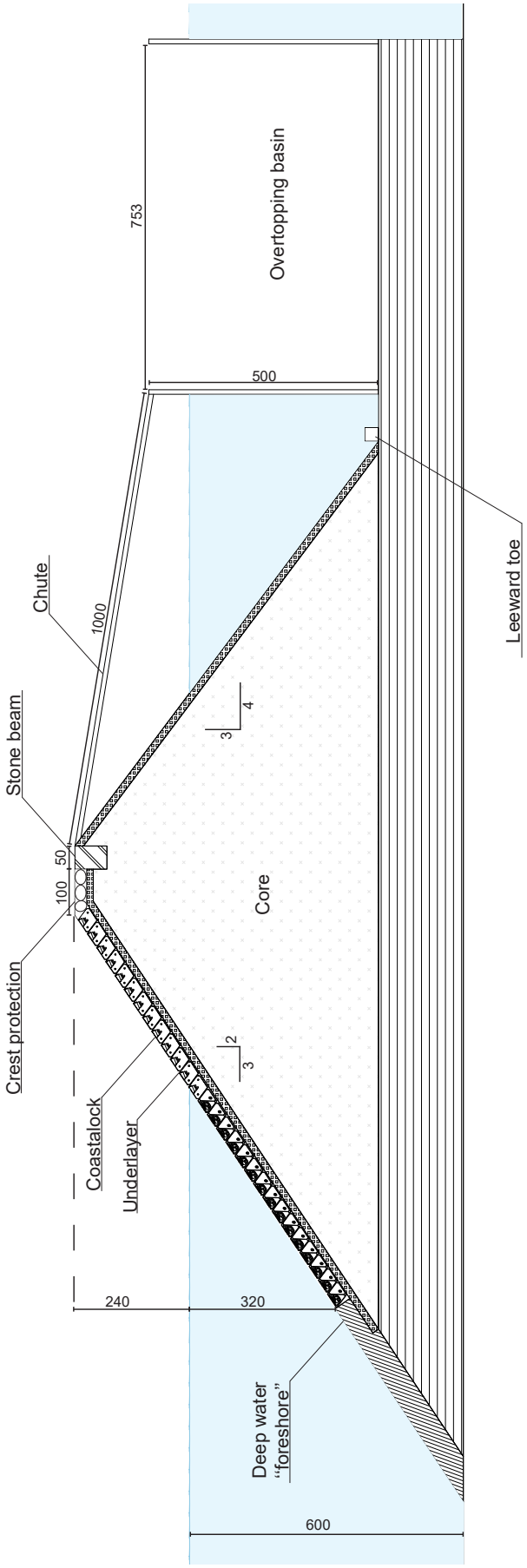

Figure E.2: Cross-section structure: Deep water; measurements are given in mm

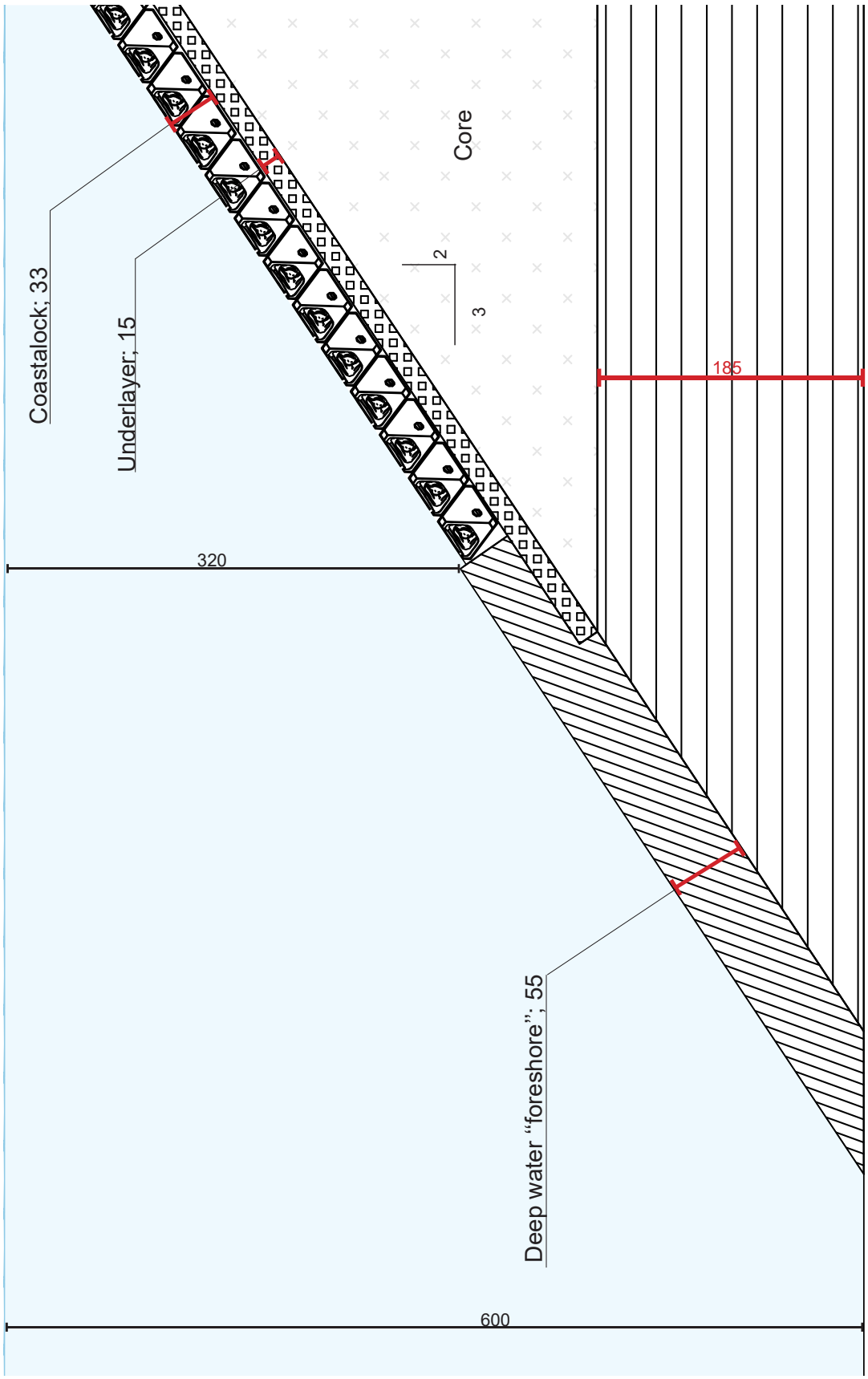

Figure E.3: Cross-section detail: Deep water "foreshore"; measurements are given in *mm*

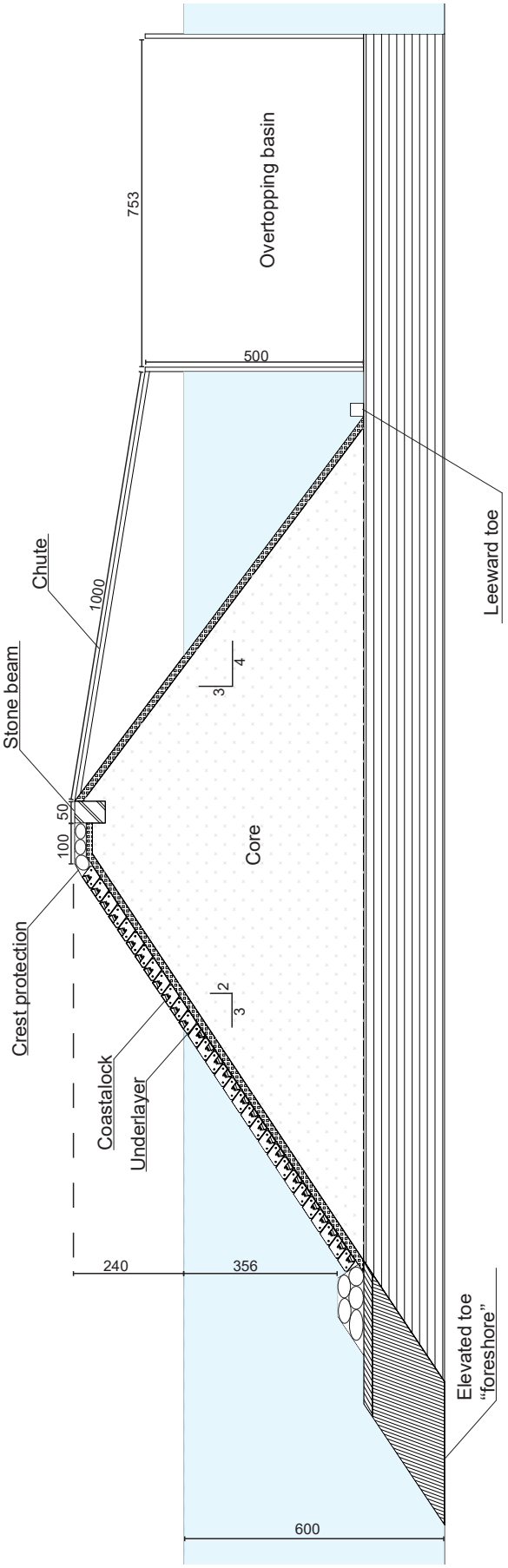

Figure E.4: Cross-section structure: Elevated toe; measurements are given in mm

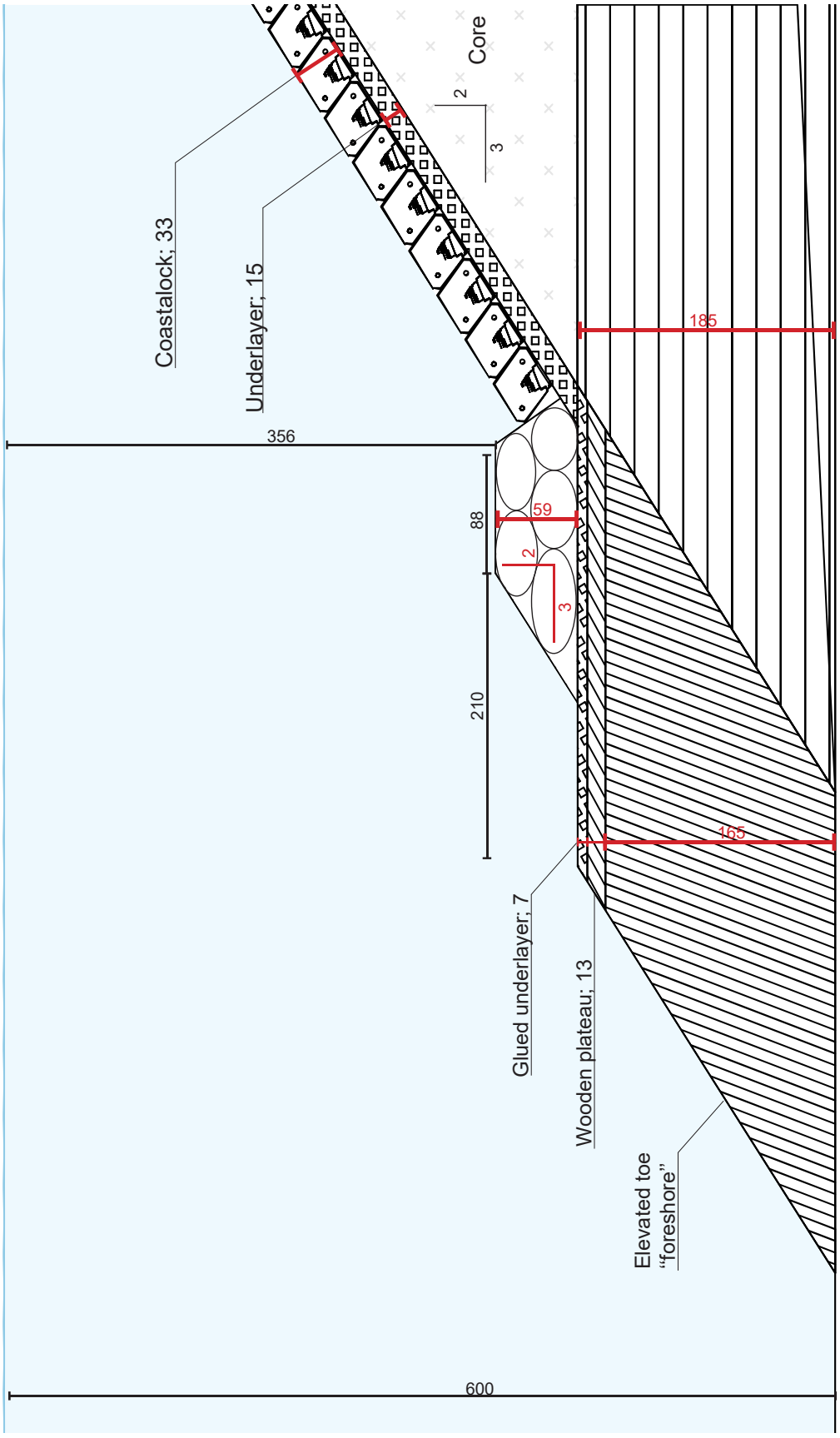

Figure E.5: Cross-section detail: Elevated toe with rough surface; measurements are given in mm

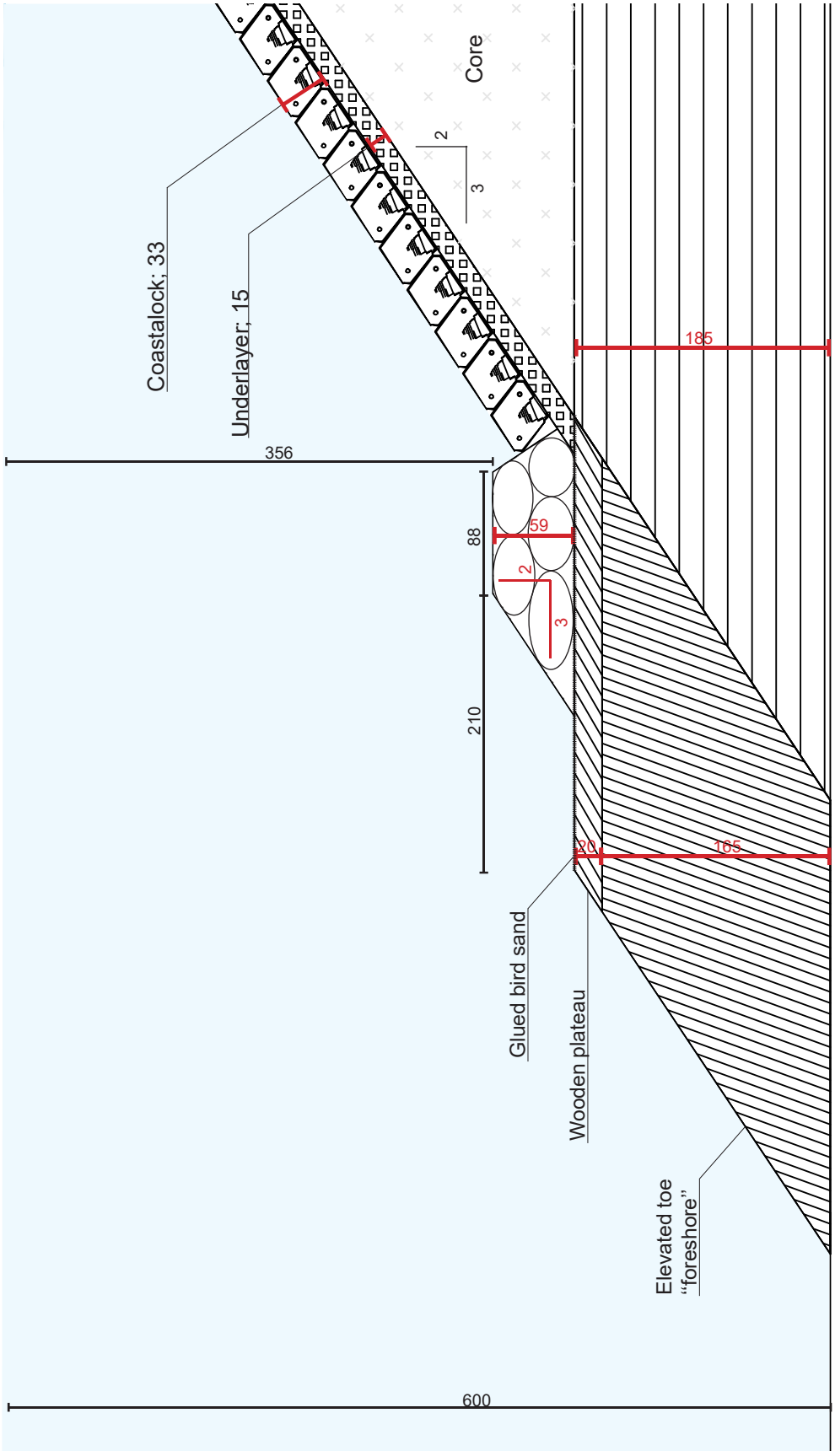

Figure E.6: Cross-section detail: Elevated toe with rough surface; measurements are given in mm

F

SfM process

Appendix F provides an overview of the functionality of Agisoft Metashape and the workflow employed and software settings used to generate the dense point clouds utilized for stability measurements.

F.1. Agisoft Metashape

The standard procedure in a Metashape project consists of two steps, as delineated in both the Agisoft Metashape manual (2023) and the United States Geological Survey (2021) guide on imagery processing with Agisoft Metashape.

The first step (Fig. F.1), the so called alignment process, involves identifying key points in each image and matching them to create tie points, reconstructing the geometry of the captured scene through aerial triangulation. In Agisoft Metashape, alignment parameters are computed locally and translated to a geographic or local coordinate system. This process refines the camera calibration model and produces calibrated camera models, estimated camera positions and orientations, calibration coefficients, geo-located tie points, and GCP locations, enhancing alignment quality. Weak tie points can be selectively removed to improve reconstruction accuracy through bundle adjustment, an optimization technique in photogrammetry. This process should maintain a balance between tie point elimination and ensuring sufficient points for alignment across the scene. The results include a Sparse Point Cloud (Fig. F.2) and camera positions, with the Sparse Point Cloud aiding in depth map determination by selecting common tie points between camera pairs for depth map calculation. The Sparse Point Cloud represents the results of image alignment and will not be directly used in further processing. The Sparse Point Cloud is necessary for the determination of depth maps, as based on the common tie points camera pairs for the depth maps calculation are selected.

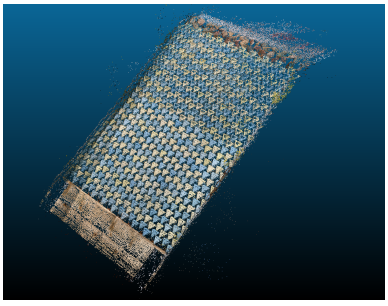

Figure F.1: Unfiltered point cloud after alignment containing low quality tie points

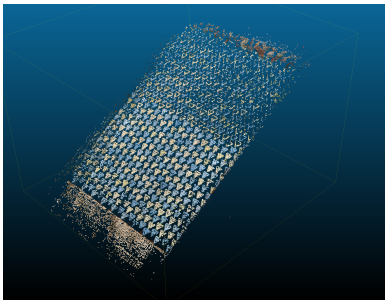

Figure F.2: Sparse Point Cloud after selection containing strong tie points for depth map creation

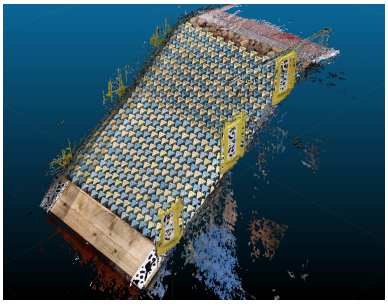

Figure F.3: Final Dense Point Cloud after merging of partial clouds based on image mapping

The second step in the process involves generating a detailed 3D surface. Metashape enables the creation

of a point cloud utilizing exterior and interior image orientation parameters. This is done through depth map calculation using dense stereo matching. Depth maps are generated for overlapping image pairs based on their relative orientation parameters. These pairwise depth maps are combined into a single map, with overlapping regions used to filter incorrect depth measurements. The combined depth maps are transformed into partial point clouds, which are then merged into a final point cloud with noise filtering applied. Surface normal vectors in the partial point clouds are calculated using plane fitting to pixel neighborhoods in the combined depth maps, and colors are sampled from the images. This process yields a highly detailed product known as the Dense Point Cloud (Fig. F.3) that is utilized for further processing.

F.2. General workflow

The workflow for generating detailed Dense Point Clouds follows these steps:

1. Start by adding captured images to the project. It's crucial to ensure that the images are of high quality, as low-quality images can negatively impact alignment (Agisoft, 2023). Metashape offers an automatic image quality estimation feature to identify and exclude images with a quality value below 0.5 units from alignment.
2. Align the remaining images using the "Highest" accuracy setting. Select "Generic preselection" to preliminarily match images using downsampled settings and find overlapping pairs before a second pass at the set accuracy. Set the key point limit to 120,000, suitable for small-scale highly detailed 3D models (Sargent, 2022). The "Tie point limit" is set to zero to apply no tie point filtering.
3. Utilize the "Detect Markers" tool for automated GCP detection.
4. Import local reference x, y, z-coordinates with a measurement accuracy of in the order of one millimeter as "Reference."
5. Add scale bars between marker pairs with known distances and sub-millimeter order of accuracy.
6. Perform Error Reduction—Optimization and Camera Calibration:
    - Camera optimization: Check the "General" coefficients [f, k1, k2, k3, cx, cy, p1, and p2] from the "Optimize Cameras" dialog. In the "Advanced" options, enable "Estimate tie point covariance" to visualize tie point errors in the Model view.
    - Filter by "Reconstruction Uncertainty": Remove points with poor camera geometry to reduce noise in the point cloud. Gradually select points with reconstruction uncertainty values, starting with one decimal accuracy up to a minimal value of 10 to remove no more than two-thirds of the present points (Betlem and Rodes, 2024). Follow up with "Optimize Cameras" step.
    - Filter by "Projection Accuracy": Assign accuracy levels to tie points based on the precision of key points intersecting to create them. Maintain tie points up to level 3 to prevent overfitting of the camera (Over et al., 2021). Follow up with "Optimize Cameras" step
    - Filter by "Reprojection Error": Reduce error between a 3D point's original and projected locations on images. Remove tie points by adjusting the reprojection error with single decimal precision. Achieving a reprojection error of 0.3 pixels should be considered adequate optimization, as any further optimization should not yield noticeable differences in the resulting product (Over et al., 2021). Repeat this process until the final error is equal to 0.3, then run "Optimize Cameras" one last time.
7. The Dense Point Cloud is created utilizing the estimated camera positions obtained from the Sparse Point Cloud. This Sparse Point Cloud retains approximately 10% of the original points after filtering, comprising high-quality tie points, in addition to the depth maps generated for each camera.The quality setting for the Dense Point Cloud is configured to 'High', ensuring optimal resolution. Additionally, the depth filtering parameter is adjusted to 'Mild' to preserve fine details and texture within the scene. Enabling 'Calculate point colors' assigns RGB values to each point, enhancing visual fidelity.
8. The Dense Point Cloud is exported in .LAS format for further processing.

G

Testing procedure

The following appendix provides an overview of the procedures carried out during the testing phase.

G.1. Testing course of action: Video-based observations

The following steps were performed during test series involving Video-based observations only, without the use of the photogrammetry technique. These steps were carried out in the wave flume during each test series to ensure proper use and correct data collection in a safe manner:

1. Set the correct foreshore in place and fasten it securely.
2. Check the underlayer for irregularities.
3. Build up the appropriate Coastalock configuration supported by the secured toe beam and check for irregularities.
4. Check the overtopping basin; a small layer of water should be present for the initial water level measurement for the wave height meter.
5. Fill the flume according to the procedure.
6. Take pictures from above, set the side camera to film, and start wave gauge measurements in DASYlab.
7. Activate the wave generator with the correct settings.
8. Make observations for any anomalies.
9. Stop the wave generator after the required time has elapsed or when one or more Coastalock units are extracted.
10. Stop the camera recording.
11. Once waves have settled in the flume, take pictures of the breakwater slope from above.
12. Once waves have settled in the overtopping basin, stop the measurements in DASYlab.
13. Repeat steps 6 to 12 to perform the next test in the test series until one or more Coastalock units are extracted or the maximum wave height is reached.
14. Empty the flume according to the procedure.

G.2. Testing course of action: Structure from motion

The following steps were performed during test series involving the use of the photogrammetry technique. These steps were carried out in the wave flume during each test series to ensure proper use and correct data collection in a safe manner:

1. Set the correct foreshore in place and secure it firmly.
2. Inspect the underlayer for irregularities.
3. Assemble the appropriate Coastalock configuration, supported by the secured toe beam or on the toe berm, and check for irregularities.
4. Check the overtopping basin; ensure a small layer of water is present for the initial water level measurement for the wave height meter.
5. Fill the flume following the established procedure.
6. Initiate the wave gauge measurements in DASYlab.
7. Activate the wave generator with the correct settings.
8. Make observations for any anomalies.
9. Halt the wave generator after the required time has elapsed or when one or more Coastalock units are extracted.
10. Stop the camera recording.
11. Partially empty the flume until just below the are of interest; be it the secured toe beam or on the toe berm.
12. Dry the Ground Control Points.
13. Capture overlapping pictures of the slope from all angles.
14. After waves have settled in the overtopping basin, stop the measurements in DASYlab.
15. If no Coastalock units are extracted nor the maximum wave height is reached, repeat steps 5 to 9 and 14 for every even test run in the test series.
16. Repeat steps 5 to 14 for every odd test run in the test series, until one or more Coastalock units are extracted or the maximum wave height is reached.
17. Empty the flume according to the established procedure.

H

Measured wave conditions

This appendix begins by addressing the encountered issues related to clipping wave data and missing wave data and their resolution. Finally, an overview is presented of the measured wave characteristics near the structure.

H.1. Wave signal clipping

Near the conclusion of the testing phase, while inspecting individual wave files, it was observed that the tops of wave profiles were clipped in several instances. Clipping occurs when the wave crest exceeds the measuring range of the wave height meters, which happens when the maximum voltage of 10V is surpassed. Subsequently, all wave files underwent a check for clipping, and the results are presented in Table H.1. The majority of the gaps were identified in files corresponding to measurements of long waves. The combination of significant incoming waves and reflected waves resulted in higher-than-expected water level fluctuations, lead to signal clipping. Additionally, upon analyzing the calibration files of the wave height meters, it was discovered that several of them were not functioning properly across the entire measuring range. This malfunction caused a reduction in the measuring range, contributing to the signal clipping as well.

s_0 [-]	N_{gaps}	N_{files}	$\mu_{gap}[s]$	$\sigma_{gap}[s]$
0.04	7	3	0.06	0.04
0.02	209	28	0.14	0.07

Table H.1: Gap check and gap characteristics of wave files

To investigate the impact of these gaps on wave decomposition, splines were used to fill in the gaps through interpolation. This process involved the following steps for each wavelength separately:

1. Training sets were generated by introducing artificial gaps in data that originally contained no gaps. These gaps were created in intervals, starting at 10V and decreasing in steps of 0.1V. The closest match to the the mean gap length of the clipped data was chosen.
2. The gaps were filled using three spline interpolation methods: cubic splines with a first derivative boundary condition, cubic splines with natural boundary conditions, and quadratic splines. The number of boundary points on both sides was varied from 2 to 10.
3. The best method was selected based on Mean Square Error and Root Mean Square Error compared to the original gap-free data.
4. The interpolated data underwent wave decomposition, and the results were compared to the original data.

$s_0[-]$	N_{gaps}	N_{files}	$\mu_{gap}[s]$	$\sigma_{gap}[s]$	Cut-off $[V]$	Interpolation	BC.	MSE $[V^2]$	RMSE $[V]$
0.04	34	15	0.06	0.03	8.9	1st dv. cubic	2	0.028	0.125
0.02	398	16	0.14	0.08	6.3	1st dv. cubic	2	0.001	0.057

Table H.2: Training set gap check and gap characteristics of wave files

No significant influence was observed on the results of the decomposition of the training data, including significant wave height, peak period, or reflection coefficient. The method was deemed suitable for the wave data with original clipping.

After supplementing the originally clipped data with the spline interpolation methods, no significant changes were found in the results of the decomposition. Hence, it was chosen to perform the analysis with the clipped data.

H.2. Missing wave signal

H.2.1. Current research

Due to an operational error, the last test of the DWP10s4U2 test series (series 17, run 7) did not record any data in DASYlab. The objective was to establish a polynomial model that accurately characterizes the relationship between the significant wave height of the wave maker input and the significant wave height near the structure. The following steps were undertaken:

1. Utilizing all remaining wave files for medium-long waves as a test series, the input significant wave height was plotted against the significant wave height measured near the structure.
2. Polynomial lines were fitted through the data points of increasing degrees.
3. The polynomials were evaluated based on their R^2 value, with a focus on predicting high significant wave height values near the structure ($H_{m0} > 0.14m$).
4. The best-fit polynomial was chosen based on these criteria and applied to the missing data.

It was observed that predictions of the missing wave height by polynomials of varying degrees (ranging from 1 to 7) were within 1% of each other. The 4th degree polynomial was selected as the best fit, providing a predicted H_{m0} near the structure of $0.151m$.

H.2.2. Preliminary research

After inspecting Molenkamp's (2022) data, it was discovered that the last test runs of the 10% spacing (series 12, run 1) and 20% spacing (series 14, run 9), with target wave heights of $H_s = 0.190m$, were prematurely ended, not reaching 1000 waves. The wave signal ceased after several minutes. To address this, the exact same procedure as described above was undertaken to supplement the measurements. Polynomial predictions of the missing wave height, ranging from degrees 1 to 7, showed consistent results within 1% of each other, yielding a predicted H_{m0} near the structure of $0.168m$.

H.3. Measured wave characteristics summary

The wave characteristic are presented in Tables H.3, H.4, and H.5 as wave setting of the wave generator (Gen.) and measured in front of the structure (Str.). The significant wave height obtained from the polynomial fitting is indicated with an asterisk.

#	Name	Run	Gen.			Str.				
			H_s	T_p	s_{0p}	H_{m0}	N_s	T_p	s_{0p}	K_r
01	DWS00s4	1	0.070	1.06	0.04	0.0652	1.684	1.049	0.0380	0.536
		2	0.085	1.17	0.04	0.0794	2.051	1.180	0.0366	0.537
		3	0.100	1.27	0.04	0.0945	2.438	1.270	0.0376	0.533
02	DWS00s2	1	0.070	1.50	0.02	0.0664	1.713	1.481	0.0194	0.662
		2	0.085	1.65	0.02	0.0786	2.030	1.652	0.0185	0.685
03	DWS10s4	1	0.070	1.06	0.04	0.0662	1.708	1,085	0.0360	0.417
		2	0.085	1.17	0.04	0.0799	2.062	1.182	0.0367	0.428
		3	0.100	1.27	0.04	0.0940	2.427	1.271	0.0373	0.447
		4	0.115	1.36	0.04	0.1081	2.791	1.343	0.0384	0.456
		5	0.130	1.44	0.04	0.1236	3.191	1.441	0.0381	0.478
		6	0.145	1.52	0.04	0.1389	3.586	1.519	0.0386	0.490
04	DWS10s2	1	0.070	1.50	0.02	0,0682	1.760	1.498	0.0194	0.551
		2	0.085	1.65	0.02	0.0828	2.136	1.759	0.0171	0.579
		3	0.100	1.79	0.02	0.0979	2.528	1.789	0.0196	0.611
		4	0.115	1.92	0.02	0.1154	2.979	1.920	0.0201	0.637
		5	0.130	2.04	0.02	0.1199	3.094	2.067	0.0180	0.660
		6	0.145	2.15	0.02	0.1414	3.649	2.147	0.0197	0.673
		7	0.160	2.26	0.02	0.1449	3.740	2.231	0.0187	0.671
		8	0.175	2.37	0.02	0.1524	3.934	2.400	0.0170	0.673
05	DWS20s4	1	0.070	1.06	0.04	0.0663	1.713	1.085	0.0361	0.393
		2	0.085	1.17	0.04	0.0802	2.071	1.166	0.0378	0.401
		3	0.100	1.27	0.04	0.0940	2.427	1.256	0.0382	0.422
		4	0.115	1.36	0.04	0.1080	2.789	1.343	0.0384	0.436
		5	0.130	1.44	0.04	0.1232	3.180	1.457	0.0372	0.455
		6	0.145	1.52	0.04	0.1385	3.575	1.519	0.0385	0.470
06	DWS20s2	1	0.070	1.50	0.02	0.0683	1.762	1.498	0.0195	0.519
		2	0.085	1.65	0.02	0.0829	2.139	1.758	0.0172	0.550
		3	0.100	1.79	0.02	0.0987	2.547	1.790	0.0197	0.585
		4	0.115	1.92	0.02	0.1160	2.994	1.941	0.0197	0.615
		5	0.130	2.04	0.02	0.1283	3.312	1.995	0.0207	0.635
		6	0.145	2.15	0.02	0.1296	3.346	2.176	0.0175	0.647
		7	0.160	2.26	0.02	0.1476	3.809	2.231	0.0190	0.654

Table H.3: Wave measurements of test series without protrusions

#	Name	Run	Gen.			Str.				
			H_s	T_p	s_{0p}	H_{m0}	N_s	T_p	s_{0p}	K_r
07	DWPLs4	1	0.070	1.06	0.04	0.0663	1.694	1.085	0.0361	0.429
		2	0.085	1.17	0.04	0.0799	2.041	1.165	0.0377	.0436
		3	0.100	1.27	0.04	0,0940	2.403	1.256	0.0382	0.452
		4	0.115	1.36	0.04	0.1076	2.745	1.343	0.0382	0.465
		5	0.130	1.44	0.04	0.1231	3.141	1.457	0.0372	0.490
		6	0.145	1.52	0.04	0.1372	3.496	1.520	0.0380	0.492
		7	0.160	1.60	0.04	0.1511	3.855	1.581	0.0387	0.507
		8	0.175	1.68	0.04	0.1643	4.192	1.715	0.0358	0.523
08	DWPLs2	1	0.070	1.50	0.02	0.0681	1.740	1.498	0.0195	0.544
		2	0.085	1.65	0.02	0.0827	2.114	1.758	0.0172	0.570
		3	0.100	1.79	0.02	0.0975	2.491	1.790	0.0195	0.605
		4	0.115	1.92	0.02	0.1146	2.925	1.921	0.0199	0.630
		5	0.130	2.04	0.02	0.1279	3.263	2.017	0.0201	0.650
		6	0.145	2.15	0.02	0.1318	3.363	2.176	0.0178	0.655
		7	0.160	2.26	0.02	0.1505	3.841	2.312	0.0181	0.662
		8	0.175	2.37	0.02	0.1531	3.905	2.400	0.0170	0.671
09	TRPLs4	1	0.070	1.06	0.04	0.0663	1.694	1.085	0.0361	0.410
		2	0.085	1.17	0.04	0.0796	2.034	1.181	0.0365	0.409
		3	0.100	1.27	0.04	0.0937	2.394	1.256	0.0381	0.423
		4	0.115	1.36	0.04	0.1075	2.744	1.343	0.0382	0.445
		5	0.130	1.44	0.04	0.1233	3.145	1.457	0.0372	0.471
		6	0.145	1.52	0.04	0.1379	3.519	1.519	0.0383	0.491
		7	0.160	1.60	0.04	0.1506	3.843	1.581	0.0386	0.508
10	TSPLs4	1	0.070	1.06	0.04	0.0664	1.697	1.085	0.0362	0.420
		2	0.085	1.17	0.04	0.0799	2.042	1.165	0.0377	0.421
		3	0.100	1.27	0.04	0.0937	2.393	1.256	0.0380	0.431
		4	0.115	1.36	0.04	0.1075	2.743	1.343	0.0382	0.452
		5	0.130	1.44	0.04	0.1235	3.150	1.457	0.0373	0.475
		6	0.145	1.52	0.04	0.1383	3.528	1.519	0.0384	0.496
		7	0.160	1.60	0.04	0.1511	3.856	1.581	0.0388	0.513

Table H.4: Wave measurements of test series with 22.5% protrusions

#	Name	Run	Gen.			Str.				
			H_s	T_p	s_{0p}	H_{m0}	N_s	T_p	s_{0p}	K_r
11	TSPSs4	1	0.070	1.06	0.04	0.0663	1.702	1.085	0.0361	0.449
		2	0.085	1.17	0.04	0.0796	2.041	1.165	0.0376	0.445
		3	0.100	1.27	0.04	0.0934	2.399	1.256	0.0380	0.455
		4	0.115	1.36	0.04	0.1078	2.763	1.343	0.0383	0.470
		5	0.130	1.44	0.04	0.1235	3.166	1.457	0.0374	0.490
		6	0.145	1.52	0.04	0.1429	3.664	1.502	0.0406	0.507
12	TRPSs4	1	0.070	1.06	0.04	0.0665	1.706	1.085	0.0362	0.440
		2	0.085	1.17	0.04	0.0799	2.049	1.182	0.0367	0.440
		3	0.100	1.27	0.04	0.0941	2.414	1.256	0.0383	0.449
		4	0.115	1.36	0.04	0.1075	2.757	1.343	0.0382	0.467
		5	0.130	1.44	0.04	0.1234	3.165	1.459	0.0372	0.491
13	DWPSs2	1	0.070	1.50	0.02	0.0682	1.748	1.498	0.0195	0.572
		2	0.085	1.65	0.02	0.0820	2.104	1.758	0.0170	0.598
		3	0.100	1.79	0.02	0.0975	2.501	1.790	0.0195	0.623
		4	0.115	1.92	0.02	0.1144	2.933	1.941	0.0195	0.649
		5	0.130	2.04	0.02	0.1195	3.064	2.065	0.0178	0.671
		6	0.145	2.15	0.02	0.1291	3.309	2.176	0.0175	0.674
		7	0.160	2.26	0.02	0.1414	3.626	2.231	0.0182	0.672
14	DWPSs4	1	0.070	1.06	0.04	0.0663	1.699	1.072	0.0369	0.443
		2	0.085	1.17	0.04	0.0799	2.049	1.165	0.0377	0.455
		3	0.100	1.27	0.04	0.0936	2.401	1.271	0.0372	0.468
		4	0.115	1.36	0.04	0.1078	2.763	1.344	0.0383	0.479
		5	0.130	1.44	0.04	0.1233	3.162	1.457	0.0372	0.490
		6	0.145	1.52	0.04	0.1396	3.578	1.539	0.0378	0.495
15	DWPSs4a	1	0.070	1.06	0.04	0.0662	1.698	1.085	0.0360	0.435
		2	0.085	1.17	0.04	0.0797	2.043	1.166	0.0376	0.445
		3	0.100	1.27	0.04	0.0937	2.401	1.256	0.0380	0.459
		4	0.115	1.36	0.04	0.1078	2.763	1.344	0.0383	0.468
		5	0.130	1.44	0.04	0.1232	3.158	1.457	0.0372	0.480
		6	0.145	1.52	0.04	0.1372	3.518	1.519	0.0381	0.490
		7	0.160	1.60	0.04	0.1466	3.758	1.619	0.0359	0.505
16	DWPSs4u	1	0.070	1.06	0.04	0.0661	1.695	1.085	0.0360	0.451
		2	0.085	1.17	0.04	0.0796	2.041	1.165	0.0376	0.459
		3	0.100	1.27	0.04	0.0936	2.401	1.256	0.0380	0.470
		4	0.115	1.36	0.04	0.1077	2.761	1.343	0.0383	0.478
		5	0.130	1.44	0.04	0.1232	3.160	1.457	0.0372	0.487
		6	0.145	1.52	0.04	0.1371	3.516	1.519	0.0381	0.493
		7	0.160	1.60	0.04	0.1518	3.893	1.583	0.0388	0.504
17	DWPSs4u2	1	0.070	1.06	0.04	0.0665	1.706	1.085	0.0362	0.450
		2	0.085	1.17	0.04	0.0797	2.044	1.166	0.0376	0.459
		3	0.100	1.27	0.04	0.0937	2.402	1.271	0.0372	0.471
		4	0.115	1.36	0.04	0.1078	2.763	1.343	0.0383	0.480
		5	0.130	1.44	0.04	0.1234	3.163	1.441	0.0381	0.491
		6	0.145	1.52	0.04	0.1372	3.519	1.519	0.0381	0.499
		7	0.160	1.60	0.04	0.1514*	3.883*			

Table H.5: Wave measurements of test series with 10% protrusions

I

Stability Results

The following appendix comprises a comprehensive overview of the stability results obtained from the SfM method. It is divided into two parts: results for short protrusions with 10% armour spacing and long protrusions with armour spacing of 22.5%. Each part includes graphs showing, for the relevant test series, the following:

- Elevation change after the test run compared to the reference profile after settling waves, expressed as a fraction of the Coastalock nominal diameter,
- Number of elevated units above threshold, expressed as a fraction of the Coastalock nominal diameter, within a strip of breakwater slope with a width equal to the nominal diameter,
- Maximum unit elevation, expressed as a fraction of the Coastalock nominal diameter,
- Width-averaged slope elevation compared to the reference profile for the relevant test series.

I.1. Short Protrusions - 10% armour spacing

'Protrusion-Optimized' configuration with SWL orientation change in 'Deep Water' set-up.

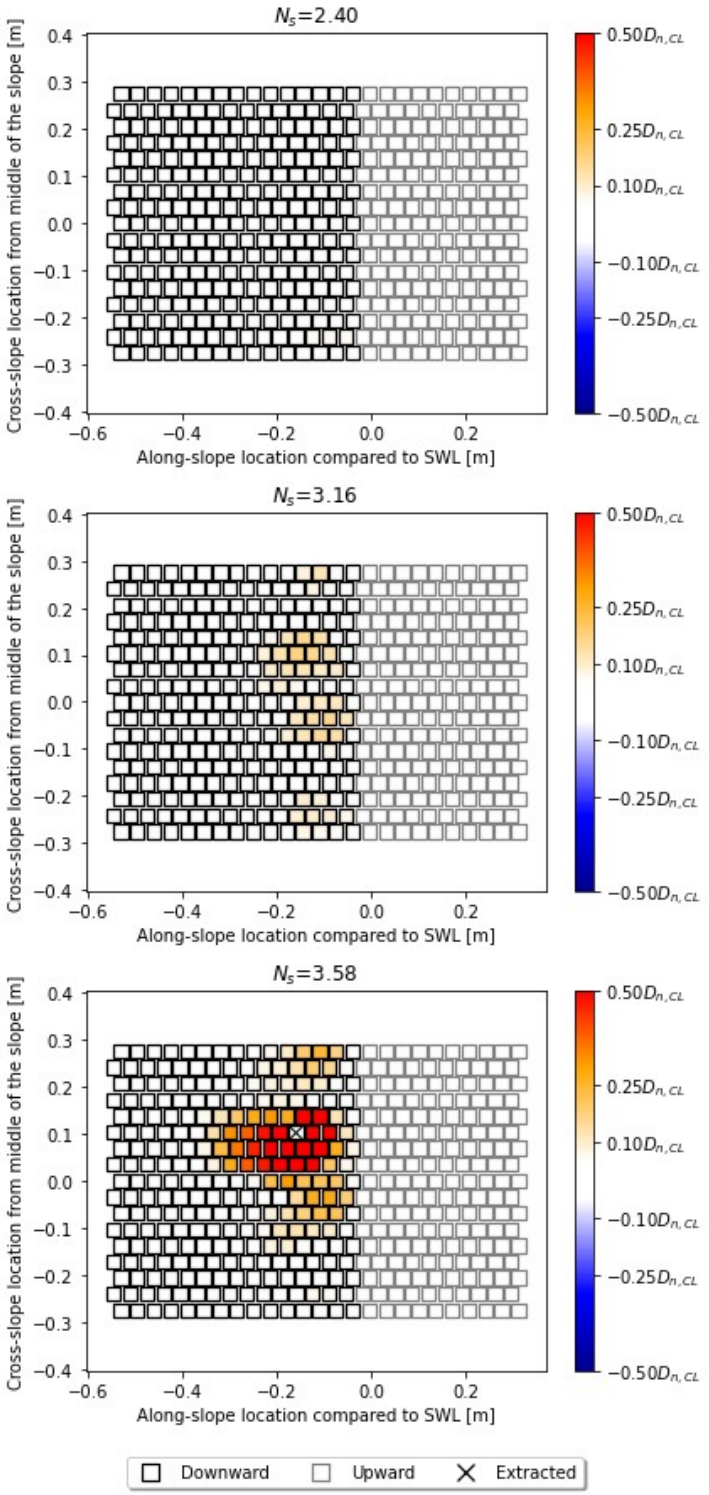

Figure I.1: Elevation change after the test run, compared to the reference profile after settling waves, expressed as a fraction of the Coastalock nominal diameter, under s_{0p} = 0.04, for short protrusions with 10% spacing in the 'PO-SWL' configuration in the 'Deep Water' set-up.

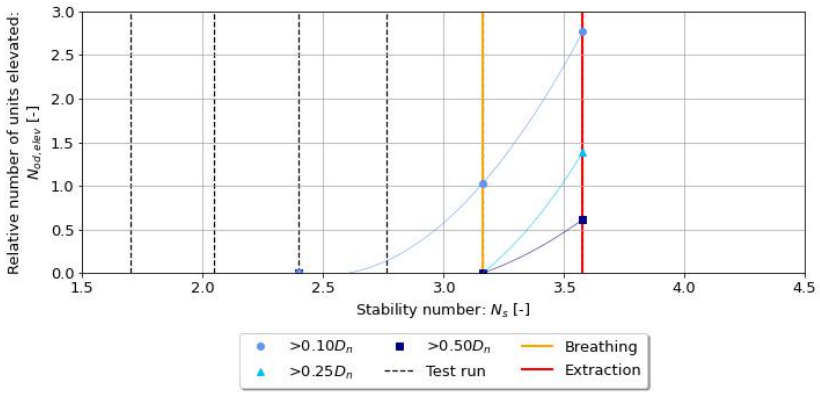

Figure I.2: Number of elevated units above threshold expressed as a fraction of the Coastalock nominal diameter within a strip of breakwater slope, with a width equal to the nominal diameter, under $s_{0p} = 0.04$, for short protrusions with 10% spacing in the 'PO-SWL' configuration in the 'Deep Water' set-up.

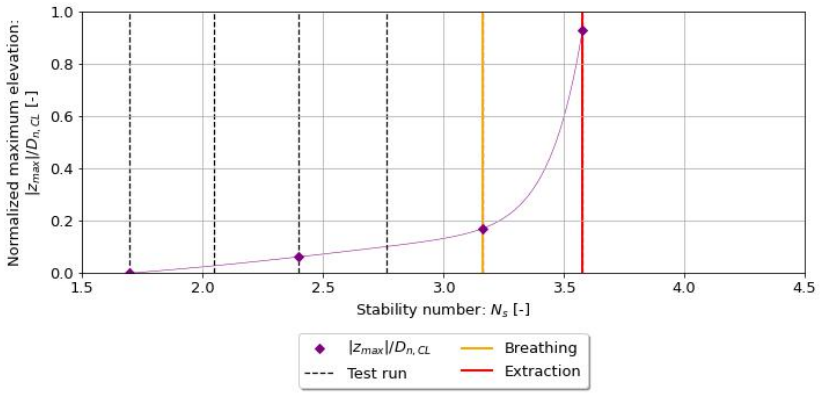

Figure I.3: Maximum unit elevation expressed as a fraction of the Coastalock nominal diameter, under $s_{0p} = 0.04$, for short protrusions with 10% spacing in the 'PO-SWL' configuration in the 'Deep Water' set-up.

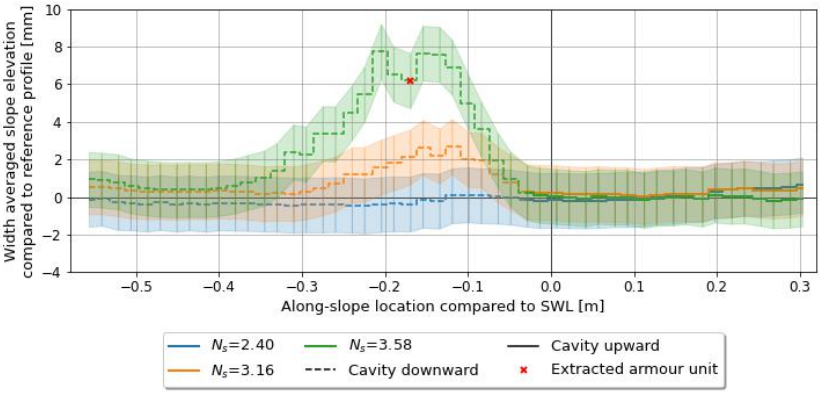

Figure I.4: Width averaged slope elevation compared to reference profile, under $s_{0p} = 0.04$, for short protrusions with 10% spacing in the 'PO-SWL' configuration in the 'Deep Water' set-up.

'Protrusion-Optimized' configuration - Midpoint orientation change in 'Deep Water' set-up

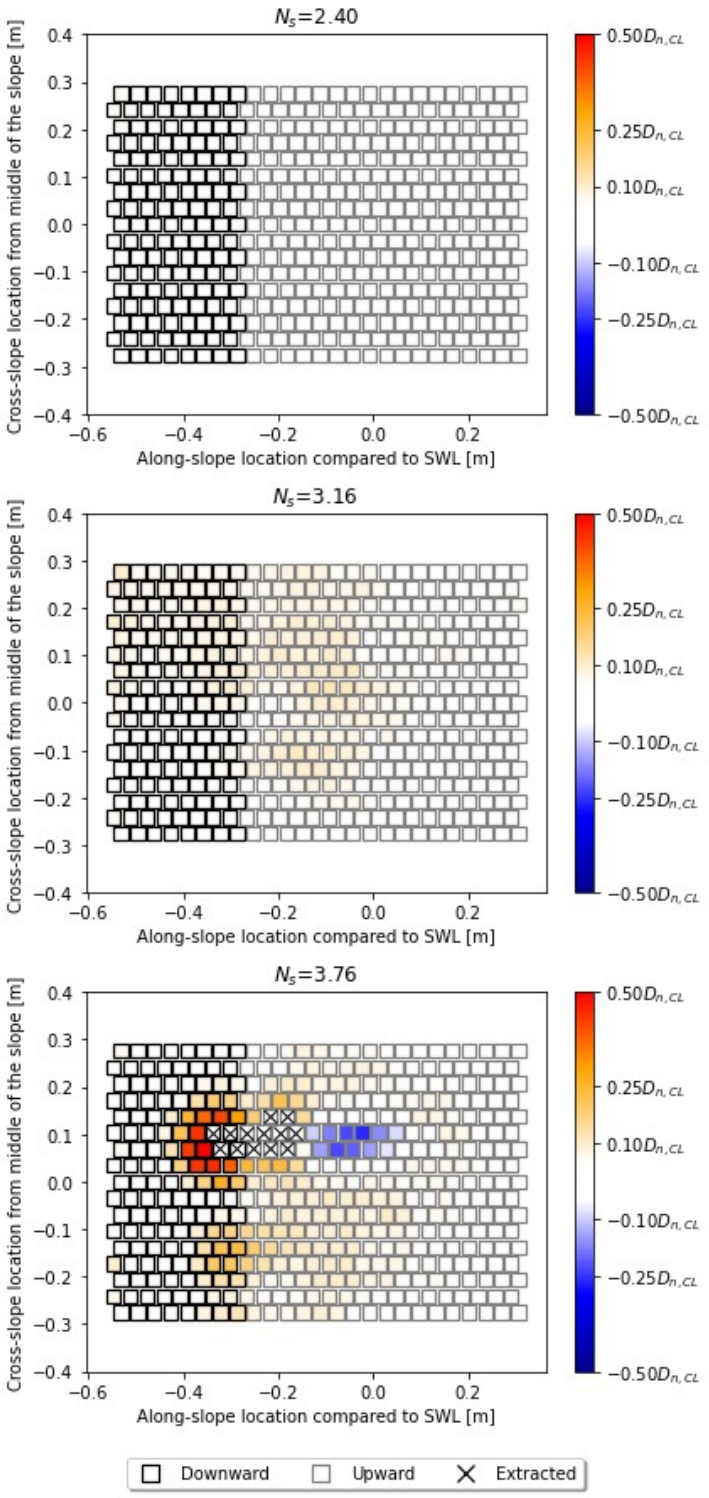

Figure I.5: Elevation change after the test run, compared to the reference profile after settling waves, expressed as a fraction of the Coastalock nominal diameter, under s_{0p} = 0.04, for short protrusions with 10% spacing in the 'PO-Mid' configuration in the 'Deep Water' set-up.

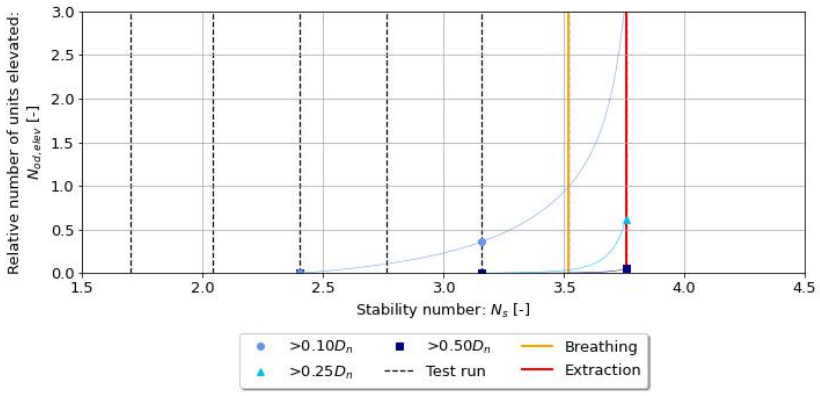

Figure I.6: Number of elevated units above threshold expressed as a fraction of the Coastalock nominal diameter within a strip of breakwater slope, with a width equal to the nominal diameter, under $s_{0p} = 0.04$, for short protrusions with 10% spacing in the 'PO-Mid' configuration in the 'Deep Water' set-up.

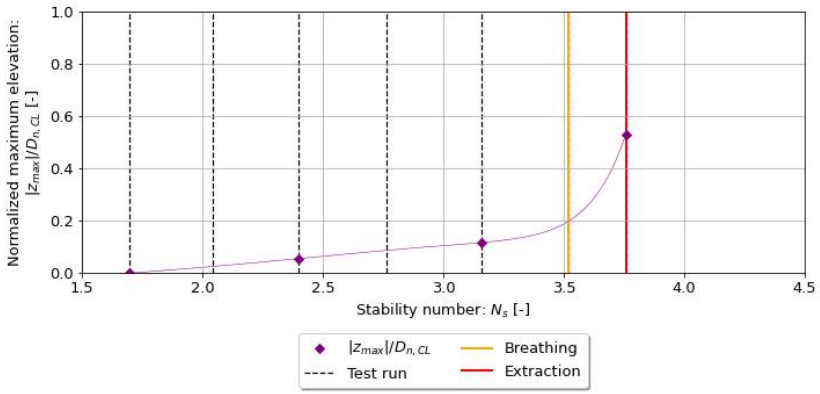

Figure I.7: Maximum unit elevation expressed as a fraction of the Coastalock nominal diameter, under $s_{0p} = 0.04$, for short protrusions with 10% spacing in the 'PO-Mid' configuration in the 'Deep Water' set-up.

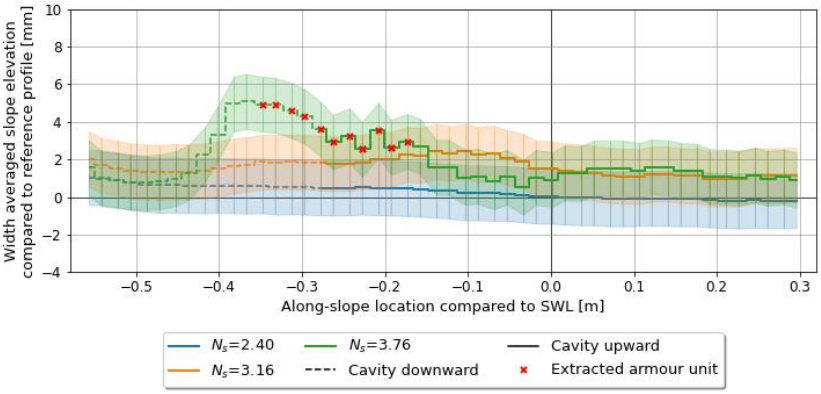

Figure I.8: Width averaged slope elevation compared to reference profile, under $s_{0p} = 0.04$, for short protrusions with 10% spacing in the 'PO-Mid' configuration in the 'Deep Water' set-up.

'Upwards' configuration in 'Deep Water' set-up.

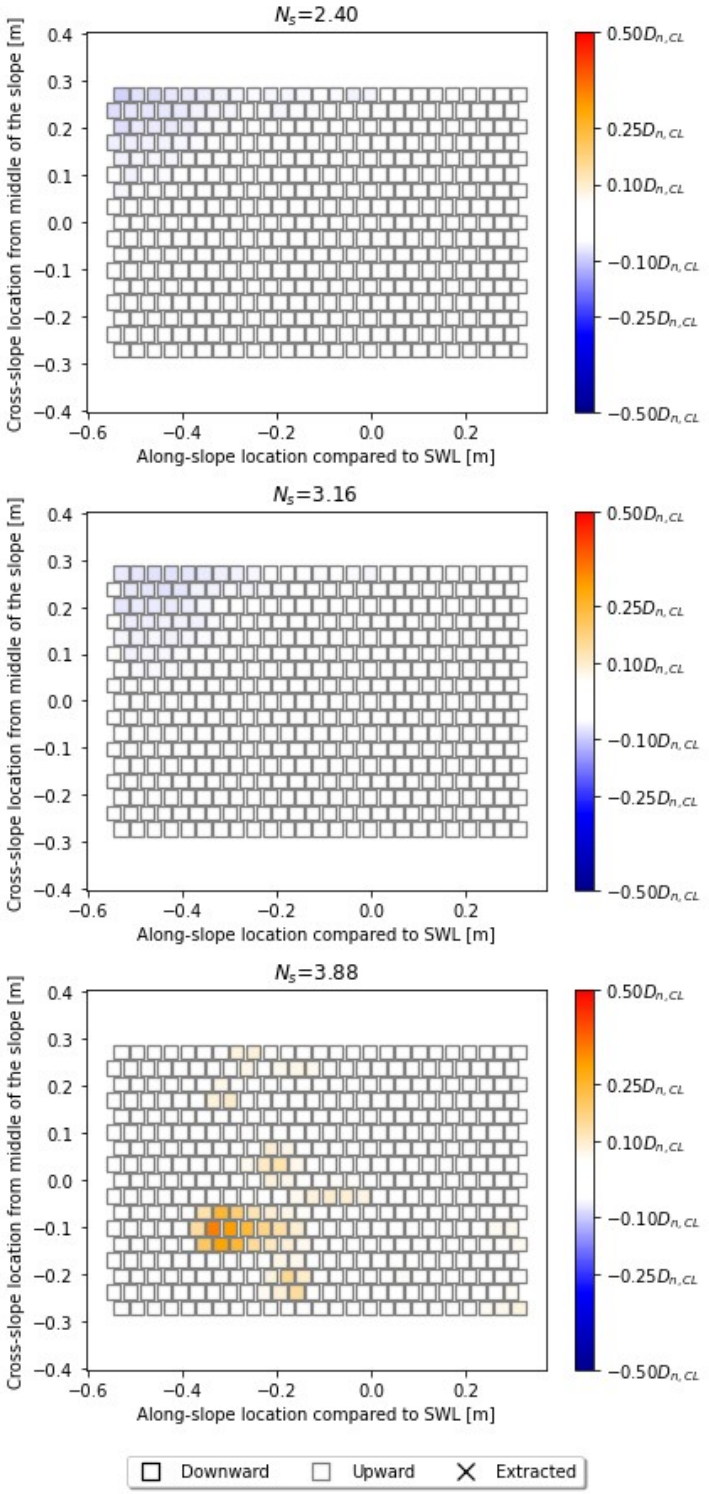

Figure I.9: Elevation change after the test run, compared to the reference profile after settling waves, expressed as a fraction of the Coastalock nominal diameter, under s_{0p} = 0.04, for short protrusions with 10% spacing in the 'Upwards' configuration in the 'Deep Water' set-up.

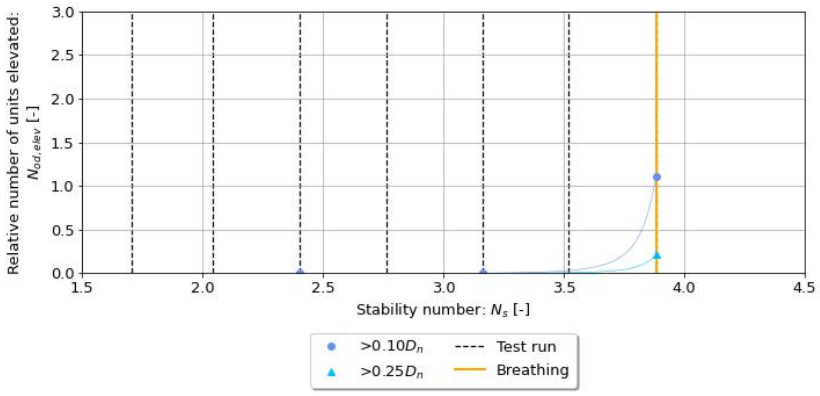

Figure I.10: Number of elevated units above threshold expressed as a fraction of the Coastalock nominal diameter within a strip of breakwater slope, with a width equal to the nominal diameter, under $s_{0p} = 0.04$, for short protrusions with 10% spacing in the 'Upwards' configuration in the 'Deep Water' set-up.

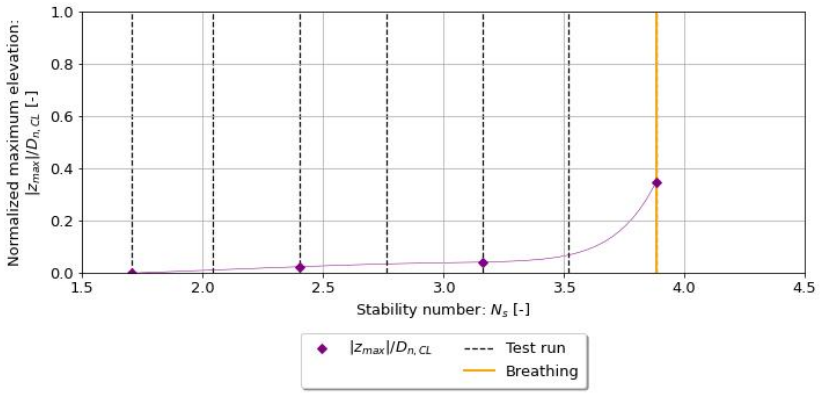

Figure I.11: Maximum unit elevation expressed as a fraction of the Coastalock nominal diameter, under $s_{0p} = 0.04$, for short protrusions with 10% spacing in the 'Upwards' configuration in the 'Deep Water' set-up.

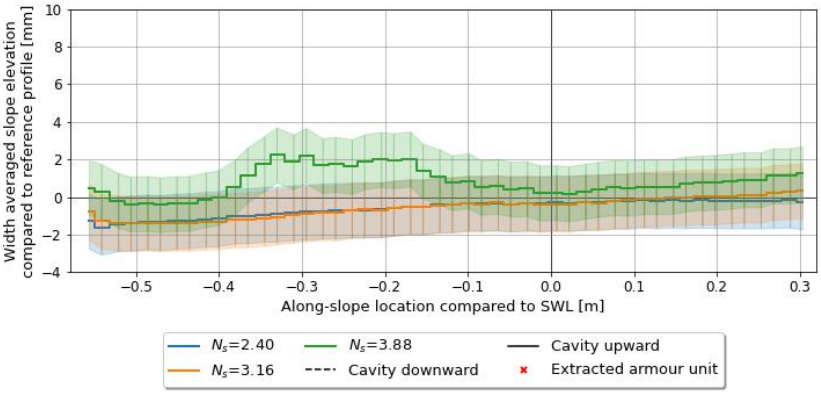

Figure I.12: Width averaged slope elevation compared to reference profile, under $s_{0p} = 0.04$, for short protrusions with 10% spacing in the 'Upwards' configuration in the 'Deep Water' set-up.

'Protrusion-Optimized' configuration with SWL orientation change in 'Toe berm on Rough' set-up

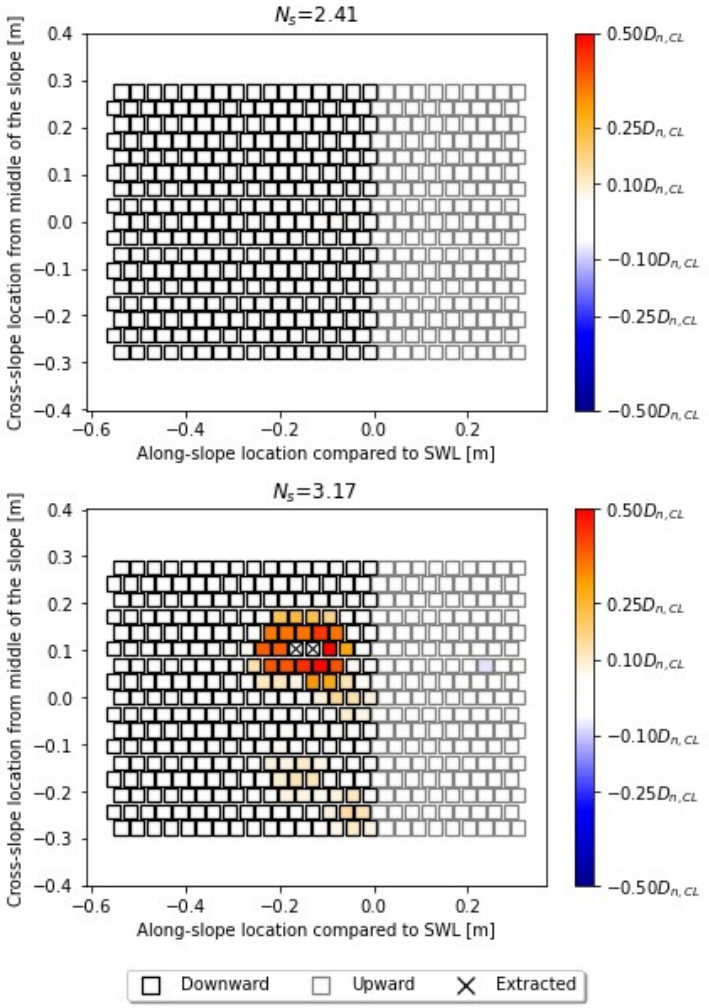

Figure I.13: Elevation change after the test run, compared to the reference profile after settling waves, expressed as a fraction of the Coastalock nominal diameter, under $s_{0p} = 0.04$, for short protrusions with 10% spacing in the 'PO-SWL' configuration in the 'Toe berm on Rough' set-up.

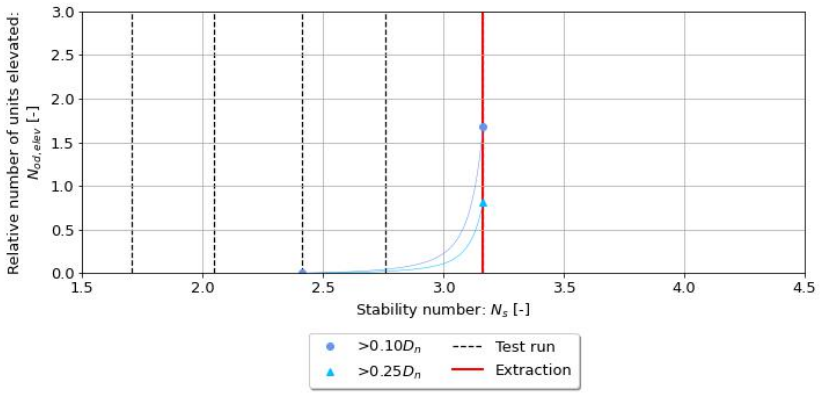

Figure I.14: Number of elevated units above threshold expressed as a fraction of the Coastalock nominal diameter within a strip of breakwater slope, with a width equal to the nominal diameter, under $s_{0p} = 0.04$, for short protrusions with 10% spacing in the 'PO-SWL' configuration in the 'Toe berm on Rough' set-up.

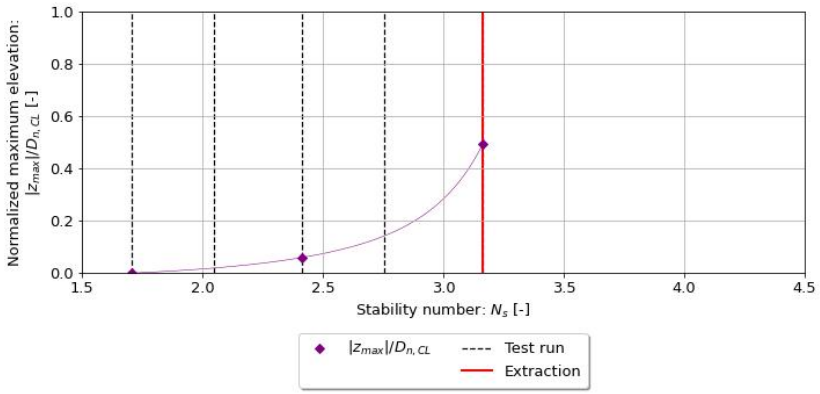

Figure I.15: Maximum unit elevation expressed as a fraction of the Coastalock nominal diameter, under $s_{0p} = 0.04$, for short protrusions with 10% spacing in the 'PO-SWL' configuration in the 'Toe berm on Rough' set-up.

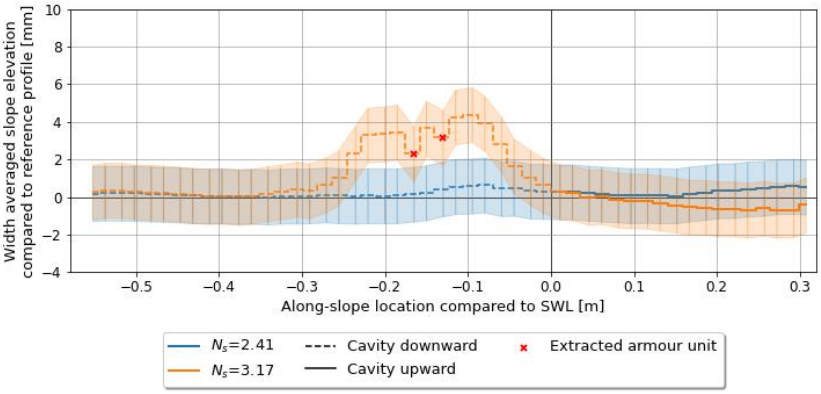

Figure I.16: Width averaged slope elevation compared to reference profile, under $s_{0p} = 0.04$, for short protrusions with 10% spacing in the 'PO-SWL' configuration in the 'Toe berm on Rough' set-up.

'Protrusion-Optimized' configuration with SWL orientation change in 'Toe berm on Smooth' set-up

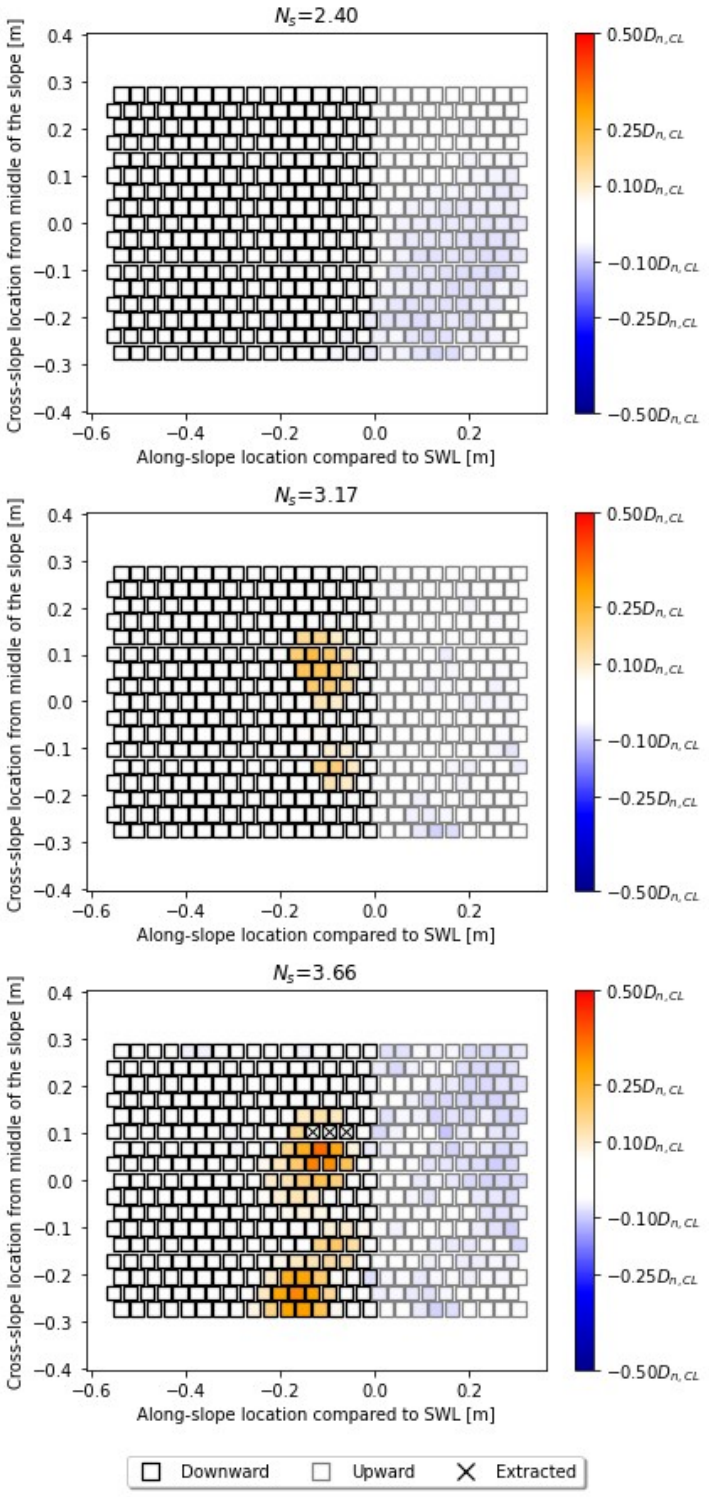

Figure I.17: Elevation change after the test run, compared to the reference profile after settling waves, expressed as a fraction of the Coastalock nominal diameter, under $s_{0p} = 0.04$, for short protrusions with 10% spacing in the 'PO-SWL' configuration in the 'Toe berm on Smooth' set-up.

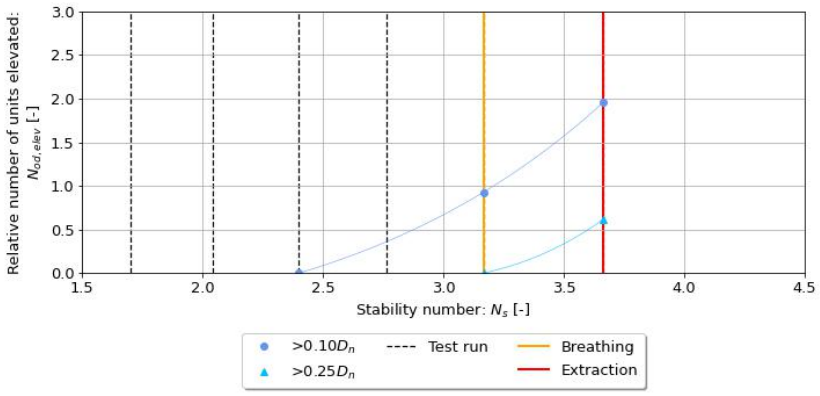

Figure I.18: Number of elevated units above threshold expressed as a fraction of the Coastalock nominal diameter within a strip of breakwater slope, with a width equal to the nominal diameter, under $s_{0p} = 0.04$, for short protrusions with 10% spacing in the 'PO-SWL' configuration in the 'Toe berm on Smooth' set-up.

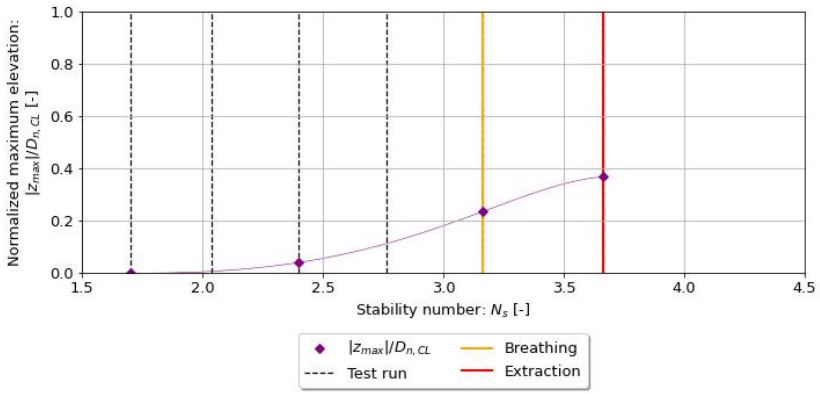

Figure I.19: Maximum unit elevation expressed as a fraction of the Coastalock nominal diameter, under $s_{0p} = 0.04$, for short protrusions with 10% spacing in the 'PO-SWL' configuration in the 'Toe berm on Smooth' set-up.

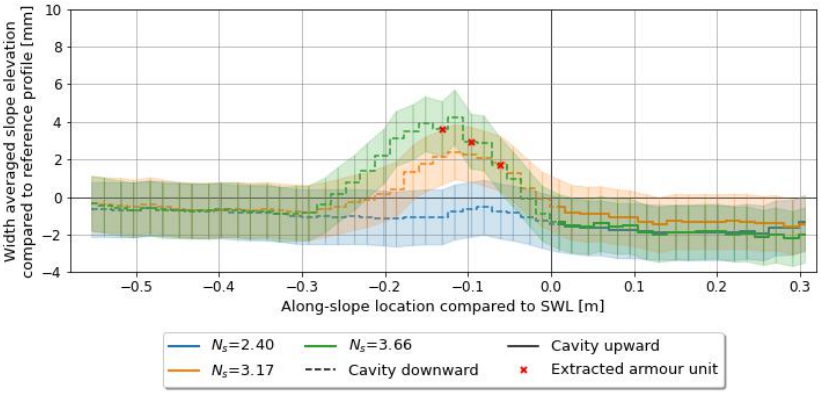

Figure I.20: Width averaged slope elevation compared to reference profile, under $s_{0p} = 0.04$, for short protrusions with 10% spacing in the 'PO-SWL' configuration in the 'Toe berm on Smooth' set-up.

I.2. Long Protrusions - 22.5% armour spacing

'Protrusion-Optimized' configuration with SWL orientation change in 'Deep Water' set-up.

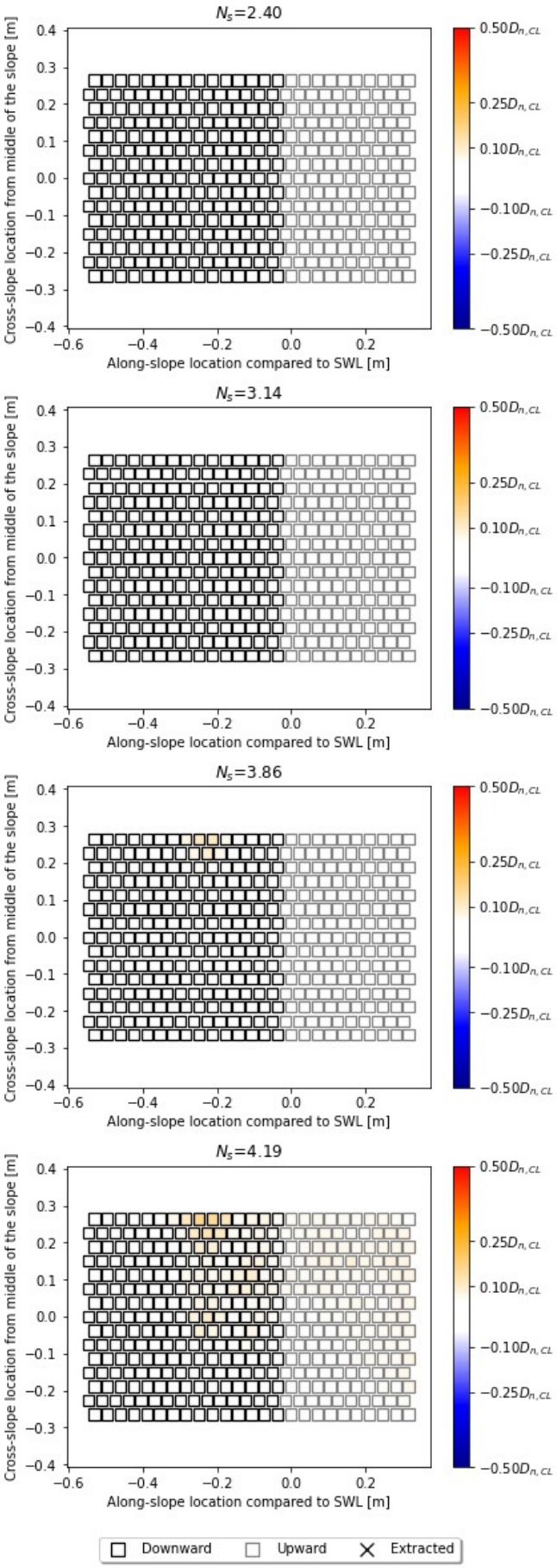

Figure I.21: Elevation change after the test run, compared to the reference profile after settling waves, expressed as a fraction of the Coastalock nominal diameter, under s_{0p} = 0.04, for long protrusions with 22.5% spacing in the 'PO-SWL' configuration in the 'Deep Water' set-up

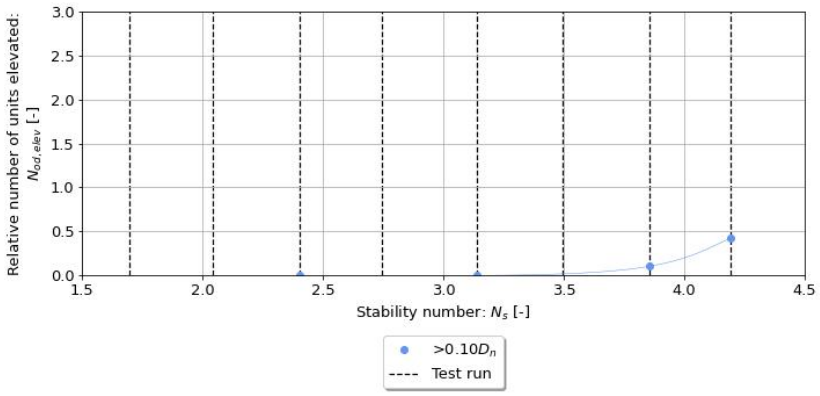

Figure I.22: Number of elevated units above threshold expressed as a fraction of the Coastalock nominal diameter within a strip of breakwater slope, with a width equal to the nominal diameter, under $s_{0p} = 0.04$, for long protrusions with 22.5% spacing in the 'PO-SWL' configuration in the 'Deep Water' set-up.

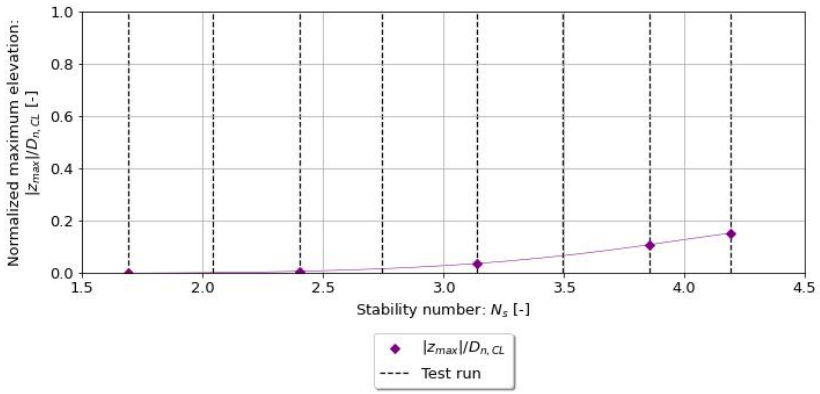

Figure I.23: Maximum unit elevation expressed as a fraction of the Coastalock nominal diameter, under $s_{0p} = 0.04$, for long protrusions with 22.5% spacing in the 'PO-SWL' configuration in the 'Deep Water' set-up.

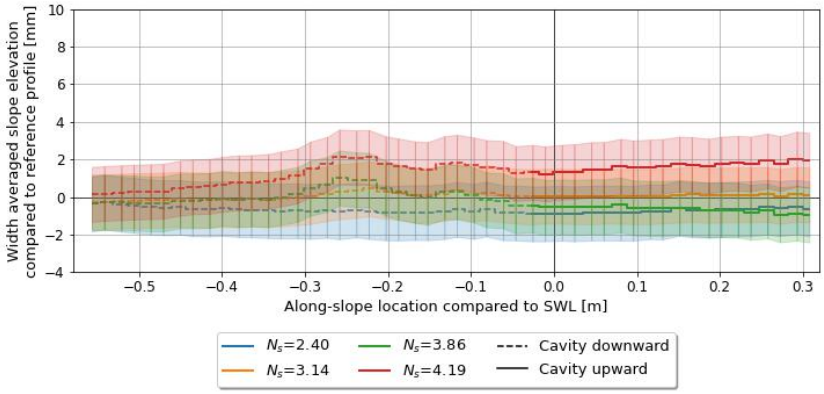

Figure I.24: Width averaged slope elevation compared to reference profile, under $s_{0p} = 0.04$, for long protrusions with 22.5% spacing in the 'PO-SWL' configuration in the 'Deep Water' set-up.

'Protrusion-Optimized' configuration with SWL orientation change in 'Toe berm on Rough' set-up.

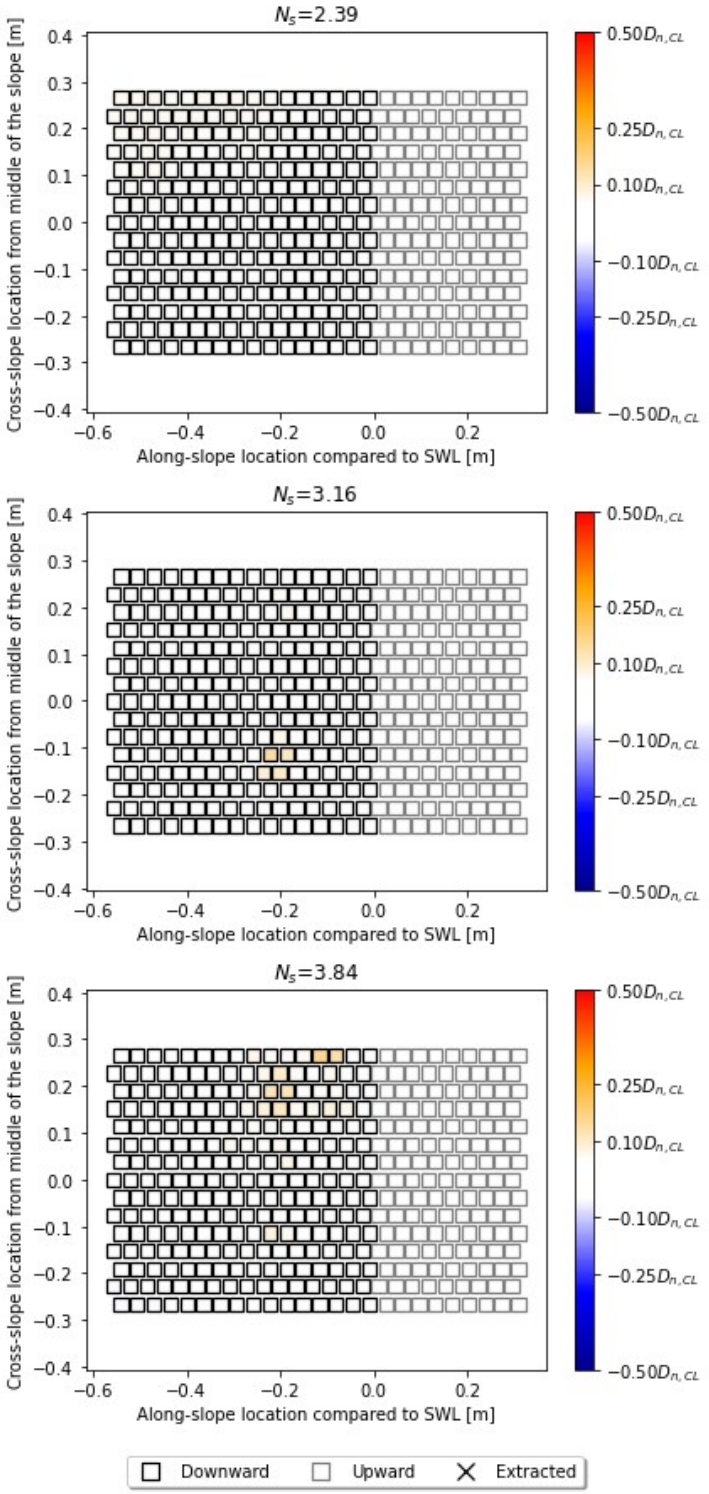

Figure I.25: Elevation change after the test run, compared to the reference profile after settling waves, expressed as a fraction of the Coastalock nominal diameter, under s_{0p} = 0.04, for long protrusions with 22.5% spacing in the 'PO-SWL' configuration in the 'Toe berm on Rough' set-up.

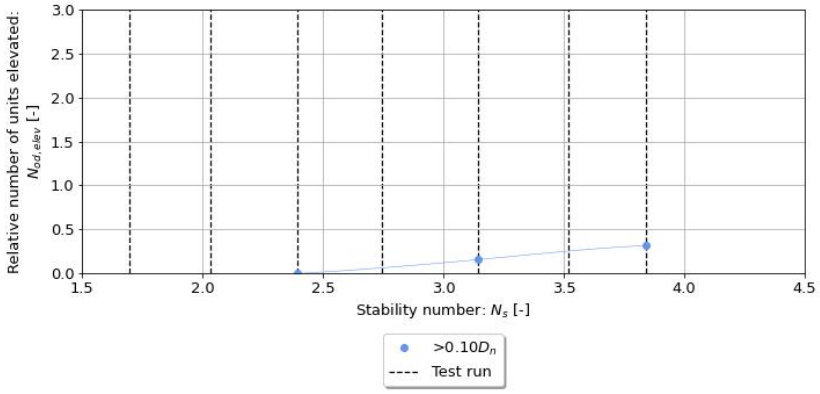

Figure I.26: Number of elevated units above threshold expressed as a fraction of the Coastalock nominal diameter within a strip of breakwater slope, with a width equal to the nominal diameter, under $s_{0p} = 0.04$, for long protrusions with 22.5% spacing in the 'PO-SWL' configuration in the 'Toe berm on Rough' set-up.

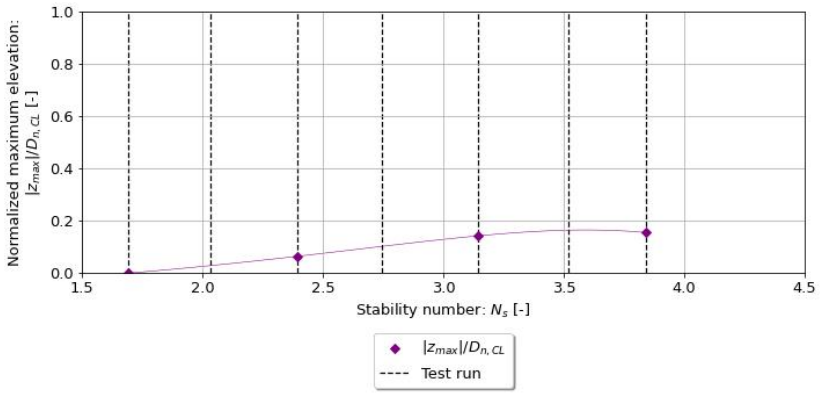

Figure I.27: Maximum unit elevation expressed as a fraction of the Coastalock nominal diameter, under $s_{0p} = 0.04$, for long protrusions with 22.5% spacing in the 'PO-SWL' configuration in the 'Toe berm on Rough' set-up.

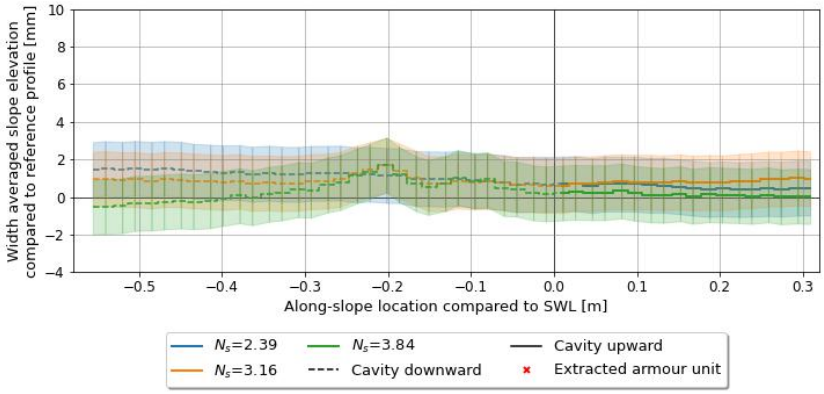

Figure I.28: Width averaged slope elevation compared to reference profile, under $s_{0p} = 0.04$, for long protrusions with 22.5% spacing in the 'PO-SWL' configuration in the 'Toe berm on Rough' set-up.

'Protrusion-Optimized' configuration with SWL orientation change in 'Toe berm on Smooth' set-up.

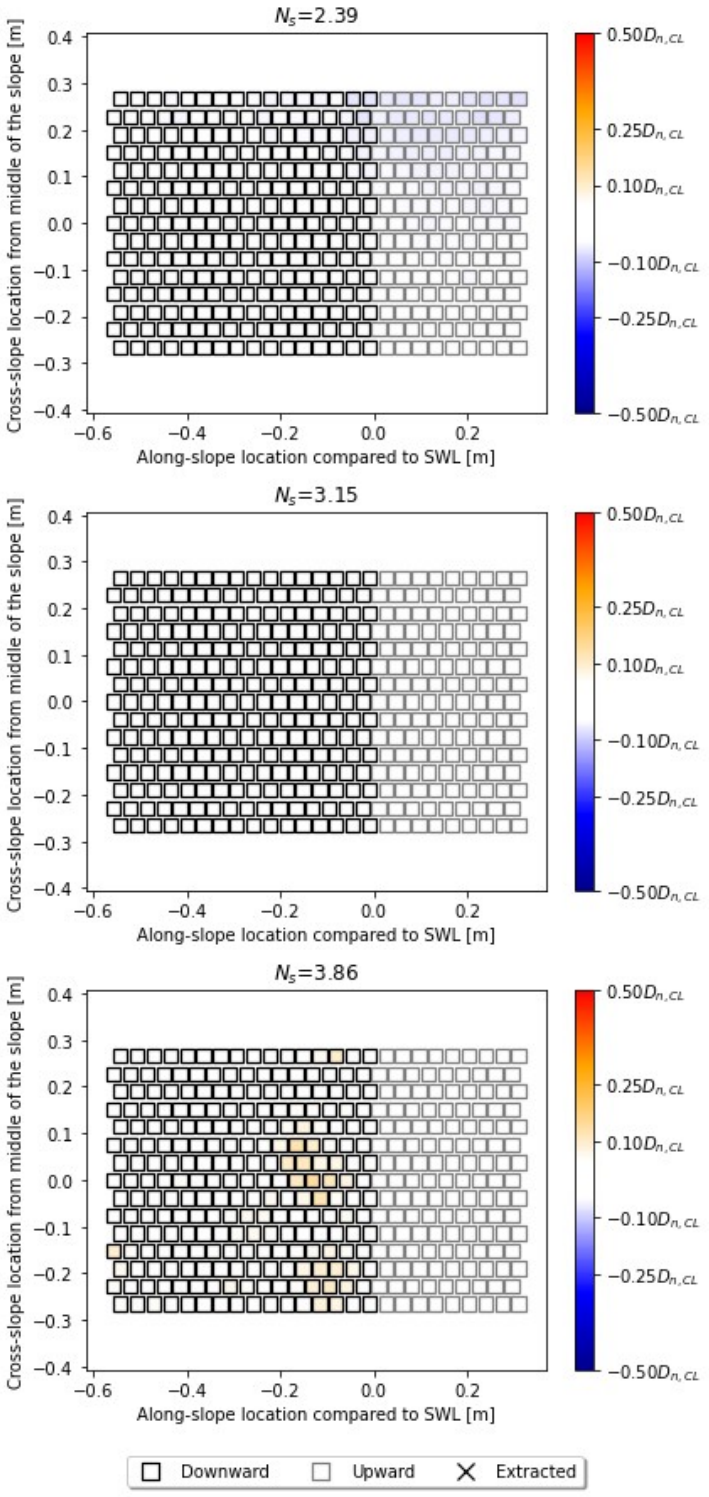

Figure I.29: Elevation change after the test run, compared to the reference profile after settling waves, expressed as a fraction of the Coastalock nominal diameter, under $s_{0p} = 0.04$, for long protrusions with 22.5% spacing in the 'PO-SWL' configuration in the 'Toe berm on Smooth' set-up.

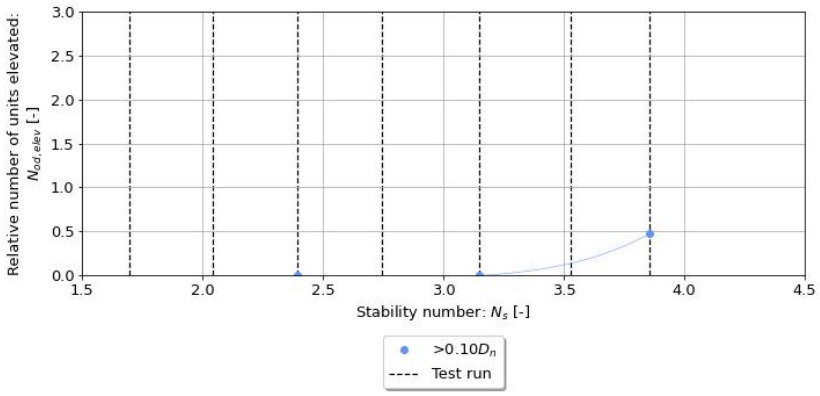

Figure I.30: Number of elevated units above threshold expressed as a fraction of the Coastalock nominal diameter within a strip of breakwater slope, with a width equal to the nominal diameter, under $s_{0p} = 0.04$, for long protrusions with 22.5% spacing in the 'PO-SWL' configuration in the 'Toe berm on Smooth' set-up.

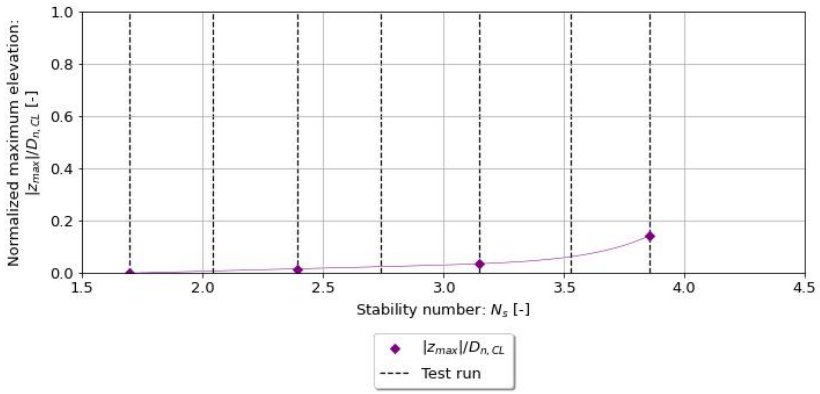

Figure I.31: Maximum unit elevation expressed as a fraction of the Coastalock nominal diameter, under $s_{0p} = 0.04$, for long protrusions with 22.5% spacing in the 'PO-SWL' configuration in the 'Toe berm on Smooth' set-up.

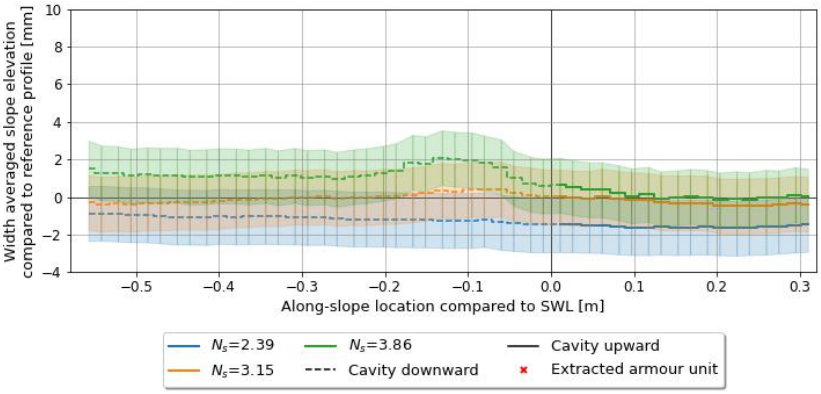

Figure I.32: Width averaged slope elevation compared to reference profile, under $s_{0p} = 0.04$, for long protrusions with 22.5% spacing in the 'PO-SWL' configuration in the 'Toe berm on Rough' set-up.